NONLINEAR FREQUENCY CONVERSION IN ISOTROPIC SEMICONDUCTOR WAVEGUIDES

Konstantinos Moutzouris

A Thesis Submitted for the Degree of PhD
at the
University of St Andrews

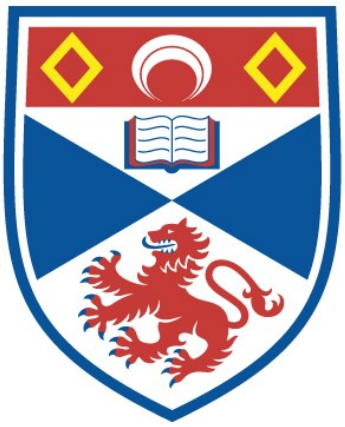

2003

Nonlinear Frequency Conversion in Isotropic Semiconductor Waveguides

Konstantinos Moutzouris

A thesis submitted to the University of St Andrews in application for the degree of Doctor of Philosophy

September 2003

ABSTRACT

This thesis describes an experimental investigation of optical frequency conversion in isotropic semiconductor waveguides by use of several phase-matching approaches.

Efficient, type I second harmonic generation of femtosecond pulses is reported in birefringently-phase-matched GaAs/Alox waveguides pumped at 2.01 μm. Practical second harmonic average powers of up to ~ 650 μW are obtained, for an average launched pump power of ~ 5 mW. This corresponds to a waveguide conversion efficiency of ~ 20 % and a normalized conversion efficiency of greater than 1000 % $W^{-1}cm^{-2}$. Pump depletion of more than 80 % is recorded.

Second harmonic generation by type I, third order quasi-phase-matching in a GaAs-AlAs superlattice waveguide is reported for fundamental wavelengths from ~1480 to 1520 nm. Quasi-phase-matching is achieved through modulation of the nonlinear coefficient $\chi_{zxy}^{(2)}$, which is realised by periodically tuning the superlattice bandgap. An average output power of ~25 nW is obtained for a launched pump power of <2.3 mW.

Type I second harmonic generation by use of first order quasi-phase-matching in a GaAs/AlAs symmetric superlattice waveguide is also reported, with femtosecond fundamental pulses at 1.55 μm. A periodic spatial modulation of the bulk-like second-order susceptibility $\chi_{zxy}^{(2)}$ is realized using quantum well intermixing by As^{+} ion implantation. A practical second harmonic average power of ~1.5 μW is detected, for a coupled pump power of ~11 mW.

Second harmonic generation through modal-phase-matching in GaAs/AlGaAs semiconductor waveguides is reported. Using femtosecond pulses, both type I and type II second harmonic conversion is demonstrated for fundamental wavelengths near 1.55 μm. An average second harmonic power of ~10.3 μW is collected at the waveguide output for a coupled pump power of <20 mW.

For a complete characterisation, the optical loss is measured in these nonlinear GaAs-based waveguides over the spectral range 1.3-2.1 μm in the infrared, by deploying a femtosecond scattering technique. Typical losses of ~5-10 dB/cm are measured for the best of the waveguides, while a systematic intensity and wavelength dependent study revealed the contribution of Rayleigh scattering and two photon absorption in the overall transmission loss.

Declarations

I, Konstantinos Moutzouris, hereby certify that this thesis, which is approximately 55000 words in length, has been written by me, that it is the record of work carried out by me and that it has not been submitted in any previous application for a higher degree.

Konstantinos Moutzouris September 2003

I was admitted as a research student in September 1999 and as a candidate for the degree of Doctor of Philosophy in September 1999; the higher study for which this is a record was carried out in the University of St. Andrews between 1999 and 2003.

Konstantinos Moutzouris September 2003

I hereby certify that the candidate has fulfilled the conditions of the Resolution and Regulations appropriate for the degree of Doctor of Philosophy in the University of St. Andrews and that the candidate is qualified to submit this thesis in application for that degree.

Dr. Majid Ebrahimzadeh September 2003

Copyright Declaration

In submitting this thesis to the University of St. Andrews I understand that I am giving permission for it to be made available for use in accordance with the regulations of the University Library for the time being in force, subject to any copyright vested in this work not being affected thereby. I also understand that the title and abstract will be published, and that a copy of the work may be made and supplied to any *bona fide* library or research worker.

Konstantinos Moutzouris September 2003

Acknowledgments

First and foremost, I wish to thank my supervisor throughout this work, ***Dr Majid Ebrahimzadeh***, for his guidance, insight and enthusiasm. For his support and encouragement I am greatly indebted.

My thanks are also due to the rest of the St. Andrews SCNLO group members, for their vital contribution to this work. That is, in a chronological order, to: ***Tom Brown*** (who introduced me to the world of experimental optics), ***Soma Venugopal Rao*** (who worked on this project for the greatest part of it), as well as the new "additions" to the group, ***Abdul***, ***Masood*** and ***Reza*** (to all of whom I wish the best in continuing this work).

Many thanks also to our collaborators from Paris, Glasgow, and Rome. Not only for contributing their expert knowledge in designing and fabricating nonlinear waveguides, but also because it was a great pleasure to work with all of them! From a long list of names, I would like to specially thank ***Alfredo De Rossi***, ***Vincent Berger,*** ***Amr Saher Helmy***, ***Khalil Zeaiter***, ***Todd Kleckner***, ***Daniele Modotto***, ***David Hutchings***, and ***Giuseppe Leo***.

Thanks also to a number of people in the school (staff and students) for their help and support. In particular, I wish to thank ***Ian Lindsay***, ***David Stothard***, ***Tom Edwards***, ***Arvydas Ruseckas***, ***Pablo Alvarez***, ***Ben Agate***, ***Michael Spurr***, ***Andrew Woodman***, ***Jonathan Phillips***, ***Julia Fenn***, ***Veneranda Garces-Chavez***, ***Edik Rafailov*** and ***Aly Gillies***, as well as, of course, the secretary ***Mary Rodger*** and the legendary workshop staff, ***George Radley*** and ***Paul Aitken***!

Many thanks to my friends in St Andrews, people like ***Kostas*** (Petridis), ***Yannis*** (Tsapras), ***Lefteris***, ***Vivi***, ***Tomas***, ***Yannis*** (Tellidis), ***Eva***, ***Petros***, ***Kostas*** (Yannopoulos), ***Kostas*** (Papathanassiou), ***Irene***, ***Yannis*** (Markouris), ***Valia***, ***Vaggelis***…

Many thanks also to ***Agapitos Roukounakis***, for causing all this.

Last but not least, thanks to ***Katrin***.

Thanks to ***Yannis*** and ***Maria***.

Kostas M.

Table of Contents

1. Prologue

The present thesis outlines work carried out at the University of St. Andrews during the period 1999-2003, in the area of nonlinear frequency conversion in III-V semiconductor waveguides. This work was performed within the frame of an ongoing European collaboration (OFCORSE project[1]), which comprised four participant members[2]. The objective of this collaboration is to exploit the optical nonlinearities in III-V semiconductor materials for efficient nonlinear frequency conversion. This could lead to the development of numerous functional devices operating in the near and mid-infrared (IR), ranging from second harmonic generation structures, to integrated devices for difference frequency generation, parametric amplification and oscillation.

Accessing the near and mid-IR spectral region is of considerable interest for a number of applications. Most molecules present vibrational resonances within the 2 to 20 μm wavelength range [1], making compact sources in the near and mid-IR imperative for spectroscopic studies [2,3], as well as for gas sensing purposes with potential use in environmental monitoring [4,5] and photo-medicine [6]. Furthermore, generation and conversion of coherent radiation at 1.55 μm could be useful for applications in wavelength division multiplexing and all-optical switching in telecommunication networks [7-9]. Nonlinear frequency conversion in this spectral range has also been proposed as a route to designing twin-photon sources for quantum optical communications [10] and for testing fundamental concepts of quantum physics and relativity [11].

Current infrared laser sources include narrow-band laser diodes [12], lead salt [13] and antimonide lasers [14]. In general these approaches require cryogenic cooling, offer modest output powers and do not produce a tunable output. A novel addition to the family of infrared sources is the quantum cascade laser [15], which is still

[1] Optical Frequency COnveRsion in Semiconductors

[2] 1) The group of Prof. Assanto at Roma University-III, which focused on theoretical studies,
2) The group of Prof. Berger at Thomson CSF (THALES), which was responsible for the design and fabrication of birefrintent materials,
3) The group of Prof. Aitchinson at Glasgow University, which concentrated its efforts on designing and fabricating quasi-phase-matched structures, and
4) The group of Dr. M. Ebrahimzadeh at St. Andrews, which undertook the responsibility of building a characterisation facility and carrying out the optical experiments on the materials.

undergoing intense development. Available quantum cascade lasers offer high output power levels and considerable temperature tuning, yet continuous-wave, room temperature operation has been proven illusive. Sources based on nonlinear frequency conversion (most notably, the optical parametric oscillation and difference frequency generation) represent an attractive alternative to accessing this spectral region [1, 4, 5, 16]. Efforts in this direction have been mostly focused on the search for materials with the desirable properties. Unquestionably, the most promising breakthrough in nonlinear material science and fabrication technology followed the development of periodically polled lithium niobate [17]. However, the transparency range of lithium niobate limits its use to wavelengths shorter than ~5 μm. Other infrared materials developed to date, such as chalcopyrites [18], still suffer from a variety of issues related to the immature growth technologies available.

In this direction, GaAs/AlGaAs emerges as a very attractive infrared nonlinear material system for a number of reasons. First and foremost, GaAs exhibits a large second order nonlinearity with reported values for the second order nonlinear coefficient $d_{14}=d_{36}$ of ~100 pm/V in the IR [19-23]. This value is approximately three times higher than the respective value for lithium niobate and two orders of magnitude larger than that of conventional birefringent materials. Further distinctive advantages of this material include its broad IR transparency (0.9-17 μm), low optical absorption, high damage threshold, high thermal conductivity and mature growth and fabrication technology, which supports the possibility of integration with semiconductor laser sources as well as the potential for mass production at low cost. On the negative side, GaAs has a cubic symmetry and thus is optically isotropic and lacks natural birefringence. Therefore, matching the phase velocities of the interacting waves (a necessity for efficient frequency conversion) is not a straightforward process. Circumventing the problem of phase-matching has been the principal challenge of this project. Three different phase-matching approaches have been proposed and studied:

- Artificial (or form) birefringence, by means of selective oxidation
- Quasi-phase-matching, through quantum well intermixing, and
- Modal-phase-matching

Within the broader framework of the OFCORSE project, scope of the present doctoral work was to investigate the feasibility of the preceding phase-matching techniques through investigations of second harmonic generation in guided-wave GaAs-based structures. The waveguide-based design yields the high intensities and provides maximised overlap between the interacting modes that are necessary for high conversion efficiencies. The significance of such a study is three-fold: Firstly, it is a step towards the establishment of GaAs as a practical nonlinear material. Secondly, it demonstrates a hybrid frequency converter with its own, independent significance. Thirdly, it serves as a guideline for the further development of integrated devices.

For this purpose, the early efforts were directed towards setting up a complete characterisation facility. A synchronously pumped, femtosecond optical parametric oscillator (OPO) was constructed and served as the pump source. The OPO was a reasonable choice, since it provides a unique wavelength tuning capability, which is necessary to overcome unavoidable inaccuracies and errors in the prediction of the phase-matching wavelength. Operation in the femtosecond regime was favoured in order to achieve the large peak powers necessary for efficient conversion. The laboratory was also equipped with a number of commercial instruments, including optic elements, end-fire coupling apparatus, IR cameras, microscopes and detection diagnostics.

The main body of the work involved experimental investigations of second harmonic generation in a large number of materials provided by the collaborators. In fact, successful harmonic generation was demonstrated by means of all three different phase-matching technologies. Experimental efforts concentrated on a) establishing that the generated signal is indeed result of a phase-matched interaction and b) determining the efficiency of the process. The latter, required theoretical calculations of a number of group-velocity dispersion related effects (that reveal the complicated dynamics in this time scale), as well as experimental determination of the propagation loss associated with the materials. Loss measurements were carried out using an improved scattering technique. Note that knowledge of the propagation loss is important not only for the purposes of the current work, but also for the calculation of the threshold pump power required for the consequent construction of integrated resonant devices by use of the same material.

This thesis is organised in eight chapters. The present (first) chapter provides a short introduction to the scope and challenges of this project. The second chapter summarises basic concepts of nonlinear optics that are fundamental to this work. The third chapter is dedicated to presenting an overview of the femtosecond optical parametric oscillator that was constructed and used as the main experimental tool for the material characterisation. The three following chapters present details of the different approaches used to solve the phase velocity synchronism problem, along with results from the corresponding harmonic generation experiments, namely: Phase-matching based on form firefringence (fourth chapter), quasi-phase-matching (fifth chapter) and modal-phase-matching (sixth chapter). The seventh chapter reports results from measurements of the propagation loss on these materials based on a femtosecond scattering technique. The thesis concludes with a summary and a comparison of the results, which is attempted in the eighth chapter. Finally, two appendices are included to discuss special issues on ultrashort pulse propagation and measurement (appendix A), and list the publications arising from this work (appendix B).

It should be mentioned that throughout these years a number of further experiments was carried out, including:

- Investigation of parametric oscillation based on a $LiInS_2$ crystal,
- Demonstration of optical rectification in GaAs waveguides, and
- Generation of femtosecond blue light pulses through frequency doubling in a BiBO crystal.

Details of these experiments (which are not directly related to the OFCORSE project) are not included on this thesis, mainly for reasons of conceptual continuity.

References

[1] K. Fradkin, A. Arie, A. Skliar, and G. Rosenman, *Tunable mid-infrared source by difference frequency generation in bulk periodically poled $KTiOPO_4$*, Appl. Phys. Lett. 74, 914, (1999)

[2] R.F. Curl, F.K. Tittel, *Tunable infrared laser spectroscopy*, Annu. Rep. Prog. Chem. Sel C 98, 217, (2002)

[3] L. Windhorn, T. Witte, J.S. Yeston, D. Proch, M. Motzkus, K.L. Kompa, and W. Fuss, *Molecular dissociation by mid-IR femtosecond pulses*, Chem. Phys. Lett. 357, 85, (2002)

[4] Y. Mine, N. Melander, D. Richter, D.G. Lancaster, K.P. Petrov, R.F. Curl, and F.K. Tittel, *Detection of formaldehyde using mid-infrared difference frequency generation*, Appl. Phys. B 65, 771, (1997)

[5] K.P. Petrov, A.T. Ryan, T.L. Patterson, L. Huang, S.J. Field, and D. J. Bamford, *Mid-infrared spectroscopic detection of trace gases using guided-wave difference frequency generation*, Appl. Phys. B 67, 357, (1998)

[6] W. Petrich, *Mid-infrared and Raman spectroscopy for medical diagnostics*, Appl. Spectr. Rev. 36, 181, (2001)

[7] S.J.B. Yoo, *Wavelength conversion technologies for WDM network applications*, IEEE J. Lightwave Tech. 14, 955, (1996)

[8] C.G. Trevino-Palacios, G.I. Stegeman, P. Baldi, and M.P.D. Micheli, *Wavelenght shifting using cascaded second order processes for WDM applications at 1.55 .µm*, Electron. Lett. 34, 2157, (1998)

[9] G.D. Landry, and T.A. Maldonado, *Switching and second harmonic generation using counterpropagating quasi-phase matching in a mirror-less configuration*, J. Lightwave Tech. 17, 316, (1999)

[10] W. Tittel, J. Brendel, N. Gisin, and H. Zbinden, Q*uantum cryptography using entangled photosin energy-time Bell states*, Phys. Rev. Lett. 84, 4737, (2000)

[11] N. Gisin, J. Brendel, H. Zbinden, A. Sergienko, and A. Muller, *Twin photon techniques for fiber measurements*, Proc. Symposium Opt. Fiber Measurements, NIST Boulder Colorado, 35, (1998)

[12] A. Joullie, E.M. Skouri, M. Garcia, P. Grech, A. Wilk, P. Christol, A.N. Baranov, A. Behres, J. Kluth, A. Stein, K. Heime, M. Heuken, S. Rushworth, E. Hulicius, and T. Simecek, *InAs(PSb)-based "W" quantum well laser diodes emitting near 3.3 µm*, Appl. Phys. Lett. 76, 2499, (2000)

[13] G.T. Forrest, D. Wall, and J. Oconnell, *Recent advances in lead salt laser technology and the implications for gas-analysis*, Proc. Soc. Photo-optical Instrumentation Engineers 461, 2, (1984)

[14] R.M. Biefeld, A.A. Allerman, S.R. Kurtz, E.D. Jones, I.J. Fritz, and R.M. Sieg, *The growth of infrared antimonide-based semiconductor lasers by metal-organic chemical vapor deposition*, J. Mater. Science 13, 649, (2002)

[15] F. Capasso, C. Gmachl, R. Paiella, A. Tredicucci, A.L. Hutchinson, D.L. Sivco, J.N. Baillargeon, A.Y. Cho, and H.C. Liu, *New frontiers in quantum cascade lasers and applications*, IEEE J. Selec. Top. Quant. Electron. 6, 931, (2002)

[16] D. Campi, and C. Cariasso, *Wavelength conversion technologies*, Photon. Tech. Lett. 2, 85, (2000)

[17] M.M. Fejer, G.A. Magel, and E.J. Lim, *Quasi-phase-matched interactions in lithium niobate*, Pros. SPIE 1148, 213, (1998)

[18] M.C. Ohmer, and R. Pandey, eds, Em*ergence of chalcopyrites and nonlinear optical materials*, Materials Research Bulletin, Special Issue, (1998)

[19] T. Skauli, K.L. Vodopyanov, T.J. Pinguet, A. Schober, O. Levi, L.A. Evers, M.M. Fejer, J.S. Harris, B. Gerard, L. Becouarn, E. Lallier, and G. Arisholm, *Measurement of the nonlinear coefficient of orientation-patterned GaAs and demonstration of highly efficient harmonic generation*, Opt. Lett. 27, 628, (2002)

[20] C.K.N. Patel, *Optical harmonic generation in the infrared using a CO_2 laser*, Phys. Rev. Lett. 16, 613, (1966)

[21] D.A. Roberts, *Simplified characterisation of uniaxial and biaxial nonlinear optical crystals – a plea for standardisation of nomenclature and conventions*, IEEE J. Quantum Electron. 28, 2057, (1992)

[22] M.M. Choy, and R.L. Byer, *Accurate second order susceptibility measurements of visible and infrared nonlinear crystals*, Phys. Rev. B 14, 1693, (1976)

[23] I. Shoji, T. Kondo, A. Kitamoto, M. Shirane, and R. Ito, *Absolute scale of second order nonlinear optical coefficients*, J. Opt. Soc. Am. B 14, 2268, (1997)

2. NONLINEAR OPTICS CONCEPTS

2.1 Review of Maxwell equations

In 1864, J.C. Maxwell enclosed the fundamental laws governing the generation, propagation and interaction of electromagnetic (EM) radiation with matter, in the famous set of equations (2-1). Expressed in MKSA units, Maxwell equations are:

$$\vec{\nabla} \times \vec{E}(\vec{r},t) + \frac{\partial}{\partial t}\vec{B}(\vec{r},t) = 0 \quad \text{(2-1 a)}$$

$$\vec{\nabla} \times \vec{H}(\vec{r},t) - \frac{\partial}{\partial t}\vec{D}(\vec{r},t) = \vec{J}(\vec{r},t) \quad \text{(2-1 b)}$$

$$\vec{\nabla} \cdot \vec{B}(\vec{r},t) = 0 \quad \text{(2-1 c)}$$

$$\vec{\nabla} \cdot \vec{D}(\vec{r},t) = \rho(\vec{r},t) \quad \text{(2-1 d)}$$

where:
$\vec{E}$ …is the electric field intensity vector in Volts/meter
$\vec{H}$ …is the magnetic field intensity vector in Ampere/meter
$\vec{B}$ …is the magnetic flux density vector in Tesla
$\vec{D}$ …is the electric displacement vector in Coulomb/meter^2
$\vec{J}$ …is the electric current density vector in Ampere/meter^2
ρ …is the electric charge density in Coulomb/meter^3

$\vec{E}, \vec{H}, \vec{B}, \vec{D}, \vec{J}$ and ρ are real functions of time t and spatial location with respect to a specific coordinate system $\vec{r}$. Solving Maxwell equations to determine the field vectors, requires three relations that reveal the behaviour of the medium under the influence of the field, known as the constitutive relations:

$$\vec{D}(\vec{r},t) = \vec{D}\{\vec{E}(\vec{r},t), \vec{H}(\vec{r},t)\} \quad \text{(2-2 a)}$$

$$\vec{B}(\vec{r},t) = \vec{B}\{\vec{E}(\vec{r},t), \vec{H}(\vec{r},t)\} \quad \text{(2-2 b)}$$

$$\vec{J}(\vec{r},t) = \vec{J}\{\vec{E}(\vec{r},t), \vec{H}(\vec{r},t)\} \quad \text{(2-2 c)}$$

If the field vectors are linearly related, the medium is said to be linear and the constitutive relations take the form:

$$\vec{D}(\vec{r},t) = \varepsilon_0 \vec{E}(\vec{r},t) + \vec{P}(\vec{r},t) = \varepsilon_0 \varepsilon(\vec{r})\vec{E}(\vec{r},t) \quad \text{(2-3 a)}$$

$$\vec{B}(\vec{r},t) = \mu_0 \vec{H}(\vec{r},t) + \vec{M}(\vec{r},t) = \mu_0 \mu(\vec{r})\vec{H}(\vec{r},t) \quad \text{(2-3 b)}$$

$$\vec{J}(\vec{r},t) = \sigma(\vec{r})\vec{E}(\vec{r},t) \quad \text{(2-3 c)}$$

where: ε_0 … is the electric permittivity of free space
μ_0 … is the magnetic permeability of free space
$\vec{P}$ … is the macroscopically averaged electric dipole (optical polarisation)
$\vec{M}$ … is the magnetisation
ε ... is the relative permittivity (dielectric constant) of the medium
μ ... is the relative permeability of the medium
σ ... is the electric conductivity of the medium

If ε, μ and σ are constant through the medium, the medium is said to be homogenous. The medium is referred to as isotropic when ε, μ and σ are scalar quantities. In the proceeding equations, it has been assumed that the polarisation (magnetisation) and the electric (magnetic) field intensity are linearly related, so that one can write:

$$\vec{P}(\vec{r},t) = \varepsilon_0 [1 - \varepsilon(\vec{r})]\vec{E}(\vec{r},t) = \varepsilon_0 \chi^{(1)} \vec{E}(\vec{r},t) \tag{2-4}$$

where:

$$\chi^{(1)} = 1 - \varepsilon \tag{2-5}$$

is known as the (first order or linear) susceptibility of the medium.

In the rest of this section some main results are outlined in the linear response limit for future reference. The most important consequence arising from Maxwell equations is that they can be formulated in a wave-motion equation and, thus, establish the existence of electromagnetic waves. For a linear, isotropic and homogeneous medium the wave equation derived by use of the standard four-step-process[1] has the well-known form:

$$\Delta\vec{E}(\vec{r},t) - \varepsilon_0\varepsilon\mu_0\mu\frac{\partial^2\vec{E}(\vec{r},t)}{\partial t^2} = \mu_0\mu\frac{\partial\vec{J}(\vec{r},t)}{\partial t} \tag{2-6}$$

where $\Delta = \nabla^2$ denotes the linear vector Laplace operator.

---

[1] (1) From (2-1 a) follows: $\vec{\nabla}\times(\vec{\nabla}\times\vec{E}) = -\mu_0\mu\frac{\partial}{\partial t}(\vec{\nabla}\times\vec{H})$

(2) Substituting $\vec{\nabla}\times\vec{H}$ from Eq. (2-1 b) gives: $\vec{\nabla}\times(\vec{\nabla}\times\vec{E}) = -\mu_0\mu\frac{\partial}{\partial t}\vec{J} - \varepsilon_0\varepsilon\mu_0\mu\frac{\partial}{\partial t^2}\vec{E}$

(3) Applying the vector identity $\vec{\nabla}\times(\vec{\nabla}\times\vec{A}) = \vec{\nabla}(\vec{\nabla}\cdot\vec{A}) - \Delta\vec{A}$ the proceeding can be rewritten as:

$\vec{\nabla}(\vec{\nabla}\cdot\vec{E}) - \Delta\vec{E} = -\mu_0\mu\frac{\partial}{\partial t}\vec{J} - \varepsilon_0\varepsilon\mu_0\mu\frac{\partial}{\partial t^2}\vec{E}$

(4) Substituting $\vec{\nabla}\cdot\vec{E}$ from Eq. (2-1 d) it follows: $\vec{\nabla}(\frac{\rho}{\varepsilon_0\varepsilon}) - \Delta\vec{E} = -\mu_0\mu\frac{\partial}{\partial t}\vec{J} - \varepsilon_0\varepsilon\mu_0\mu\frac{\partial}{\partial t^2}\vec{E}$

The last equation is identical to Eq. (2-5), under the assumption that the electric charge density is homogeneous and thus: $\vec{\nabla}\rho = 0$.

It can be readily recognised that Eq. (2-6) manifests the existence of electromagnetic waves that propagate with a velocity given by:

$$\upsilon = \frac{1}{\sqrt{\varepsilon_0 \varepsilon \mu_0 \mu}} = \frac{c}{\sqrt{\varepsilon \mu}} = \frac{c}{n} \tag{2-7}$$

where $c = 1/\sqrt{\varepsilon_0 \mu_0}$ is the propagation velocity in free space and

$$n = \sqrt{\varepsilon \mu} \tag{2-8}$$

is the refractive index of the medium. The disturbance term $\partial \vec{J} / \partial t$ on the right hand side of the wave equation has a dual interpretation. Firstly, it indicates that time-varying currents (i.e., accelerated charges) are responsible for EM wave generation. Secondly, it represents a loss factor for wave propagation in conductive materials ($\sigma \neq 0$). To simplify the treatment, in the rest of this chapter considerations are limited to non-conductive, loss-less ($\vec{J} = \sigma = 0$), non-magnetic ($\vec{M} = 0, \mu = 1$) media with no free charges ($\rho = 0$).

One family of solutions to the wave equation (2-6) comprises functions that vary sinusoidally in time with a single angular frequency, the conventional representation of which reads:

$$\vec{E}(\vec{r}, t) = \vec{E}(\vec{r}) \exp(-i\omega t) + \vec{E}^*(\vec{r}) \exp(i\omega t) \tag{2-9}$$

where: $\vec{E}(\vec{r})$ is the complex field amplitude, ω is the frequency and the second term of the summation is the complex conjugate of the first term, to ensure that the instantaneous electric field $\vec{E}(\vec{r}, t)$ is a real quantity. This type of fields, known as time-harmonic, is of particular interest for two reasons. The first reason is that any arbitrary solution of Maxwell equations can be reconstructed by Fourier superposition according to:

$$\vec{E}(\vec{r}, t) = \int_{-\infty}^{+\infty} \vec{E}(\vec{r}, \omega) e^{-i\omega t} d\omega \tag{2-10}$$

where the Fourier amplitude $\vec{E}(\vec{r}, \omega)$ denotes the complex field amplitude for each individual frequency component. The second reason is that time harmonic fields can be used to eliminate the explicit time dependency in Maxwell equations and, thus, facilitate the study of EM phenomena in the frequency domain. In fact, by substituting Eq. (2-9) into the set of equations (2-1), the time-independent form of Maxwell equations can be obtained.

$$\vec{\nabla} \times \vec{E}(\vec{r}) = i\omega \cdot \vec{B}(\vec{r}) \qquad \vec{\nabla} \times \vec{H}(\vec{r}) = -i\omega \cdot \vec{D}(\vec{r})$$

$$\vec{\nabla} \cdot \vec{B}(\vec{r}) = 0 \qquad \vec{\nabla} \cdot \vec{B}(\vec{r}) = 0$$

Following the same four-step process a wave equation in the frequency domain can be derived, which for non-conductive, non-magnetic, charge-free, linear, isotropic and homogeneous media has the form:

$$\Delta\vec{E}(\vec{r}) + \omega^2 \varepsilon_0 \varepsilon \mu_0 \mu \vec{E}(\vec{r}) = 0 \tag{2-11}$$

The solutions of Eq. (2-11) are known as monochromatic or continuous EM waves and cover the entire EM spectrum. In fact, Eq. (2-11) is satisfied by functions of the form:

$$\vec{E}(\vec{r}) = \vec{E} \exp(i\vec{k}\vec{r}) \tag{2-12}$$

where $\vec{E}$ is a constant complex amplitude vector and $\vec{k}$ is known as the propagation vector. Therefore, combining Eqs. (2-9) and (2-12) the real field vector emerges:

$$\vec{E}(\vec{r},t) = \vec{E} \exp(i(\vec{k}\vec{r} - \omega t)) + \vec{E}^* \exp(-i(\vec{k}\vec{r} - \omega t)) \tag{2-13}$$

It is evident that for any given real vector $\vec{k}$, a constant phase front of the field (i.e., a surface on which the field amplitude is constant) is defined by setting $\vec{k} \cdot \vec{r} = \text{constant}$. In turn, this condition implies that a constant phase front is a plane surface normal to $\vec{k}$ that propagates in the direction of $\vec{k}$. Such waves are known as plane waves. Substitution of Eq. (2-12) into Eq. (2-11) yields the dispersion relation:

$$k = \omega\sqrt{\varepsilon_0 \varepsilon \mu_0 \mu} = \frac{n\omega}{c} \tag{2-14}$$

where $k = |\vec{k}|$ is the propagation constant (or wave number). It is convenient here to define the spatial and temporal period of the wave, known as wavelength λ and period *T*, which readily from Eq. (2-13) can be expressed as:

$$\lambda = \frac{2\pi}{k} = \frac{2\pi c}{n\varpi} \qquad \text{and} \qquad T = \frac{1}{\nu} = \frac{2\pi}{\omega} \tag{2-15}$$

where *ν* is the frequency of the wave. It can be seen from the above equations that the wave propagation velocity is related to the frequency and the wavelength via:

$$\upsilon = \frac{c}{n} = \lambda\nu \tag{2-16}$$

The wavelength λ_0 in free space (n=1) can also be introduced via $c=\lambda_0 \nu$, so that one can write $\lambda = \lambda_0 / n$ and:

$$k = \frac{2\pi n}{\lambda_0} \tag{2-17}$$

Note that the operation of ∇ on the spatial dependency $\exp(i\vec{k}\vec{r})$ is equivalent to replacing ∇ with $i\vec{k}$. Using this, the Maxwell equations in the frequency domain for a linear, isotropic and homogeneous medium can be rewritten as:

$$\vec{k} \times \vec{E}(\vec{r}) = -\omega \cdot \vec{B}(\vec{r}) \qquad \vec{k} \times \vec{H}(\vec{r}) = \omega \cdot \vec{D}(\vec{r})$$

$$\vec{k} \cdot \vec{B}(\vec{r}) = 0 \qquad \vec{k} \cdot \vec{D}(\vec{r}) = 0$$

These equations (viewed in combination with the constitutive relations for a linear and isotropic medium which suggest that $\vec{E} // \vec{D}$ and $\vec{B} // \vec{H}$) underline the transverse vectorial nature of plane EM waves, usually referred to as polarisation. In other words, they imply that $\vec{E}$ and $\vec{H}$ are orthogonal and lie in a plane orthogonal to the propagation direction.

Finally, it should be noted that the product of the electric field vector by the magnetic field vector is a quantity with dimensions of Watt/meter^2, i.e. it has units of power flux density. Based on that (and without any further mathematical proof here), the Poynting vector:

$$\vec{S} = \vec{E} \times \vec{H} \tag{2-18}$$

can be introduced to represent the flow of electromagnetic energy with regard to both its magnitude and direction of propagation.

This section presented a brief overview of the Maxwell equations and useful results in the linear-optics limit. In particular, the formulation of Maxwell equations in a wave-motion equation was outlined and the plane wave solutions presented. In this analysis, considerations were limited to isotropic and homogeneous media. In a later section (2.2.2), the consequences of expanding the scalar dielectric constant (and hence the linear susceptibility) into a tensor to account for the optical anisotropy, which is present in a number of media, will be discussed. In what follows, a short introduction to the optical polarisation of matter under the influence of an external field is given to serve as a transition to the nonlinear response regime.

2.2 On the optical polarisation of matter

It has been shown that linear optics is based on the assumption that the EM field vectors are linearly related according to the constitutive relations (2-3). In turn, this imposes the condition that the optical polarisation of matter under the influence of the field is also linearly related to the electric field intensity, as Eq. (2-4) indicates. Evidently, the optical polarisation itself becomes a vital quantity for an accurate description of EM phenomena. Generally, the optical polarisation represents the macroscopically averaged electric dipole and is given by:

$$\vec{P} = -N \cdot e \cdot \vec{\delta} \tag{2-19}$$

where N is the number of atoms over which the averaging is taking place, e is the electron charge and $\vec{\delta}$ is the electron displacement from the equilibrium position.

For the calculation of the optical polarisation, the classical atomic model of Lorentz can be used in the linear limit. According to the model, an external field causes a harmonic oscillator type of electronic motion around the nuclei. However, in presence of sufficiently strong fields, the deviation of electrons from the equilibrium position can become large enough to break the harmonicity of the electron oscillators. Extension of the standard model to that of an anharmonic oscillator by Bloembergen [1] set the foundations of the field of nonlinear optics

2.2.1 The anharmonic oscillator treatment of the optical polarisation

A number of authors [1-5] have discussed the anharmonic oscillator model of the optical polarisation in a quantum mechanics context. Such a study is beyond the scope of this thesis. Instead, an overview of the problem in a classical formalism will be allowed [6]. To simplify the problem further, the electron coordinate $\vec{\delta}$ will be constrained in one dimension [7]. The scalar electron coordinate δ is required to satisfy the equation of motion of a one-dimensional anharmonic oscillator driven by a field, which in the most general case has a number of individual frequency components:

$$E(r,t) = \sum_n \frac{1}{2}[E_n(r) \cdot e^{-i\omega_n t} + E_n^*(r) \cdot e^{i\omega_n t}] \tag{2-20}$$

Note that in this one-dimensional analysis the field is also taken as scalar, while the assumption of *n* discrete frequency components allows reduction of the integral field expression (2-10) to the preceding summation form. Assuming a damping force $-2m\gamma\dot{\delta}$, and correcting the linear (harmonic) restoring force by a series of infinite higher order factors:

$$F_{res} = -m\omega_0^2\delta - m\sum_{l=2}^{\infty} a_l \cdot \delta^l \tag{2-21}$$

where ω_o is the atomic resonance frequency and *m* the electronic mass, the equation of motion of the anharmonic oscillator can be written as:

$$\ddot{\delta} + 2\gamma\dot{\delta} + \omega_0^2\delta + \sum_{l=2}^{\infty} a_l \cdot \delta^l = -\frac{e}{m} \cdot E(r,t) \tag{2-22}$$

There is no known analytical solution to Eq. (2-22). However, under the assumption that the anharmonic coefficients α_l are small compared to the linear ω_0, it is useful to try a solution of the form:

$$\delta = \sum_{s=1}^{\infty} \delta^{(s)} = \sum_{s=1}^{\infty} \xi_s \cdot E^s(r,t) \tag{2-23}$$

where the following definition is used:

$$\delta^{(s)} = \xi_s \cdot E^s(r,t) \tag{2-24}$$

Inserting (2-23) into (2-22) gives:

$$\sum_{s=1}^{\infty} \ddot{\delta}^{(s)} + 2\gamma\sum_{s=1}^{\infty} \dot{\delta}^{(s)} + \omega_0^2\sum_{s=1}^{\infty} \delta^{(s)} + \sum_{l=2}^{\infty} a_l [\sum_{s=1}^{\infty} \delta^{(s)}]^l = -\frac{e}{m\xi_1}\delta^{(1)} \tag{2-25}$$

Terms of same order in $E(r,t)$ can now be collected and required to satisfy (2-25) separately. From the definition of the field (2-20) it is clear that all $\delta^{(s)}, \dot{\delta}^{(s)}$ and $\ddot{\delta}^{(s)}$ are of *s*-order in $E(r,t)$. Therefore, each individual term of the three first summations in the left side of (2-25) contributes to an *s*-order term. The fourth double-summation, contributes terms in orders varying for each value of *l*, from *l* to ∞, where $l \geq 2$. The right side term is of first order. Hence, equation (2-25) is equivalent to a system of infinite differential equations of increasing order, the first three of which are clearly:

$$\ddot{\delta}^{(1)} + 2\gamma\dot{\delta}^{(1)} + \omega_0^2\delta^{(1)} = -\frac{e}{m\xi_1}\delta^{(1)} \tag{2-26 a}$$

$$\ddot{\delta}^{(2)} + 2\gamma\dot{\delta}^{(2)} + \omega_0^2\delta^{(2)} + a_2(\delta^{(1)})^2 = 0 \tag{2-26 b}$$

$$\ddot{\delta}^{(3)} + 2\gamma\dot{\delta}^{(3)} + \omega_0^2\delta^{(3)} + 2a_2\delta^{(1)}\delta^{(2)} + a_3(\delta^{(1)})^3 = 0 \qquad \text{(2-26 c)}$$

Equation (2-26 a) can be recognized as the motion equation of a harmonic oscillator, the solution of which is rather trivial and coincides with the result of the conventional Lorenz model:

$$\delta^{(1)} = -\frac{e}{m}\sum_n \frac{1}{2}\left[\frac{E_n(r)\cdot e^{-i\omega_n t}}{D(\omega_n)} + c.c.\right] \qquad \text{(2-27)}$$

where the following definition is used:

$$D(\omega_n) = \omega_0^2 - 2\gamma i\omega_n - \omega_n^2 \qquad \text{(2-28)}$$

Combining equations (2-24), (2-27) and (2-28), equation (2-26 b) gives:

$$\delta^{(2)} = \frac{e^2 a_2}{m^2}\sum_n\sum_m \frac{1}{2}\left[\frac{E_n(r)\cdot E_m(r)\cdot e^{-i(\omega_n+\omega_m)t}}{D(\omega_n)\cdot D(\omega_m)\cdot D(\omega_n+\omega_m)} + c.c.\right] \qquad \text{(2-29)}$$

Now the third order term can be calculated from (2-26 c) and so forth for higher orders. From the definition of the polarisation density it is obvious that the Eq. (2-23) suggests that the polarisation is given by a series of the form:

$$P = \sum_s P^{(s)} = -N\cdot e\cdot\sum_s \delta^{(s)} \qquad \text{(2-30)}$$

where the first order or linear polarisation is:

$$P^{(1)} = N\frac{e^2}{m}\sum_n \frac{1}{2}\left[\frac{E_n(r)\cdot e^{-i\omega_n t}}{D(\omega_n)} + c.c.\right] \qquad \text{(2-31)}$$

and the second order nonlinear polarisation is:

$$P^{(2)} = -N\frac{e^3 a_2}{m^2}\sum_n\sum_m \frac{1}{2}\left[\frac{E_n(r)\cdot E_m(r)\cdot e^{-i(\omega_n+\omega_m)t}}{D(\omega_n)\cdot D(\omega_m)\cdot D(\omega_n+\omega_m)} + c.c.\right] \qquad \text{(2-32)}$$

It is interesting to point out that the linear polarisation comprises same frequency components as the incident field. On the other hand, the second order polarisation involves all possible frequency components of the form:

$$\omega_q = \omega_n + \omega_m \qquad \text{(2-33)}$$

Separating the polarisation frequency components, equations (2-31) and (2-32) can be written in the equivalent form:

$$P^{(1)}(\omega_n) = \frac{N\cdot e^2/m}{D(\omega_n)}\cdot E_n(r)\cdot e^{-i\omega_n t} \qquad \text{(2-34)}$$

$$P^{(2)}(\omega_q,\omega_n,\omega_m) = \frac{N\cdot e^3(-a_2/m^2)}{D(\omega_n)\cdot D(\omega_m)\cdot D(\omega_q)}\cdot E_n(r)\cdot E_m(r)\cdot e^{-i\omega_q t} \qquad \text{(2-35)}$$

The complex conjugate terms of (2-31) and (2-32) appear in (2-34) and (2-35), respectively, through the allowed negative values of ω_n and ω_m. Clearly, the second order polarisation of matter can be viewed as the interaction of two monochromatic electromagnetic waves at frequencies ω_n and ω_m, giving rise to all possible frequency components ω_q such as defined in (2-32), namely:

- $\omega_q = \pm(2\omega_n)$ and $\omega_q = \pm(2\omega_m)$ (second harmonic component)
- $\omega_q = \pm(\omega_n + \omega_m)$ (sum frequency component)
- $\omega_q = \pm(\omega_n - \omega_m)$ (difference frequency component) and
- $\omega_q = 0$ (DC component).

The third and higher order polarisation of matter is responsible for many interesting phenomena, such as the Kerr effect [8], two-photon absorption [9], Brillouin and Raman scattering [10], four wave mixing [11], etc. However, all effects of interest for the present work are related to the second order nonlinear polarisation and therefore no further discussion on the higher order terms need be included.

Finally, it should be noticed that the anharmonic restoring force assumed in (2-21) corresponds to a potential energy function of the form:

$$U(\delta) = -\int F_{res}\, d\delta = \frac{1}{2} m\omega_0^2 \delta^2 + \sum_s \frac{1}{s+1} a_s \cdot \delta^{s+1} \tag{2-36}$$

It is clear that in the case of materials possessing a centre of symmetry, the electronic potential energy should reflect the symmetry in a way such that: $U(\delta) = U(-\delta)$. This implies that only even powers of δ should appear in (2-36) and consequently only odd values are allowed for the variable *s*. Hence, for a centrocymmetric material ($a_2 = 0$) the equation responsible for the excitation of second order polarisation (2-10 b) reduces to:

$$\ddot{\delta}^{(2)} + 2\gamma\dot{\delta}^{(2)} + \omega_0^2 \delta^{(2)} = 0$$

Since this is the equation of an oscillator damped but not driven, the steady-state solution is $\delta^{(2)} = 0$. Therefore, no second order polarisation is present in centrosymmetric media.

2.2.2 Nonlinear susceptibility

Previously the linear (or first order) susceptibility was introduced as the quantity that relates the electric field to the first order polarisation (see Eq. (2-5)). In a similar manner, the nth-order susceptibility $\chi^{(n)}$ is defined as the quantity that relates the electric filed with the *n*th-order polarisation. For instance, the second order susceptibility is given by:

$$P^{(2)}(\omega_q, \omega_n, \omega_m) = \varepsilon_0 \chi^{(2)}(\omega_q, \omega_n, \omega_m) E_n(r,t) E_m(r,t) \tag{2-37}$$

Eqs. (2-5) and (2-37), complemented with Eqs. (2-34) and (2-35), respectively, provide direct analytical expressions for the first and second order susceptibility:

$$\chi^{(1)}(\omega_n) = \frac{N \cdot e^2 / (m \cdot \varepsilon_0)}{D(\omega_n)} \tag{2-38}$$

$$\chi^{(2)}(\omega_q, \omega_n, \omega_m) = \frac{N \cdot e^3 [-a_2 / (m^2 \cdot \varepsilon_0)]}{D(\omega_n) \cdot D(\omega_m) \cdot D(\omega_q)} \tag{2-39}$$

It can therefore be seen that:

$$\chi^{(2)}(\omega_q, \omega_n, \omega_m) \propto \chi^{(1)}(\omega_q) \chi^{(1)}(\omega_n) \chi^{(1)}(\omega_m) \tag{2-40}$$

The general expression (2-37) clearly implies that the polarisation components at the second harmonic, sum mixing, and difference mixing frequencies are:

$$P^{(2)}(2\omega_n, \omega_n, \omega_n) = 1/2 \chi^{(2)}(2\omega_n, \omega_n, \omega_n) \varepsilon_0 E_n^2(r,t) \tag{2-41 a}$$

$$P^{(2)}(\omega_n + \omega_m, \omega_n, \omega_m) = \chi^{(2)}(\omega_n + \omega_m, \omega_n, \omega_m) \varepsilon_0 E_n(r,t) E_m(r,t) \tag{2-41 b}$$

$$P^{(2)}(\omega_n - \omega_m, \omega_n, -\omega_m) = \chi^{(2)}(\omega_n - \omega_m, \omega_n, -\omega_m) \varepsilon_0 E_n(r,t) E_m^*(r,t) \tag{2-41 c}$$

where, by definition, $E_m^*(r,t)$ is the field at the frequency $-\omega_m$.

The factor 1/2 appearing in the expression for second harmonic generation, known as the degeneracy factor, originates from the fact that during this process two of the interacting waves are degenerate. On the contrary, for sum and difference frequency mixing this degeneracy is clearly broken, since three distinctive waves are interacting. It should be mentioned that since ω_q, ω_n and ω_m are uniquely related through (2-33), which can be viewed as the fundamental expression of energy conservation in the three wave mixing process, it is not technically necessary to include all three arguments in the expressions for the second order susceptibility and polarisation.

Up to this point, this ongoing discussion limited the electronic oscillations, the electric field and the polarisation in one dimension. To allow for a proper description of optical polarisation, the deduced results need be extended to three dimensions. The electric field as defined in (2-20) should now be written as:

$$\vec{E}(\vec{r},t) = \sum_n \frac{1}{2}[E_n(\vec{r}) \cdot e^{-i\omega_n t} + E_n^*(\vec{r}) \cdot e^{i\omega_n t}] \tag{2-42}$$

The second order susceptibility in three dimensions is correspondingly given by a third rank tensor. Hence, for the *i*-component of the second order polarisation equation (2-37) expands to:

$$P_i^{(2)}(\omega_q, \omega_n, \omega_m)_i = \chi_{ijk}^{(2)}(\omega_q, \omega_n, \omega_m)\varepsilon_0 E_n(\vec{r},t)_j E_m(\vec{r},t)_k \tag{2-43}$$

where the Einstein summation convention is used and *i, j, k* take values *X,Y,Z* corresponding conventionally to the crystalline piezoelectric axis.

It is clear that 27 different nonlinear susceptibility components are required to describe the second order polarisation at ω_q, for all combinations of *i, j, k*. Furthermore, two more frequency components need be determined, namely: $\vec{P}^{(2)}(\omega_m, \omega_q, -\omega_n)$ and $\vec{P}^{(2)}(\omega_n, \omega_q, -\omega_m)$, each one of which introduces 27 more nonlinear susceptibility components, increasing the total number to 81. It has been shown though by Armrtong et al [3], that $\chi^{(2)}$ is invariant with permutations in frequencies ω_q, ω_n and ω_m, as long as the indices *i, j, k* are simultaneously permuted in the same way. This in essence reduces the number of independent nonlinear susceptibilities to 27. A second symmetry condition, introduced by Kleinman [12], extends the first one to state that, in the case of lossless media, the indices *i, j, k* can be permuted without permuting the frequencies.

Commonly, the nonlinear coefficient matrix *d* is used in place of the nonlinear susceptibility, defined as[1]:

$$d_{ijk} = 1/2\,\chi_{ijk}^{(2)}(\omega_q, \omega_n, \omega_m) \tag{2-44}$$

Clearly the matrix consists of 27 elements when expressed fully. However, when Kleinman condition applies, d_{ijk} can be expressed in a reduced notation d_{il}, where *l*

[1] Depending on the definition of $\chi^{(2)}$, a factor of ½ may or may not appear in the definition of the nonlinear coefficient.

takes values from 1 to 6 according to Table 2.1. Using this conventional reduced notation, the nonlinear coefficient is a 3x6 matrix, which allows us to re-write equations (2-26) for second harmonic generation, sum and difference frequency mixing in three dimensions as follows:

$$\begin{bmatrix} P^{(2)}(2\omega_n)_X \\ P^{(2)}(2\omega_n)_Y \\ P^{(2)}(2\omega_n)_Z \end{bmatrix} = \varepsilon_0 \begin{bmatrix} d_{11} & d_{12} & d_{13} & d_{14} & d_{15} & d_{16} \\ d_{21} & d_{22} & d_{23} & d_{24} & d_{25} & d_{26} \\ d_{31} & d_{32} & d_{33} & d_{34} & d_{35} & d \end{bmatrix} \cdot \begin{bmatrix} (\vec{E}_n^{\,2})_X \\ (\vec{E}_n^{\,2})_Y \\ (\vec{E}_n^{\,2})_Z \\ 2(\vec{E}_n)_Y(\vec{E}_n)_Z \\ 2(\vec{E}_n)_X(\vec{E}_n)_Z \\ 2(\vec{E}_n)_X(\vec{E}_n)_Y \end{bmatrix}$$

$$\begin{bmatrix} P^{(2)}(\omega_n+\omega_m)_X \\ P^{(2)}(\omega_n+\omega_m)_Y \\ P^{(2)}(\omega_n+\omega_m)_Z \end{bmatrix} = 2\varepsilon_0 \begin{bmatrix} d_{11} & d_{12} & d_{13} & d_{14} & d_{15} & d_{16} \\ d_{21} & d_{22} & d_{23} & d_{24} & d_{25} & d_{26} \\ d_{31} & d_{32} & d_{33} & d_{34} & d_{35} & d \end{bmatrix} \cdot \begin{bmatrix} (\vec{E}_n)_X \cdot (\vec{E}_m)_X \\ (\vec{E}_n)_Y \cdot (\vec{E}_m)_Y \\ (\vec{E}_n)_Z \cdot (\vec{E}_m)_Z \\ (\vec{E}_n)_Y(\vec{E}_m)_Z + (\vec{E}_n)_Z(\vec{E}_m)_Y \\ (\vec{E}_n)_X(\vec{E}_m)_Z + (\vec{E}_n)_Z(\vec{E}_m)_X \\ (\vec{E}_n)_X(\vec{E}_m)_Y + (\vec{E}_n)_Y(\vec{E}_m)_X \end{bmatrix}$$

$$\begin{bmatrix} P^{(2)}(\omega_n-\omega_m)_X \\ P^{(2)}(\omega_n-\omega_m)_Y \\ P^{(2)}(\omega_n-\omega_m)_Z \end{bmatrix} = 2\varepsilon_0 \begin{bmatrix} d_{11} & d_{12} & d_{13} & d_{14} & d_{15} & d_{16} \\ d_{21} & d_{22} & d_{23} & d_{24} & d_{25} & d_{26} \\ d_{31} & d_{32} & d_{33} & d_{34} & d_{35} & d \end{bmatrix} \cdot \begin{bmatrix} (\vec{E}_n)_X \cdot (\vec{E}_m^*)_X \\ (\vec{E}_n)_Y \cdot (\vec{E}_m^*)_Y \\ (\vec{E}_n)_Z \cdot (\vec{E}_m^*)_Z \\ (\vec{E}_n)_Y(\vec{E}_m^*)_Z + (\vec{E}_n)_Z(\vec{E}_m^*)_Y \\ (\vec{E}_n)_X(\vec{E}_m^*)_Z + (\vec{E}_n)_Z(\vec{E}_m^*)_X \\ (\vec{E}_n)_X(\vec{E}_m^*)_Y + (\vec{E}_n)_Y(\vec{E}_m^*)_X \end{bmatrix}$$

where for space economy the argument of the electric fields $(\vec{r},t)$ has been neglected and $P^{(2)}(2\omega_n,\omega_n,\omega_n)$ has been reduced to $P^{(2)}(2\omega_n)$ with similar argument simplification for the sum and difference mixing components.

j,k	*X,X*	*Y,Y*	*Z,Z*	*Y,Z Z,Y*	*X,Z Z,X*	*X,Y Y,X*
l	1	2	3	4	5	6

Table 2.1 Contracted index notation. X,Y,Z are piezoelectric axis directions.

It can be seen that an explicit use of Kleinman symmetry denotes that in the case of lossless crystals not all of the 18 elements of the nonlinear coefficient matrix are independent (for example, $d_{12} = d_{122} = d_{212} = d_{26}$). Applying this idea systematically, the number of independent elements in the 3x6 coefficient matrix reduces to 10 and *d* takes the form:

$$d = \begin{bmatrix} d_{11} & d_{12} & d_{13} & d_{14} & d_{15} & d_{16} \\ d_{16} & d_{22} & d_{23} & d_{24} & d_{14} & d_{12} \\ d_{15} & d_{24} & d_{33} & d_{23} & d_{13} & d_{14} \end{bmatrix} \tag{2-45}$$

Further reduction of the number of independent elements can be realised on the grounds of the crystal symmetry. For example, cubic crystals belonging to the $43\overline{m}$ class system (GaAs), present only three non vanishing elements and only one independent coefficient, resulting in the nonlinear coefficient matrix:

$$d = \begin{bmatrix} 0 & 0 & 0 & d_{14} & 0 & 0 \\ 0 & 0 & 0 & 0 & d_{14} & 0 \\ 0 & 0 & 0 & 0 & 0 & d_{14} \end{bmatrix}$$

Establishing the exact expression for the nonlinear coefficient of a material allows the calculation of a scalar quantity d_{eff} which, for a specific wave interaction (i.e known propagation direction and polarisation axis of the waves), can be used with the scalar amplitudes of the interactive waves to describe the three wave mixing process. The calculation of this scalar effective nonlinear coefficient for the various crystal classes has been discussed in a number of sources [13-15] and allows the second harmonic generation, sum and difference frequency mixing to be expressed, respectively, via:

$$P^{(2)}(2\omega_n) = d_{eff}\,\varepsilon_0\,|E_n^{(2)}(\vec{r},t)| \tag{2-46 a}$$

$$P^{(2)}(\omega_n + \omega_m) = 2d_{eff}\,\varepsilon_0\,|E_n(\vec{r},t)||E_m(\vec{r},t)| \tag{2-46 b}$$

$$P^{(2)}(\omega_n - \omega_m) = 2d_{eff}\,\varepsilon_0\,|E_n(\vec{r},t)||E_m^*(\vec{r},t)| \tag{2-46 c}$$

where $|E_n(\vec{r},t)|$ is the scalar amplitude along the propagation direction of the wave at ω_n. The effective nonlinear coefficient is almost explicitly used in all applications.

2.3 Propagation of electromagnetic waves in nonlinear media

It has been shown that electromagnetic waves at given frequencies can induce a polarisation at other frequencies in appropriate (nonlinear) media. This induced polarisation will now be inserted as a source term in Maxwell equations (2-1) to unfold how this leads to the generation of new electromagnetic waves at the converted frequencies and how power is transferred between the interacting fields.

2.3.1 Coupled wave equations for nonlinear frequency conversion

Maxwell equations for a non-conductive, non-magnetic, source free second order nonlinear medium (i.e., $\vec{M} = \vec{J} = \rho = 0$ and $\vec{P}^{(2)} \neq 0$) are:

$$\vec{\nabla} \times \vec{E}(\vec{r},t) + \frac{\partial}{\partial t}(\mu_0 \vec{H}(\vec{r},t) = 0 \qquad \text{(2-47 a)}$$

$$\vec{\nabla} \times \vec{H}(\vec{r},t) - \frac{\partial}{\partial t}[\varepsilon_0 \varepsilon \vec{E}(\vec{r},t) + \vec{P}^{(2)}] = 0 \qquad \text{(2-47 b)}$$

$$\vec{\nabla} \cdot \vec{B}(\vec{r},t) = 0 \qquad \text{(2-47 c)}$$

$$\vec{\nabla} \cdot [\varepsilon_o \varepsilon \vec{E}(\vec{r},t) + \vec{P}^{(2)}] = 0 \qquad \text{(2-47 d)}$$

The trivial four-step process of formulating Maxwell equations in a wave motion equation [16] can be followed to obtain:

$$\nabla^2 \vec{E}(\vec{r},t) - \mu_0(\varepsilon_0 \varepsilon_r \frac{\partial^2 \vec{E}(\vec{r},t)}{\partial t^2} + \frac{\partial^2 \vec{P}^{(2)}}{\partial t^2}) = 0 \qquad \text{(2-48)}$$

In the absence of the nonlinear source term, Eq. (2-48) decays to the standard linear wave equation. Without compromising the physical context of the nonlinear wave equation, the treatment can be simplified by considering fields propagating in the *z*-axis. Eq. (2-48) can then be written in a scalar form:

$$\frac{\partial^2 \vec{E}(z,t)}{\partial z^2} - \mu_0(\varepsilon_0 \varepsilon \frac{\partial^2 \vec{E}(z,t)}{\partial t^2} + \frac{\partial^2 \vec{P}^{(2)}}{\partial t^2}) = 0 \qquad \text{(2-49)}$$

Assuming that the nonlinear term is “small” compared to the linear one, plane-wave-like solutions can be adopted, with the proper introduction of a complex field amplitude $\vec{E}(z)$, which is not a constant as in Eq. (2-13), but a slowly varying function of *z*:

$$\vec{E}(z,t) = \frac{1}{2}[\vec{E}(z) \cdot e^{i(k_1 z - \omega_1 t)} + \vec{E}(z) \cdot e^{i(k_2 z - \omega_2 t)} + \vec{E}(z) \cdot e^{i(k_3 z - \omega_3 t)} + c.c] \qquad \text{(2-50)}$$

Each individual frequency component of the field is required to satisfy Eq. (2-49). Taking as an example the sum frequency component $\omega_3 = \omega_1 + \omega_2$ and substituting the nonlinear polarisation term by use of Eq. (2-46 b), the wave equation gives:

$$\frac{\partial^2}{\partial z^2} E_3(z) e^{i(k_3 z - \omega_3 t)} - \mu_0 \varepsilon_0 \varepsilon E_3(z) \frac{\partial^2}{\partial t^2} [e^{i(k_3 z - \omega_3 t)}] -$$

$$- \mu_0 2\varepsilon_0 d_{eff} E_1(z) E_2(z) \frac{\partial^2}{\partial t^2} [e^{i[(k_1 + k_2) z - (\omega_1 + \omega_2) t]}]\} = 0$$

Carrying out the calculations for the derivatives and ignoring the term $d^2 E_3(z)/dz^2$, which is an acceptable approximation within the limits of the slowing varying envelope assumption, we find:

$$2ik_3 \frac{dE_3(z)}{dz} - k_3^2 E_3(z) + \mu_o \varepsilon_0 \varepsilon_r \omega_3^2 E_3(z) + 2\mu_0 \varepsilon_0 d_{eff} \omega_3^2 E_1(z) E_2(z) e^{i(k_1 + k_2 - k_3) z} = 0$$

Similar expressions can be found for the waves at $\omega_2 = \omega_3 - \omega_1$ and $\omega_1 = \omega_3 - \omega_2$, substituting this time the nonlinear term with the difference frequency polarisation component given by (2-46 c). With appropriate use of equations (2-8), (2-14) and introducing the definition:

$$\Delta k = k_3 - k_2 - k_1 \tag{2-51}$$

these expressions can be rewritten in the most commonly used form:

$$\frac{dE_1(z)}{dz} = i \frac{\omega_1}{n_1 c} d_{eff} E_3(z) E_2^*(z) e^{i\Delta k z} \tag{2-52 a}$$

$$\frac{dE_2(z)}{dz} = i \frac{\omega_2}{n_2 c} d_{eff} E_3(z) E_1^*(z) e^{i\Delta k z} \tag{2-52 b}$$

$$\frac{dE_3(z)}{dz} = i \frac{\omega_3}{n_3 c} d_{eff} E_1(z) E_2(z) e^{-i\Delta k z} \tag{2-52 c}$$

Equations (2-58) are called “coupled wave equations” and describe the general three wave mixing process. They manifest that the interacting fields are coupled through the nonlinear coefficient, d_{eff}, which enables energy flow from one frequency component to another.

Similarly, the driving polarisation component at the second harmonic (2-46 a) can be used to obtain the following set of coupled wave equations for second harmonic generation:

$$\frac{dE_{\omega}(z)}{dz} = i\frac{\omega}{n_{\omega}c} d_{eff} E_{2\omega}(z) E_{\omega}^{*}(z) e^{i\Delta kz} \tag{2-53 a}$$

$$\frac{dE_{2\omega}(z)}{dz} = i\frac{2\omega}{2n_{2\omega}c} d_{eff} E_{\omega}^{2}(z) e^{-i\Delta kz} \tag{2-53 b}$$

2.3.2 The Manley-Rowe relations

The coupled wave equations can be rewritten in an equivalent form by substituting the electric fields with the intensity of the electromagnetic wave, which is defined through:

$$I_i = \frac{1}{2}\left(\frac{\varepsilon_0}{\mu_0}\right)^{1/2} n_i E_i(z) E_i^{*}(z) \tag{2-54}$$

The spatial variation of the intensity corresponding to the frequency component ω_1 (for example) is then:

$$\frac{dI_1}{dz} = \frac{1}{2}\left(\frac{\varepsilon_0}{\mu_0}\right)^{1/2} n_1 [E_1(z)\frac{d}{dz}E_1^{*}(z) + E_1^{*}(z)\frac{d}{dz}E_1(z)]$$

Inserting (2-52 a), the last equation gives:

$$\frac{dI_1}{dz} = \frac{1}{2}\left(\frac{\varepsilon_0}{\mu_0}\right)^{1/2} n_1 \frac{\omega_1}{n_1 c} d_{eff} [E_1(z)(-i)E_3^{*}(z)E_2(z)e^{-i\Delta kz} + iE_1^{*}(z)E_3(z)E_2^{*}(z)e^{i\Delta kz}] \Leftrightarrow$$

$$\frac{dI_1}{dz} = \frac{1}{2}\left(\frac{\varepsilon_0}{\mu_0}\right)^{1/2} n_1 \frac{\omega_1}{n_1 c} d_{eff} [i\{E_1^{*}(z)E_2^{*}(z)E_3(z)e^{i\Delta kz}\} - i\{E_1^{*}(z)E_2^{*}(z)E_3(z)e^{i\Delta kz}\}^{*}]$$

Similar expressions can be found for the other two frequency components. Using the identity: $1/2(iA - iA^{*}) = -\mathrm{Im}(A) = \mathrm{Im}(A^{*})$ and after some rearrangement, these expressions can be written in the form:

$$\frac{dI_1}{dz} = -\frac{\varepsilon_0}{c^2} d_{eff}\omega_1 \,\mathrm{Im}\{E_1^{*}(z)E_2^{*}(z)E_3(z)e^{i\Delta kz}\} \tag{2-55 a}$$

$$\frac{dI_2}{dz} = -\frac{\varepsilon_0}{c^2} d_{eff}\omega_2 \,\mathrm{Im}\{E_1^{*}(z)E_2^{*}(z)E_3(z)e^{i\Delta kz}\} \tag{2-55 b}$$

$$\frac{dI_3}{dz} = \frac{\varepsilon_0}{c^2} d_{eff}\omega_3 \,\mathrm{Im}\{E_1^{*}(z)E_2^{*}(z)E_3(z)e^{i\Delta kz}\} \tag{2-55 c}$$

Equations (2-55) suggest that the following relationship holds:

$$\frac{d}{dz}\left(\frac{I_1}{\omega_1}\right)=\frac{d}{dz}\left(\frac{I_2}{\omega_2}\right)=-\frac{d}{dz}\left(\frac{I_3}{\omega_3}\right) \tag{2-56}$$

Relations (2-55), known as Manley-Rowe relations, describe the intensity change for the three interacting waves. They clearly imply that the growth of one field component will be at the expense of another of the fields coupled through the nonlinear coefficient. In an equivalent frame, they manifest the conservation of the total intensity field. This can also be viewed mathematically through the following equation, which is always satisfied due to Eqs. (2-55):

$$\frac{dI_1}{dz}+\frac{dI_2}{dz}+\frac{dI_3}{dz}=0 \tag{2-57}$$

2.3.3 Second order nonlinear frequency conversion processes and gain

Having established the coupled differential equations (2-52) and (2-53) that govern the interaction of three waves in a nonlinear medium, it is evident that four distinctive processes are possible, shown schematically in Fig. 2.1. These processes, namely second harmonig generation (SHG), sum generation (SG), parametric generation (PG) and difference generation (DG), are identical in their nature but differ in the direction of power growth.

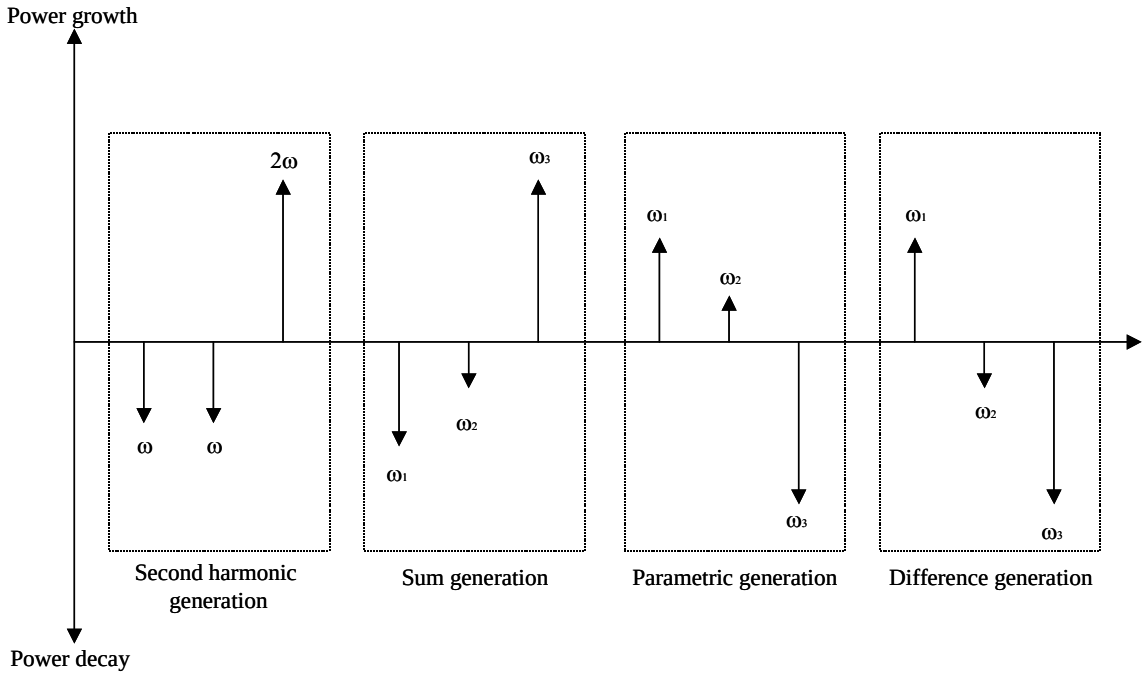

Fig 2.1 Schematic diagram of possible $\chi^{(2)}$ processes

Calculating the gain of a specific interaction requires solving the coupled wave equations. The general treatment of this problem can be found in [1]. For the scope of the present discussion, an example will be given through the special case of the undepleted second harmonic generation.

The coupled wave equations for second harmonic generation (2-53), assuming that the driving field at ω does not undergo strong depletion, and hence $E_\omega(z) = E_\omega = const$, give:

$$\int_0^l dE_{2\omega}(z) = i\frac{2\omega}{2n_{2\omega}c} d_{eff} E_\omega^2 \int_0^l e^{-i\Delta kz} dz \Rightarrow$$

$$E_{2\omega}(l) - E_{2\omega}(0) = i\frac{\omega}{n_{2\omega}c} d_{eff} E_\omega^2 \frac{(e^{-i\Delta kl} - 1)}{-i\Delta k} \Rightarrow$$

$$E_{2\omega}(l) - E_{2\omega}(0) = i\frac{\omega}{n_{2\omega}c} l d_{eff} E_\omega^2 \frac{(e^{i\Delta kl/2} - e^{-i\Delta kl/2})}{2i(l\Delta k/2)} e^{-i\Delta kl/2}$$

where l is the interaction length. Assuming the initial condition of zero input second harmonic field, the last equation takes the form:

$$E_{2\omega}(l) = i\frac{\omega}{n_{2\omega}c} l d_{eff} E_\omega^2 \sin c\{\frac{l\Delta k}{2}\} e^{-i\Delta kl/2} \tag{2-58}$$

where by definition: $\text{sinc}(x) = \sin x / x = (e^{ix} - e^{-ix})/(2ix)$. Multiplying the last equation with its complex conjugate, a similar expression can be obtained in terms of the field intensities:

$$E_{2\omega}(l) E_{2\omega}^*(l) = (\frac{\omega}{n_{2\omega}c} l d_{eff})^2 [E_\omega E_\omega^*]^2 \sin c^2\{\frac{l\Delta k}{2}\} \Rightarrow$$

$$I_{2\omega}(l) = (\frac{\omega}{n_{2\omega}c} l d_{eff})^2 I_\omega^2 [\frac{1}{2}(\frac{\varepsilon_0}{\mu_0})^{1/2} n_\omega]^{-1} \sin c^2\{\frac{l\Delta k}{2}\} \Rightarrow$$

$$I_{2\omega}(l) = [\frac{2l^2 d_{eff}^2}{\varepsilon_0 c^3} \frac{\omega^2}{n_{2\omega} n_{2\omega} n_\omega}] \cdot I_\omega^2 \cdot \sin c^2\{\frac{l\Delta k}{2}\} \tag{2-59}$$

The intensity gain experienced by the second harmonic field is thus:

$$G_{2\omega}(l) = \frac{I_{2\omega}(l)}{I_\omega} = \Gamma^2 l^2 \sin c^2\{\frac{l\Delta k}{2}\} \tag{2-60}$$

where the gain coefficient Γ has been introduced, such as:

$$\Gamma^2 = \frac{2\omega^2 d_{eff}^2}{\varepsilon_0 c^3 n_{2\omega}^2 n_\omega} I_\omega \tag{2-61}$$

Since the directly measurable quantity is power rather than intensity, the nonlinear conversion efficiency n_{SHG} is commonly used instead of the intensity gain. Within the limits of the plane-wave approximation, an interaction area A can be assumed and (2-60) can be written in terms of powers to give:

$$n_{SHG} = \frac{P_{2\omega}}{P_\omega} = [\frac{2\omega^2 d_{eff}^2}{\varepsilon_0 c^3 n_{2\omega}^2 n_\omega}] \cdot l^2 \cdot \frac{P_\omega}{A} \cdot \sin c^2\{\frac{l\Delta k}{2}\} \qquad (2\text{-}62)$$

Similar analysis can be followed for all other processes. Avoiding the details of these mathematical problems, we will only point out that in the limit of the plane wave approximation and assuming no depletion (low conversion efficiency limit), it is possible to express the intensity gain in a form identical to (2-60), as summarised in Table 2:

$\chi^{(2)}$ Process	Initial Conditions	Gain Coefficient Γ^2	Gain
SHG	$I_{2\omega}$(z=0)=0	$\frac{2\omega^2 d_{eff}^2}{\varepsilon_0 c^3 n_{2\omega}^2 n_\omega} I_\omega$	$G_{2\omega}(l) = \frac{I_{2\omega}(l)}{I_\omega(0)} = \Gamma^2 l^2 \sin c^2\{\frac{l\Delta k}{2}\}$
SG	$I_{\omega 3}$ (z=0)=0	$\frac{2\omega_3^2 d_{eff}^2}{\varepsilon_0 c^3 n_{\omega_1} n_{\omega_2} n_{\omega_3}} I_{\omega_2}$	$G_{\omega_3}(l) = \frac{I_{\omega_3}(l)}{I_{\omega_1}(0)} = \Gamma^2 l^2 \sin c^2\{\frac{l\Delta k}{2}\}$
PG	$I_{\omega 2}$ (z=0)=0	$\frac{2\omega_1\omega_2 d_{eff}^2}{\varepsilon_0 c^3 n_{\omega_1} n_{\omega_2} n_{\omega_3}} I_{\omega_3}$	$G_{\omega_2}(l) = \frac{I_{\omega_2}(l)}{I_{\omega_2}(0)} - 1 = \Gamma^2 l^2 \sin c^2\{\frac{l\Delta k}{2}\}$
DG	$I_{\omega 1}$ (z=0)=0	$\frac{2\omega_1^2 d_{eff}^2}{\varepsilon_0 c^3 n_{\omega_1} n_{\omega_2} n_{\omega_3}} I_{\omega_3}$	$G_{\omega_1}(l) = \frac{I_{\omega_1}(l)}{I_{\omega_2}(0)} = \Gamma^2 l^2 \sin c^2\{\frac{l\Delta k}{2}\}$

Table 2 Gain expressions for second order nonlinear processes.

From the preceding, the general conclusion can be derived that the efficiency of a second order nonlinear process depends on the physical parameters of the material (nonlinearity, dispersion profile, physical length), the interacting wavelengths and scales with $\sin c^2(l\Delta k/2)$, as plotted in Fig. 2.2.

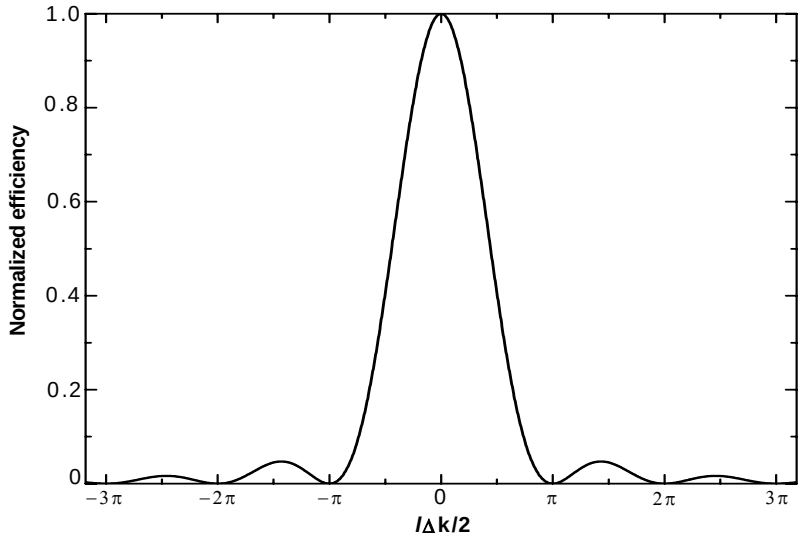

Fig 2.2 The dependence of the nonlinear conversion efficiency on the phase-mismatch parameter $l\Delta k/2$.

Fig. (2.2) demonstrates that, for a finite length material, the efficiency of a nonlinear interaction maximises when:

$$\Delta k = k_3 - k_2 - k_1 = 0 \tag{2-63}$$

Equation (2-63) is known as the phase-matching condition. Note that the phase-matching condition as expressed above is a result of the scalar wave approximation. In the most general case the three wave-vectors should be matched instead:

$$\Delta\vec{k} = \vec{k}_3 - \vec{k}_2 - \vec{k}_1 = 0$$

The wave vectors under phase-matching can be either collinear (scalar phase-matching) or noncollinear (vector phase-matching) [17]. In the most interesting case for the purposes of the present work, that of scalar phase-matching, (2-63) can be written in the equivalent form:

$$n_3\omega_3 = n_1\omega_1 + n_2\omega_2 \tag{2-64}$$

Clearly, in a dispersion-free material (i.e. $n_3 = n_2 = n_1$) the phase-matching condition is spontaneously satisfied. In all practical cases though, a higher degree of sophistication is required to compensate for dispersion and phase-match the nonlinear interactions. In what follows, a further insight into the physical content of the phase-matching condition, along with an outline of the two main approaches of achieving phase-matching in dispersive media will be given.

2.4 Phase-Matching

2.4.1 The physical content of phase-matching

In the previous sections, the different nonlinear processes were distinguished and the gain experienced by the growing field evaluated. The subsequent step is to reveal the physical criteria that favour the growth of one field component to the other. For this purpose, a phasor model will be used to illustrate how the relative phase of the fields influences the power competition process.

It is evident that the direction of change in power of the field at ω_3 (for example) is determined by the sign of the differential equation (2-52 c), which for the needs of the present discussion will be written in the form:

$$\delta E_3(z) = i\kappa E_1(z) E_2(z) e^{-i\Delta kz} \delta z$$

where κ is a real constant. The field amplitudes $E_1(z)$, $E_2(z)$ and $E_3(z)$ are complex quantities and can be represented by a vector in the complex plane with phases φ_1, φ_2 and φ_3, respectively. With only the relative phase of the fields $\Delta\varphi = \varphi_3 - \varphi_1 - \varphi_2$ being of interest, we can choose for simplicity the phase of the field at ω_3 to be zero. Furthermore, having assumed a slowly varying envelope, it is acceptable to consider that φ_1, φ_2 and φ_3=0 remain constant with z. Thus:

$$\delta E_3(z) \propto \exp i \cdot (\varphi_1 + \varphi_2 + \frac{\pi}{2} - \Delta kz) = \exp i\Phi(z) \qquad (2\text{-}65)$$

where by definition:

$$\Phi(z) = \varphi_1 + \varphi_2 + \frac{\pi}{2} - \Delta kz \qquad (2\text{-}66)$$

The situation described above is presented schematically in Fig. 2.3.

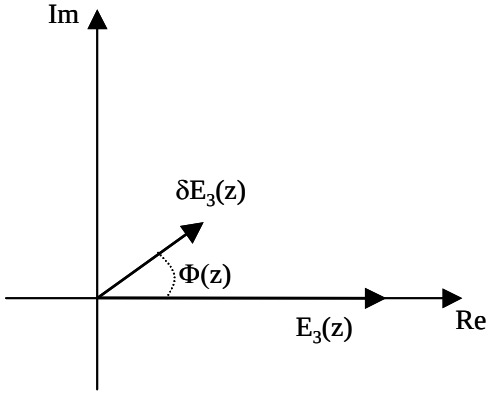

Fig. 2.3 Phasor representation of the amplitude and increment change of the field E_3 for an arbitrary relative phase.

At the point the process is initiated, that is at z=0, the field E_3(z) experiences a maximum increase when the incremental change $\delta E_3(z=0)$ lies along the positive-real axis. On the other hand, the filed experiences a maximum decrease when $\delta E_3(z=0)$ lies along the negative-real axis. The dependence of the magnitude and direction of the power change on the relative phase follows immediately:

- Maximum increase in E_3 occurs when: $\Phi(0) = 0 \Rightarrow \Delta\varphi = \varphi_3 - \varphi_1 - \varphi_2 = \frac{\pi}{2}$
- Maximum decrease in E_3 occurs when: $\Phi(0) = \pi \Rightarrow \Delta\varphi = \varphi_3 - \varphi_1 - \varphi_2 = -\frac{\pi}{2}$

It is generally accepted that at z=0, the relative phase adjust itself to the value that ensures power flow from the strong input field the weaker field. As the fields propagate through the medium and z increases, in presence of a phase-mis-match Δk, the value of Φ varies periodically with z and so does the direction of power exchange between the fields. The spatial period over which the un-phase-matched process builds up in one direction is called coherence length l_c. From Fig 2.3, it can be seen that E_3 builds up for values of Φ(z) between -π/2 and π/2, or equivalently for $-\pi/2 \le z\Delta k \le \pi/2$. It follows that:

$$l_c = \frac{\pi}{\Delta k} \tag{2-67}$$

On the contrary, when the phase-matching condition is satisfied, Φ(z) acquires a constant value and the interaction proceeds one-way over unlimited lengths. The last conclusion reveals the physical content of the phase-matching condition, in agreement with the calculated nonlinear gain presented in Table 2 and plotted in Fig. 2.2.

For standard nonlinear materials and interactions in the visible and near infrared, the coherence length takes typical values of the order of 1-10 μm. In order for meaningful power levels to be obtained, the nonlinear process should keep growing over distances much longer than the coherence length. The most established techniques for achieving phase-matching in dispersive media, known as birefringent-phase-matching (BPM) and quasi-phase-matching (QPM), are presented in the following sections.

2.4.2 Birefringent-phase-matching (BPM)

The natural birefringence present in a number of nonlinear crystals was first employed to phase-match interactions by Giordmaine [18] and Maker et al [19]. Birefringence [20] is a linear optical effect resulting from the expansion of the dielectric constant in three dimensions. For anisotropic materials, the dielectric constant is represented by a tensor rather than a scalar. Therefore, the refractive index of an anisotropic material, uniquely related to the dielectric constant via Eq. (2-8), depends on both the propagation direction and polarisation state of the involved waves. It can be shown that in all anisotropic materials three distinctive directions exist that can be used to express the dielectric constant in a diagonal matrix format. These directions are known as the principal dielectric axes *x*, *y*, *z*. It is thus always possible to express the refractive indices of an anisotropic crystal at a given wavelength, in terms of the refractive indices for waves polarised along the principal dielectric axes, known as the principal refractive indices, n_x, n_y, and n_z. The refractive index of the crystal can then be visualised via a three-dimensional ellipsoid referred to as the index ellipsoid, as shown in Fig. 2.4.

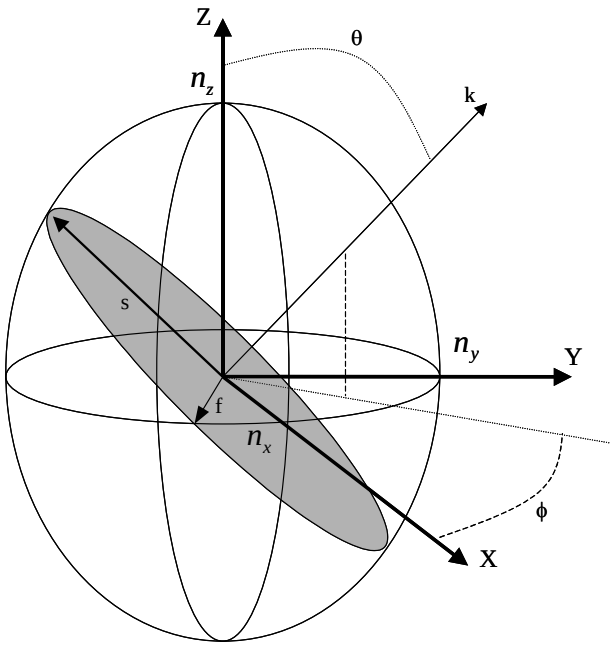

Fig 2.4 Index ellipsoid for an anisotropic crystal: $\frac{x^2}{n_x}+\frac{y^2}{n_y}+\frac{z^2}{n_z}=1$.

(Here it has been assumed: $n_z > n_y > n_x$).

The propagation direction along the wave vector *k* is at an angle θ from the *z*-axis, while the projection of k in the *x*-*y* plane is at an angle ϕ from the x-axis. The wave propagating in the *k*-direction will be polarised in a plane normal to *k*. The region of this plane confined by the index ellipsoid, shown shaded in Fig. 2.4 and referred to as the refractive index surface, is bounded by an ellipse that satisfies [21-23]:

$$\frac{\sin^2\theta\cdot\cos^2\phi}{n^{-2}-n_x^{-2}}+\frac{\sin^2\theta\cdot\sin^2\phi}{n^{-2}-n_y^{-2}}+\frac{\cos^2\theta}{n^{-2}-n_z^{-2}}=0 \qquad (2\text{-}68)$$

where in the most general case $n_z \neq n_y \neq n_x \neq n_z$. The index ellipsoid presents two inclined sections for which the bounding ellipse degenerates to a cycle and the refractive index surface becomes a circular disk. Waves propagating normal to these two sections, along what is called the optic axis, experience refractive indices independent of polarisation. In presence of two distinctive optic axes, both of which lies in the plane containing the smaller and larger principal refractive indices (*x*-*z* plane in the case of Fig. 2.4), the anisotropic material is referred to as biaxial. Equation (2-68) has generally two real positive solutions, corresponding to the refractive indices for the two allowed orthogonal polarisations of the wave. The larger of the two solutions, corresponds to the polarisation marked as "*s*" (slow-ray) in Fig. 2.4 and the smaller to the polarisation marked as "*f*" (fast-ray). In the following, these solutions will be denoted by n_s and n_f, respectively.

The polarisation dependence of the refractive index can be readily used to satisfy the scalar phase-matching condition. Following the standard nomenclature, two different phase-matching geometries can be applied: The first, known as Type I phase-matching, involves parallel polarisations for the two interacting waves of lower frequency. In Type II phase-matching, the two low-frequency waves have orthogonal polarisations. Clearly, in the case of SHG, Type I phase-matching implies that the fundamental consists of a single polarisation orthogonal to the second harmonic, while Type II phase-matching implies a mixed polarisation of the fundamental. The scalar phase-matching condition (assuming normally dispersive medium: $n_3 > n_2 > n_1$ with $\omega_3 > \omega_2 > \omega_1$) can now be rewritten for each type as:

Type I: $n_{f,3}\omega_3 = n_{s,1}\omega_1 + n_{s,2}\omega_2$ (2-69 a)

Type II: $n_{f,3}\omega_3 = n_{s,1}\omega_1 + n_{f,2}\omega_2$ (2-69 b)

Given the frequency-dependent principal refractive indices from the Sellmeier equations of the specific material, equation (2-68) can be solved and substituted into either of (2-69) to determine the phase-matching geometry. This problem is generally rather complicated and has been treated elsewhere [24,25]. For the sake of clarity, a special case of greater simplicity will be discussed here.

This simplified case assumes a crystal in which two of the principal refractive indices are equal, say: $n_x = n_y = n_o \neq n_z = n_e$. In this case, the two optic axes coincide with the *z*-axis and the crystal is therefore called *uniaxial* (Fig. 2.5).

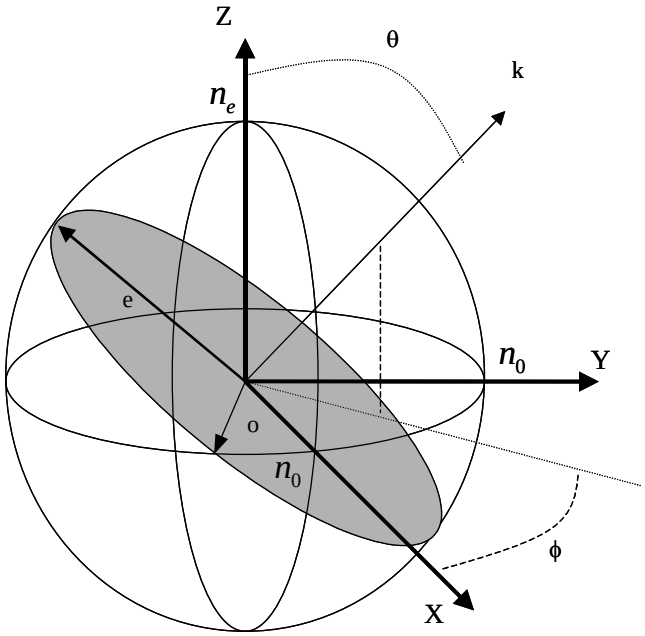

Fig 2.5 Index ellipsoid for a positive uniaxial crystal ($n_x = n_y < n_z$)

Clearly, in a uniaxial crystal a wave polarised parallel to the *x*-*y* plane[1] experiences a refractive index independent of the angle ϕ, named *ordinary* refractive index n_o. The wave polarised orthogonal to that (e-ray) experiences an *extra-ordinary* refractive index $n_e(\theta)$ varying from n_o to n_e as θ increases from 0 to 90 degrees. This can also be viewed through equation (2-68), which for the uniaxial case reduces to:

$$\frac{1}{n_e^2(\theta)} = \frac{\cos^2\theta}{n_o^2} + \frac{\sin^2\theta}{n_e^2} \tag{2-70}$$

[1] Note that due to the symmetry of the object, *x* and *y* axis can be freely chosen in the *x*-*y* plane.

There are two classes of uniaxial crystals: Those with $n_0<n_e$, commonly referred to as positive uniaxial crystals and those with $n_0>n_e$, known as negative uniaxial crystals. In the notation of *o*- and *e*-rays, the fast and slow rays correspond to:

- Positive crystals: $n_f = n_o$ and $n_s = n_e(\theta)$.
- Negative crystals: $n_s = n_o$ and $n_f = n_e(\theta)$.

For a positive uniaxial crystal, Eqs. (2-69) can now be rewritten as:

$$\text{Type I:} \quad n_{o,3}\omega_3 = [\frac{\cos^2\theta}{n_{o,1}^2} + \frac{\sin^2\theta}{n_{e,1}^2}]^{-1/2}\omega_1 + [\frac{\cos^2\theta}{n_{o,2}^2} + \frac{\sin^2\theta}{n_{e,2}^2}]^{-1/2}\omega_2$$

$$\text{Type II:} \quad n_{o,3}\omega_3 = [\frac{\cos^2\theta}{n_{o,1}^2} + \frac{\sin^2\theta}{n_{e,1}^2}]^{-1/2}\omega_1 + n_{o,2}\omega_2$$

While for a negative uniaxial crystal:

$$\text{Type I:} \quad [\frac{\cos^2\theta}{n_{o,3}^2} + \frac{\sin^2\theta}{n_{e,3}^2}]^{-1/2}\omega_3 = n_{0,1}\omega_1 + n_{0,2}\omega_2$$

$$\text{Type II:} \quad [\frac{\cos^2\theta}{n_{o,3}^2} + \frac{\sin^2\theta}{n_{e,3}^2}]^{-1/2}\omega_3 = n_{0,1}\omega_1 + [\frac{\cos^2\theta}{n_{o,2}^2} + \frac{\sin^2\theta}{n_{e,2}^2}]^{-1/2}\omega_2$$

The polar angle θ that phase-matches the mixing process for three fixed wavelengths, can be directly calculated from the above equations[1]. Note that the treatment of a biaxial crystal is identical to that of a uniaxial crystal if propagation is confined in a principal plane. For example, assuming propagation in the *x*-*y* plane (θ=0), Eq (2-68) gives:

$$\frac{1}{n^2(\phi)} = \frac{\cos^2\phi}{n_y^2} + \frac{\sin^2\phi}{n_x^2}$$

which is symmetrical to Eq. (2-70).

It has been shown that the optical anisotropy present in a number of crystals can be used to perfectly phase-match nonlinear interactions. Under perfect phase-matching (Δk=0), the only limitation to the useful interaction length is set by the Poynting vector walk-off. The Poyinting vector (or spatial) walk-off can be described as

[1]Note that for Type II geometries, with the lower frequency waves orthogonally polarised, ω_1 and ω_2 can be exchanged. Often in bibliography the possible phase-matching geometries are denoted as: Positive I: *oee*, Positive II: *oeo* (*ooe*), Negative I: *eoo* and Negative II: *eoe* (*eeo*). In any case, at least one of the interacting waves must be extraordinarily polarised. It should be pointed out that this notation is somewhat ambiguous, and often the following definition is used: *eee* to describe an interaction with all waves polarised along the *z*-axis, i.e., all waves experiencing a refractive index n_e. The later notation will be used in the next chapter to describe quasi-phase-matched process in PPLN.

follows: From the introduction to Maxwell equations presented in paragraph 2.1, it is evident that the Poynting vector is perpendicular to the electric field vector ($\vec{S} \perp \vec{E}$), while the electric displacement vector is perpendicular to the wave propagation direction ($\vec{k} \perp \vec{D}$). For isotropic media, the electric field and electric displacement vectors are related through a scalar constitutive relation and hence are parallel. One can recognise that in this case the wave vector and the Poynting vector are also parallel, suggesting that the energy propagates along the wave. However, in anisotropic media the relative permitivity is no longer scalar and the electric field vector is generally not parallel to the displacement vector. This results in a walk-off angle ρ between the directions of wave propagation and energy transmission, which for uniaxial crystals (or biaxial crystals with propagation taken along one of the principle planes) is given by an equation of the form [26]:

$$\tan\rho = (n_e(\theta))^2 \left[\left(\frac{\sin(\theta)}{(n_e(\theta))^{-2} - n_y^{-2}} \right)^2 + \left(\frac{\cos(\theta)}{(n_e(\theta))^{-2} - n_z^{-2}} \right)^2 \right]^{-1/2} \qquad (2\text{-}71)$$

In presence of walk off the geometry is usually referred to as critical phase-matching and the spatial overlap of the interacting waves will suffer, resulting in a decrease of the nonlinear efficiency, until a length is reached at which the process is halted. A possible solution to this problem is choosing the suitable geometry for which ρ=0. From the preceding equation it can be seen that this occurs for θ=π/2. This geometry, usually refereed to as non-critical phase-matching, involves propagation in one of the two (indistinguishable) ordinary dielectric axis. Although non-critical phase-matching solves the problem of spatial walk-off and allows nonlinear interactions to build over extensive material lengths, it restricts the wavelength choice of the interaction and (possibly) fails to access the larger nonlinear coefficients.

The geometry constrains related to birefringent-phase-matching can be avoided with use of a different technique, namely quasi-phase-matching, which is outlined in the following section.

2.4.3 Quasi-phase-matching (QPM)

An alternative technique for achieving phase-matching (quasi-phase-matching), involves the engineered spatial modulation of the effective nonlinear coefficient along the propagation axis. Though QPM with aperiodic modulation of the nonlinearities has been discussed and demonstrated [27-29], here only the conclusions of the periodic quasi-phase-matching treatment carried out in [30-35] are summarised.

Being a periodic function, the spatially varying nonlinear coefficient can be expanded in a Fourier series:

$$d_{eff}^{QPM}(z) = d_{eff} \cdot \sum_{m=-\infty}^{\infty} G_m e^{ik_m z} \tag{2-72}$$

where d_{eff} is the bulk coefficient, Λ the period of modulation and k_{m} the wave (or grating) vector of the *m*-th harmonic of the series, given by:

$$k_m = \frac{2\pi}{\Lambda} m \tag{2-73}$$

The couple wave equations, using (2-72) give:

$$\frac{dE_3(z)}{dz} = i\frac{\omega_3}{n_3 c}[d_{eff} \cdot \sum_{m=-\infty}^{\infty} G_m e^{ik_m z}] \cdot E_1(z)E_2(z)e^{-i\Delta kz} \tag{2-74}$$

Following an analysis similar to that in paragraph 2.3.3, the generated field after a distance *l* is:

$$E_3(l) = i\frac{\omega_3}{n_3 c} d_{eff} E_1 E_2 \sum_{m=-\infty}^{\infty} G_m \int_0^l e^{-i\Delta k_Q z} dz \Rightarrow$$

$$E_3(l) = i\frac{\omega_3}{n_3 c} d_{eff} E_1 E_2 \sum_{m=-\infty}^{\infty} l \cdot G_m \sin c\{\frac{\Delta k_Q l}{2}\} e^{-\frac{i\Delta k_Q l}{2}} \tag{2-75}$$

where the following definition is used:

$$\Delta k_Q = \Delta k - k_m = k_3 - k_1 - k_2 - \frac{2\pi}{\Lambda} m \tag{2-76}$$

From the behaviour of the sinc-function (Fig. 2.2), it is evident that as *l* increases, the contribution of the *m*-th harmonic in the summation of (2-75) is small for all non-zero values of Δk_{Q}. Therefore, if a value of *m* exists such as:

$$\Delta k_Q = \Delta k - k_m = k_3 - k_1 - k_2 - \frac{2\pi}{\Lambda} m = 0 \tag{2-77}$$

then all the other harmonics can be ignored and (2-75) reduces to:

$$E_3(l) = i\frac{\omega_3}{n_3 c} l d^{QPM} E_1 E_2 \sin c\{\frac{\Delta k_Q l}{2}\} e^{-\frac{i\Delta k_Q l}{2}} \tag{2-78}$$

where:

$$d^{QPM} = (G_m d_{eff}) \tag{2-79}$$

Comparing (2-78) with (2-58), suggests that a periodically quasi-phase-matched interaction can be analysed in the same way as an interaction taking place in the bulk material, provided Δk and d_{eff} are replaced by Δk_{Q} and d^{QPM} respectively.

The most meaningful shape of modulation is that in which the effective nonlinear coefficient switches from $+d_{\text{eff}}$ to $- d_{\text{eff}}$ over a period Λ, with positive sections of length l_+ and a duty cycle D given by:

$$D = \frac{l_+}{\Lambda} \tag{2-80}$$

The Fourier coefficient of the m-th harmonic is then equal to:

$$G_m = \frac{2}{\pi \cdot m} \sin(\pi \cdot m \cdot D) \tag{2-81}$$

Clearly, the efficiency of the QPM process is maximised for a 50% duty cycle and odd values of m, in which case (2-79) simplifies to:

$$d^{QPM} = \frac{2}{\pi \cdot m} d_{eff} \tag{2-82}$$

Equation (2-82) implies that in a QPM interaction the nonlinear coefficient is reduced by a factor $(2/\pi m)$ compared to that of the bulk material. The highest QPM nonlinear coefficient is accessed for m=1 (first order QPM). A final point of interest arises from combining the quasi-phase-matching condition (2-77) with (2-67), to obtain:

$$\Delta k_Q = 0 \Leftrightarrow \Lambda = (2l_c)m \tag{2-83}$$

Equation (2-83) states that the quasi-phase-matching condition can be met only if the period of modulation is equal to an integer multiple of $2l_{\text{c}}$. Taking into account the optimum condition of a 50% duty cycle, suggests that the sign of the nonlinear coefficient is to be switched every m coherence lengths (m=1,3,5…). The above analysis can be physically understood through Fig. 2.6. The intensity of the second harmonic[1] field is plotted against the interaction length.

[1] SHG is chosen as an example, although the results for other nonlinear processes are fundamentally similar.

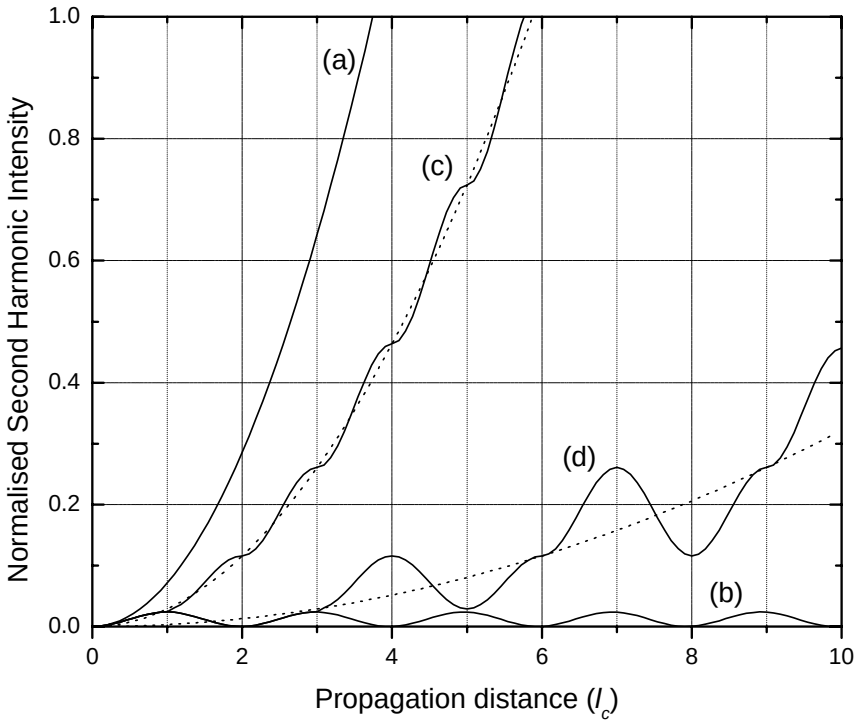

Fig 2.6 SHG intensity growth against the propagation distance under (a) perfect phase-matching (b) phase-mismatch Δk_1 (c) first order QPM (d) third order QPM

Curve (a) shows the quadratic growth of the field under perfect (birefringent) phase-matching in the bulk material resulting from an effective nonlinear coefficient d_{eff}. Curve (b) represents the un-phase-matched interaction in the bulk. Clearly, the field grows from zero reaching a peak after one coherence length. At this point, the phase-difference between the interacting waves is equal to π and the sign of the coupled wave equations reverses: the interaction proceeds in expense of the second harmonic field, until it reaches again zero at the end of the second coherence length. The interaction goes on periodically thereafter.

Curve (c) shows the intensity growth for the first order, 50% duty cycle[2] QPM interaction. Since not actually phase-matched, the field behaves as in curve (b) until it reaches the first coherence length. A this point, the phase-mismatch of the interacting waves reverses the sign of the coupled wave equations as in (b). However, the sign of the nonlinear coefficient is also reversed, compensating for the phase-mismatch: the interaction keeps growing on the same direction. The building up of the intensity oscillates around a quadratic curve, shown dashed in Fig 2.6, which corresponds to

[2] Clearly, a duty cycle of less (more) than 50% results in a lower efficiency, since the growth of intensity beyond the un-phase matched level starts before (after) the maximum is reached

the intensity growth under perfect phase-matching and due to an effective nonlinear coefficient reduced by $(2/\pi)$ in agreement with (2-82).

Similarly, curve (d) describes the intensity growth for third order QPM. This case is conceptually identical to the first order QPM, taking into account that the intensity starts growing beyond the un-phase-matched level at the third coherence length, oscillating around a quadratic curve (dashed line) that corresponds to a perfectly phase-matched interaction due to an effective nonlinear coefficient reduced by $(2/3\pi)$. The magnitude of the quasi-phase-matched interaction, being proportional to the square of the effective coefficient, is $(2/m\pi)^2$ smaller than the magnitude of the birefringent-phase-matched interaction. While this is an obvious physical advantage of BPM over QPM, it should be seen in parallel with a number of factors that may establish QPM as the most attractive approach for a number of applications.

Firstly, BPM requires at least one of the interacting waves being polarised as a *fast* ray. This limitation does not generally allow access to the maximum nonlinear coefficient and results in Poynting vector walk off. In quasi-phase-matching; however, the propagation and polarisation directions can be selected to avoid these complications and hence interactions over unlimited lengths can be achieved.

Secondly, BPM is only possible in anisotropic crystals and the frequencies that can be phase-matched are determined by the dispersion profile of the material. In contrast, QPM offers external control over the phase-matched frequencies, since the period of modulation introduced to the phase-matching condition (2-76) can be (in principle) freely varied.

The major drawback for QPM nonlinear frequency conversion arises from difficulties in fabricating suitable, uniform, micrometer-scale periodic structures that maintain the nonlinearity and transparency of the bulk material throughout. Current technology limits the QPM candidates to ferroelectric materials. Ferroelectrics have as their basic building block atomic groups (domains) which present a spontaneous built-in polarisation as a result of their structure. Periodic reversal of the ferroelectric domains corresponds to a periodic sign reversal of the nonlinear coefficients. Although a few techniques have been proposed [36-39], the only reliable method to date for achieving domain reversal is via electric field poling [40-43].

2.4.4. Phase-matching acceptance bandwidths

It can be understood that variations in any of the parameters that affect the values of the wave constants will have an impact on the phase-mismatch Δk and hence on the phase-matching condition. Such parameters are the wavelengths of the interaction, the temperature (which influences the refractive index) and the angle of propagation (which influences the refractive index in anisotropic media). It is therefore imperative to evaluate the tolerances of the nonlinear interactions to changes in any of these parameters, by calculating the effect of such changes on the efficiency of the interaction. It has been shown that for propagation in a nonlinear medium of length L the conversion efficiency scales with:

$$\sin c^2\left(\frac{\Delta kL}{2}\right)$$

From the above, it is easy to show that the efficiency reduces to 50% of its peak value when:

$$\frac{\Delta kL}{2} = \pm 0.443\pi \tag{2-84}$$

This result can be used to calculate the range over which a parameter ζ should be scanned to reduce the efficiency of the process by a factor of 1/2, usually refereed to as the full width at half maximum (FWHM) acceptance bandwidth in ζ. This calculation is based on an expansion of the phase-mismatch to a Taylor series about the value ζ_0 which achieves $\Delta k(\zeta_0)=\Delta k_0=0$ (perfect phase-matching) according to:

$$\Delta k = \Delta k_0 + \frac{\partial \Delta k}{\partial \zeta}\Big|_{\zeta_0} \delta\zeta + \ldots \tag{2-85}$$

Clearly, only the first two terms of the expansion has been accounted, which is an acceptable approximation provided Δk has a first order dependence on ζ. The FWHM acceptance bandwidth in ζ, which will be denoted $\Delta\zeta$, is then found by:

1) fixing all other parameters to a set value
2) solving Eq. (2-85) for the value of $\delta\zeta$ that satisfies Eq. (2-84) and
3) using: $\Delta\zeta=2\,\delta\zeta$

This procedure gives:

$$\Delta\zeta = \frac{5.57}{L}\left[\frac{\partial \Delta k}{\partial \zeta}\Big|_{\zeta_0}\right]^{-1} \tag{2-86}$$

Analytical expressions for the acceptance bandwidths will now be derived for the indicative case of second harmonic generation (SHG). For perfect phase-matching, the scalar phase-matching condition for SHG can be expressed as:

$$\Delta k = k_{SHG} - 2k_F = \frac{2\pi n_{SHG}}{\lambda_{SHG}} - 2\frac{2\pi n_F}{\lambda_F} = \frac{4\pi}{\lambda_F}(n_{SHG} - n_F) = 0 \tag{2-87}$$

where λ_F, λ_{SHG}(=1/2 λ_F), n_F and n_{SHG} are the free space wavelengths and refractive indices for the fundamental and second harmonic, respectively, at perfect phase-matching. Thus, the derivative with respect to the fundamental wavelength is given by:

$$\frac{\partial \Delta k}{\partial \lambda_F} = \frac{\partial}{\partial \lambda_F}\left[\frac{4\pi}{\lambda_F}(n_{SHG} - n_F)\right] = \frac{4\pi}{\lambda_F}\left[-\frac{n_{SHG} - n_F}{\lambda_F} + \frac{1}{2}\frac{\partial n_{SHG}}{\partial \lambda_{SHG}} - \frac{\partial n_F}{\partial \lambda_F}\right]$$

Substituting to Eq. (2-86) yields the fundamental (or pump) wavelength acceptance bandwidth:

$$\Delta\lambda_F = \frac{0.44\lambda_F}{L}\left[\frac{1}{2}\frac{\partial n_{SHG}}{\partial \lambda}\Big|_{\lambda_{SHG}} - \frac{\partial n_F}{\partial \lambda}\Big|_{\lambda_F} - \frac{n_{SHG} - n_F}{\lambda_F}\right]^{-1} \tag{2-88}$$

Similarly, the temperature acceptance bandwidth can be calculated:

$$\Delta T = \frac{0.44\lambda_F}{L}\left[\frac{\partial n_{SHG}}{\partial T}\Big|_{T_0} - \frac{\partial n_F}{\partial T}\Big|_{T_0}\right]^{-1} \tag{2-89}$$

where the derivatives are calculated at the perfect phase-matching temperature T_0.

In the case of quasi-phase-matching, the grating period term should be added to Eq. (2-87), resulting in an SHG phase-matching condition:

$$\Delta k = k_{SHG} - 2k_F - k_m = \frac{4\pi}{\lambda_F}(n_{SHG} - n_F) - \frac{2\pi m}{\Lambda} = 0 \tag{2-90}$$

where Λ is the grating period, which clearly is independent of wavelength. Therefore, the pump acceptance bandwidth is given by equation (2-88) that was obtained for perfect phase-matching. On the contrary, Λ does depend on temperature since the material undergoes thermal expansion. Hence, for quasi-phase-matching the temperature acceptance bandwidth is given by:

$$\Delta T = \frac{0.44\lambda_F}{L}\left[\frac{\partial n_{SHG}}{\partial T}\Big|_{T_0} - \frac{\partial n_F}{\partial T}\Big|_{T_0} - \frac{m}{2}\frac{\partial 1/\Lambda}{\partial T}\Big|_{T_{0/}}\right]^{-1} \tag{2-91}$$

Studies of acceptance bandwidths for three wave mixing processes as well as expressions for angular acceptance bandwidths, can be found elsewhere [1,2].

2.5 Nonlinear interactions with Gaussian beams

In section 2.3.3 the coupled wave equations for SHG were solved to establish the efficiency of the undepleted nonlinear process assuming zero input, plane wave propagation in a lossless medium. In most practical cases, however, focused Gaussian beams are used in nonlinear interactions, in order to increase the fundamental power density P_ω / A and therefore the generated second harmonic intensity. A general theory of focused Gaussian beams interactions has been discussed by a number of authors [44-48]. Being relatively simple, it is interesting to examine the special case of SHG in a short length nonlinear material as illustrated in Fig 2.7.

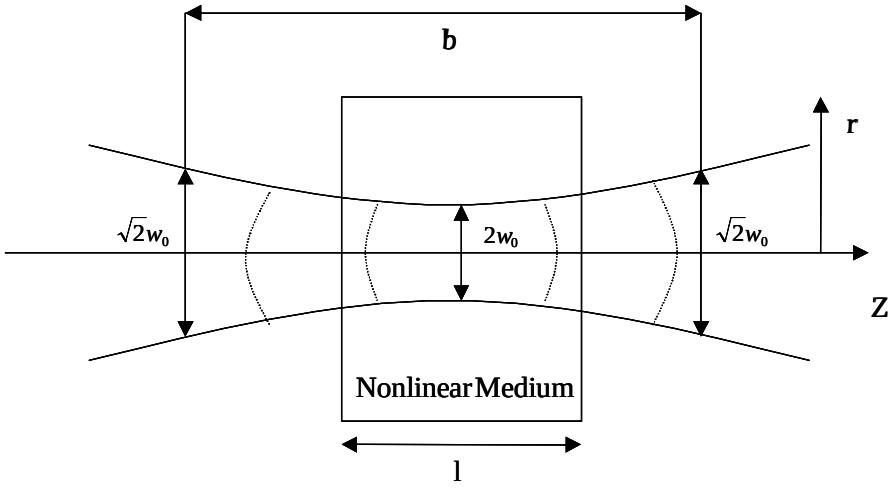

Fig 2.7 Gaussian beam geometry with beam radius at waste w_0 and confocal parameter *b* larger than the length of the nonlinear medium. Dashed lines show the increase in curvature of the wavefronts with distance from the waist.

It has been assumed that the length of the crystal is smaller than the confocal parameter *b* of the focused Gaussian beam, defined as the length over which the beam size acquires the value $\sqrt{2}w_0$, where w_0 is the beam waist. The confocal parameter *b* is related to beam waist via [49]:

$$b = k_\omega \cdot w_o^2 \tag{2-92}$$

In this case, it is a valid approximation to consider the beam as being collimated throughout the interaction length. In this near field limit, the field can be expressed as:

$$E_\omega \cong E_{0,\omega} \cdot e^{-\frac{r^2}{w_0^2}} \tag{2-93}$$

Multiplying (2-93) by its complex conjugate the corresponding intensity can be expressed as:

$$I_\omega = \frac{1}{2}(\frac{\varepsilon_0}{\mu_0})^{1/2} n_\omega E_\omega E_\omega^* = I_{0,\omega} e^{-2\frac{r^2}{w_0^2}} \tag{2-94}$$

where the following substitution is used:

$$I_{0,\omega} = \frac{1}{2}(\frac{\varepsilon_0}{\mu_0})^{1/2} n_\omega E_{0,\omega} E_{0,\omega}^* \tag{2-95 a}$$

The power of the field can readily be calculated:

$$P_\omega = \int I_\omega dxdy = I_{0,\omega} \int e^{-2\frac{r^2}{w_0^2}} = I_{0,\omega} \int_{-\infty}^{\infty}\int_{-\infty}^{\infty} e^{-2\frac{(x^2+y^2)}{w_0^2}} dxdy \Rightarrow$$

$$P_\omega = I_{0,\omega}(\frac{1}{2}\pi w_0^2) \tag{2-95 b}$$

The same process can be followed for the generated SH field. Assuming that the fundamental and generated fields have equal confocal parameters, the beam waist of the second harmonic beam is equal to $w_0 / \sqrt{2}$, thus:

$$I_{0,2\omega} = \frac{1}{2}(\frac{\varepsilon_0}{\mu_0})^{1/2} n_\omega E_{0,2\omega} E_{0,2\omega}^* \tag{2-96 a}$$

$$P_{2\omega} = I_{0,2\omega}(\frac{1}{4}\pi w_0^2) \tag{2-96 b}$$

By definition, $I_{0,\omega}$ and $I_{0,2\omega}$ are the field intensities along the propagation axis (r=0) and are expected to satisfy the plane wave result (2-59):

$$I_{0,2\omega}(l) = [\frac{2l^2 d_{eff}^2}{\varepsilon_0 c^3}\frac{\omega^2}{n_{2\omega} n_{2\omega} n_\omega}] \cdot I_{0,\omega}^2 \cdot \sin c^2\{\frac{l\Delta k}{2}\} \Rightarrow \tag{2-97 a}$$

$$P_{2\omega}(l) = [\frac{2l^2 d_{eff}^2}{\varepsilon_0 c^3}\frac{\omega^2}{n_{2\omega} n_{2\omega} n_\omega}] \cdot P_\omega^2 \cdot (\frac{1}{\pi w_0^2}) \cdot \sin c^2\{\frac{l\Delta k}{2}\} \tag{2-97 b}$$

resulting in a nonlinear efficiency:

$$n_{SHG}^{Gauss} = \frac{P_{2\omega}}{P_\omega} = [\frac{2\omega^2 d_{eff}^2}{\varepsilon_0 c^3 n_{2\omega}^2 n_\omega}] \cdot l^2 \cdot \frac{P_\omega}{\pi w_0^2} \cdot \sin c^2\{\frac{l\Delta k}{2}\} \tag{2-98}$$

It is clear that the efficiency of the process increases as the beam waist decreases, that is, as focusing becomes tighter. Therefore, the maximum efficiency is achieved at the limit: $l \to b$ (confocal focusing), corresponding to a value:

$$(\frac{P_{2\omega}}{P_{\omega}})_{\max} = [\frac{2\omega^2 d_{eff}^2}{\varepsilon_0 c^3 n_{2\omega}^2 n_{\omega}}] \cdot k_{\omega}{}^2 w_o^2 \cdot \frac{P_{\omega}}{\pi} \cdot \sin c^2 \{\frac{l\Delta k}{2}\} \quad (2\text{-}99)$$

Further focusing results in a reduced efficiency, due to strong difraction within the crystal.

A more accurate analysis by Boyd and Kleinman [44] includes the effects of double refraction and results in an expression identical to (2-83), introducing though a reduction factor $h_m(\xi,\rho)$, where $\xi = l/b$ is the focusing parameter and ρ the Poynting vector walk off angle given by (2-63). Numerical evaluation of the reduction factor can be found in the original work [44].

2.6 Summary

In this chapter a brief review of basic nonlinear optics concepts was given. It was shown that the nonlinearity in light-matter interactions arises from a distortion in the harmonicity of the atomic dipole oscillators in presence of efficiently strong fields. The nonlinear susceptibility was introduced to develop expressions for the resulting higher order optical polarisation in matter. The second order polarisation was then inserted into Maxwell equations to obtain a wave equation. Solving the wave equation allowed the description of the interaction of three waves via a set of three differential equations known as the coupled wave equations. It was shown that the coupled wave equations predicted that the strength of a nonlinear interaction maximises when the phase-matching condition is satisfied.

The complications in achieving phase-matching in dispersive media were discussed and the standard phase-matching methods presented. It was shown that the optical anisotropy of a medium can be used to perfectly phase-match nonlinear interactions, while the alternative technique of quasi-phase-matching through spatially modulating the nonlinear coefficients was described. A final discussion on the use of Gaussian beams instead of plane waves in nonlinear interactions was allowed.

In the following chapter, the theory presented here will be used to provide an insight into a nonlinear device that was constructed and served as the pump source for the experiments in this thesis: The femtosecond optical parametric oscillator.

References

[1] N. Bloembergen, *Nonlinear Optics*, W.A Benjamin Inc, 1965

[2] R W Boyd, *Nonlinear Optics*, Academic Press, 1992

[3] J A Armstrong, N Bloembergen, J Ducuing and PS Pershan, *Interactions between light waves in a nonlinear dielectric*, Phys. Rev. 127, 1918-1939, (1962)

[4] A.Yariv, *Quantum Electronics*, 3rd Edition, John Wiley & Sons Inc, 1989

[5] Hanna, Yuratich, Cotter, *Nonlinear Optics of Free Atoms and Molecules*, Springer-Verlag Berlin, 1979

[6] F Zernike and J E Midwinter, *Applied nonlinear optics*, J Wiley & Sons Inc, 1973

[7] C.G.B Garret and F.N.H Robinson, *Miller's Phenomenological Rule for computing Nonlinear Susceptibilities*, IEEE J Quant. Elec. QE-2, 328 (1966)

[8] R.W Minck, R.W. Terhune and C.C Wang, *Nonlinear Optics*, Applied Opttics 5, 1595-1612, (1966)

[9] W. Kaiser and G.C.B. Garrett, *Two photon excitation in CaF2; Eu2+*, Phys. Rev. Let 7, 229-231 (1961)

[10]Y.R Shen and N Bloembergen, *Theory of stimulated Brilluin and Raman scattering*, Physical Review 137, A1787-11805, (1965)

[11] R. W. Hellwarth, *Generation of time-reversed wave fronts by nonlinear refraction*, J Opt. Soc. Am, 67:1-3, (1977)

[12] D.A. Kleinman, *Nonlinear dielectric polarisation in optical media*, Phys. Rev. 126, 1977-1979 (1962)

[13] K.V. Diesperov and V.G Dmitriev, *Effective nonlinear coefficient for sum-frequency generation with collinear phase matching calculated taking account of the birefringence in biaxial crystals*, Quant. Elec. 27 (5), 433-436 (1997)

[14] K.Asaumi, *Approximate effective nonlinear coefficient of 2nd harmonic generation in $KTiOPO_4$*, Applied Optics 32 (30), 5983--5985 (1993)

[15] V.G Dmitriev and D.N. Nikogosyan, *Effective nonlinear coefficients for 3-wave interactions in biaxial crystals of mm2 point group symmetry*, Opt. Com. 95 (1-3), 173-182 (1993)

[16] *see for example:* J.D Jackson, *Classical electrodynamics*, J Wiley & Sons Inc, 3rd Ed. (1999)

[17] H.J. Liu, G.F.Chen, W. Zhao, Y.S. Wang and S.H. Zhao, *Phase matching analysis of noncollinear optical parametric process in nonlinear anisotropic crystals*, Optics Communications, 197 (4-6) pp. 507-514 (2001)

[18] J.A Giordmaine, *mixing of light beams in crystals*, Physical Review Letters 8, 19-20, (1962)

[19] P.D. Maker, R.W. Terhune, N. Nisenoff and C. Savage, *Effects of dispersion and focusing on the production of optical harmonics*, Physical Review Letters 8, 21-22, (1962)

[20] *see for example:* M. Borh and E Wolf, *Principles of optics*, Cambridge University Press, 7th edition (1999)

[21] J.Q. Yao and T.S Fahlen, *Calculations of optimum phase match parameters for the biaxial crystal $KTiOPO_4$*, J. Appl. Phys. 55 (1), 65-68, (1984)

[22] J. Yao, W. Sheng and W. Shi, *Accurate calculation of optimum phase matching parameters in three wave interactions with biaxial nonlinear optical crystals*, J. Opt. Soc. Am. B 9 (6), 891-902, (1992)

[23] M.A. Dreger and J.H. Erkkila, *Improved method for calculating phase matching criteria in biaxial nonlinear material*, Opt. Let. 17 (11), 787-788, (1992)

[24] M.V. Hobden, *Phase matched second harmonic generation in biaxial crystals*, J. Appl. Phys. 38, 4365-4372 (1967)

[25] V.G Dmitriev, G.G Gurzadyan and D.N. Nikogosyan, *Handbook of nonlinear optical crystals*, Springer-Verlag, (1991)

[26] F Brehat, and B. Wyncke, *Calculation of double refraction walk off angle along the phase matching directions in nonlinear biaxial crystals*, J. Phys. B: At. Mol. Opt. Phys. 22, 1891-1898 (1989)

[27] T. Suhara and H. Nishihara, *Theoretical analysis of wave-guide 2^{nd} harmonic generation phase matched with uniform and chirped gratings*, IEEE J Quantum Electronics, (26) 1265, (1990)

[28] K. Mizuuchi, K. Yamamoto, M. Kato and H. Sato, *Broadening of the phase matching bandwidth in quasi-phase matched second harmonic generation*, IEEE J Quantum Electronics, (30) 1596, (1994)

[29] L.M. Bortz, M. Fujimura and M.M. Fejer, *Increased acceptance bandwidth for quasi-phase matched second harmonic generation in $LiNbO_3$ waveguides*, Electron Letters, (30) 34, (1994)

[30] S. Somekh and A. Yariv, *Phase matching by periodic modulation of nonlinear coefficients*, Opt. Comm., (6) 301-304, (1972)

[31] Y. Yacobi, R.L. Aggarwal and B. Lax, *Phase matching by periodic variation of nonlinear coefficients*, J. Appl. Phys., (44) 3180-3181, (1973)

[32] J.D. McMullen, *Optical parametric interactionsin isotropic materials using a phase corrected stack of nonlinear dielectric plates*, J. Appl. Phys., (46) 3076-3081, (1975)

[33] A. Szilagyi, A. Hordvik and H. Schlossberg, *A quasi phase matched technique for efficient optical mixing and frequency doubling*, J. Appl. Phys., (47) 2025-2032, (1976)

[34] K.C Rustagi, S.C. Mehendale and S. Meenakshi, *Optical frequency conversion in quasi phase matched stacks of nonlinear crystals*, IEEE J. Quantum Electron., (QE18) 1029-1041, (1982)

[35] M.M Fejer, G.A. Magel, D.H Jundt and R.L. Byer, *Quasi phase matched second harmonic generation: tining and tolerances*, IEEE J. Quantum Electron., (28) 2631-2654, (1992)

[36] E.J. Lim, M.M Fejer and R.L. Byer, *Second harmonic generation of green light in periodically poled planar lithium niobate waveguide*, Electron. Lett., (25) 174-175, (1989)

[37] H. Ito, C. Takyu and H Inaba, *Fabrication of periodic domain grating in $LiNbO_3$ by electron beam writing for application of nonlinear optical processes*, Electron. Lett., (27) 1221-1222, (1991)

[38] Y. Lu, L. Mao and N.B. Ming, *Blue light generation by frequency doubling of an 810nm cw GaAlAs diode laser in a quasi phase matched $LiNbO_3$ crystal*, Opt. Lett., (19) 1037-1039, (1994)

[39] M. Houe and P.D. Townsend, *An introduction to methods of periodic poling for second harmonic generation*, J. Phys. D: Appl. Phys., (28) 1747-1763, (1995)

[40] M. Yamada, N. Nada, M. Saitoh and K. Watanabe, *First order quasi phase matched $LiNbO_3$ waveguide periodically poled by applying an external field for efficient blue second harmonic generation*, Appl. Phys. Lett., (62) 435-436, (1993)

[41] J. Webjorn, V. Pruneri, P.S.J. Russel, J.R.M. Barr and D.C. Hanna, *Quasi phase matched blue light generation in bulk lithium niobate, electrically poled via periodic liquid electrodes*, Electron. Lett., (30) 894-895, (1994)

[42] L.E. Myers, R.C. Eckardt, M.M Fejer, R.L. Byer and W.R. Bosenberg, *Quasi phase matched optical parametric oscillation in bulk periodically poled $LiNbO_3$*, J. Opt. Soc. Am. B, (12) 2102-2116, (1995)

[43] L.E. Myers and W.R. Bosenberg, *Periodically poled lithium niobate and quasi phase matched optical parametric oscillators*, IEEE J. Quantum Electron., (33) 1663-1672, (1997)

[44] G.D. Boyd and D.A Kleinman, *Parametric interaction of focused Gaussian light beams*, J. Appl. Phys., (39) 3597-3639, (1968)

[45] J.E. Bjorkholm, *Optical second harmonic generation using a focused Gaussian laser beam*, Physical Rev., (142) 126, (1966)

[46] P.D Maker, R.W. Terhune, N. Nisenoff and C. Savage, *Effects of dispersion and focusing on the production of optical harmonics*, Physical Rev. Lett., (8) 21-22, (1962)

[47] R. Asby, *Theory of optical parametric amplification from a focused Gaussian beam*, Physical Rev. B, (2) 4273-4282, (1970)

[48] S. Guha, F.J. Wu and J. Falk, *The effects of focusing on parametric oscillation*, IEEE J. Quantum Electron, (QE-18) 907-912, (1982)

[49] *see for example:* A.E Siegman , *Lasers*, University Science Books, (1986)

3. FEMTOSECOND OPTICAL PARAMETRIC OSCILLATOR

3.1 Introduction

The generation of tunable optical pulses in the infra-red (IR), with picosecond and femtosecond durations, has been one of the main objectives of laser research in view of a variety of applications, ranging from time-resolved spectroscopy of molecules to carrier dynamics in semiconductors. It is also vital for the investigation of phase-matched nonlinear processes where high peak power levels and tunable pump beams are desirable. One successful approach for ultrashort pulse generation relies on mode-locking of conventional laser media with broad gain bandwidths, such as dye or vibronic solid state lasers (most notably the Ti: sapphire). However, these sources are limited in wavelength below ~ 1 μm. The potential of nonlinear frequency conversion as an alternative means for tunable light generation in previously unavailable wavelengths was established in 1965 with the realisation of the first optical parametric oscillator (OPO) by Giordmaine and Miller [1].

An OPO down-converts a higher frequency pump beam (ω_p) provided by a laser source into lower frequency signal (ω_s) and idler (ω_i) beams through parametric generation in a second order nonlinear material. The signal and idler wavelengths are determined by the phase-matching condition in the crystal. Parametric oscillation has been demonstrated in both birefringent and quasi-phase-matched media. Modifying the phase-matching condition by controlling the angle, the temperature, the pump wavelength or the quasi-phase-matching period makes the OPO a versatile source of coherent radiation, with tuning limited in principle only by the transparency range of the material. Comprehensive reviews on optical parametric devices can be found in a number of sources [2-10].

This Chapter is dedicated to presenting results from a synchronously pumped optical parametric oscillator (SPO) that was constructed and used as the pump source for all the experiments related to this work, along with an introduction to this class of devices.

3.2 Synchronously pumped optical parametric oscillators

3.2.1 Optical parametric devices: An overview

Optical parametric devices have been operated in a number of configurations. In the most general case, the incident pump laser beam is focused into the crystal providing parametric gain at the signal and idler frequencies. In the absence of a complementary source of signal or/and idler beams at the input, the initial supply of down-converted photons for the initialisation of the interaction is provided spontaneously through a process referred to as parametric fluorescence. For sufficiently high gain, macroscopic amplification of the parametric waves can be achieved with a single pass through the crystal. Devices based on this principle are parametric generators (OPG) and parametric amplifiers (OPA) [11]. Optical parametric oscillators form a different type of parametric device, which can be schematically represented by a nonlinear crystal in a cavity. In this case, when the parametric gain exceeds the cavity loss, the OPO exceeds threshold and oscillates in a manner similar to a laser oscillator, with the clear difference that the instantaneous $\chi^{(2)}$ process results in lack of gain storage. An immediate distinction can be made between doubly resonant OPO's (DRO) operating with resonant feedback at both the signal and idler frequencies [12,13], and singly resonant OPO's (SRO) with only one resonant parametric field [14,15]. Doubly resonant devices operate with lower pump threshold intensities than SROs, since both generated waves experience minimal loss. However, they suffer from instabilities caused by cavity length or pump frequency variations due to the fact that both signal and idler waves need to be properly resonated. Other architectures include SRO or DRO devices with resonant pump enhancement [16] by use of a separate pump source as well as OPO's with the nonlinear crystal placed inside the cavity [17] of the pump laser where large intracavity intensities are available.

Parametric oscillators are classified as cw [12-17] or pulsed [1, 18-20] devices, depending on the means of pumping. Pulsed devices (typically driven by Q-switched lasers) offer the advantage of large input intensities compared to cw OPOs. However, in the former case operation above threshold requires that pump pulse duration is larger than the time required for the parametric gain to built up above the intracavity loss, known as rise time [21]. This limits the applicability of pulsed OPOs to nanosecond time scales. Picosecond [22-25] and femtosecond [26-30] pulses can be

attained by means of a different geometry, involving synchronous pumping. A synchronously pumped OPO (SPO) is designed so that the device cavity length is matched to the cavity length of the pump source. In this way, the intracavity parametric pulses return to the nonlinear crystal entrance at the same time as the subsequent pump pulse, ensuring that the amplification process is repeated over every round trip of the resonant pulses. The pump pulses in a SPO may arrive in the form of either a continuous sequence or a train of pulses contained within a nano/microsecond envelope. In the first case, the device operates in a quasi-cw fashion (cw SPO) and a steady state analysis can be applied to describe its performance, considering that the peak pump power determines the nonlinear gain. In the later case (pulsed SPO), a more complicated transient analysis is required accounting for the rise time effects present in pulsed OPOs.

3.2.2 Steady-state analysis of the continuous wave, singly resonant OPO

A simple model [2] providing a guide to the operational characteristics of the cw-SRO, which is of paramount interest for the purposes of this work, can be outlined based on the following assumptions: a) all interacting waves can be approximated by plane waves, b) the pump and the non resonated parametric filed (idler, say) are single passed through the nonlinear crystal so that the parametric waves are amplified in the forward direction only, c) the pump is not depleted. In this case and under steady state operation the resonant signal field may be taken as constant throughout the length of the nonlinear medium. On the contrary, the idler field grows from zero at the entrance to a finite value at the exit of the crystal, before abandoning the cavity after a single pass.

The threshold condition for the SRO occurs when the parametric gain equals the round trip power loss at the resonated signal, which is denoted by a_s and accounts for the leakage of the coupler mirror, as well as any other parasitic losses in the cavity. In turn, the parametric gain coefficient has been presented in Table 2.1:

$$\Gamma^2 = \frac{2\omega_s \omega_i d_{eff}^2}{\varepsilon_0 c^3 n_s n_i n_p} I_p(0) \tag{3-1}$$

where the usual notation is used. It should be noted that Eq. (3-1) implies that the parametric gain obtains a maximum at the degenerate case when $\lambda_s = \lambda_s = 2\lambda_p$ and decreases for operation away from degeneracy. However, in practical SRO devices

operation very close to degeneracy is disturbed since the two parametric fields are indistinguishable. Assuming a crystal length L, the threshold condition can therefore be expressed as:

$$\Gamma^2 L^2 = a_s$$

resulting by use of (3-2) in a threshold pump intensity:

$$I_p^{th} = \frac{\varepsilon_0 c^3 n_s n_i n_p a_s}{2\omega_s \omega_i d_{eff}^2 L^2} \tag{3-2}$$

The exchange of energy between the interacting waves is explicitly described by a system of equations which includes: a) the photon conservation relation[1] (3-3), which is a modified form of the Manley-Rowe relations to account for the intracavity loss for the signal (a_s) and idler (a_i), and b) the coupled wave equations (3-4) for three wave mixing, modified appropriately to account for the assumptions of constant signal field and (for simplicity) perfectly phase-matched process:

$$\frac{a_s I_s}{\hbar\omega_s} = \frac{a_i I_i}{\hbar\omega_i} = \frac{I_p(z=0) - I_p(z=L)}{\hbar\omega_p} \tag{3-3}$$

$$\frac{dE_i}{dz} = i\frac{\omega_i}{n_i c} d_{eff} E_p E_s^* \qquad \frac{dE_s}{dz} = 0 \qquad \frac{dE_p}{dz} = i\frac{\omega_p}{n_p c} d_{eff} E_s E_i \tag{3-4}$$

Differentiating the last of Eq. (3-4) with respect to the propagation length z and substituting the first of (3-4) to eliminate the idler wave amplitude, the equation of motion of a harmonic oscillator arises as:

$$\frac{d^2 E_p}{dz^2} = -[\frac{\omega_p \omega_i}{n_p n_i}\frac{d_{eff}^2}{c^2}(E_s E_s^*)] \cdot E_p \tag{3-5}$$

The general solution is thus given by:

$$E_p = A\sin(\Omega z) + B\cos(\Omega z) \tag{3-6}$$

where A, B are constants and

$$\Omega = [\frac{\omega_p \omega_i}{n_p n_i}\frac{d_{eff}^2}{c^2}(E_s E_s^*)]^{1/2} \tag{3-7}$$

Applying the boundary conditions that at z=0, both E_i and hence dE_p/dz are zero, the constants A and B are readily determined (A=0 and B=E_p(0)), so that:

[1] Relation (3-3) suggests that every lost pump photon inside the medium generates one signal and one idler photon at the output

$$E_p(L) = E_p(0)\cos(\Omega L) \Rightarrow I_p(L) = I_p(0)\cos^2(\Omega L) \tag{3-8}$$

With appropriate use of the intensity definition[2], as well as of equations (3-3) and (3-2), the harmonic oscillator frequency Ω can be simplified:

$$\Omega = [\frac{\omega_p \omega_i}{n_p n_i}\frac{d_{eff}^2}{c^2}\frac{2}{c\varepsilon_0 n_s} I_s]^{1/2} = [\frac{\omega_p \omega_i}{n_p n_i}\frac{d_{eff}^2}{c^2}\frac{2}{c\varepsilon_0 n_s}\frac{(I_p(0) - I_p(L))\cdot \omega_s}{a_s \omega_p}]^{1/2} \Rightarrow$$

$$\Omega = [\frac{I_p(0) - I_p(z))}{I_p^{th} L^2}]^{1/2} \tag{3-9}$$

Combining (3-8) and (3-9), the transmitted pump intensity at the exit facet of the nonlinear medium can be given as a function of the input pump intensity:

$$I_p(L) = I_p(0)\cos^2\left[\left(\frac{I_p(0) - I_p(L)}{I_p^{th}}\right)^{1/2}\right] \tag{3-10}$$

For input pump intensities below the threshold intensity Eq. (3-10) has no real solution. At the limit when the input pump intensity equals the threshold intensity, Eq. (3-10) suggests that all the pump power available in the entrance transmits through the crystal and hence no conversion takes place. As the input pump increases beyond threshold, the transmitted pump starts converting into signal and idler waves until it is 100% converted ($I_p(L)$=0) for an input pump intensity 2.47 times the threshold pump intensity. With further increase of the input intensity the efficiency of the process is actually reduced, since the pump wave begins to grow at the expense of the signal. This behaviour is depicted in Fig. 3.1.

It is pointed out again that the above discussion is valid for both cw SROs and quasi-cw synchronously pumped SROs, with use in the second case of peak pump intensities. A more sophisticated analysis of the SRO dynamics can be found in a number of sources [3,31]. The main results, however, including the condition for 100% conversion, remain the same for operation a few times above threshold. It is shown that threshold can be reduced by a factor of 2 if the pump wave is double-passed through the nonlinear medium, or by a factor of 4 if the pump and the non-resonant parametric waves are double passed.

[2] $I = \frac{1}{2}(\frac{\varepsilon_0}{\mu_0})^{1/2} n(EE^*) = \frac{1}{2} c\varepsilon_0 n(EE^*)$

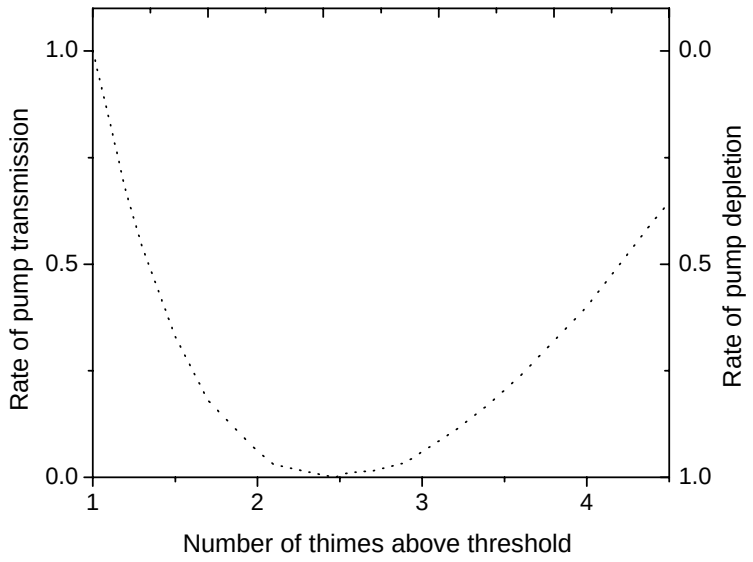

Fig 3.1 Transmitted ($I_p(L)/I_p(0)$) and depleted ($1-I_p(0)/I_p(L)$) pump intensity as a function of the number of times above threshold ($I_p(0)/I_p^{th}$) for a continuous wave, singly resonant OPO in the plane wave limit.

3.2.3 SPO spectral considerations

In general, the spectral properties of an OPO are determined by the phase-matching condition and the energy conservation requirement, the cumulative effect of which, for scalar BPM and QPM, respectively, is given by:

$$\Delta k = \frac{2\pi n_p}{\lambda_p} - \frac{2\pi n_s}{\lambda_s} - \frac{n_i(\lambda_s - \lambda_p)}{c\lambda_p\lambda_s} = 0$$

$$\Delta k^{QPM} = \frac{2\pi n_p}{\lambda_p} - \frac{2\pi n_s}{\lambda_s} - \frac{n_i(\lambda_s - \lambda_p)}{c\lambda_p\lambda_s} - \frac{2\pi m}{\Lambda} = 0$$

One of the most important consequences is that the OPO is a widely tunable optical source, since evidently from the above equations the output signal wavelength can be adjusted by means of pump wavelength, refractive index and grating period control (in the case of QPM). Refractive index control can be achieved with exploitation of the temperature or angle of incidence dependence of the refractive index (the second method limited to anisotropic media), as prescribed explicitly by the Sellemeier equations for the nonlinear crystal. Among all available techniques, grating period tuning is often the most flexible since: a) pump wavelength tuning is limited by the laser gain bandwidth, b) temperature tuning requires time for thermal equilibrium to be reached, and c) angle tuning complicates cavity alignment. In the following section

it will be shown that synchronously pumped OPOs are privileged with an additional tuning method due to temporal effects, namely cavity length mismatch tuning.

The preceding discussion refers to a single spectral line of the pump. With ultrashort pulses, however, the pump spectrum is expected to be relatively broad (typically ~10 nm for transform limited pulses in the femtosecond regime). Efficient parametric conversion, therefore, requires that the pump acceptance bandwidth as described in Chapter 2 is sufficiently high to provide gain even in the extremes of the pump spectrum. It has been shown that the acceptance bandwidth is inversely proportional to the length of the interaction, thus the crystal length should be short enough to allow participation of the entire input spectrum in the process. For many common nonlinear materials this limit corresponds to ~4-5 mm. It will be shown next that temporal effects impose more severe restrictions to the desired crystal length. Other spectral implications that might be of importance with ultrashort pulses include self-phase modulation but may be neglected to a first approximation.

3.2.4 SPO temporal considerations

With the use of ultrashort pulses the effects of group velocity dispersion (GVD) and walk-off as well as third order dispersion[3] need be considered in an analysis of the operational dynamics of the SPO. Advanced models have been developed to simulate the growth of the parametric pulses using both the plane wave limit [32] and Gaussian beam theory [33]. One of the main conclusions of these studies is that, in absence of GVD, the parametric pulses from a SPO are always shorter than the pump pulse. Furthermore, it is shown that the output pulse duration increases with increasing pump depletion.

In practice, however, the generated pulses experience temporal broadening due to GVD and higher order dispersion. To a first approximation, third or higher order dispersion can be neglected for pulses with duration longer than ~50 fs. Second order dispersion (GVD), although not always welcome, has an interesting side effect: it introduces a complementary means of tuning through manual cavity length mismatch. In fact, a gradual change in the cavity length from the optimised synchronous geometry results in a shift of the output wavelength before it brings operation to a

[3] A discussion on ultrashort pulse propagation can be found in Appendix A.

halt. This can be understood in terms of GVD alone as follows: Even for slightly mismatched cavity (shorter length, say), the SPO keeps running at the same repetition rate as the pump source since the parametric gain is instantaneous. Assuming positive GVD, sufficient temporal overlap between the pump and resonated pulse is only available for shorter (and thus slower) output wavelength components. Hence, shorter cavity lengths favour shorter signal wavelengths and vice versa. It can be shown that the cavity length tuning rate $d\lambda/dL$ is related to the net single pass cavity dispersion by [33,34]:

$$GVD(fs^2) = \frac{\lambda^2}{2\pi c^2}\left(\frac{d\lambda}{dL}\right)^{-1} \tag{3-11}$$

For common nonlinear crystals (PPLN for example) this suggests that a tuning range of the order of hundreds of nanometers is attainable (provided a similarly broad gain bandwidth is supported) with sub-mm cavity length adjustment. The rate of cavity length tuning can be reduced (or abolished in case of zero GVD) when dispersion compensation optics are introduced. Third order dispersion can be usually neglected in near and mid-IR wavelengths for pulse durations longer than ~50 fs.

Finally, group velocity mismatch between the pump, signal and idler becomes a dominating temporal effect, especially with femtosecond pulses, restricting the actual interaction length. Clearly, the temporal separation due to group velocity mismatch between the pump and the resonant field (signal, in our standard example) has a direct effect to the efficiency of the interaction. However, mismatch between the pump and the non-resonant fields (idler) also has an impact on the interaction since it restricts the pump-idler mixing process. In the near and mid-IR, many standard nonlinear materials produce a walk-off value of a few hundreds of fs/mm for the pump-signal propagation, suggesting that crystals lengths in excess of ~1-2 mm are not suited. Compared to the 4-5 mm limitation set by gain bandwidth considerations, it is evident that group velocity walk-off sets the ultimate limit to the crystal length. It should be noted that the quoted values refer to femtosecond systems. In the case of picosecond OPOs temporal effects become less critical.

3.2.5 SPO design considerations

In designing a SPO a number of issues concerning the pump source, the nonlinear medium, and the cavity geometry should be addressed properly. With respect to the first, the main parameters determining the potential of a laser as a pump source are output wavelength and intensity, in order to access the desired λ_p and maximise the parametric gain. For synchronous pumping, the repetition rate of a laser is also important. In fact, a repetition rate of at least a few tens of MHz is required to restrict the synchronous OPO cavity to practical lenghts (~1 m) for a standard optical table. Additionally, a low output divergence is necessary to allow proper focusing of the pump beam into the crystal.

In choosing the gain medium, an obvious requirement is the presence of sufficiently large optical nonlinearity. In parallel, the dispersion profile of the medium should allow phase-matching in wavelength regions of interest. The linear optical properties of the material also determine the magnitude of walk-off and acceptance bandwidths, all of which play important role in OPO operation. The transparency range of the medium is also crucial, since absorption may result in rapid reduction in parametric gain. Moreover, absorption may cause heat or mechanical damage of the crystal, destabilizing or even halting the operation. In general, material damage threshold has a strong dependence on wavelength and pulse energy and can only be experimentally determined for conditions that apply to a specific device.

The SPO cavity specifications are influenced to a great extent by the need to focus the pump beam into the crystal so as to maximise the pump intensity and hence the parametric gain. A detailed theoretical analysis of the SRO threshold power [35,36] for focused Gaussian beams resulted in the following expression:

$$P_p^{th} = \frac{a_s n_s n_i n_p c^3 (k_s + k_p)}{(128\omega_s \omega_i \chi^2 \pi^2 k_s k_p L) h_s}$$

In the above, units are in the MKSA system, h_s is a focusing related reduction factor which is a function of the confocal parameter b (Eq. (2-76)) and all other variables have been defined earlier. Numerical calculations [36] show that the focusing factor maximises – and thus threshold obtains a minimum value – when:

$$\frac{L}{b} = 2.7 \Rightarrow w_0 = \left(\frac{L\lambda}{5.4\pi} \right)^{1/2} \tag{3-12}$$

With femtosecond pulses, the optimum length of the nonlinear medium is typically limited to ~1 mm. Substituting this value for L and assuming an indicative process with generated signal at ~1.5 μm, Eq. (3-11) gives an optimum beam waist radius w_0 ~ 10 μm.

The stability range of the OPO resonator can be analysed in a similar way to laser resonators using an ABCD matrix analysis [37,38]. This problem is beyond the scope of the present discussion. It should be mentioned, however, that stable resonators with corresponding spot sizes of the order ~ 10 μm are available with three (V) and four mirror (X, Z) standing-wave configurations. Ring (travelling wave) oscillators have also been demonstrated but present significant alignment complications [39]. One of the most extensively studied is the V-type cavity resonator shown in Fig. 3.2a. Typically, an input lens focuses the pump beam into the crystal. For cavity loss reduction, antireflection-coated crystals are commonly used at normal incidence. An alternative approach involves a Brewster-angled crystal, which however restricts angle tuning of the OPO. The fold-angle θ is kept small (<2-3 degrees) to minimise aberrations caused by astigmatism. The curvature of the cavity mirrors determines the spot size of the resonated parametric wave and thus the mode overlap between the interacting fields. Finally, the optimum transmission of the output coupler mirror is solely determined by the 100% depletion condition accounting for the maximum available pump power from the laser source. In Fig. 3.2b a semimonolithic variation of the V-cavity is shown [40,41]. Although in many aspects similar to the V-cavity, the semimonolithic design involves lower cavity loss (due to the smaller number of mirror surfaces) as well as easier collection of the non-resonated (idler) beam.

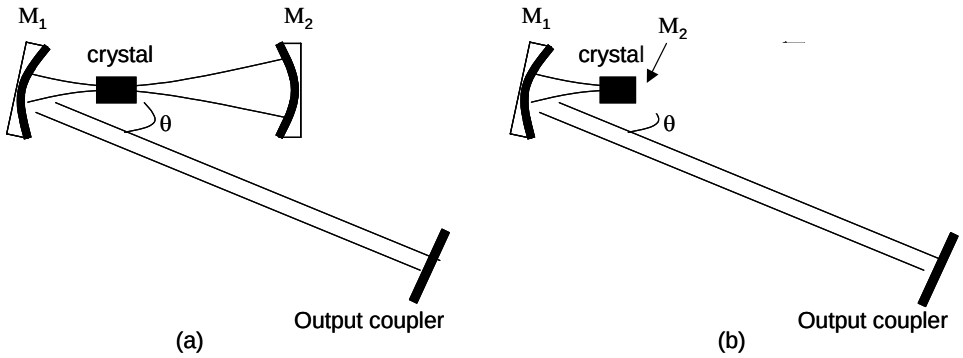

Fig. 3.2 Standard V-cavity (a) and semimonolithic (b) OPO configurations.

3.3 OPO construction and performance

3.3.1 Periodically poled lithium niobate

Our aim was to construct a device able to provide femtosecond pulses and access the IR wavelength range in which GaAs-based waveguides are candidates for nonlinear frequency conversion investigations, namely the ~1.5 to ~2 μm. Synchronously pumped OPOs based on periodically polled lithium niobate (PPLN) uniquely serve this task. In fact, lithium niobate ($LiNbO_3$) is a cornerstone material in the area of nonlinear optical devices with special reference to OPOs. This is mainly due to its large optical transparency, which extends from[4] ~0.33 μm to ~6.0 μm, and its exceptionally high nonlinearity. Furthermore, lithium niobate is ferroelectric and mature technology exists for fabrication of QPM structures through domain reversal by means of periodical poling [42]. Periodically poled lithium niobate (PPLN) has been extensively used in a number of applications ranging from SHG in the visible [43] to IR light generation by DFG [44] and parametric oscillation [45,46]. On the negative side, PPLN is susceptible to photorefractive damage[5] [45]. The photorefractive effect increases with decreasing wavelength, yet it remains substantial with IR parametric processes due to unavoidable non-phasematched SHG of the pump as well as pump-signal mixing that result in visible light generation. It is commonly accepted that photorefractive damage can be minimised by heating the crystal to temperatures above ~120 degrees.

Lithium niobate is a negative uniaxial crystal belonging to the crystallographic group *3m* and hence it has three independent non-zero nonlinear coefficients [47]: d_{22}~2.1 pm/V, d_{31}~-4.3 pm/V and d_{33}~-27 pm/V. A QPM interaction with all waves polarised along the *z*-optic axis is very attractive since it avoids spatial walk-off complications and also accesses the larger effective coefficient: $d_{eff}^{QPM} = 2d_{33}/\pi \sim -17\,\text{pm/V}$. From different reports of refractive index studies, the temperature dependent dispersion

[4] A second window exists in the range 6.3-7.5 μm

[5] This effect can be understood as a combination of the electro-optic effect (refractive index modulation in presence of an electrostatic field) and photoconductivity (conductivity due to illumination). In fact, when a beam with spatially varying intensity distribution propagates through PPLN, charge from high light intensity regions enters the conduction band and is transported to regions of low light intensity. In steady state, this charge separation creates a static space charge field, which induces a modulation in the index profile.

relation for the extraordinary index in Ref. [48] was adopted to evaluate the magnitude of group velocity dispersion and walk-off.

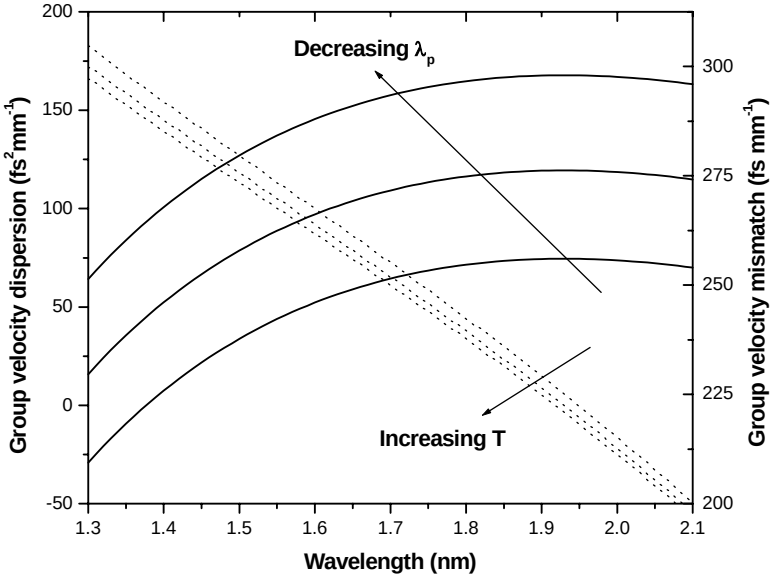

Fig. 3.3 Group velocity dispersion (dotted curves) and mismatch (solid curves) for PPLN in a wavelength range 1.3-2.1 μm. Group velocity dispersion varies with temperature as the arrow indicates (T=25, 150 and 300^0 C). Group velocity mismatch has been calculated between a pump pulse at 800, 815 and 830 nm and a signal/idler pulse in the 1.3 to 2.1 μm wavelength range.

Shown in Fig. 3.3, it is clear that PPLN presents a GVD of ~ 150 fs^2mm^{-1} at wavelengths near ~1.5 μm and crystal temperatures ranging from 25 to 30 ^{0}C. This suggests that temporal broadening is significant for femtosecond pulses travelling through lengths as short as ~1 mm. Fig. 3.3 also depicts the group velocity mismatch between a pulse at 800, 815 and 830 nm and a signal/idler pulse in the wavelength range 1.3-2.1 μm. It can be seen that walk-off is of the order of ~250 fs/mm in this wavelength range. The selection of the spectral range over which calculations were carried out is not random. In fact, a straight forward calculation shows that the 1.3-2.1 μm range corresponds to the output wavelengths of a PPLN OPO with a grating period Λ of ~21 μm, when pumped with a Ti:sapphire laser typically tunable between ~800 and 840 nm. Theoretical and experimental results for this device, along with the details of the actual PPLN crystal, will be given in following sections.

3.3.2 Device configuration and alignment

A continuous wave, singly resonant at the signal, semimonolithic, synchronously pumped femtosecond OPO [40] based on PPLN was constructed and served as the main source for all the experiments presented later in this thesis. The OPO was pumped by a home-made, Kerr-lens mode-locked, X-cavity Ti;sapphire laser [49], which produced pulses of ~120 fs duration at a repetition rate of ~89.5 MHz. The laser had a mode-locked tuning range of ~800 nm to ~840 nm with a spectral FWHM of ~ 6 nm and a bandwidth-duration product of $\Delta\nu\Delta\tau$~0.321, indicating transform limited pulses. Stable operation was achieved for long periods of time and output average power levels up to ~1 W were obtained throughout the tuning range, with corresponding peak powers exceeding ~90 kW. The Ti:sapphire laser was optically pumped by a commercial diode-pumped, cw, frequency doubled Nd:YVO_4 laser (Spectra-Physics Millennia 2000) which produced ~5W of output power at 532 nm. The OPO pump system is well established, it operates routinely in a number of laboratories and thus no further details regarding its construction and characterisation need be presented here.

The SPO cavity configuration is portrayed in Fig. 3.4. An optical Faraday isolator was introduced between the OPO and the pump laser to prevent feedback from the OPO, which could disturb the mode-locking process. A half-wave plate was also included to enforce the horizontal polarisation state of the pump required to access the optimum $e \rightarrow e+e$ interaction. The input pump beam was first expanded, through a two-lens telescope, and then focused at the back facet of the PPLN crystal via a 100-mm focal length input lens. The beam radius at the waist had a measured value of ~17 μm. The cavity comprises an input concave focusing mirror M_1 with a radius of curvature R_1=100 mm and a plane output coupler M_3. The mirror M_1 was coated[1] for high transmission (T>99%) at pump wavelengths and had high reflectivity (R>99.5%) over the signal wavelength range. The output coupler M_3 was highly reflecting at the signal wavelength range (a collection of output couplers was available, with corresponding reflectivities R=99%, R=94% and R=87%). The cavity was completed with a plane mirror M_2 directly coated at the exit facet of the nonlinear crystal, providing high

[1] Coating bandwidths are: (a) Pump range: ~0.77 -0.91 μm (b) Signal range: ~1.3-1.55 and (c) Idler range:~1.6-2.4 μm

reflection at the signal (R>99%) and pump (R>90%) and high transmission (T>80%) at the idler wavelength range. This allowed double-pass of the pump with a resulting reduction of the threshold power as well as easy extraction of the idler. The front facet of the crystal was also coated for high transmission at the pump (T>98%) and anti-reflection for the signal (R<0.25%) range. Two more plane high reflectors at the signal were inserted to fold the beam for practical purposes. The entire round-trip length of the cavity was ~336 cm. A pair of SF 14 prisms with an apex separation of ~19 cm was used for dispersion compensation. The prism separation length followed calculations based on the equations of Appendix A.

The PPLN crystal was provided by D.H. Jundt of Crystal Technology Inc. It comprised eight evenly spaced gratings of periods ranging from Λ_{min}=20.6 μm to Λ_{max}=22 μm in steps of 0.2 μm, chosen to access the desired wavelength range near ~1.5 μm (signal) and ~2 μm (idler). The length of the crystal was 1 mm, after group velocity mismatch considerations (plot 3.3) were taken into account. Its aperture was 0.5 mm (width) by 12 mm (height). The crystal orientation was such that collinear e→e+e interaction was employed with a horizontal input polarisation as described before. The PPLN was mounted on a three-dimension rotational and translation control stage and was maintained at temperatures of 120-200 ^{0}C in a specially designed servo-controlled oven.

The OPO alignment involved the following steps. First, the pump propagation axis X was marked on the optical table and the isolator, the telescope, the input focusing lens and the input mirror M_1 were positioned properly with respect to the X axis. The nonlinear crystal was then placed in the path near the beam waist and the back reflection of the pump from the crystal facet was aligned with the incoming beam to ensure normal incidence. The subsequent steps were greatly assisted by the non-phase- matched frequency doubling of the pump, which generated visible (blue) light. This visible light provided an indication as to the optimal relative positions of the input lens, the input mirror M_1 and the crystal. In fact, by locking one of these elements (M_1, say) to a permanent position, the input lens was linearly translated on X-axis until the blue light power was maximised. Then, the reflection of the visible light from the crystal was collimated by linearly translating on X-axis the crystal. These two steps were repeated until both maximum power and beam collimation were

achieved simultaneously. Following that, the folding mirrors were inserted and an intracavity path was impressed. The output coupler M_3 was placed at a distance matching the cavity length of the pump laser. That the output coupler was perpendicular to the beam path was ensured by overlapping the back reflected blue light with the intracavity beam. The OPO operation should readily kick in with fine translation of M_3 perpendicular to the intracavity path. Having achieved operation for the un-compensated system, a small amount of glass from the first prism was inserted, allowing the OPO to continue its operation but redirecting part of the intracavity beam to another path. This redirected beam was used to set the prism in a Brewster angle and consequently the second prism was added in the same way and at the calculated distance from the first prism. These two prisms defined the intracavity path of the compensated cavity, which was terminated by a second output coupler placed at the correct distance. The compensated OPO should require only fine adjustment of the (second) output coupler for oscillation to begin.

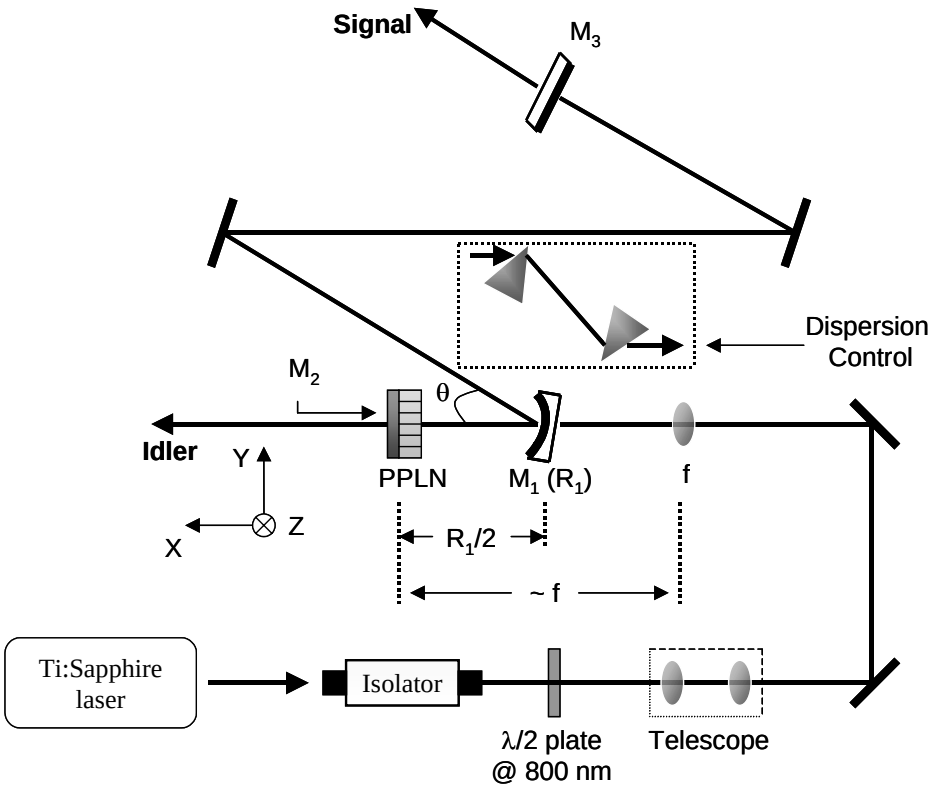

Fig. 3.4 Semimonolithic OPO arrangement. The input focusing lens has focal length f=100 mm. The input cavity mirror M_1 has a radius of curvature R_1=100 mm. The folding angle θ is set to less than 3 degrees, while the prism separation is 19 cm and the total one-way cavity length is 168 cm.

3.3.3 Device performance

Maximum output power from the compensated OPO cavity was obtained with an 87% output coupler. Average powers exceeding 100 mW for the signal and 50 mW for the idler were routinely attainable without the need of major maintenance work for periods of many months. The corresponding pump power reaching the crystal front facet was ~750 mW, indicating that the total available power from the laser (~1 W) was reduced by a factor of ~25% due to loss in the intermediate optics (a ~7 % loss contribution was measured form the optical isolator alone). The pump threshold power was less than ~200 mW, suggesting that the OPO was operated approximately 4 times above threshold. Increasing the cavity loss by use of a higher transmission output coupler would thus result in stronger conversion efficiency. No further studies were carried out in this direction since the power levels available with the 87% coupler were sufficient for the applications the system was dedicated to.

The combination of grating period, cavity length, pump wavelength and temperature tuning enabled coverage of the ~1.28-1.58 μm range for the signal branch and, correspondingly, ~1.71-2.28 μm for the idler branch. However, practical powers (>5mW) were only obtained in the ~1.3 μm to 1.58 μm and ~1.8 μm to 2.1 μm bands. It is evident that the dominant limiting factor in the OPO tuning range is the bandwidth of the mirror coatings. Fig. 3.5 presents typical OPO spectra throughout the tuning range of the device. The peak of each curve indicates the measured average power that corresponds to the specific wavelength. The spectral FWHM bandwidth was ~10 nm for the signal and ~26 nm for the idler. The strong modulation in the signal spectra near ~1.4 μm is due to absorption lines of water vapour in air.

A two-photon absorption autocorrelator was built to measure the signal and idler pulse duration. The apparatus of this instrument is shown in Appendix A. The necessity for autocorrelation quadratic response to input power was met by use of a Si photodiode [50] for the signal and an InGaAs photodiode for the idler [30]. Typical intensity and interferometric autocorrelations for both parametric pulses are shown in Fig. 3.6. With a good reproducibility, the signal pulse duration was found to be of the order of ~250 fs, while the idler duration was ~185 fs. Accounting for a ~90 MHz repetition rate, the resulting peak powers are ~ 4.5 kW for the signal and ~ 3 kW for the idler, with corresponding pulse energies of ~1.1 nJ and ~0.5 nJ. Furthermore, with

use of the measured spectral FWHM the bandwidth-duration product is $\Delta\nu\Delta\tau$~0.33 and $\Delta\nu\Delta\tau$~0.36 for the signal and idler, respectively, indicating near transform limited pulses.

A further insight into the tuning behaviour of the OPO is shown in Figs. 3.7 and 3.8. As discussed previously, the phase-matching condition involves four parameters, namely the parametric wavelength, the pump wavelength, the grating period and the temperature. In Figs. 3.7-3.8 two of these parameters are kept constant and the normilised gain is plotted in the two-dimensional space defined by the two remaining variable parameters. Perfect phase-matching (Δk=0) follows the solid lines. The parametric gain reduces to zero (Δk=$\pm 2\pi$) across the dashed lines and varies from 0.9 to 0.1 (in steps of 0.1) in the intermediate paths indicated by the dotted lines. These theoretical calculations were carried out with use of the dispersion relations given in Ref. [48]. In the case of Fig. 3.7 (grating period tuning diagram), the constant parameters are temperature: T=170^{0}C and pump wavelength: (a) λ_p=800 nm (b) λ_p=815 nm (c) λ_p=830 nm. In Fig. 3.8 (temperature tuning diagram), the constant parameters are grating period: Λ=21 μm and pump wavelength: λ_p=815 nm. These plots are supplied with corresponding experimental data obtained by means of cavity length tuning and shown as open circles.

A plethora of useful information can be obtained from these plots. It can be seen, for example, that the device operated in regions where normalised gains as low as ~10% were available. Furthermore, Fig. 3.7 indicates that (for a temperature of 170 ^{0}C) the pump wavelength has to be scanned in the ~817-835 nm range in order to achieve oscillation with use of all the available gratings. Most importantly, one can recognise that the amount of tuning through cavity length mismatch far exceeds the tuning available by grating period, temperature or indeed pump wavelength control. In fact, the parametric wavelength could be continuously shifted as mach as ~ 250 nm for the signal and ~ 400 nm for the idler output. Again it is clear that the OPO tuning is limited by the bandwidth of the coatings.

The cavity length tuning rate $d\lambda/dL$ at ~1.5 μm was found to be -0.0067 (that is, ~100 nm increase in wavelength for ~15 μm of cavity length decrease). Substituting this value in Eq. (2-11) results in a single-pass cavity GVD greater than -500 fs^2.

Accounting for a theoretical prediction (Fig. 3.3) of GVD~125 fs^2 due to a single pass through 1 mm of PPLN, as well as for some additional positive GVD in the air and mirror surfaces, this result suggests that the prism pair contributes a large amount of negative GVD. This is also supported by the fact that the resonated signal field had longer pulse duration than the idler wave. In fact, for the 87% output coupler the average signal pulse lifetime in the cavity is ~7.6 roundtrip times, and thus a total amount of GVD as large as (~15×500=) -7500 fs^2 emerges. Of course, the output signal pulse is not as temporally broad as one might expect in the presence of such large GVD, since other effects play important role in the pulse evolution, including shelf-phase modulation and temporal overlap between the pump and the parametric pulses. However, the prism pair was successful in removing chirp from the output pulses, by cancelling out the positive chirp due to self-phase modulation and positive GVD in the crystal. This was evident from spectral and autocorrelation measurements for the prism-free cavity, which indicated a bandwidth-duration product for the signal $\Delta\nu\Delta\tau \cong 0.715$. Further studies to achieve improved dispersion compensation as well as to fully understand the reasons behind the discrepancy between calculations and measurements, might be part of future work[1].

It should be noted that the device specifications presented here and summarised in Table 3.1 were obtained immediately after the OPO construction was finished. Having operated the system for long periods of time, maintenance and re-optimisation work was necessary and the characteristics were often slightly changed. In the next chapters, the details of the OPO behaviour during each experiment will be explicitly summarised.

	Tuning range[2]	Average power	Pulse duration	$\Delta\nu\Delta\tau$
Signal	1.3-1.58 μm	>100 mW	~250 fs	~0.33
Idler	1.8-2.1 μm	>50 mW	~185 fs	~0.36

Table 3.1 Femtosecond OPO operational characteristics

[1] For the purposes of the investigations described in the following chapters, the OPO as such is actually more attractive than a truly compensated device. In particular, for zero GVD operation shorter output pulse durations (~150 fs) should be expected, with a resulting compromise in the (walk-off limited) length of interaction in the waveguides.

[2] Practical tuning range is shown (output power bigger than 5 mW)

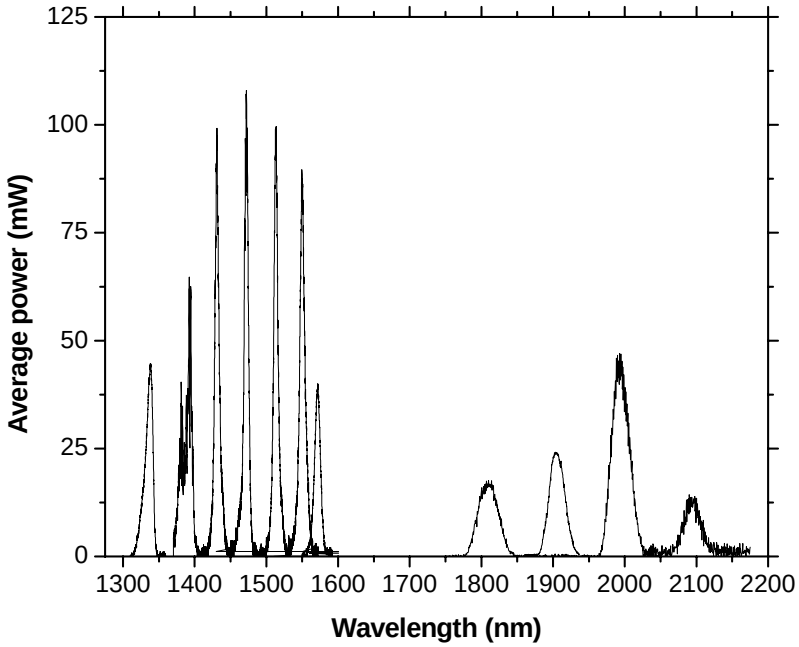

Fig. 3.5 Signal and idler spectra throughout the tuning range of the OPO.

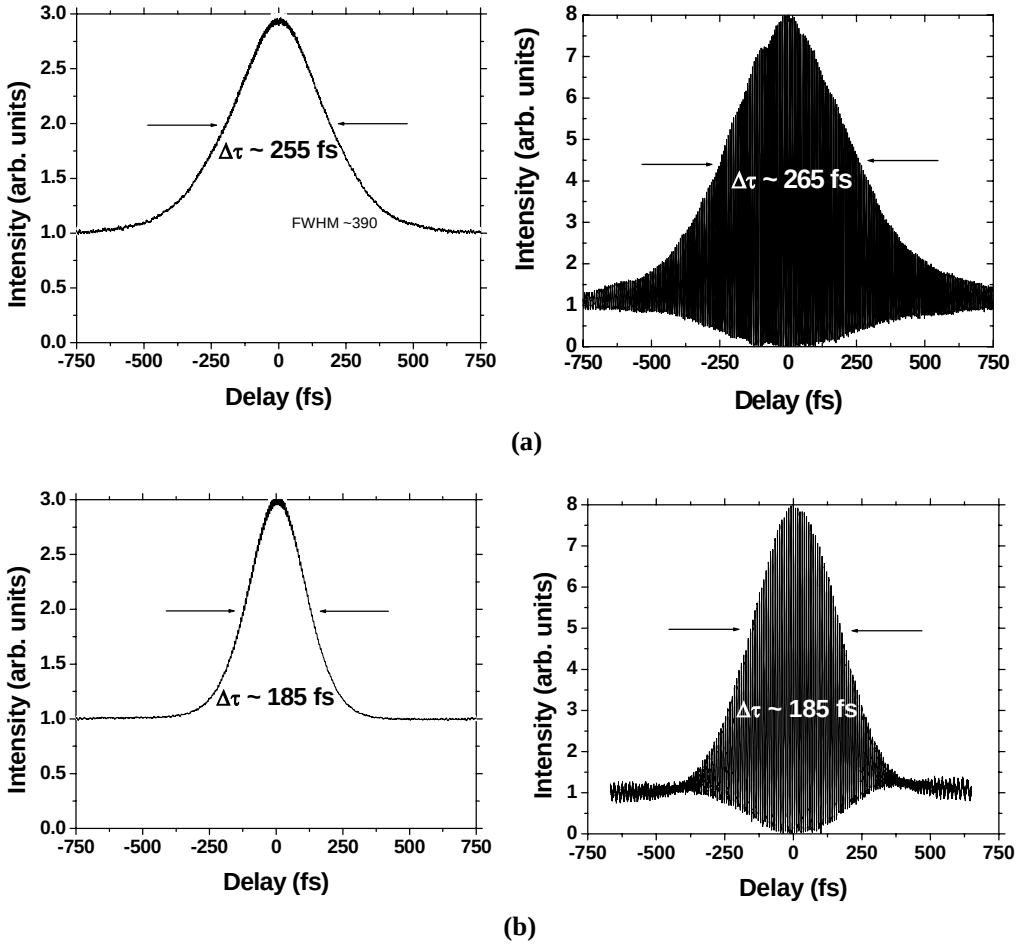

Fig. 3.6 Intensity (left) and interferometric (right) autocorrelations for the signal (a) and idler (b) at ~1.5 μm and ~2 μm respectively.

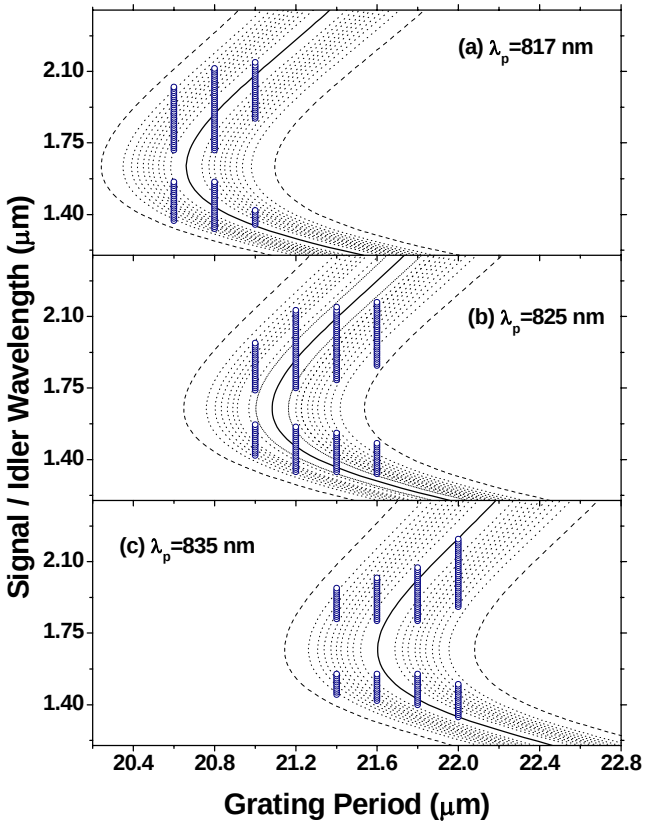

Fig. 3.7 Grating period tuning diagram for (a) λ_p=817 nm (b) λ_p=825 nm and (c) λ_p=835 nm. Solid (dashed) curves indicate areas of maximum (minimum) parametric gain. Dotted lines depict the variation of gain from 90% to 10%. Open cycles show corresponding experimental data. Both theoretical calculations and measurements were carried out at T=170^{0}C.

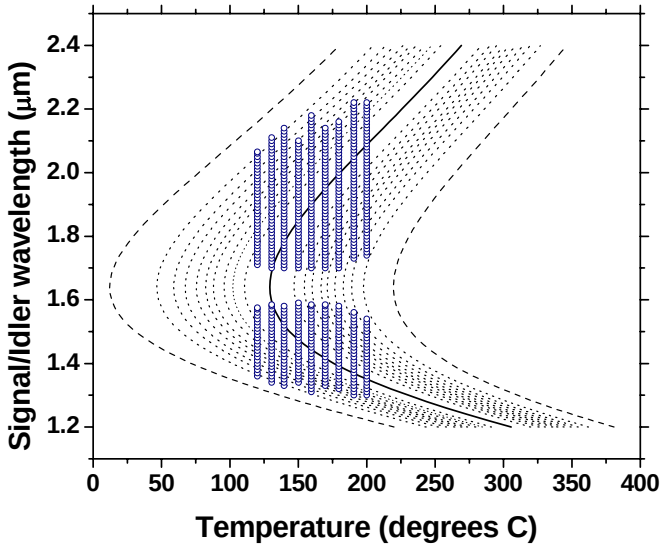

Fig. 3.8 Temperature tuning diagram for grating period Λ=21 μm and λ_p=815 nm. Lines and symbols indicate the same as in Fig. 3.7

3.4 Conclusions

The design and performance of a femtosecond optical parametric oscillator based on periodically polled lithium niobate and operating in the near to mid infrared was described. The device was configured in a semimonolithic, singly resonant at the signal cavity and was synchronously pumped at a ~90 MHz repetition rate by a self-mode-locked Ti: sapphire laser. Maximum average power levels of more than 100 mW (50 mW) were observed for the signal (idler), with corresponding peak powers of ~4.5 kW (~3 kW) and pulse energies of ~1.1 nJ (0.5 nJ). The pump power threshold was ~ 200 mW with an 87 % output coupler and typical operation was at four times above threshold. Output pulses of ~250 fs and ~185 fs duration were obtained for the signal and idler, respectively, with corresponding spectral FWHM bandwidths of ~10 nm and ~26 nm, indicating near-transform limited pulses. The OPO offered continuous coverage of the ~1.28 μm to ~1.58 μm (signal) and 1.71 μm to ~2.28 μm (idler) wavelength range. The device operated in a stable fashion for many hours a day and did not require maintenance for periods of many months.

Accessing the vital wavelengths near ~1.5 μm and ~2 μm and providing significant peak powers made the OPO an attractive source for demonstration of nonlinear frequency conversion in GaAs-based waveguides. In the following chapter results are presented from experimental studies of second harmonic generation in birefringently phase-matched Ga-As waveguides pumped with this OPO system.

References

[1] J.A. Giordmaine and R.C. Miller, *Tunable coherent parametric oscillation in $LiNbO_3$ at optical frequencies,* Phys. Rev. Lett. 14, 973, (1965)

[2] M. Ebrahimzadeh and M. Dunn, *Optical parametric oscillators,* in Handbook of optics IV, OSA, McGraw Hill, 2201, (2000)

[3] S.E. Harris, *Tunable optical parametric oscillators,* Proc. IEEE 57, 2096, (1969)

[4] R.L. Byer, *Parametric oscillators and nonlinear materials,* Proc. 16th Scottish Universities Summer School in Physics, 47, (1975)

[5] R.L. Byer, *Optical parametric oscillators,* in Quantum Electronics I: A treatise, Academic Press, 588, (1975)

[6] M. Dunn and M. Ebrahimzadeh, *Parametric generation of tunable light from continuous wave to femtosecond pulses,* Science 286, 1513, (1999)

[7] M. Ebrahimzadeh, *Pulsed parametric oscillators,* Proc. 47th Scottish Universities Summer School in Physics, 229, (1995)

[8] M. Ebrahimzadeh, R.C. Eckardt, and M. Dunn (Ed), *Optical parametric devices and processes,* Special Issue, J. Opt. Soc. Am. B16, 1477 (1999)

[9] W.R. Bosenberg and R.C. Eckardt, M. (Ed), *Optical parametric devices,* Special Issue, J. Opt. Soc. Am. B12, 2084, (1995)

[10] R.L. Byer and A.S Piskarskas (Ed), *Optical parametric oscillation and amplification* , Special Issue, J. Opt. Soc. Am. B10, 1956, (1993)

[11] R. Danielius, A. Piskarskas, A. Stabinis, G.P. Banfi, P. Di Trapani and R. Righini, *Travelling wave parametric generation of widely tunable, highly coherent femtosecond light pulses,* J. Opt. Soc. Am. B10, 2222, (1995)

[12] R.G Smith, J.E. Geusic, H.J. Levinstein, J.J. Rubin, S. Singh, and L.G. Van Uitert, *Continuous optical parametric oscillation in $Ba_2NaNb_5O_{15}$,* App. Phys. Lett. 12, 308, (1968)

[13] R.L. Byer, M.K. Oshman, J.F. Young, and S.E. Harris, *Visible cw parametric oscillator,* Appl. Phys. Lett. 13, 109, (1968)

[14] S.T. Yang, R.C Eckard, and R.L. Byer, *Continuous wave singly resonant optical parametric oscillator pumped by a single frequency resonantly doubled Nd;YAG laser,* Opt. Lett. 18, 971, (1993)

[15] W.R. Bosenberg, A. Drobshoff, J.I. Alexander, L.E. Mayers, and R.L. Byer, *Continuous wave singly resonant optical parametric oscillator based on periodically poled $LiNbO_3$,* Opt. Lett. 21, 713, (1996)

[16] G. Robertson, M.J. Padgett, and M.H. Dunn, *Continuous wave singly resonant pump enhanced type II optical parametric oscillator,* Opt. Lett. 19, 1735, (1994)

[17] F.G. Colville, M.H. Dunn, and M. Ebrahimzadeh, *Continuous wave singly resonant intracavity parametric oscillator,* Opt. Lett. 22, 75, (1997)

[18] J.E. Bjorkholm, *Efficient optical parametric oscillation using doubly and singly resonant cavities,* Appl. Phys. Lett. 13, 53, (1968)

[19] R.W. Wallace, *Stable, efficient optical parametric oscillator pumped with doubled Nd:Yag,* Appl. Phys. Lett. 17, 497, (1970)

[20] D.C. Hanna, B. Luther-Davis, and R.C. Smith, *Singly resonant proustite parametric oscillator tuned from 1.22 to 8.5 μm*, Appl. Phys. Lett. 22, 440, (1973)

[21] S.J. Brosnan and R.L Byer, *Optical parametric oscillator threshold and linewidth studies*, IEEE. J. Qunat. Electron. QE15, 415, (1979)

[22] L.J. Bromley, A. Guy, and D.C. Hanna, *Synchronously pumped optical parametric oscillation in KTP*, Opt. Commun. 70, 350, (1989)

[23] S. Burdulis, R. Grifonis, A. Piskarskas, G. Sinkevicius, V. Sirutkaitis, A. Fix, J. Nolting, and R. Wallenstein, *Visible optical parametric oscillation in synchronously pumped beta-barium borate*, Opt. Commun. 74, 398, (1990)

[24] M. Ebrahimzadeh, G.J. Hall, and A.I. Ferguson, *Broadly tunable, all-solid-state, visible and infrared picosecond optical parametric oscillator*, Opt. Lett. 18, 278, (1993)

[25] S. French, M. Ebrahimzadeh, and A. Miller, *High-power, high-repetition-rate picosecond optical parametric oscillatetor for the near- to mid-infrared*, Opt. Lett. 21, 131, (1996)

[26] D.C. Edelstein, E.S. Wachman, and C.L. Tang, *Broadly tunable high repetition rate femtosecond optical parametric oscillator*, Appl. Phys. Lett. 54, 1728, (1989)

[27] R. Laenen, H. Graener, and A. Laubereau, *Broadly tunable femtosecond pulses generated by optical parametric oscillation*, Opt. Lett. 15, 971, (1990)

[28] Q. Fu, G. Mak, and H.M. van Driel, *High-power, 62-fs infrared optical parametric oscillator synchronously pumped by a 76-MHz Ti:Sapphire laser*, Opt. Lett. 17, 1006, (1992)

[29] J.D. Kafka, M.L. Watts, and J.W. Pieterse, *Synchronously pumped optical parametric oscillators with LiB_3O_5*, J. Opt. Soc. Am. B12, 2147, (1995)

[30] D.T. Reid, C. McGowan, M. Ebrahimzadeh, and W. Sibbett, *Characterisation and modelling of a noncollinearly phase matched femtosecond optical parametric oscillator based on KTA and operating beyond 4 μm*, IEEE J. Quant. Electron. 33, 1, (1997)

[31] J.E. Bjorkholm, *Some effects of spatially nonunifirm pumping in pulsed optical parametric oscillators*, IEEE J. Quant. Electron. QE7, 109, (1971)

[32] M.F. Becker, D.J. Kuizanga, D.W Phillion, and A.E Siegman, *Analytic expressions for ultrashort pulse generation in mode-locked optical parametric oscillators*, J. Appl. Phys. 45, 3996, (1974)

[33] E.C. Cheung, and J.M. Liu, *Theory of synchronously pumped optical parametric oscillator in steady state operation*, J. Opt. Soc. Am. B7, 1385, (1990)

[33] D.T. Reid, G.T. Kennedy, A. Miller, W. Sibbett, M. Ebrahimzadeh, *Widely tunable, near to mid-IR femtosecond optical parametric oscillators using periodically poled $LiNbO_3$ and $RbTiOAsO_4$*, IEEE J. Sel. Top. Quant. Electron. 4, 238, (1998)

[34] D.T. Reid, M. Ebrahimzadeh, and W. Sibbett, *Broadly tunable infrared femtosecond optical parametric oscillator based on periodically poled $RbTiOAsO_4$*, Opt. Lett. 22, 1397, (1997)

[35] S.E. Harris, *Method to lock an optical parametric oscillator to an atomic transition*, Appl. Phys. Lett. 14, 335 (1969)

[36] S. Guha, F. Wu, and J. Falk, *The effects of focusing on parametric oscillation*, IEEE J. Quant. Electron. 18, 907, (1982)

[37] H. Kogelnik, and T. Li, *Laser beams and resonators*, Proc. IEEE 54, 1312, (1966)

[38] A.E. Siegman, *Lasers*, University Science Books, Mill Valley, (1986)

[39] K.C. Burr, C.L. Tang, M.A. Arbore, and M.M Fejer, *High repetition rate femtosecond optical parametric oscillator based on periodically polled lithium niobate*, Appl. Phys. Lett. 70, 3341, (1997)

[40] P.J. Phillips, S. Das, and M. Ebrahimzadeh, *High-repetition-rate, all-solid-state, Ti:Sapphire-pumped optical parametric oscillator for the mid-infrared*, Appl. Phys. Lett. 77, 469, (2000)

[41] D.T. Reid, C. McGowan, W. Sleat, M. Ebrahimzadeh, and W. Sibbett, *Compact, efficient 344-MHz repetition rate femtosecond optical parametric oscillator*, Opt. Lett. 22, 525, (1997)

[42] M. Yamada, N. Nada, M. Saitoh, and K. Watanabe, *First order quasi-phase matched $LiNbO_3$ waveguide periodically poled by applying an external electric field for efficient blue second-harmonic generation*, Appl. Phys. Lett. 62, 435, (1993)

[43] A. Feisst and P. Koidl, *Current induced periodic ferroelectric domain structures in $LiNbO_3$ applied for efficient nonlinear optical frequency mixing*, Appl. Phys. Lett. 47, 1125, (1985)

[44] L. Goldberg, W.K. Burns, and R.W McElhanon, *Difference frequency generation of tunable mid-infrared radiation in bulk periodically poled $LiNbO_3$*, Opt. Lett. 22, 274, (1997)

[45] L.E. Myers and W.R. Bosenberg, *Periodically poled lithium niobate and quasi-phase matched optical parametric oscillators*, IEEE J. Quant. Electron. 33, 1663, (1997)

[46] C. McGowan, D.T. Reid, Z.E Penman, M. Ebrahimzadeh, and W. Sibbett, and D.H. Jundt, *Femtosecond optical parametric oscillator based on periodically poled lithium niobate*, J. Opt. Soc. Am. B 15, 694, (1998)

[47] V.G. Dimitriev, G.G Gurzadyan, and D.N. Nicogosyan, *Handbook of nonlinear optical crystals*, Springer series in optical science 64, Springer-Verlag, (1991)

[48] D.H. Jundt, *Temperature dependent Sellmeier equation for the index of refraction, n_e, in congruent lithium niobate*, Opt. Lett. 22, 1553, (1997)

[49] D.E. Spence, P.N. Kean, and W. Sibbett, *60-femtosecond pulse generation from a self-mode locked Ti: Sapphire laser*, Opt. Lett. 16, 42, (1991)

4. EFFICIENT SECOND HARMONIC GENERATION IN BIREFRINGENTLY-PHASE-MATCHED GaAs/Al_2O_3 WAVEGUIDES

4.1 Introduction

Since the first report of birefringent-phase-matching (BPM) in isotropic GaAs [1], there has been considerable interest in this class of materials for potential applications in various functional devices, ranging from second harmonic generation (SHG) structures to integrated devices for difference frequency generation (DFG), all-semiconductor optical parametric oscillators, optical communications and all-optical signal processing [2], [3]. The advantages of GaAs-based devices over existing materials have been discussed in detail previously and include large second order nonlinear coefficients, broad range of mid-infrared transparency, room-temperature operation and mature growth and fabrication technology. Birefringent-phase-matching offers higher conversion efficiencies compared to quasi-phase-matching (QPM) schemes in the same material, due to lower transmission loss. It can also offer advantages over modal-phase-matching (MPM) techniques, due to the higher overlap between the interacting modes.

Based on BPM, several second order processes including SHG [4], DFG [5-6], and parametric fluorescence [7] have been successfully demonstrated in GaAs/AlGaAs waveguides. This chapter presents experimental work that resulted in efficient SHG of near-IR femtosecond pulses in birefringently-phase-matched GaAs waveguides. This represented the first demonstration of nonlinear frequency conversion in such waveguides in the femtosecond regime. The use of femtosecond pulses for frequency conversion is attractive because it offers the potential for employment of GaAs-based waveguides in wavelength and time division multiplexing applications.

A short theoretical discussion will be initially presented, aiming to expose the technology for engineering birefringence in isotropic media and its application to phase-matched nonlinear processes.

4.2 Birefringent-phase-matching technologies in isotropic materials

4.2.1 Form birefringence in a laminar structure

The birefringent properties of a variety of crystals due to the intrinsic anisotropy at a microscopic (molecular) level have been discussed in Chapter 2. Here, it is shown that birefringence can be engineered by use of many alternating layers of two different homogenous and isotropic materials in a much larger scale (*form birefringence*). The propagation of electromagnetic waves in finely layered media has been studied by numerous authors [8-10]. The exact calculation of the multilayer system birefringence is carried out directly from Maxwell equations. More recently, an alternative explanation was suggested for waveguide structures, using modal wavefunction considerations [1]. For the needs of the present work, a somewhat simplified yet revealing discussion on the origin and magnitude of form birefringence will be presented, based on [11].

We start by investigating the continuity of the electromagnetic vector quantities in an interface between two different media [12]. By means of Gauss and Stokes theorems, the differential Maxwell equations (2-1 a) and (2-1 d) can be written in an equivalent integral form:

$$\int_A (\vec{\Delta} \times \vec{E}) \cdot d\vec{a} = \int \vec{E} \cdot d\vec{l} = -\int_A \frac{\partial}{\partial t} \vec{B} \cdot d\vec{a} \qquad \text{(4-1 a)}$$

$$\int_V \vec{\Delta} \cdot \vec{D} \cdot dV = \int \vec{D} \cdot d\vec{a} = \int_V \rho \cdot dV \qquad \text{(4-1 b)}$$

In (4-1 a) the first and third integrations are carried out over an area *A* and the second along the boundary line of *A*. Similarly, in (4-1 b) the first and third integrals are over a volume *V* and the middle one over the surrounding surface of *V*. The volume *V* and the area *A* can now be chosen around the interface of the two materials as shown in Fig. 4.1. Assuming source-free materials ($\rho=0$) and allowing the height of the cylindrical volume *V* as well as the short arms of the rectangular area *A* to become infinitely small, Eqs. 4.1 suggest that the following boundary relations are valid at the interface:

$$\int \vec{E} \cdot d\vec{l} = \int \vec{D} \cdot d\vec{a} = 0 \qquad \text{(4-2)}$$

The line element $d\vec{l}$ being parallel and the surface element $d\vec{a}$ being perpendicular to the interface (as evident from Fig. 4.1), the last relations establish that the tangential component of the electric filed vector and the normal component of the electric displacement vector are continuous across a discontinuity surface.

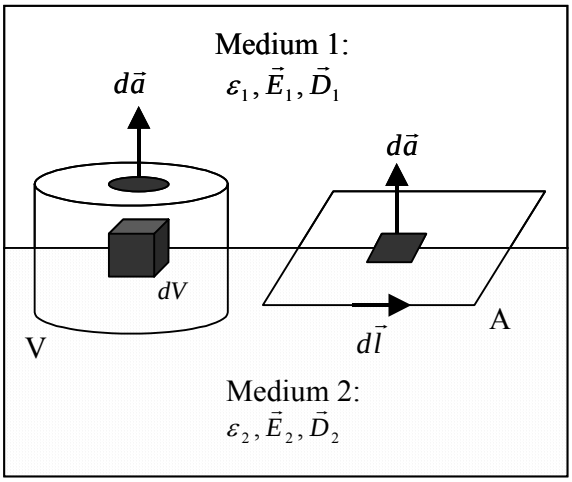

Fig 4.1 Schematic diagram of plane interface between different media, with a volume *V* and a surface *A* selected half in one medium and half in the other.

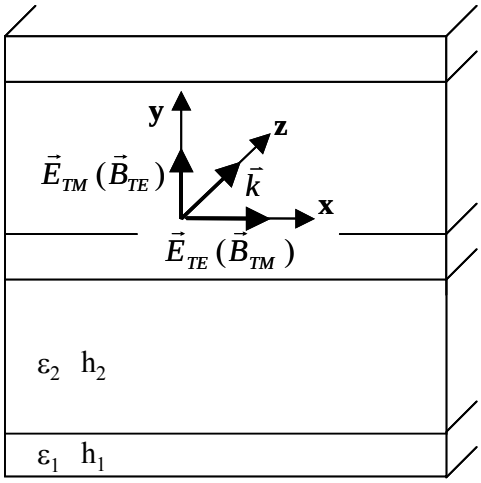

Fig 4.2 Periodical layered structure consisting of two isotropic materials. Propagation of light is assumed parallel to the layers

The results of the above analysis can be applied to allow for an accurate calculation of the effective dielectric constant in the case of the laminar structure depicted in Fig. 4.2. The period of the structure comprises two sandwiched layers of different media with bulk dielectric constants ε_1 and ε_2.The thickness of each layer is h_1 and h_2 respectively. We first consider a plane monochromatic wave propagating parallel to the plates along *Z*-axis, with its electric field vector parallel to the interface between the plates along *X*-axis (TE- polarisation). Further, assuming that h_1 and h_2 are small compared to the wavelength, the field in each region may be considered to be uniform. In this case, one can make use of the continuity of the tangential component of the electric field vector to write the electric displacements in the two layers as:

$$\vec{D}_1 = \varepsilon_1 \cdot \vec{E} \text{ and } \vec{D}_2 = \varepsilon_2 \cdot \vec{E}$$

The mean electric displacement can be found in an elementary way with a direct averaging over the total volume:

$$\tilde{\tilde{D}}_{TE} = \frac{h_1 \cdot \varepsilon_1 \cdot \vec{E} + h_2 \cdot \varepsilon_2 \cdot \vec{E}}{h_1 + h_2}$$

An effective dielectric constant and refractive index can therefore be defined:

$$\varepsilon_{TE} = n_{TE}^2 = \frac{\tilde{\tilde{D}}_{TE}}{\vec{E}} = \frac{h_1 \cdot \varepsilon_1 + h_2 \cdot \varepsilon_2}{h_1 + h_2} \tag{4-3}$$

One can proceed to examine the case in which the field propagating along *Z*-axis has its electric vector perpendicular to the interface, along *Y*-axis (TM – polarisation). Here; the continuity of the normal component of the electric displacement can be used, allowing with similar arguments for the uniformity of the field to extract the field vectors in the two regions as:

$$\vec{E}_1 = \frac{\vec{D}}{\varepsilon_1} \text{ and } \vec{E}_2 = \frac{\vec{D}}{\varepsilon_2}$$

The mean electric field averaged over the total volume is now:

$$\tilde{\tilde{E}}_{TM} = \frac{h_1 \cdot \vec{D}/\varepsilon_1 + h_2 \cdot \vec{D}/\varepsilon_2}{h_1 + h_2}$$

Hence, an effective dielectric constant and refractive index can be introduced:

$$\frac{1}{\varepsilon_{TM}} = \frac{1}{n_{TM}^2} = \frac{\tilde{\tilde{E}}_{TM}}{\vec{D}} = \frac{h_1/\varepsilon_1 + h_2/\varepsilon_2}{h_1 + h_2} \tag{4-4}$$

This discussion has restricted the direction of propagation along the Z-axis. By allowing the propagation direction to be rotated with respect to Z-axis, one can recognise that, due to the symmetry of the structure, (4-3) is valid for all polarisation states that lie in the *X*-*Z* plane. On the contrary, a wave polarised along the *Y*-axis will experience a refractive index that changes with the direction of propagation, since the relative thicknesses of the layers depend on the propagation direction. The laminar structure, therefore, resembles a uniaxial crystal with $n_X = n_Z = n_{TE} = n_0$ and $n_Y = n_{TM} = n_e$ and optical axis parallel to *Y*. Additionally, the difference of the TE and TM effective refractive indices is always positive, since from (4-3) and (4-4):

$$\frac{n_{TE}^2}{n_{TM}^2} = 1 + \frac{h_1 \cdot h_2}{(h_1 + h_2)^2} \cdot \frac{(\varepsilon_1 - \varepsilon_2)^2}{\varepsilon_1 \cdot \varepsilon_2} > 1 \tag{4-5}$$

Equation (4-5) implies that the assembly specifically behaves like a negative uniaxial crystal ($n_0 > n_e$).

4.2.2 Phase-matching by use of form birefringence

Exploitation of form birefringence in a laminar structure to phase-match second order nonlinear processes is a concept proposed as early as 1975 by Van der Ziel [13]. Following his proposal, the result of (4-5) can be employed to compensate for normal dispersion in a SHG interaction for TE fundamental and TM second harmonic (type I geometry). The phase-mismatch is obtained by combining (4-3) and (4-4) and the scalar phase-matching condition is given by:

$$n_{TM}^{2\omega} - n_{TE}^{\omega} = (\varepsilon_{TM}^{2\omega})^{1/2} - (\varepsilon_{TE}^{\omega})^{1/2} = 0$$

or, in terms of the dielectric constants and relative thicknesses of the two layers:

$$[1 - \frac{\varepsilon_2^{\omega}}{\varepsilon_2^{2\omega}}] \cdot (\frac{h_2}{h_1})^2 + [2 - \frac{\varepsilon_2^{\omega}}{\varepsilon_1^{2\omega}} - \frac{\varepsilon_1^{\omega}}{\varepsilon_2^{2\omega}}] \cdot (\frac{h_2}{h_1}) + [1 - \frac{\varepsilon_1^{\omega}}{\varepsilon_1^{2\omega}}] = 0 \qquad (4\text{-}6)$$

Phase-matched SHG interaction in this structure, therefore, requires that (4-6) has real and positive solutions. These requirements, viewed from a slightly different perspective than that of [13], impose the following conditions[1]:

$$[2 - \frac{\varepsilon_2^{\omega}}{\varepsilon_1^{2\omega}} - \frac{\varepsilon_1^{\omega}}{\varepsilon_2^{2\omega}}]^2 \geq 4 \cdot [1 - \frac{\varepsilon_2^{\omega}}{\varepsilon_2^{2\omega}}] \cdot [1 - \frac{\varepsilon_1^{\omega}}{\varepsilon_1^{2\omega}}] \qquad (4\text{-}7\text{ a})$$

$$\frac{\varepsilon_2^{\omega}}{\varepsilon_1^{2\omega}} + \frac{\varepsilon_1^{\omega}}{\varepsilon_2^{2\omega}} > 2 \qquad (4\text{-}7\text{ b})$$

Equation (4-7 b) restricts the utility of form birefringence as a phase-matching method to the case of two layers with sufficiently different refractive indices. As an example, we consider SHG in GaAs with fundamental at 2 μm ($n_{GaAs}^{\omega} \cong 3.35$ and $n_{GaAs}^{2\omega} \cong 3.50$). Standard fabrication technology allows growth of ultra-thin alternating layers (superlattices) of GaAs/ $Al_xGa_{1-x}As$ as well as GaAs/GaP systems, making these materials attractive candidates. Index data for $Al_xGa_{1-x}As$ [14] suggest that maximum index contrast is available in AlAs (x=1), with $n_{AlAs}^{\omega} \cong 2.90$ and $n_{AlAs}^{2\omega} \cong 2.95$. These values however, do not satisfy (4-7 b). The same is indeed the case with GaP for which the index contrast is even smaller.

[1] A second-order equation of the form Ax^2+Bx+C has real solutions x_1 and x_2 when $B^2-4AC \geq 0$, in which case $x_1 \cdot x_2 = C/A$ and $x_1+x_2 = -B/A$. In this notation and assuming normal dispersion, it is evident that for Eq. (4-6) the value of C/A is always positive. Hence, $x_1, x_2 > 0$ or $x_1, x_2 < 0$. Requiring positive solutions implies that the summation $x_1+x_2 = -B/A$ must be positive. Applying again the assumption of normal dispersion, (4-6) has a positive coefficient A and therefore the last condition is equivalent to $B<0$.

Due to a lack of a suitable material pairs with sufficient index contrast, the experimental realisation of Van der Ziel's proposal had not been achieved until the early 1990's when a wet oxidation technique was developed [15] to selectively convert AlAs into an oxide (Al_2O_3 or "Alox"), with refractive index $n_{Alox} \cong 1.6$ in the near-IR. Alox is an amorphous, centrocymmetric material ($\chi^{(2)}=0$), highly transparent in the near-IR and thus non-dispersive to a permissible approximation. Due to its high refractive index contrast with GaAs, Alox has attracted attention in the development of semiconductor lasers [16] and Bragg reflectors [17]. The birefringent properties of GaAs/Alox multilayers have also been studied recently and enhancement of form birefringence after oxidation by a factor greater than 2 was reported [18-19]. In fact, this amount of birefringence is enough to phase-match SHG at ~2 μm. This can be seen from (4-6) which - under the assumption of a constant value for n_{Alox} - has a single non-zero solution for the GaAs/Alox system ($h_{GaAs}/h_{Alox} \cong 30$) with a corresponding effective refractive index for the TE fundamental and the TM second harmonic $n_{TE}^{\omega} = n_{TM}^{2\omega} \cong 3.3$. It should be noted that the effective nonlinearity of the multilayer structure scales with the weighted nonlinearities of each component layer. That the solution requires a much thicker layer of GaAs is, therefore, to the benefit of the overall nonlinearity.

From a descriptive point of view [1], the novel properties of the GaAs/Alox assembly can be interpreted as a consequence of the breaking of the cubic symmetry of GaAs due to the presence of Alox in a way that the artificial medium has similar linear optical behaviour to KDP. Therefore, phase-matching in GaAs/Alox structures exploits the microscopic nonlinear properties of GaAs and the macroscopically engineered linear asymmetry of the final structure.

It has been shown that birefringence can be artificially induced in a laminar isotropic medium and used to phase-match nonlinear processes. The requirement for sufficient index contrast was discussed and it was established that near-IR SHG is possible in a GaAs/Alox system. In the following section, details of the oxidised waveguide used in our experiment are presented.

4.3 Optical experiment

4.3.1 Sample details

The nonlinear waveguides used for the SHG experiment were designed and fabricated by collaborators[2] at Thomson CSF. The basic structure is portrayed at Fig. 4.3. It consists of a multilayer GaAs/$Al_xGa_{1-x}As$/AlAs structure, grown by molecular beam epitaxy on a non-intentionally doped GaAs substrate. For optical confinement, a cladding layer with refractive index lower than the effective index experienced by the interacting waves ($n \cong 3.2$) is required. This is possible with high Al composition Al_xGa_xAs ($x>0.7$). The use of plane AlAs ($x=1$) was not favoured because of its chemical instability. On the other hand, an Alox cladding layer would require a great oxidation thickness resulting in mechanical instabilities. In the actual sample, the lower cladding is constituted by two 1-μm-thick layers of $Al_{0.92}Ga_{0.08}As$ and $Al_{0.7}Ga_{0.3}As$. A single 2 μm-thick layer of $Al_{0.92}Ga_{0.08}As$ would naturally be more efficient but fragile. The waveguide core comprises four 250-nm-thick GaAs layers sandwiched between five 50-nm-thick layers of AlAs. The top cladding was a 1-μm-thick layer of $Al_{0.7}Ga_{0.3}As$, while a 30-nm GaAs cap was added to the structure for protection. The processing of the waveguides consists basically of three steps. First, the optical ridge (4-12 μm wide) is obtained by standard photolithography and reactive ion etching, in order to provide a 2D optical confinement. Second, a deeper and larger mesa is etched in order to allow lateral oxidation of all 50-nm-thick AlAs layers. Finally, the sample is oxidized in a furnace under a controlled flux of nitrogen and water vapors. It is estimated that oxidization reduces the Alox layer thickness by ~ 20%.

The alloy composition and layer thickness were designed so that the SHG wavelength would be phase-matched near 1.0 μm. There is an obvious discrepancy between the value of $h_{GaAs}/h_{Alox} \cong 30$, calculated in section 4.2.2, and the value implemented in the sample ($h_{GaAs}/h_{Alox} \cong 6.25$, accounting for the 20% factor). In fact, equations (4-3) and (4-4) fail to adequately describe the interaction in this case, because the thickness of the layers is not small enough compared to the interacting wavelengths. A more useful model was developed by scientists at Thomson CSF. Fig. 4.4 shows the dispersion curves predicted by both models for TE and TM polarisation.

[2] A. De Rossi, V. Berger, M. Calligaro and V. Ortiz

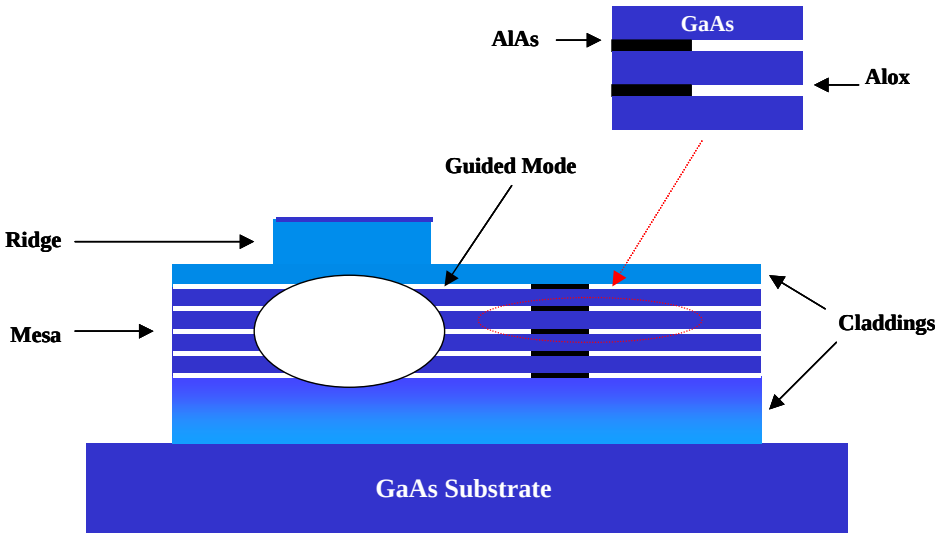

Fig 4.3 Structure of the GaAs/Alox waveguide used in the SHG experiment. It consists of GaAs substrate / 1000-nm $Al_{0.92}Ga_{0.08}As$ / 1000-nm $Al_{0.7}Ga_{0.3}As$ / 4 × (50-nm AlAs / 250-nm GaAs) / 50-nm AlAs / 1000-nm $Al_{0.7}Ga_{0.3}As$ / 30-nm GaAs. The magnified section shows the oxidation front between AlAs and Alox.

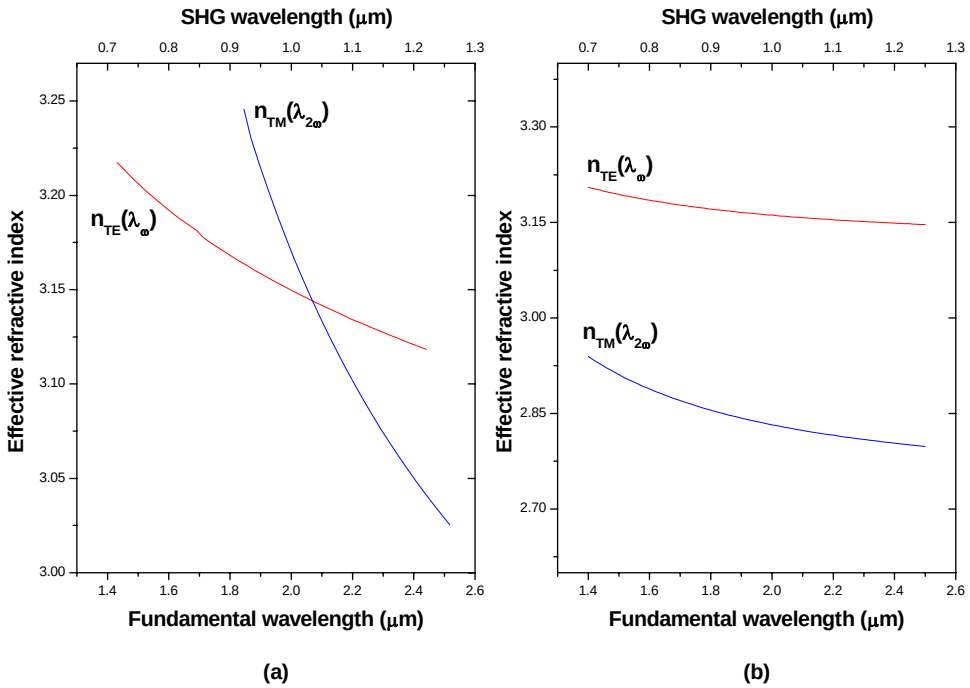

Fig 4.4 Effective indices of TE and TM modes in the waveguide calculated using (a) the transfer matrix algorithm developed by collaborators at Thomson, and (b) using equations (4-3) and (4-4).

4.3.2 Experimental set-up

A schematic of the apparatus used for our experiment is displayed in Fig. 4.5. The pump source was the singly resonant, femtosecond PPLN OPO, described previously in Chapter 3. Configuring the OPO in a semi-monolithic cavity design permitted maximum extraction of the idler power, which was used as the source of fundamental (pump) pulses. The idler pulses had a duration of ~200 fs at a repetition rate of ~90 MHz ($\Delta\tau\Delta\nu$~0.38, indicating near-transform-limited pulses) and were tunable over a range 1.8-2.1 μm, with average power levels of ~50 mW routinely attainable.

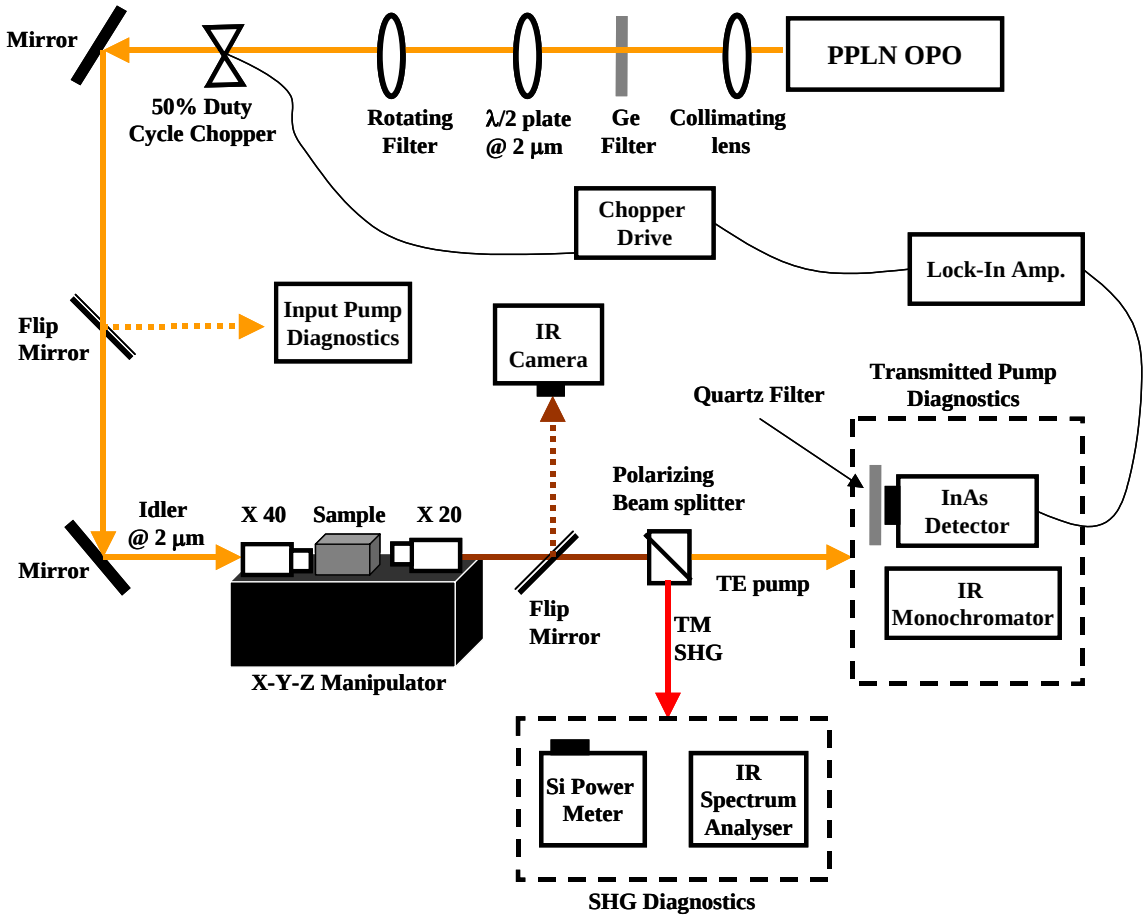

Fig. 4.5 Experimental apparatus

Due to a slight divergence of the beam, a lens was placed after the PPLN crystal to allow for idler collimation. The idler beam was then passed through a germanium filter, which blocked any residual signals below 1.5 μm, ensuring that only the useful fundamental wavelengths were directed into the waveguide. A half-wave plate centred at 2 μm was placed in the beam path to control the polarisation state of the pump, while the input power was controlled by use of a rotating density filter. A

flipper mirror was inserted to redirect the input beam into a thermal power meter and an IR monochromator, allowing for measurements of the input beam power and spectrum. An end-fire coupling rig was used for mounting the sample. The TE-polarised pump pulses from the OPO were focused into the waveguide by a 40X microscope objective. The transmitted SHG and the pump were collected by use of a second 20X microscope objective. An IR camera was used to optimise the coupled pump into the waveguide. A polarising beam splitter was placed at the output to separate out the TE pump and the TM second-harmonic signal. The transmitted pump power was measured with an InAs detector (sensitive in the 0.5-3.0 μm range) and a lock-in amplifier combination. The detector-amplifier system was calibrated using a collection of neutral density filters. As shown in Fig. 6.4, the response was found to be linear for idler power levels ranging from ~0.04 to ~1 mW, with a corresponding slope efficiency of ~3.5 Volts/Watt. The required modulation of the fundamental for lock-in amplification was introduced via a 50% duty cycle chopper, placed before the input objective. The exact measurement of the transmitted pump power was further ensured by inserting a long-pass quartz filter (T<1% for λ<1.6 μm) before the InAs detector. Transmitted pump spectra were collected again using the IR monochromator. The power of the SHG signal was measured with a Si-head power meter. SHG spectra were obtained using an IR spectrum analyser.

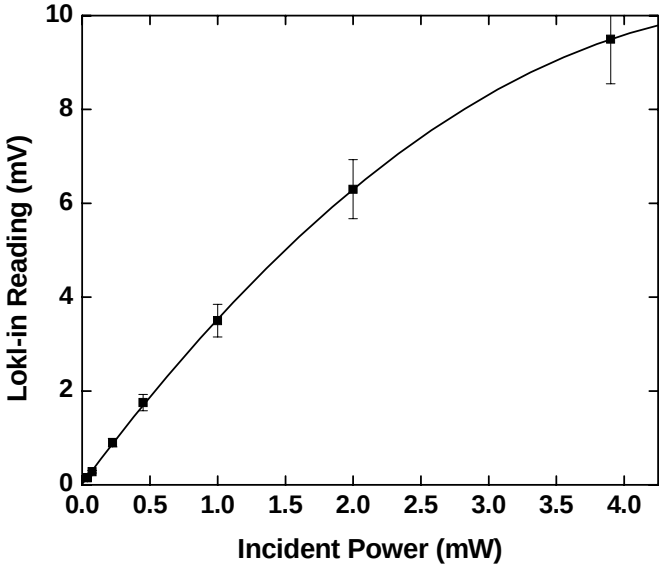

Fig. 4.6 InAs detector calibration measurements

4.3.3 Results and discussion

Two samples, identical in design and fabrication but of different lengths (1.0 and 2.2 mm), were investigated. For appropriate tuning of the pump wavelength, a signal could be readily observed at the waveguide output on an IR card or even a white piece of paper (evidently the SHG signal). For both samples and a variety of waveguides, the selection rules were put to test and it was established that the polarisation states of the pump and the generated signal satisfy the condition ($TE_0(\omega) \rightarrow TM_0(\omega)$) for type I phase-matching. As the pump polarisation was rotated, the intensity of the generated signal was reduced until eventually reaching noise-levels for TM_0 input. Spectra of the observed signal along with the corresponding pump were recorded. Fig. 4.6 illustrates a typical set of such spectra for both samples. Clearly, the generated signal is located at half the pump wavelength.

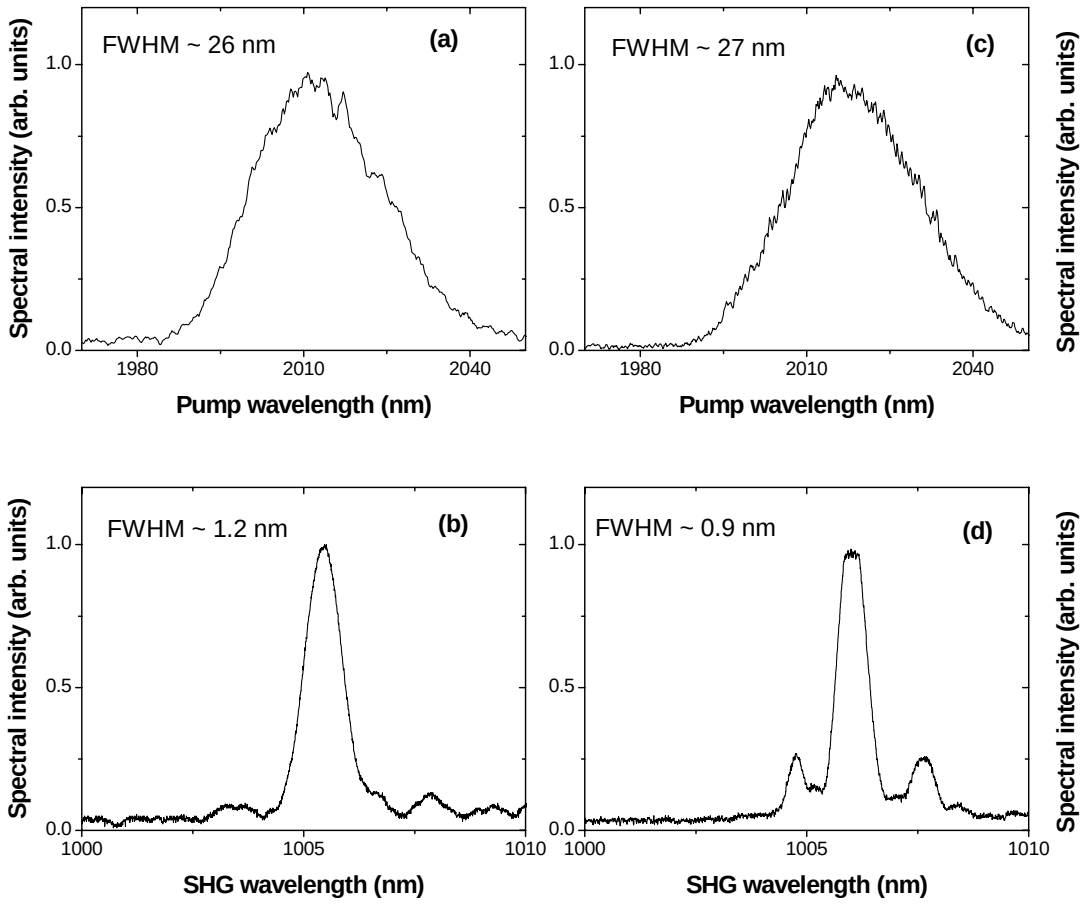

Fig 4.6 Input pump (a), (c) and output SHG (b), (d) spectra for a 1 mm and a 2.2 mm long waveguide respectively.

As can be seen in Fig. 4.6, both sample presented phase-matching at about the same wavelength (λ~2010 nm), indicating a strong accuracy in the engineering of the structure parameters. The input pump has a FWHM bandwidth of ~26 nm. The corresponding FWHM spectral width of SHG is ~1.2 nm for the shorter waveguide and ~0.9 nm for the longer one. With such a broad input spectrum, the secondary peaks of the $sinc^2$ nonlinear gain function could be resolved. Evidently, the pump spectral acceptance is twice that of the SHG linewidth. Therefore, less than 2.5 nm of the broad input spectrum from the femtosecond fundamental was utilised in the conversion process. Assuming a Gaussian spectral shape, this suggests that less than 50% of the available input power is actually engaged in the interaction[3]. That this is so is clearly verified by the incomplete spectral depletion (conversion into SHG and loss processes) of the transmitted pump, shown in Fig. 4.7. Here it is illustrated that, although the off-resonance transmitted spectrum (curve c) is smooth and Gaussian-like, a strong dip appears in on-resonance spectra. As the pump (curve a) is slightly de-tuned within the acceptance bandwidth (curve b), no shift is observed in the position of the dip in the transmitted pump spectrum or in the position of the peak in the SHG spectrum (curve d). These measurements were clear confirmation that the SHG process was indeed phase-matched. It is interesting to point out that the FWHM of the off-resonance transmitted spectrum is ~35 nm, that is significantly broader than the input pump spectrum. This broadening could be an artefact of the low available power levels, which enforced the use of wider monochromator slits, or indeed a real effect related to higher-order nonlinear processes (e.g. self-phase modulation).

Spectral depletion was also examined as a function of the input power. With decreasing pump power, it is expected that the conversion efficiency and hence the spectral depletion is reduced. This is clearly illustrated in Fig. 4.8. The undepleted

[3] In detailed, we assumed a normalised Gaussian function: $\frac{1}{\sigma \cdot \sqrt{2\pi}} e^{-\lambda^2/(2\sigma^2)}$ where the standard deviation σ is related to the FWHM by: FWHM=26 nm= $2(2\ln 2)^{1/2}\sigma$. The overall power corresponding to a 2.5 nm band centred at the peak of the Gaussian is then given by the integral: $\int_{-1.3}^{+1.3} \frac{1}{\sigma \cdot \sqrt{2\pi}} e^{-\lambda^2/(2\sigma^2)} d\lambda \cong 10\%$. In the preceding we quote "less than 50%" to ensure that the efficiency is not over-estimated (see next paragraph).

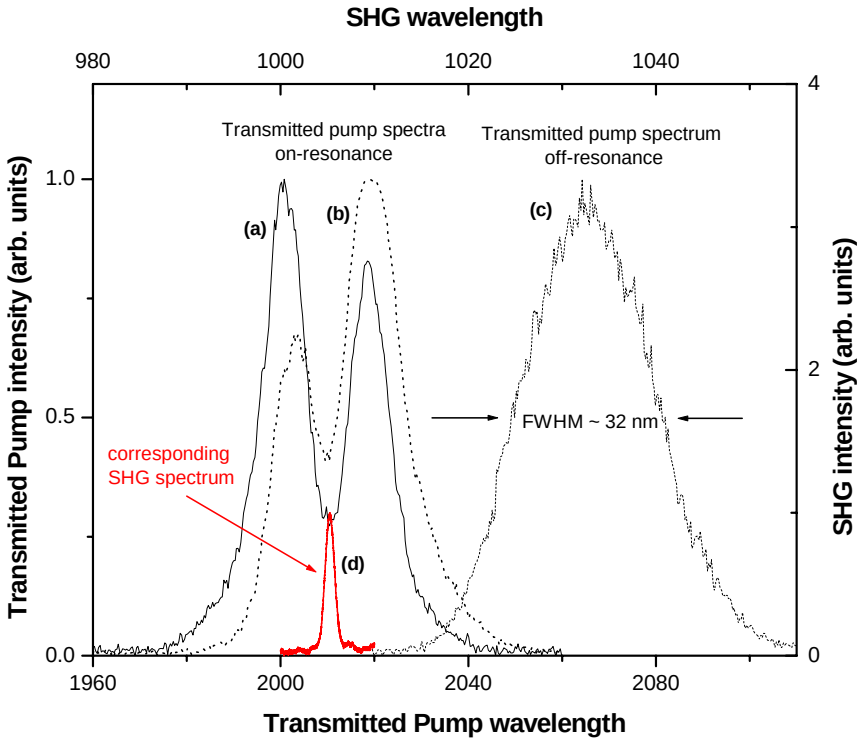

Fig 4.7 Transmitted pump spectra with clear depletion on-resonance (a, b) and Gaussian-like transmitted pump spectrum off-resonance (c). The corresponding SHG spectrum is shown in red (d). All spectra were collected for a 1-mm waveguide.

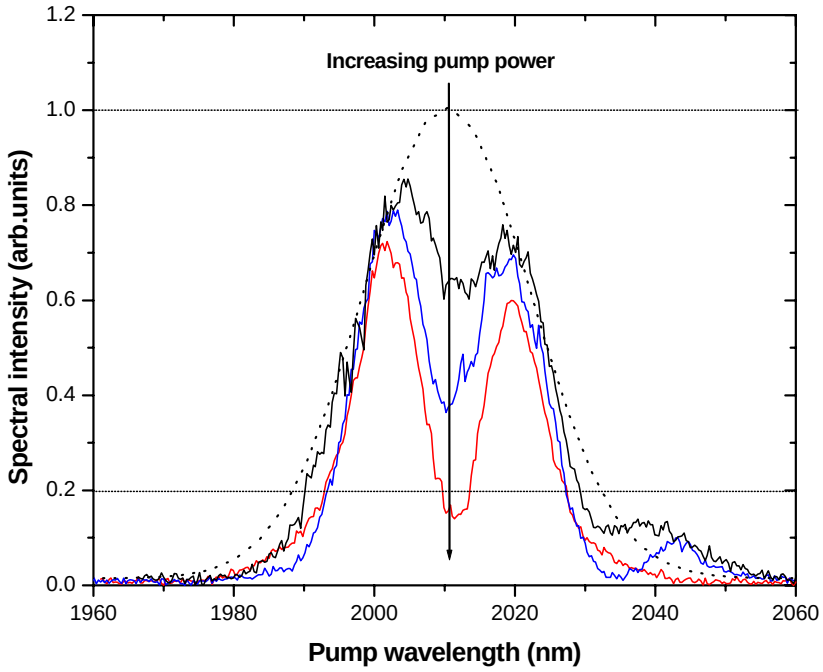

Fig 4.8 Pump depletion as a function of the input power. The black dotted curve shows a Gaussian fit to the corresponding input spectrum.

dashed curve is a qualitative Gaussian fit. The FWHM of the fit (~25 nm) is comparable to that of the input pump spectrum. This is an indication that the spectral broadening of the transmitted pump depicted in Fig. 4.7 is real, since the depleted on-resonance spectra do not seem to suffer from (nonlinear and thus power-dependent) broadening mechanisms. Although not suitable for extraction of quantitative conclusions, it is evident from Fig. 4.8 that within the conversion bandwidth the depletion of the pump is in fact greater than 80%. The validity of spectral pump depletion is supported by pump power depletion measurements, in which the transmitted pump power was recorded on and off resonance. Clearly, for constant input power, any difference in the transmitted power on and off resonance is due to pump depletion. Numerous waveguides were tested and typical values of 20 to 40% of pump power depletion were calculated. These values were indeed expected, since they approximately equal the product of the input power that is taking part in the interaction (<50%) and the observed spectral depletion within the conversion bandwidth (≥80%).

For a 1-mm (2-mm) waveguide, the maximum usable average SHG power measured after the output objective was ~650 μW (390 μW) for a pump average power of ~50 mW measured before the input objective. This maximum power represents an overall external efficiency of 1.3% (0.78%). A more detailed discussion on the efficiencies will be carried out in the next section. Different input microscope objectives were used (20X and 10X) to vary the input beam spot size and it was established that maximum second-harmonic power was indeed generated with the initial 40X objective. It should be noted that the SHG power was measured after removing the chopper (which reduced the average pump power by a factor of 2) from the input beam path. Fig. 4.9 shows the variation of the (square root of the) generated SHG average power with the pump average power for waveguides of different lengths. As expected, the SHG power has a quadratic dependence on the input power. For a 1-mm waveguide, saturation of gain is observed for pump power levels exceeding ~25 mW. Apart from pump depletion, multi-photon absorption could be responsible for the saturation of gain. The facts that the 1-mm long waveguides a) experienced saturation of gain, b) presented broader SHG spectra, and c) had a measured higher efficiency than the 2.2-mm waveguides, are consistent with one another.

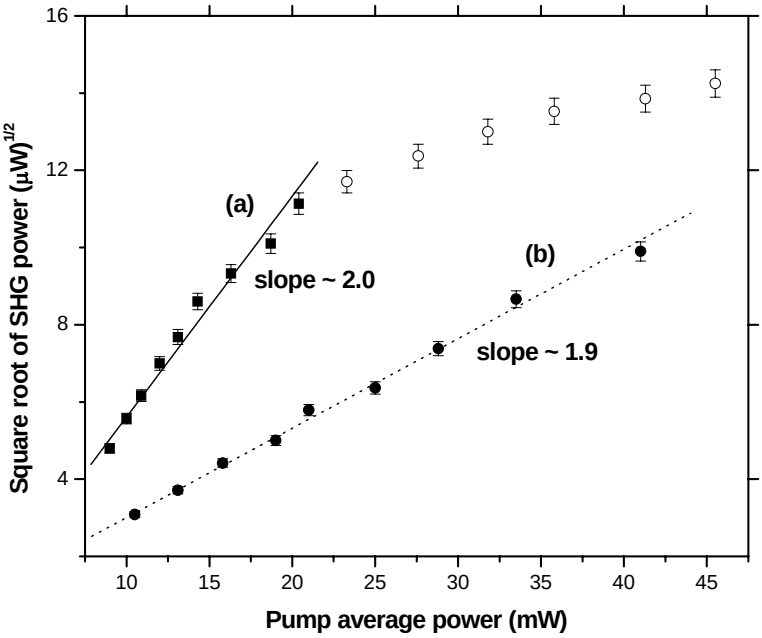

Fig 4.9 Square root of the second-harmonic power plotted as a function of the pump power for a 1-mm (a) and a 2.2-mm (b) waveguide.

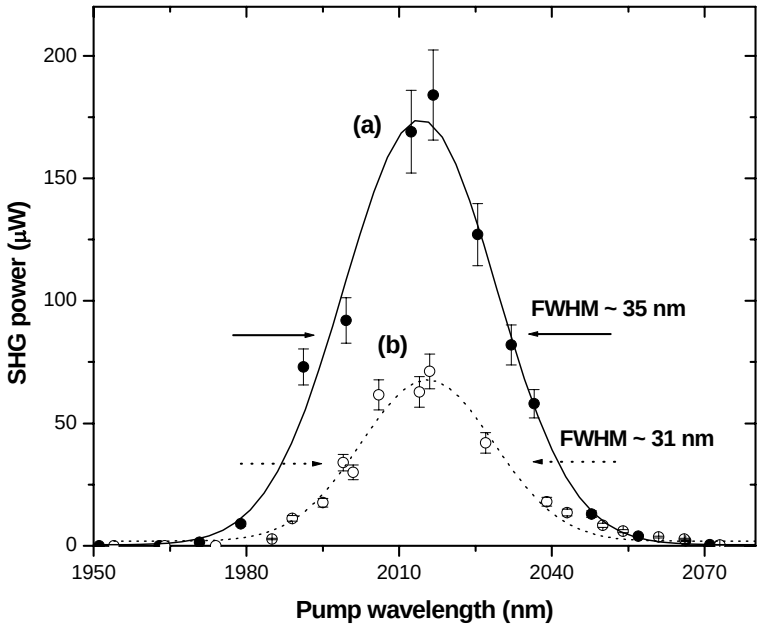

Fig 4.10 Second harmonic average power plotted as a function of the input central pump wavelength (tuning curve) for a 1-mm (a) and 2.2-mm (b) waveguide. The corresponding FWHM is ~35 nm and ~31 nm, respectively.

Figure 4.10 shows the second-harmonic power versus the central pump wavelength (tuning curve) for a typical waveguide in each sample. During these measurements, the input power was kept constant at ~ 30 mW. One can clearly see a phase-matching peak at ~ 2010 nm. The FWHM of this peak was ~ 35 nm and ~ 31 nm for a 1-mm and 2.2-mm-long waveguide, respectively. The bandwidth of the tuning curve depends on the convolusion of the pump spectra (FWHM ~26 nm) with the phase-matching spectral acceptance (FWHM ~ 1.2 nm). Therefore, one should expect that the tuning curves present a FWHM of ~28 nm. Two complementary scenarios can be employed to explain the broadening of the tuning curves. The first one involves the possible off-resonance pump spectral broadening. According to this picture, as a slightly off-resonance input pulse propagates through the waveguide, it experiences a gradual spectral broadening until eventually it enters the phase-matching acceptance bandwidth initiating the SHG. According to the second scenario, the tuning curve broadening reflects a broadening of the actual SHG acceptance bandwidth due to temporal walk-off effects[4].

An attempt to gain an insight to the complicated dynamics of the process was made by developing a Mathcad program to evaluate β_2-related quantities (see Appendix 1). Table 4.1 presents results obtained for bulk GaAs as well as for the structure of Fig. 4.3. A group velocity dispersion (GVD) smaller than 1000 fs^2mm^{-1} suggests that temporal pulse broadening is not significant for propagation length of ~2 mm (the corresponding dispersion length is ~20 mm). However, temporal walk-off restricts the interaction length to less than ~200 μm, which is 5 times smaller than the physical length of the shortest waveguides. This translates to a theoretical value for the pump acceptance bandwidth of more than ~10 nm, which is clearly much larger than one should expect accounting for the measured FWHM of the SHG spectrum.

Examination of the dependence of SHG spectral and efficiency characteristics on the width of the waveguide was also attempted, but no systematic or significant differences were observed.

[4] As has been shown in Chapter 2, the SHG acceptance bandwidth is inversely proportional to the interaction length, which with fs pulses is limited by group velocity mismatch (temporal walk-off).

Bulk GaAs with λ_p=2μm (λ_p=1.5μm)		
Pump GVD	$\left.\frac{\lambda_p^3}{2\pi c^2}\frac{d^2n}{d\lambda^2}\right\|_{\lambda_p}$	990 fs^2mm^{-1} (1400 fs^2mm^{-1})
SHG GVD	$\left.\frac{\lambda_{SHG}^3}{2\pi c^2}\frac{d^2n}{d\lambda^2}\right\|_{\lambda_{SHG}}$	630 fs^2mm^{-1} (1100 fs^2mm^{-1})
Temporal walk-off	$\Delta\upsilon_g^{-1}=\left(\frac{n(\lambda_p)}{c}-\frac{\lambda_p}{c}\left.\frac{dn}{d\lambda}\right\|_{\lambda_p}\right)-\left(\frac{n(\lambda_{SHG})}{c}-\frac{\lambda_{SHG}}{c}\left.\frac{dn}{d\lambda}\right\|_{\lambda_{SHG}}\right)$	880 $fsmm^{-1}$ (1860 $fsmm^{-1}$)
Interaction length	$L=\frac{\Delta\tau}{\Delta\upsilon_g^{-1}}$	230 μm (100 μm)
Pump acceptance bandwidth	$\Delta\lambda_p=\frac{5.57}{L}\left[\left.\frac{d}{d\lambda}\left(\frac{4\pi}{\lambda_p}\left(n(\lambda_{SHG})-n(\lambda_p)\right)\right)\right\|_{\lambda_p}\right]^{-1}$	18 nm (10 nm)
Oxidised sample with λ_p=2μm		
Pump GVD	$\left.\frac{\lambda_p^3}{2\pi c^2}\frac{d^2n_{TE}}{d\lambda^2}\right\|_{\lambda_p}$	900 fs^2mm^{-1}
SHG GVD	$\left.\frac{\lambda_{SHG}^3}{2\pi c^2}\frac{d^2n_{TM}}{d\lambda^2}\right\|_{\lambda_{SHG}}$	280 fs^2mm^{-1}
Temporal walk-off	$\Delta\upsilon_g^{-1}=\left(\frac{n_{TE}(\lambda_p)}{c}-\frac{\lambda_p}{c}\left.\frac{dn_{TE}}{d\lambda}\right\|_{\lambda_p}\right)-\left(\frac{n_{TM}(\lambda_{SHG})}{c}-\frac{\lambda_{SHG}}{c}\left.\frac{dn_{TM}}{d\lambda}\right\|_{\lambda_{SH}}\right.$	1050 $fsmm^{-1}$
Interaction length	$L=\frac{\Delta\tau}{\Delta\upsilon_g^{-1}}$	190 μm
Pump acceptance bandwidth	$\Delta\lambda_p=\frac{5.57}{L}\left[\left.\frac{d}{d\lambda}\left(\frac{4\pi}{\lambda}\left(n_{TM}(\lambda_{SHG})-n_{TE}(\lambda_p)\right)\right)\right\|_{\lambda_p}\right]^{-1}$	35 nm

Table 4.1 Calculated values of GVD, temporal walk-off, interaction length and pump acceptance bandwidth for bulk GaAs and the actual, oxidised sample. All quantities are given as functions of refractive indices and interacting wavelengths. For the refractive index n of GaAs, Afromowitz [14] model was adopted. Indices n_{TE} and n_{TM} were calculated from equations (4.3) and (4-4) respectively. Pulse duration $\Delta\tau$=200 fs was assumed for the evaluation of the interaction lengths. Calculations were made for pump wavelength λ_p=2μm and for bulk interaction at λ_p=1.5μm (the latest values shown in parenthesis).

4.3.4 Efficiency considerations

In the previous section it was stated that for the most efficient 1-mm waveguide, the maximum collectable SHG average power after the output objective was ~650 μW for an input average power of ~50 mW measured before the input objective, resulting in an overall practical efficiency of 1.3%. This figure is of interest when viewing the experimental set up as a "black box" nonlinear frequency converter. From the material standpoint, however, the internal waveguide efficiency should be calculated instead. That the internal efficiency is significantly higher is evident from the strong depletion of the pump. Furthermore, when pump pulses are employed, the normalised nonlinear conversion efficiency is most commonly used:

$$\eta(\%W^{-1}cm^{-1}) = \frac{P_{peak}^{SHG}}{(P_{peak}^{Pump} \cdot L)^2} \qquad (6.1)$$

The revealing nature of the normalised efficiency as defined above is manifest, since it measures the equivalent SHG power generated from 1 centimetre of the material and 1 W of continuous-wave pump power.

Accounting for a measured 10% loss from the input microscope objective, a calculated 30% reflection loss[5] in the waveguide facet and a geometrical coupling factor[6] (due to the difference in the shape of the field outside and the modal wave function inside the waveguide), we estimate that only ~10% of the available pump power is actually coupled into the waveguide. Typical transmission losses of ~ 5 to ~ 10 dB/cm were measured[7] in these waveguides in the wavelength range of ~1.3 - 2 μm. This translated to an estimated transmission of >80 % for both the pump and the second-harmonic through 1-mm-long waveguide. Moreover, due to the output facet reflectivity, the output objective transmission loss and the divergence of the output beam, the output detection efficiency is lower than 50%. The validity of the quoted values is supported by measurements of the off-resonance (and hence undepleted) transmitted pump power, which did not exceed ~1 mW for ~25 mW of input power, indicating an overall transmission of 4%.

[5] The standard expression for the reflection coefficient at normal incidence was used:
$R = \frac{(n_{air} - n_{GaAs})^2}{(n_{air} + n_{GaAs})^2}$, where the refractive index is ~1 in the air and ~ 3.4 in GaAs.

[6] The geometrical coupling factor has been calculated by collaborators at Thomson-CSF.

[7] The loss measurement technique, along with the detailed results, is presented independently in Chapter 7.

Following the discussion of the loss parameters, the internal efficiency can be readily calculated. The maximum collected SHG average power of ~650 μW suggests that ~1.3 mW of second-harmonic reaches the output facet of the waveguide. In addition, out of the ~50 mW of available input power only ~5mW is actually coupled into the waveguide. This results in an internal efficiency greater than 20%.

Extraction of the normalised internal efficiency is more complicated, since it requires knowledge of the real interaction length. As discussed in the previous section, with femtosecond pulses, group velocity walk-off limits the effective interaction length to an estimated 200 μm. Taking into account the duty cycle of the pump source (1.8×10^{-5}), the peak powers corresponding to 5 mW of coupled fundamental and 1.3 mW of internally generated SHG are ~ 275 W and ~70 W respectively. This results in a normalised conversion efficiency of greater than 250 $\%W^{-1}cm^{-2}$. Moreover, given that no more than one half of the pump spectrum is utilised in the conversion process, this corresponds to a waveguide conversion efficiency of at least 1000 $\%W^{-1}cm^{-2}$. This represents an increase of over 2 orders of magnitude from the reported value in [4]. That the quoted efficiency is not over-estimated is clear because we have ignored: a) SHG propagation loss, which is significant due to the short interaction length, b) temporal pulse broadening due to GVD, which reduces pump peak power (the effect of GVD is smaller for the SHG as shown in Table 6.1), and c) possible higher-order nonlinear effects such as self-phase modulation of the pump and multi-photon absorption of the SHG. It should also be mentioned that after the first effective length, the process can start building up again for a second length and so forth, creating a train of SHG pulses. In this discussion, we have assumed that the contribution of all train pulses after the first is negligible, due to strong depletion of the pump.

For the longer sample, the respective values are reduced by a factor of (390 μW / 650 μW =) 0.6. This reduction – under the assumption that the two samples have same facet quality – should be attributed to the extra amount of SHG propagation loss present in the longer sample. In fact, this is an indirect method for estimating the propagation loss at the SHG wavelength which, accounting for a 60% loss through 1.2 mm, is equal to ≥ 15dB/cm - that is notably higher than the measured values for the best waveguides.

4.4 Conclusions

It has been shown that form birefringence externally induced in an isotropic material can be used to phase-match second-order nonlinear processes in isotropic material systems. Efficient SHG in type I birefringently-phase-matched GaAs/Alox waveguides was demonstrated using femtosecond pulses at 2.01 μm. Practical average SHG powers of ~ 650 μW, with an overall external efficiency of ~ 1.3% and a corresponding normalized waveguide efficiency of greater than 1000%$W^{-1}cm^{-2}$ have been obtained with an input pump average power of ~ 50 mW. Depletions of as much as 40% in the transmitted pump power were achieved, with more than 80% spectral depletion in the converted pump bandwidth. Extension of these experiments to the 1.2-1.6 μm wavelength band will open up the possibility for development of a new class of integrated nonlinear frequency conversion devices for telecommunications applications based on GaAs technology.

References

[1] A. Fiore, V. Berger, E. Rosencher, P. Bravetti, and J. Nagle, *Phase matching using an isotropic nonlinear optical material*, Nature 391, 463 (1998).

[2] J.S. Aitchison, M.W. Street, N.D. Whitbread, D.C. Hutchings, J.H. Marsh, G.T. Kennedy and W. Sibbett, *Modulation of the second-order nonlinear tensor components in multiple-quantum-well structures*, IEEE J. Sel. Top. Quantum Electron. 4, 695 (1998)

[3] J.B. Khurgin, E. Rosencher, and Y.J. Ding, *Analysis of all-semiconductor intracavity optical parametric oscillators*, J. Opt. Soc. Am. B 15, 1726 (1998).

[4] A. Fiore, S. Janz, L. Delobel, P. van Meer, P. Bravetti, V. Berger, E. Rosencher, and J. Nagle, *Second harmonic generation at λ=1.6 μm in AlGaAs/Al_2O_3 waveguides using birefringent phase matching*, Appl. Phys. Lett. 72**,** 2942 (1998).

[5] A. Fiore, V. Berger, E. Rosencher, P. Bravetti, N. Laurent, and J. Nagle, *Phase-matched mid-infrared difference frequency generation in GaAs-based waveguides*, Appl. Phys. Lett. 71, 3622 (1997).

[6] P. Bravetti, A. Fiore, V. Berger, E. Rosencher, J. Nagle, and O. Gauthier-Lafaye, *5.2-5.6-mu m source tunable by frequency conversion in a GaAs-based waveguide*, Opt. Lett. 23, 331 (1998).

[7] G. Leo, V. Berger, C. OwYang, and J. Nagle, *Parametric fluorescence in oxidized AlGaAs waveguides*, J. Opt. Soc. Am. B 16, 1597 (1999).

[8] L.M Brekhovskikh, *Waves in layered media*, Academic Press NewYork, (translated by D. Lieberman) (1960)

[9] M.L. Levin, *The propagation of a plane electromagnetic wave in a periodical layered medium*, J. Tech. Phys. (USSR) 81, 1399 (1948)

[10] S.M. Rytov, *The electromagnetic properties of a finely layered medium*, Soviet Phys. 2, 466 (1956)

[11] M. Borh and E Wolf, *Principles of optics*, Cambridge University Press, 7th edition (1999)

[12] J.D Jackson, *Classical electrodynamics*, J Wiley & Sons Inc, 3rd Ed. (1999)

[13] J.P. van der Ziel, *Phase-matched harmonic generation in a laminar structure with wave propagation in the plane of the layers*, Appl. Phys. Lett 26, 60 (1975)

[14] M. A. Afromowitz, *Refractive index of $Ga_{1-x}Al_xAs$*, Solid State Communications 15, 59 (1974)

[15] J.M. Dallesasse, J.N. Holonyak, A.R. Sugg, T.A. Richard and N. El-Zein, *Hydrolysation oxidation of AlGaAs-AlAs-GaAs quantum well heterostructures and superlattices*, Appl. Phys. Lett. 57, 2844 (1990)

[16] D.L Huffaker, D.G. Deppe and K. Kumar, *Native-oxide defined ring contact for low-threshold vertical cavity lasers*, Appl. Phys. Lett. 65, 97 (1994)

[17] M.H. MacDougal, H. Zao, P.D. Dapkus, M. Ziair and W.H Steier, *Wide-bandwidth distributed bragg reflectors using oxide/GaAs multilayers*, Electron. Lett. 30, 1147 (1994)

[18] A. Fiore, V. Berger, E. Rosencher, N. Laurent, S. Theilmann, N. Vodjdani and J. Nagle, *Huge birefringence in selectively oxidized GaAs/AlAs optical waveguides*, Appl. Phys. Lett. 68, 1320 (1996)

[19] A. Fiore, V. Berger, E. Rosencher, S. Crouzy, N. Laurent, and J. Nagle, *$\Delta n=0.22$ birefringence measurements by surface emmiting second harmonic generation in selectively oxidized GaAs/AlAs optical waveguides*, Appl. Phys. Lett. 71, 2587, (1997)

5. SECOND HARMONIC GENERATION IN QUASI-PHASE-MATCHED GaAs/AlAs WAVEGUIDES

5.1 Introduction

It has been discussed in detail that the large $\chi^{(2)}$ coefficients present in III-V semiconductors establish them as excellent candidates for efficient optical frequency conversion. It has also been made clear that, due to the lack of intrinsic birefringence and large dispersion in these material systems, it is difficult to phase-match second-order nonlinear processes. Previously, the use of artificial birefringence by means of embedding native oxide layers in a GaAs-based waveguide structure to compensate for normal dispersion was demonstrated through second harmonic generation studies. An alternative scheme to attack the problem of phase-matching relies upon the realisation of structures with a periodic modulation of the nonlinear coefficient, which introduces an additional wave (or grating) vector, Λ, in the phase-mismatch parameter and thus allows quasi-phase-matched (QPM) interactions. QPM technology generally offers greater flexibility than BPM approaches, through the control of the wave vector. However, traditional methods for producing quasi-phase-matched structures (e.g., electric field poling) are only available with ferroelectric crystals.

In this chapter, emerging quantum well intermixing technologies for the realisation of quasi-phase-matched GaAs-based structures will be outlined. Results will also be presented from two experiments that resulted in the respective demonstrations of first and third order (respectively) quasi-phase-matched SHG in GaAs/AlAs symmetric superlattice waveguides. To our knowledge, these experiments were the first demonstrations of nonlinear frequency conversion exploiting the large bulk-like $\chi_{zxy}^{(2)}$ nonlinear coefficient by means of quantum well intermixing. Furthermore, it is believed that for the first time quasi-phase-matching through quantum well intermixing was achieved in GaAs-based waveguides by use of first-order grating periods.

5.2 Quasi-phase-matching technologies in III-V semiconductors

Early reports [1-3] on QPM interactions in semiconductors involved the epitaxial growth of $Al_xGa_{1-x}As$ on a patterned substrate; where the periodic crystal domain inversion was achieved using selective etching and wafer bonding. Although this is the most direct method, efforts were limited by relatively large losses in these structures. An alternative approach is based on the control of the second-order nonlinearities in semiconductor heterostructures by means of quantum-well-intermixing. This technique is of special interest for this work and some space will be given to describe the basic principles behind it.

5.2.1 Quantum-well-intermixing (QWI)

The forthcoming discussion requires the introduction of some elementary quantum mechanics ideas. Although a comprehensive treatment of quantum well formation in superlattices and quantum well intermixing is in fact not trivial, here a vivid picture of the basic concepts will be provided.

It is understood that the solutions of the time-independent Schrödinger equation for a free atom suggest the existence of distinctive electronic energy levels. For bulk solids the interference of the carrier wavefunctions causes the energy levels to degenerate to quasi-continuous energy bands, known as the valence (lower) and the conduction (upper) band. The valence and conduction bands are separated by an energy bandgap that depends on the specific material properties. Superlattices (SL) are more complicated structures, consisting of alternating layers of two semiconductors with different bandgaps and typical thicknesses of ~10 nm. In superlattices, a discontinuity is induced in the conduction and valence bands of the engineered structure. This is depicted in Fig. 5.1 for the indicative case of a GaAs/AlAs system. In this example, the layers of the greater bandgap material (AlAs) act as barriers, while the layers of the lower bandgap material (GaAs) confine the carriers (electrons and holes) in what is known as a quantum well. The small size of the wells causes the carrier energy levels to quantise, as quantitatively represented in Fig. 5.1.

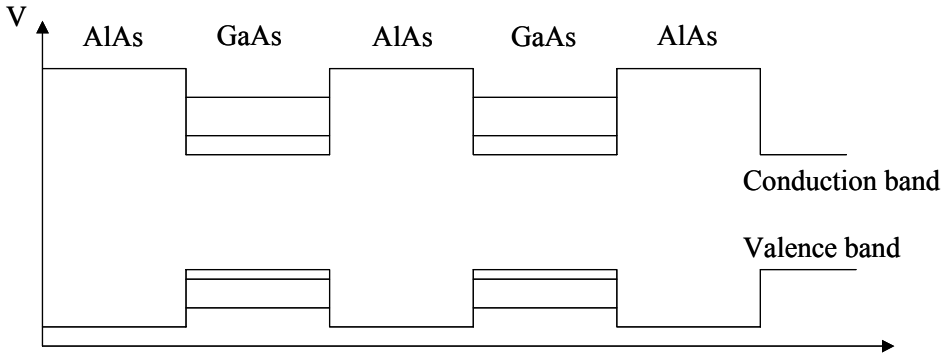

Fig. 5.1 Quantum well formation in a GaAs/AlAs superlattice.

Quantum well intermixing (QWI) [4] refers to a number of post-growth techniques that have been developed to control the properties of semiconductor quantum well structures, typically allowing the energy bandgap to be increased (blue-shifted). In general, QWI results from elevating the structure's temperature (annealing) in order to excite the atoms and thus cause intermixing with surrounding atomic constituents. To date, a number of QWI approaches have been demonstrated including impurity induced intermixing [5], impurity free vacancy disordering [6-8], and laser induced disordering [9]. The first approach is based on diffusion of impurities to reduce the required annealing temperature for intermixing and thus suffers from high optical absorption caused by the dopants. Laser induced methods avoid such complications, but offer limited spatial resolution. For these reasons, impurity-free techniques are most promising for a variety of applications. In the following, two successful and interesting impurity-free techniques for the purposes of the present work are briefly described.

The first technique of relevance is often referred to as dielectric cap annealing [6] and is illustrated in Fig. 5.2. Fig. 5.2-a shows the atomic structure of an as-grown GaAs/AlaAs superlattice. The sample is coated with a layer of silica (SiO_2) and then annealed. At elevated temperatures, silica tends to absorb gallium providing a mechanism by which group III vacancies are generated. The vacancies defuse from their high concentration region at the surface to areas deeper inside the superlattice in a "random" way. The effect of the vacancy migration is to intermix the regular layered structure of the as-grown supperlattice, as depicted in Fig. 5.2-b. In turn, the effect of intermixing on the band structure is illustrated in Fig. 5.3. The red lines show the conduction and valence bands for the as-grown material. Intermixing causes Al

atoms to diffuse into, and Ga atoms out of, the quantum well, with the net result that the quantum well becomes shallower and wider and thus the bandgap is increased (or, in other words, the absorption edge is shifted to shorter wavelengths) as shown by blue lines. The second technique is known as ion implantation induced intermixing [8] and differs from the dielectric cap technique in that the Ga vacancies are generated through displacement of lattice atoms due to collisions with implanted ions (typically As^+). Therefore, the bandgap modulation, depicted in Fig. 5.3, applies equally to the ion implantation method.

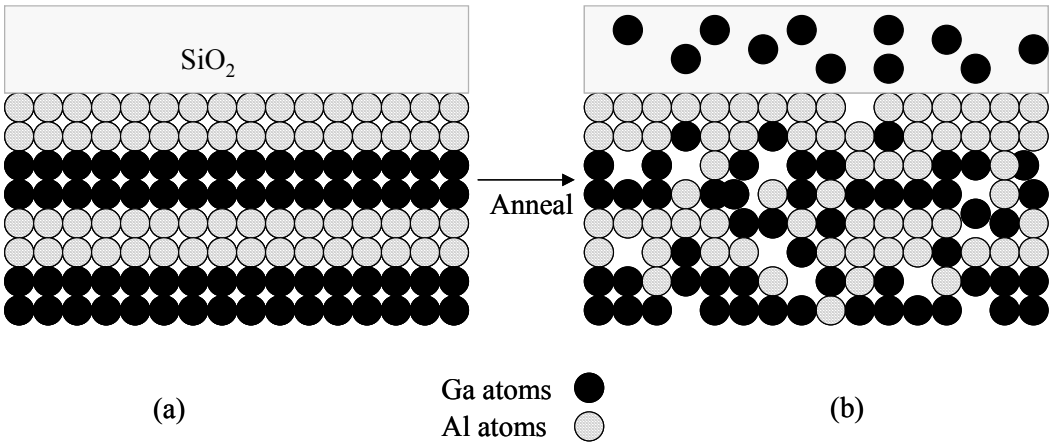

Fig. 5.2 GaAs/AlAs supperlattice atomic structure before (a) and after (b) intermixing.

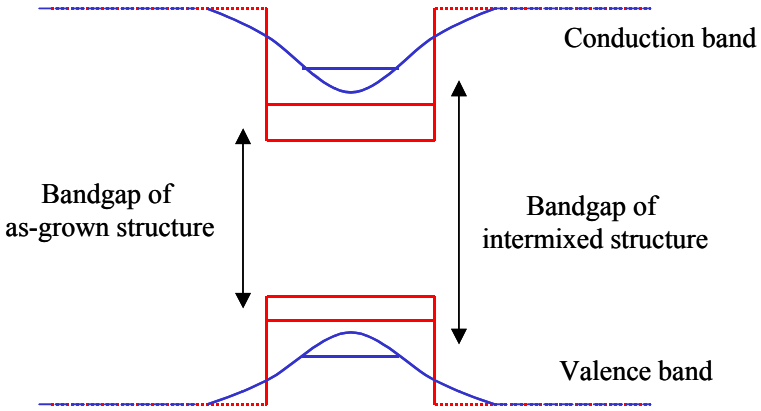

Fig. 5.3 Bandgap structure of a GaAs/AlAs superlattice before (red lines) and after (blue lines) intermixing.

There are two key issues related to QWI technologies. Firstly, the capability is offered of intermixing selective areas in the sample, while the rest remains in the as-grown form. This can be achieved through lithographic definition of the silica film in the case of dielectric cap intermixing, or alternatively, via deposition of a patterned protective mask to localise ion penetration in the case of implantation induced intermixing. Typically, the spatial resolution of the different QWI techniques is in the μm region, with possibly ion implantation induced intermixing offering optimum sub-μm resolution [10].

Secondly, the modulation of the superlattice bandgap provides a mechanism through which the linear [11] and nonlinear [12-14] optical properties of the structure can be controlled. Interpretation of the influence of bandgap modulation on the second-order susceptibility is based on theoretical studies [15], which indicated that the dispersive $\chi^{(2)}$ for bulk GaAs presents peaks when one of the optical frequencies (e.g., second harmonic) approaches the bandgap energy. Therefore, it is anticipated that the blue-shift of the band-edge on intermixing leads to a reduction in the magnitude of the second-order nonlinearity at a specific frequency.

Considerable work has been carried out in developing models for band-structure predictions in superlattice structures. This includes the modified Kroning-Penney model of Masselink *et al* [16], as well as algorithms that account for general (diffused) potential profiles [17] which can thus be applied to simulate intermixed regions. Further algorithms have been developed [18] to compute the $\chi^{(2)}$ dispersion profile as a function of the bandgap. Simulations suggested [19] that for a 14:14 monolayer GaAs/AlAs supperlattice, the bandgap blue-shift upon complete intermixing (i.e., for a resulting uniform alloy of $Al_{0.5}Ga_{0.5}As$) is of the order of ~150 nm. Complete intermixing, however, is difficult to achieve in practise and thus less substantial shifts should be expected. Hutchings and Kleckner computed [20], for the same material system and complete intermixing, a reduction in the second-order bulk susceptibility at 1.55 μm of ~50 pmV^{-1}. Although in relative terms this is a modest modulation (the larger bulk GaAs coefficient in the IR is $\chi^{(2)}_{xyz}$~340 pmV^{-1}), it is still comparable to the absolute modulation in periodically poled $LiNbO_3$.

Note that the uncertainties imposed by the material processing and the limited accuracy in knowledge of the material parameters, necessitate the development of experimental methods to evaluate both the bandgap shift and the nonlinear coefficient modulation [21]. The former is typically done by comparing the photoluminescence emission wavelength of an as-grown and an intermixed sample. Modulation in the nonlinearity upon QWI is commonly measured by comparing the un-phase-matched SHG power obtained by use of an as-grown and an intermixed sample [13].

The linear refractive index of the superlattice is also of great importance for all applications. However, existing heterostructure models fail to provide results of sufficient accuracy for quantum well structures [19,22], including the form birefringence model described in Chapter 4. The problem is further complicated by inaccuracies of the available bulk GaAs refractive index models for wavelengths near the bandgap. Thus, one has to retreat to experimental methods, most notably the grating coupler technique [23], for an accurate evaluation of the superlattice index of refraction. Note that with the use of superlattices for quasi-phase-matched processes, such individual-point measurements of the refractive index dispersion profile can be substituted to the phase-matching condition and thus allow prediction of the interacting wavelengths. Additionally, refractive index measurements are necessary for evaluation of the coherence length, which for SHG can be expressed as:

$$L_c = \frac{\lambda_\omega}{4(n_{2\omega} - n_\omega)}$$

In turn, knowledge of the coherence length is vital for QPM duty cycle predictions. These measurements alone, however, do not provide analytical refractive index expressions and hence can not be used to calculate GVD related effects (where the derivative of the index appears) when short pulses are used.

All aspects of QWI technologies for nonlinear frequency conversion in superlattices have been the focus of another doctoral thesis within the OFCORSE II collaboration [19]. Therein, all the concepts briefly described in this section (as well as in much of the rest of this chapter), including the theoretical models and computed results, are discussed in great detail.

5.2.2 Quasi-phase-matching strategies by use of QWI

It has been shown that QWI can be used to suppress the superlattice nonlinear coefficients. It was also explained that it is possible to intermix selective regions of the as-grown sample. This capability of selectively modulating the nonlinear coefficients can be used to engineer quasi-phase-matching geometries. Recall that the QPM condition for SHG is:

$$\Delta k^{QPM} = k_{2\omega} - 2k_{\omega} - k_m = \frac{2\pi n_{2\omega}}{\lambda_{2\omega}} - 2\frac{2\pi n_{\omega}}{\lambda_{\omega}} - \frac{2\pi m}{\Lambda} = 0$$

where the usual notation applies. Evidently, the phase-matching wavelength is solely determined by the grating vector, Λ, and does not depend on the depth of modulation, which is commonly introduced through the parameter (1-γ), where γ is defined as:

$$\gamma = d_{eff}^{\text{int}\,ermixed} / d_{eff}^{as-grown} \tag{5-1}$$

On the contrary, the effective nonlinear coefficient (and hence the efficiency of the process) – being proportional to the spatial Fourier component- does depend on the factor (1-γ) according to:

$$d^{QPM} = \frac{(1-\gamma)}{\pi m} d_{eff}^{as-grown} \tag{5-2}$$

Note that under ideal domain inversion (γ=-1), Eq. (5-2) degenerates to the expression (2-82). Ideal domain disordering (γ=0) sets an upper limit to the QPM conversion efficiency achievable by means of QWI, equal to 1/4 of the QPM efficiency under ideal domain inversion (or 1/4 $(2/m\pi)^2$) of the efficiency under perfect phase-matching). As discussed previously, due to the fact that the effective nonlinearity of the as-grown material is large, only relatively small modulation depths are required to access competitive conversion efficiencies.

There are two possible routes by which QPM structures can be realised using QWI [13]. The first is based on engineering an asymmetric multiple quantum well (AMQW) structure, with the symmetry breaking along the surface normal (*z*) direction. Such an AMQW structure is associated with additional second-order nonlinear coefficients, namely $\chi_{zxz}^{(2)} = \chi_{yzy}^{(2)}$, $\chi_{zxx}^{(2)} = \chi_{zyy}^{(2)}$ and $\chi_{zzz}^{(2)}$, which otherwise vanish in bulk $Al_xGa_{1-x}As$, as well as with the bulk-like coefficients $\chi_{ijk}^{(2)}$; $i \neq j, i \neq k, j \neq k$. Upon selective intermixing, the structure acquires a higher degree of symmetry and the bandgap is blue shifted, with both of these mechanisms giving rise

to a reduction in the asymmetry-induced nonlinearity. By means of QWI in AMQW structures, SHG has recently been demonstrated [24,25], but efficiencies were limited due to the small values [26] of the induced coefficients (typically, < 10 pmV^{-1}).

The second route promises much higher efficiencies by directly accessing the large bulk-like $Al_xGa_{1-x}As$ coefficients, which are readily available in a symmetric quantum well structure. Again, upon selective intermixing these coefficients are suppressed, providing a means of engineering a QPM device. Some attention has to be paid to the geometry of the interaction [27]. A conventionally orientated waveguide is depicted in Fig. 5.4 (growth parallel to [001], cleavage planes parallel to [110]). Following this convention, the waveguide is cut parallel to the (*Z'*,*X'*) plane and propagation is taken along Y' axis, where (*X'*,*Y'*,*Z'*) denote the waveguide orientation. On the other side, the crystal orientation (*X*,*Y*,*Z*) is such that the *Z* axis is normal to the wafer and overlaps with *Z'*, while *X* and *Y* axis exhibit a 45^0 orientation with respect to the corresponding waveguide axis (*X'* and *Y'*). One can easily recognise that the TE, TM and propagation directions are parallel to unit vectors according to Table 5.1.

	Waveguide orientation (*X'Y'Z'*)	Crystal orientation (*X*,*Y*,*Z*)
TE direction unit vector	(1,0,0)	$(1/\sqrt{2}, 1/\sqrt{2}, 0)$
TM direction unit vector	(0,0,1)	(0,0,1)
Propagation direction unit vector	(0,1,0)	$(-1/\sqrt{2}, 1/\sqrt{2}, 0)$

Table 5.1 Unit vectors defining (1) a TE wave, (2) a TM wave, and (3) the propagation direction in the orientation of the waveguide and the crystal.

By using Eq. (2-43) and accounting for the fact that $Al_xGa_{1-x}As$ has non-zero tensor elements $\chi^{(2)}_{ijk}$ only when $i \neq j, i \neq k, j \neq k$, it is evident that the following two possibilities exist:

- A TE input, having electric field components along *X* and *Y* crystal axis, exploits $\chi^{(2)}_{zxy}$ to produce a polarisation component along *Z*-axis (TM). This TE→TM process corresponds to a type I phase-matching geometry.

- A TM+TE input, having electric field components along *Z* and *X*, *Y* axis, exploits simultaneously $\chi^{(2)}_{xzy}$ and $\chi^{(2)}_{yzx}(=\chi^{(2)}_{xzy})$ to produce two equal polarisation components along *X* and *Y* which add together to give a net polarisation component along *X*'-axis (TE polarisation). This TM+TE→TE process corresponds to a type II phase-matching geometry.

Note that the superlattice breaks the degeneracy between $\chi^{(2)}_{zxy}$ and $\chi^{(2)}_{xzy}$ that exists in bulk $Al_xGa_{1-x}As$, but is restored upon QWI, with the larger modulation predicted for $\chi^{(2)}_{xzy}$ [18].

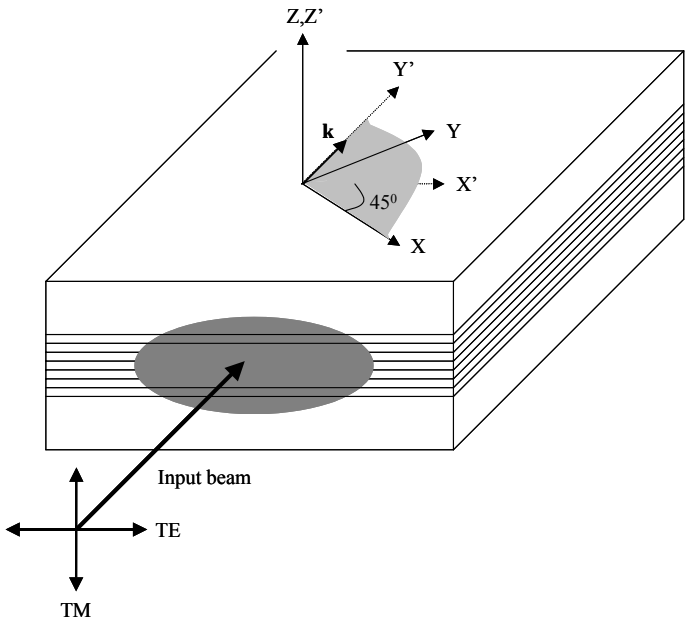

Fig. 5.4 Crystal orientation with respect to the waveguide.

In what follows, results are presented from two experiments that resulted in demonstration of SHG in QPM GaAs/AlAs superlattice waveguides. The first experiment was based on a third-order QPM structure fabricated by means of dielectric cap annealing. The second experiment demonstrated first-order quasi-phase-matching (and thus greater conversion efficiencies), based on sufficient improvement of the spatial resolution of the grating period achieved by use of ion implantation induced intermixing.

5.3 Initial efforts: Third-order quasi-phase-matching experiment

5.3.1 Sample details and experimental set-up

The sample used in this experiment, designed and fabricated by collaborators* at Glasgow University, was 4 mm long and comprised third-order grating periods between 5.8 μm to 12.4 μm. The structure is depicted in Fig. 5.5 and was composed of 0.6 μm of a symmetric superlattice waveguide core made of 14:14 monolayers of GaAs:AlAs, respectively. The lower and upper cladding were bulk $Al_{0.6}Ga_{0.4}As$ of 4 μm and 1.5 μm width, respectively. A 100-nm GaAs cap was used to cover the upper cladding. The structure was nominally undoped and grown by molecular beam epitaxy on a GaAs substrate.

The room temperature photoluminescence (PL) emission wavelength of the structure was 745 nm from the central portion of the wafer*. This design allowed an operating fundamental wavelength of 1550 nm at 30 meV below the half-bandgap, (avoiding two-photon absorption), and used the modulation attained in the resonant component of $\chi^{(2)}$ as the bandgap of the structure is shifted. Domain disordering was achieved using a slight variation of the dielectric cap annealing method outlined previously [7] (often referred to as sputtered silica defect induced intermixing), with electron gun deposited silica caps to suppress the process. The sputtered-silica induced intermixing process is not expected to introduce any significant optical loss [28]. Relative measurements indicated that the best of the waveguides exhibited loss of ~20 dB/cm. After annealing of the present sample, room temperature PL wavelength peaks were observed at 725 nm and 680 nm; the peaks originated from the as-grown and the disordered regions, respectively. The reduction of the PL emission wavelength from the as-grown regions upon intermixing indicates some lateral vacancy diffusion. The periodic modulation in the superlattice bandgap induces a modulation in $\chi^{(2)}$, as illustrated in Fig. 5.5, where intermixing occurs under the sputtered silica caps only.

* A. S. Helmy, D.C. Hutchings, T.C. Kleckner, A.C. Bryce, J.M. Arnold, C.R. Stanley, and J.S. Aitchison. Note that results obtained by these collaborators and presented in this chapter, are explicitly denoted by the star symbol.

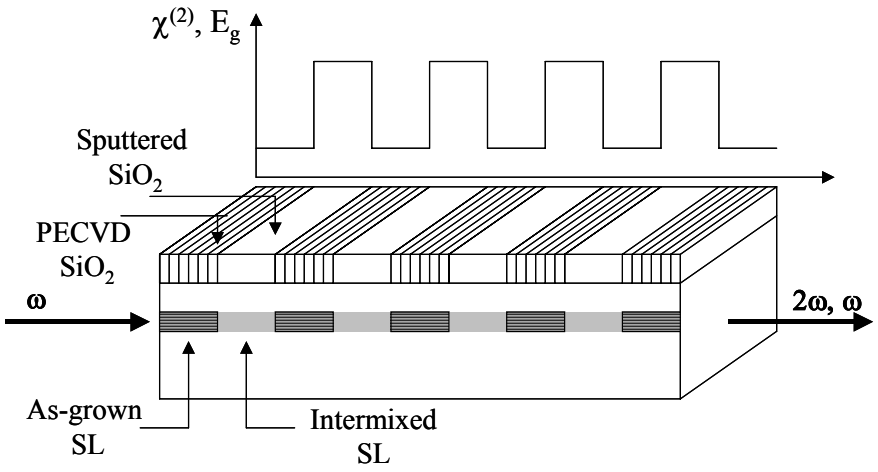

Fig. 5.5 Design of the sample used in this experiment, along with the corresponding second-order susceptibility modulation along the propagation axis.

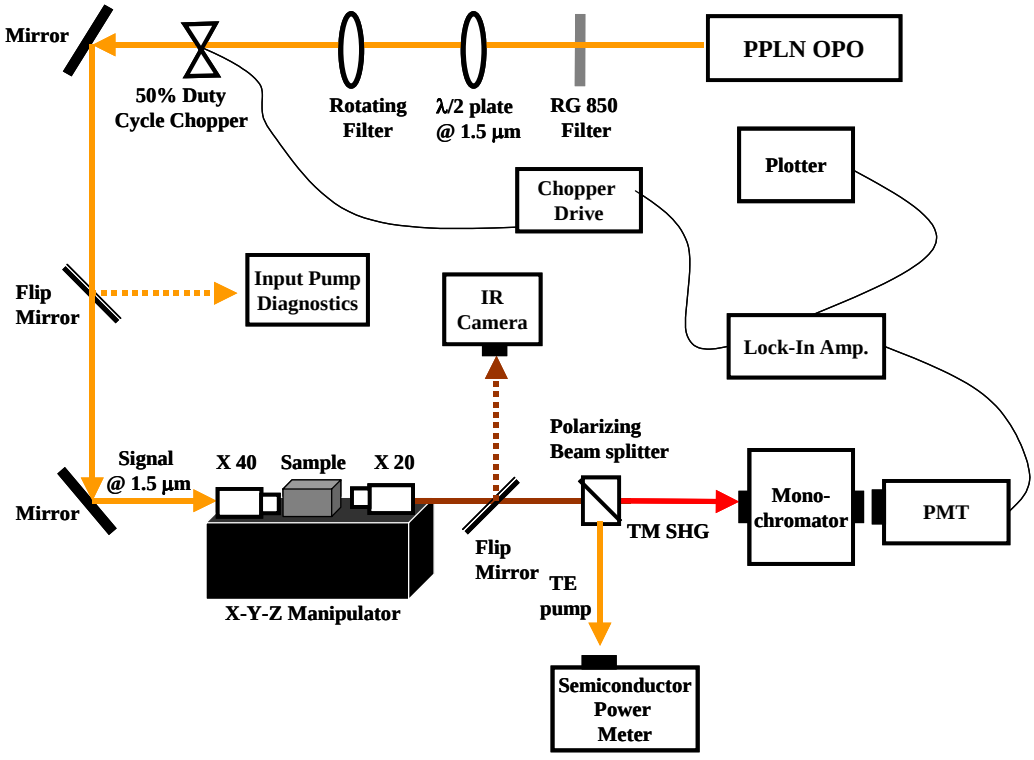

Fig. 5.6 Schematic representation of the experimental apparatus.

The experimental arrangement is shown in Fig. 5.6. The optical source used in the measurements was the synchronously pumped, singly resonant femtosecond PPLN OPO described in Chapter 3. Note, however, that these experiments were carried out at a very early stage of this work and the source was operating at the time without intracavity dispersion control prisms. In fact, the signal (which was used as the fundamental beam for the conversion process) had a pulse duration ~500 fs and a corresponding spectral FWHM of ~11 nm near 1.5 μm, indicating chirped pulses ($\Delta\nu\Delta\tau > 0.7$). The OPO was running at a ~90 MHz repetition rate. An average power of 80 mW was obtained in the OPO signal, which was tuneable in the ~1.3-1.58 μm range.

Appropriate polarisation optics and filters were introduced to ensure that only the TE polarised signal was coupled into the waveguide. The input diagnostics consisted of a thermal power meter and a commercial spectrometer. A 50% duty cycle chopper was inserted before the waveguide for lock-in detection. The sample was mounted on an end-fire coupling rig and two microscope objectives were used to couple the input, and collect the output, beam from the waveguide. The coupling procedure was assisted by monitoring the waveguide output with an IR camera. The output of the waveguide was passed through a polarising beam splitter to verify the polarisation state of the second harmonic and separate the generated beam (TM) from the transmitted fundamental (TE). The second harmonic signal was aligned into a monochromator with a ~0.1 nm resolution. A photomultiplier tube (PMT) was then used to detect the second harmonic at the output of the monochromator using an internal PMT amplifier, and a lock-in amplifier. The PMT had a spectral range ~185 nm to 900 nm, and therefore no signal resulting form the fundamental could be detected. Measurements of the input fundamental power into the waveguide as a function of the detected fundamental power at the waveguide output confirmed the linearity of their relation, ensuring that there is no significant two-photon absorption of the pump, neither in the detector nor in the waveguide itself. The electrical current reading of the detection scheme was translated into optical power by use of calibration tables provided by the producer of the PMT.

5.3.2 Results and discussion

It has been explained in the previous section that there are two possible phase-matching geometries: (1) type-I phase-matching exploiting the modulation in $\chi^{(2)}_{zxy}$, accessed by launching the fundamental in TE polarisation at the input and the SH expected in TM polarisation, and (2) type-II phase-matching exploiting the modulation in $\chi^{(2)}_{xyz}$, accessed with a mixed TE:TM polarisation for the fundamental, with the SH expected in TE polarisation. These two cases will be phase-matched at different QPM grating periods due to the difference in propagation constant with polarisation mode.

A typical measurement of the type-I second harmonic along with the corresponding fundamental spectra are shown in Fig. 5.7, in which there is a clear SH signal for TM polarisation and there is no signal for the TE. The measured bandwidth of the SH (FWHM of ~3 nm) is limited by the finite width of the monochromator slit at an acceptable signal-to-noise ratio, whereas the measured FWHM is 11 nm for the fundamental. Additional spectral narrowing occurs, owing to the finite acceptance bandwidth of the QPM grating. The second harmonic signal appears only when the output spectrum of the OPO is tuned so that it contains the appropriate wavelength for the QPM grating under test. Fig. 5.8 shows a typical result for the dependence of the SH power on the fundamental power. The best fit to the slope on a log-log plot is 1.9, confirming the expected parabolic power dependence with no observed saturation. The wavelength of the SH generated as a function of various grating periods available in the sample is plotted in Fig. 5.9. As the grating period is decreased, the QPM wavelength also decreases in this normally dispersive medium. The lower wavelength limit was reached when the SH photon energy approaches the material bandgap and experiences excessive band-edge absorption.

The largest average SH power measured by the PMT was 25 nW for a wavelength of 758 nm. However; the optical measurement system had a measured 5-dB loss between the waveguide and PMT. With a further 30% reflection loss at the rear facet of the waveguide, a maximum average SH power of ~110 nW inside the waveguide is expected. In this case, a transmitted fundamental average power of 250 μW was measured (for ~80 mW of available input) which, with a 30% loss at the rear facet and a measured optical loss of ~20 dB/cm in the waveguide, translates to an average

pump power of ~2.3 mW just after the front facet of the waveguide. Note that there is a reduction of approximately 2 orders of magnitude in the fundamental power between the OPO output and the guided-mode, due principally to coupling losses.

Following the definitions introduced in the last chapter, an overall practical efficiency as low as $3x10^{-5}$ % can be calculated, corresponding to an internal efficiency of just ~0.005 %. Evidently, there is a reduction of approximately five orders of magnitude in the conversion efficiency of the present scheme compared to the BPM structure presented earlier. This exceeds by far the theoretically expected reduction factor of $(1/m\pi)^2$~100. Further reduction should be attributed to a number of factors, including sample quality and length. In fact, the QPM sample was ~4 times longer than the most efficient BPM sample, while group-velocity mismatch is expected to limit the interaction length at 1.5 μm to less than half its value at 2 μm. However, the scope of this initial experiment was to demonstrate the potential of quantum well intermixing techniques for engineering QPM structures, rather than to obtain competitive efficiencies.

Following the relative success of the present set-up, a number of samples were later fabricated and tested with the aim of enhancing conversion efficiencies, by means of improving the sample, as well as the pump source, quality. Efforts by collaborators were focused on designing first-order QPM gratings. However, the sample processing required for the necessary micron-scale resolution has been difficult to reproduce and conversion efficiency improvements have proved elusive in spite of extensive process development and optimisation [29]. These fabrication limitations are now believed to be unavoidable as the sputtered silica process creates group-III vacancies at the wafer surface, which then have to migrate across the waveguide cladding and the core regions to promote intermixing and some lateral spreading is inevitable. Indeed, significantly higher efficiencies were only achieved with use of first-order QPM waveguides, which were realised after abandoning the dielectric cap annealing technique and retreating to the alternative of ion implantation induced intermixing. Results from the latest experiment are presented in the following section.

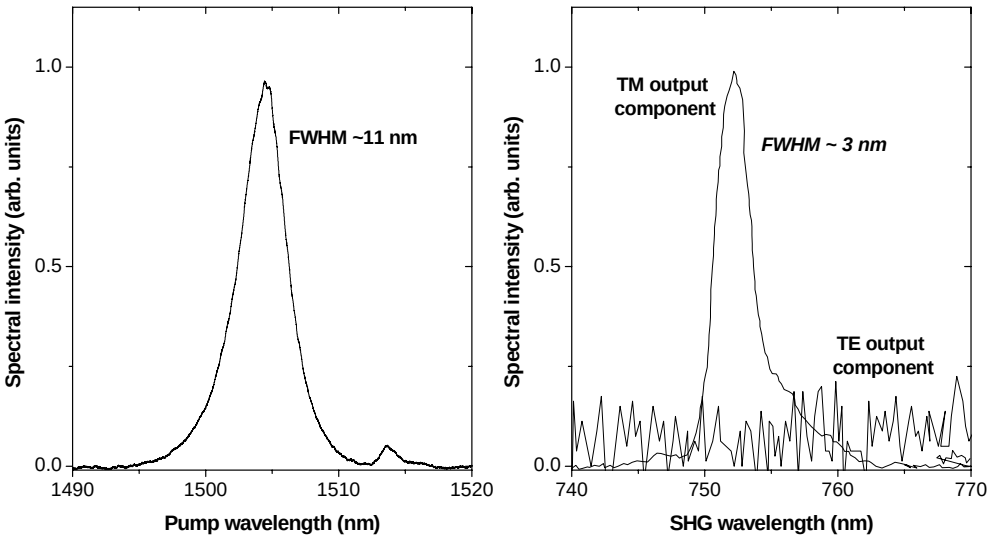

Fig. 5.7 TE fundamental (left) and SH (right) spectra confirming type-I phase-matching process.

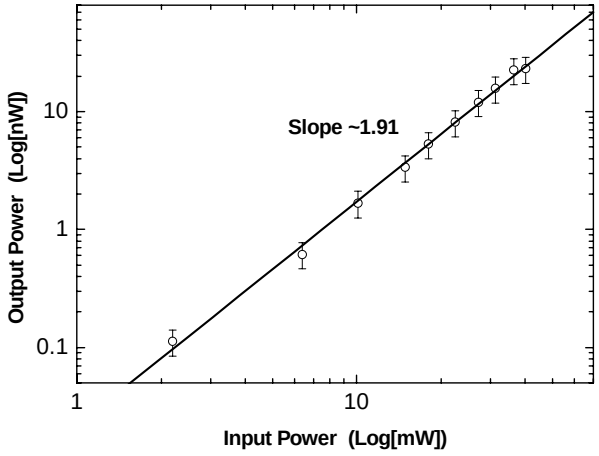

Fig. 5.8 Output power as a function of the input power on a log-log scale.

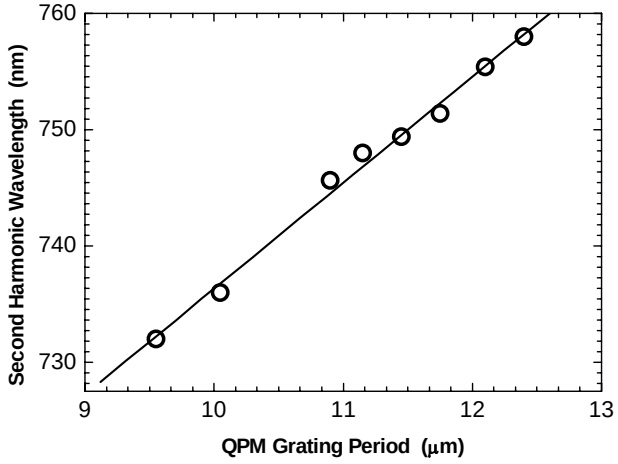

Fig. 5.9 Tuning curve indicating the SH wavelength as a function of the QPM grating period.

5.4 Optimised design: First-order quasi-phase-matching experiment

5.4.1 Sample details and experimental set-up

The layer structure of the sample used in this study, which was also fabricated by collaborators at Glasgow University, was similar to the third-order QPM structure presented earlier: it consisted of a 0.6-μm core of GaAs/AlAs superlattice comprising 75 periods of 14:14 monolayer and was clad on either side with 0.3-μm $Al_{0.56}Ga_{0.44}As$ buffer layers. The lower and upper cladding layers were bulk $Al_{0.6}Ga_{0.4}As$ of 4 μm and 0.8 μm thickness, respectively. The upper cladding layer was capped with 100 nm of GaAs to prevent any undesirable Al oxidation. The structure was nominally undoped, grown by molecular beam epitaxy (MBE) on a GaAs substrate. The room temperature photoluminescence emission wavelength of the structure was 750 nm from the central portion of the wafer. This design allowed the operating fundamental wavelength, ~1550 nm, at 30 meV below the half-bandgap to avoid two-photon absorption and used the modulation attained in the resonant component of $\chi^{(2)}$ as the bandgap of the structure is shifted. The sample was initially 2-mm-long and included a number of first-order gratings with periods near ~3.7 μm, that is, the expected phase-matched period for a fundamental wavelength at 1.5 μm, calculated using the effective refractive index data measured by using the coupler grating technique. However, only a couple high quality waveguides were actually found in the final sample, possibly due to physical damage that occurred during its transport from the fabrication room in Glasgow to the test laboratory in St. Andrews.

Superior intermixing resolution, suitable for engineering first-order QPM gratings, was achieved using As^+ ion implantation, in order to avoid introducing any impurity defects into the material. Commercially available software simulation predicted that ion energy of 4 MeV corresponds to an ion range of 1.7 μm and a lateral straggle of 0.45 μm, adequate for the creation of group-III vacancies in the superlattice layers yet maintaining the desired spatial resolution. A gold mask of ~1.5 μm thickness, which was predicted to be sufficient to protect the desired regions from the As^+ ions, was grown. This was done by firstly transferring the QPM pattern on a photoresist layer by using electron beam lithography technology, and then submerging the sample in a gold solution. Once the gold pattern had been grown, the photoresist was stripped off

using hot acetone. After implantation, the gold mask was removed by wet etching. The sample was annealed face down in a rapid thermal annealer at 850°C for 30 seconds. Fig. 5.10 shows the photoluminescence peak wavelength blue shift in the large-area intermixed samples in comparison to the as-grown sample, as a function of ion flux. It can be seen that the photoluminescence blue shift is approaching its saturation value of ~60 nm for a dosage 10^{13}-10^{14} ion/cm^2. High ion dosages would substantially increase optical losses due to amorphisation. Rib waveguides were fabricated using reactive-ion etching and the sample was cleaved on each side. Loss measurements at a wavelength of 1.55 μm yielded a value of ~21 dB/cm in the QPM sample implanted with an ion dosage of 10^{14} ion/cm^2, which was employed in the nonlinear measurements described below.

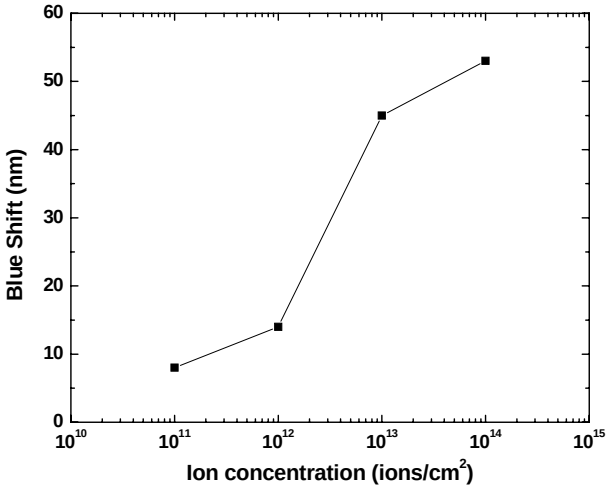

Fig. 5.10 Photoluminescence (at 77 K) blue shift as a function of As^+ ion flux at 4 MeV energy. Samples were annealed at 850°C for 30 seconds. These measurements were carried out by our collaborators.

The experimental arrangement is similar to that of Fig. 5.6, with only two major differences. Firstly, the synchronously pumped, femtosecond PPLN OPO was dispersion-controlled by means of intracavity prisms. This configuration allowed an average signal power of ~80 mW to be routinely attainable in pulses of ~250 fs duration at ~90 MHz repetition rate. Accounting for a measured spectral FWHM bandwidth for the signal of ~10 nm, a time-bandwidth product of $\Delta\nu\Delta\tau$~0.33 can be calculated, indicating near-transform-limited pulses. Secondly, the improvement in the conversion efficiency was sufficient to allow replacement of the monochromator-PMT combination in the output diagnostics set-up, with simply a commercial semiconductor head power meter and an IR optical spectrum analyser.

5.4.2 Results and discussion

Linearly polarised light from the OPO was launched into one of the few high quality waveguides available in the sample, with the output of the waveguide directed to the spectrum analyser. Typical second harmonic spectra, along with the corresponding pump spectra, are shown in Fig. 5.11. As expected for type-I phase-matching, the detected SH signal was TM-polarized with a TE fundamental polarization. There was no SH signal detected for a TM-polarized fundamental. Fig. 5.11 shows that the SHG signal appeared only when the output spectrum of the OPO was tuned to provide the appropriate wavelength for the QPM grating under test. By tuning the pump away from the phase-matching wavelength, a broad-bandwidth non-phase-matched signal was also observed at lower power levels (~100 nW). This is depicted in the inset of Fig. 5.11, where the fundamental was detuned by ~20 nm with respect to the optimal phase-matching wavelength. The measured bandwidth of the fundamental was ~10 nm (FWHM), while that of the phase-matched SHG, determined by the finite bandwidth of the QPM grating, was ~0.9 nm. Using longer grating periods, third-order QPM could be observed with an appropriate drop in SHG power.

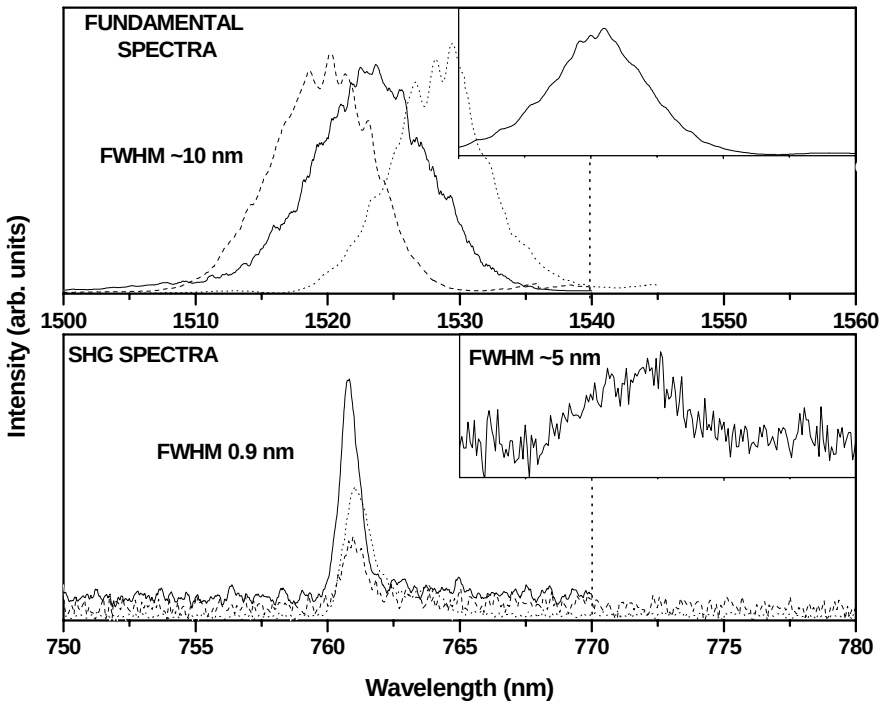

Fig. 5.11 Observed second harmonic (bottom) and the fundamental (top) spectra. Fine-tuning of the pump results in a change in SHG power, but the SHG wavelength remains locked, confirming phase-matched process. Inset shows the non-phase-matched SHG spectrum corresponding to a larger detuning of ~20 nm.

The measured average SHG power is plotted in Fig. 5.12 as a function of the peak fundamental wavelength for a constant input power level. As the source is not monochromatic, the line shape is determined by the fundamental spectrum rather than the $sinc^2$ gain function. A Gaussian fit to the data resulted in a ~10 nm FWHM bandwidth of this wavelength tuning curve, which is comparable to the pump spectral bandwidth. Figure 5.13 shows a typical result for the dependence of the average SHG power on the fundamental power. The corresponding best fit to the slope on a log-log scale is 2.04, confirming the expected quadratic power dependence. Saturation of the SHG power was observed for input average powers exceeding ~40 mW.

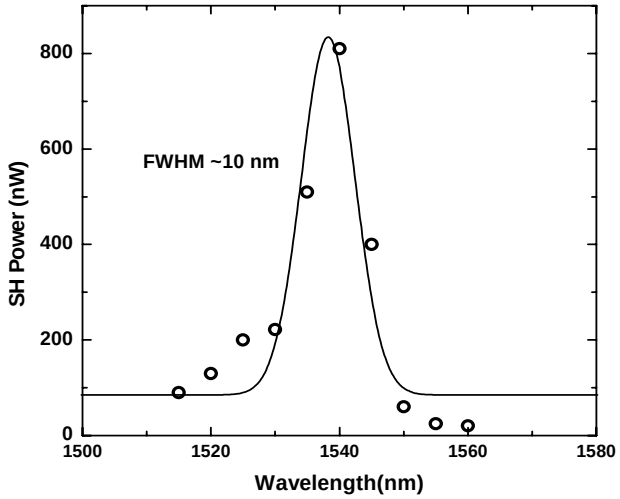

Fig. 5.12 SHG power as a function of the input wavelength (wavelength tuning curve), exhibiting a FWHM of 10 nm.

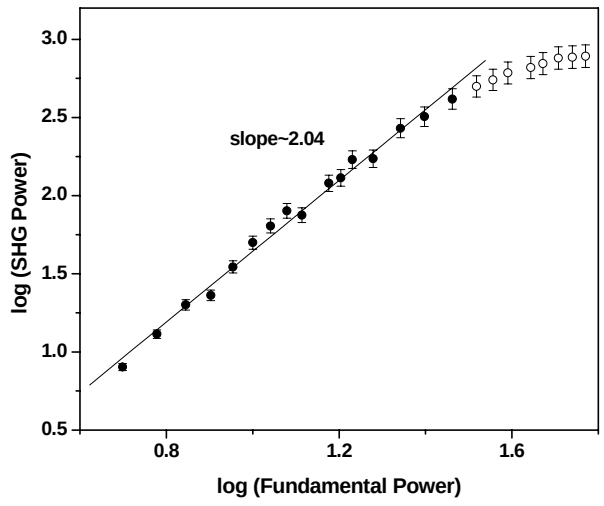

Fig. 5.13 SHG average power as a function of the fundamental input average power on a log-log scale. The best fit to the slope is 2.04 confirming the expected quadratic power dependence.

The largest SHG average power measured was 1.5 μW at a wavelength of 767 nm. Taking into account an estimated 5 dB loss between waveguide and detector and 30% reflection loss at the rear facet of the waveguide, an average SHG power of ~7 μW generated within the waveguide is estimated. The average power in the transmitted fundamental was ~2.9 mW which, with a 30% loss at the rear facet and a measured optical loss of ~21 dB/cm in the waveguide, translates to an average pump power of ~11 mW just after the front facet of the waveguide. This corresponds to an end-fire coupling efficiency of around 18%, increased by a factor of ~5 compared to the third-order QPM sample presented earlier. Therefore, the overall practical conversion efficiency of the present set-up was ~0.002 % and the corresponding internal conversion efficiency ~0.06 %. These values represent an improvement in the internal efficiency of at least one order of magnitude compared to the third-order QPM result. Combined with the increase in the coupling efficiency by a factor of ~5, this naturally yields an observed improvement in the overall practical efficiency of almost two orders of magnitude.

It was outlined earlier that existing theoretical models for superlattice refractive index predictions exhibit limited accuracy. This gives rise to difficulties in calculating the actual interaction length and consequently the normalised efficiency in the present QPM waveguides. Using the results of table 4.1 for bulk GaAs, one can substitute the value of ~100 μm for the interaction length to obtain an indicative value for the normalised efficiency of the first-order QPM sample of ~1.2 $\%W^{-1}cm^{-2}$. Similar calculations for the third order QPM sample resulted[1] in an indicative value for the normalised conversion efficiency of ~0.15 $\%W^{-1}cm^{-2}$. This one order-of-magnitude difference between the internal efficiencies for first- and third-order QPM is in good agreement[2] with the theoretically expected reduction by a factor of (3^2=) 9.

[1] Note that in the evaluation for the third order QPM sample, a ~500 fs pulse duration should be used for the calculation of the interaction length and peak powers.

[2] A direct comparison between first- and third-order QPM internal efficiencies should account for the following facts:

a) The SHG spectral bandwidth (and hence the utilised pump spectrum) was larger for third-order phase-matching and
b) The sample length (and hence the SHG propagation loss) was also larger for third-order phase-matching.

(a) should result in a reduction of the theoretical factor of 9, while (b) should result in an increase in this factor. It seems that the combination of these two differences in the present set up cancel out.

Although significant output power improvement was observed in this-first order QPM experiment, the obtained efficiencies were still more than two orders of magnitude smaller than the efficiency of the BPM sample presented in Chapter 4. This reduction is far larger than the expected reduction by a factor of $(1/\pi)^2 \sim 0.1$, corresponding to first-order QPM under ideal domain disordering[1]. Additional efficiency reduction should be attributed primarily to (a) limitations in the modulation depth factor, γ, that can be achieved using QWI, and (b) possible departure from the ideal 50:50 square-wave QPM grating duty cycle, due to the defect out-diffusion at high annealing temperature in addition to the ion implantation lateral straggle. Furthermore, it has been predicted that the associated modulation in the linear refractive index will also compromise conversion efficiency by ~30% [30,31].

Hence, there is considerable scope for improvement of the present set-up, with main efforts directed towards fabrication of lower-loss samples. In fact, the optical losses of the waveguides under test were relatively high in comparison to previous intermixed waveguides. This may be partly due to the surface damage caused by the gold etch. An additional protective silica layer is being introduced in future samples to avoid this problem. It may also be desirable to use a lower ion dosage to trade off some of the modulation of the nonlinear coefficient for lower losses. Moreover, an increase in the normalised efficiency, as well as a more conclusive evaluation of this critical parameter, is considered possible with a reproduction of the experiment using a picosecond OPO. Such a test is expected to result in exploitation of the entire fundamental spectrum and avoid group velocity dispersion and temporal walk-off complications.

[1] The reduction factor of ~6 assumes that the oxidised GaAs/AlAs BPM structure and the QPM GaAs/AlAs superlattice exhibit the same effective nonlinear coefficients.

5.5 Conclusions

It was shown that quantum well intermixing can be used to modulate the second-order susceptibility of GaAs/AlAs superlattices and thus provide a means for engineering QPM structures. Although different reports of quasi-phase-matching in asymmetric superlattice structures exist, in this chapter two experiments were presented, both demonstrating SHG in symmetric GaAs/AlAs superlattice via exploitation of the large bulk-like $\chi_{zxy}^{(2)}$ nonlinear coefficient. To our knowledge, these were the first reports of this kind.

The first experiment utilised sputtered silica defect-induced intermixing to achieve third-order gratings in a GaAs/AlAs superlattice waveguide. Type I phase-matched SHG was demonstrated for fundamental wavelengths from 1480 to 1520 nm, in third-order gratings with periods from 10.5 to 12.4 μm. The second harmonic signal spectra were found to exhibit spectral narrowing owing to the finite QPM acceptance bandwidth. An average power of 110 nW was obtained at the output facet of the best waveguide for the second harmonic with an average coupled pump power of ~2.3 mW, corresponding to an internal efficiency of 0.005 %.

The second experiment provided results from first-order gratings in a symmetric GaAs/AlAs superlattice waveguide, which was realised by use of quantum well intermixing induced by As^+ ion implantation. In this case, practical second harmonic average powers of ~ 7 μW were obtained inside the waveguide through a type I process, for ~11 mW of coupled average input power, corresponding to an enhanced internal efficiency of ~0.06 %. Further improvement in internal efficiencies is expected to be possible through reduction of propagation losses and use of picosecond pulses.

References

[1] S.J. Yoo, R. Bhat, C. Caneau, and M.A. Koza, *Quasi phase matched second harmonic generation in AlGaAs waveguides with periodic domain inversion achieved by wafer bonding*, Appl. Phys. Lett. 66, 3410, (1995)

[2] S.J. Yoo, C. Caneau, R. Bhat, M.A. Koza, A. Rajhel, and Neo Antoniades, *Wavelength conversion by difference frequency generation in AlGaAs waveguides with periodic domain inversion achieved by wafer bonding*, Appl. Phys. Lett. 68, 2609, (1996)

[3] C.B. Ebert, L.A. Eyers, M.M. Fejer, and J.S. Harris, *MBE growth of antiphase GaAs films using GaAs/Ge/GaAs heteroepitaxy*, J. Crust. Growth 201, 187, (1999)

[4] J.H. Marsh, *Quantum well intermixing*m Semicond. Sci. Techno. 8, 1136, (1993)

[5] W.D. Laidig, N. Holonyak, M.D. Camras, K. Hess, J.J. Coleman, P.D. Dapkus, and J. Bardeen, *Disorder of an AlAs-GaAs superlattice by impurity diffusion*, Appl. Phys. Lett. 38, 776, (1981)

[6] E.V.K. Rao, A. Hamoudi, P. Krauz, M. Juhel, and H. Thibierge, *New encapsulant source for III-V quantum well disordering*, Appl. Phys. Lett. 66, 472, (1995)

[7] O.P Kowalski, C.J. Hamilton, S.D. McDougal, J.H. Marsh, A.C. Bryce, R.M. De La Rue, B. Vogele, C.R. Stanley, C.C. Button, and J.S. Roberts, *A universal damage induced technique for quantum well intermixing*, Appl. Phys. Lett, 72, 581, (1998)

[8] P. Gavrilovic, D.G. Deppe, K. Meehan, N. Holonyak, J.J. Coleman, and R.D. Burnham, *Layer disordering of $Al_xGa_{1-x}As$ superlattices*, Appl. Phys. Lett. 47, 130, (1985)

[9] C.J. McLean, J.H. Marsh, R.M. DeLaRue, A.C. Bryce, B. Garrett, and R. W. Glew, *Layer selective disordering by photoabsorption induced thermal diffusion in InGaAs/InP based multi-quantum well structures*, Electr. Lett. 28, 1117, (1992)

[10] B.S. Ooi, Y.S. Tang, A.S. Helmy, A.C. Bryce, J.H. Marsh, M. Paquette, and J. Beauvais, *Optical characterisation of GaAs/AlGaAs quantum well wires fabricated using arsenic implantation induced intermixing*, J. Appl. Phys. 83, 4526, (1998)

[11] S.I. Hansen, J.H. Marsh, and J.S. Roberts, *Polarisation dependence of refractive index of MQW waveguides*, IEE Proceedings 138, 309, (1991)

[12] M.W Street, N.D. Whitebread, C.J. Hamilton, B. Vogele, C.R. Stanley, D.C. Hutchings, J.H. March, J.S. Aitchison, G.T. Kennedy, and W. Sibbett, *Modification of the second order optical nonlinearities in AlGaAs asymmetric multiple quantum well waveguides by quantum well intermixing*, Appl. Phys. Lett. 70, 2804, (1997)

[13] J.S. Aitchison, C.J. Hamilton, M.W. Street, N.D. Whitebread, D.C. Hutchings, J.H. Marsh, G.T. Kennedy, and W. Sibbett, *Control of the second and third order nonlinearities in GaAs-AlGaAs multiple quantum wells*, Pure Appl. Opt. 7, 327, (1998)

[14] M.W Street, N.D. Whitebread, D.C. Hutchings, J.M. Arnold, J.H. Marsh, J.S. Aitchison, G.T. Kennedy, and W. Sibbett, *Quantum well intermixing for the control of second order nonlinear effects in AlGaAs multiple quantum well waveguides*, Opt. Lett. 22, 1600, (1997)

[15] D.J. Moss, J.E. Sipe, and H.M van Driel, *Empirical tight-binding calculation of dispersion in the second order nonlinear optical constant for zinc-blende crystals*, Phys. Rev. B 36, 9708, (1987)

[16] W.T Masselink, P.J. Pearah, J. Klem, C.K. Peng, and H. Morkoc, *Absorption coefficients and exciton oscillator strengths in AlGaAs-GaAs superlattices*, Phys. Rev. B 32, 8027, (1985)

[17] D.C. Hutchings, *Electronic bandstructure of disordered superlattices*, Superlattices Microstruct. 26, 195, (1999)

[18] D.C. Hutchings, *Modulation of the second order susceptibility in GaAs/AlAs superlattices*, Appl. Phys. Lett. 76, 1362, (2000)

[19] T.C Kleckner, *Quasi-phase-matched frequency conversion in periodically disordered GaAs/AlAs supelattice core waveguides*, PhD Thesis, University of Glasgow, (2002)

[20] D.C. Hutchings, and T.C. Kleckner, *Quasi phase matching in semiconductors by intermixing: optimisation considerations*, J. Opt. Soc. Am. B 19, 890, (2002)

[21] A.S. Helmy, A.C. Bryce, C.N. Ironside, J.S. Aitchison, J.H. Bryce, S.G. Ayling, I Gontijo, and G.S. Buller, *Optical diagnostics of microstructures fabricated using quantum well intermixing*, Symposium on Infrared applications of semiconductors III, (1999)

[22] Y.F. Li, and J.W.Y. Lit, *General formulas for the guiding properties of a multiplayer slab waveguide*, J. Opt. Soc. Am. A 4, 671, (1987)

[23] T. Tamir, *Integrated optics*, New York, Springer-Verlag, (1975)

[24] S. Janz, F. Chatenoud, and R. Normandin, *Quasi-phase matched second harmonic generation from asymmetric quantum wells*, Opt. Lett. 19, 622, (1994)

[25] J.P. Bouchard, M. Tetu, S. Janz, D.X. Xu, Z.R. Wasilewski, P.G. Piva, U.G. Akano, and I.V. Mitchell, *Quasi-phase matched second harmonic generation in an $Al_xGa_{1-x}As$ asymmetric quantum well waveguide using ion implantation enhanced intermixing*, Appl. Phys. Lett. 77, 4247, (2000)

[26] D.C. Hutchings, and J.M Arnold, *Determination of second order nonlinear coefficients in semiconductors using pseudospin equations for three level systems*, Phys. Rev. B, 56, 4056, (1997)

[27] D.C. Hutchings, Private communication

[28] S.D. McDougal, O.P. Kowalski, C.J. Hamilton, F. Camacho, B. Qiu, M. Ke, R.M. De La Rue, A.C. Bryce, and J.H. Marsh, *Monolithic integration via a universal damage enhanced quantum well intermixing technique, IEEE J. Sel. Top. Quantum Electron. 4, 632, (1998)*

[29] K. Zeaiter, T.C. Kleckner, J.S. Aitchison and D.C. Hutchings, *Characterisation and process evolution ofquasi-phase matched semiconductor superlattice waveguide using intermixing*, Nonlinear Guided Waves and their Applications, Paper MD37, OSA (2002).

[30] C. De Angelis, F. Gringoli, M. Midrio, D. Modotto, J. S. Aitchison and G. F. Nalesso, *Conversion efficiency for second harmonic generation in photonic crystals*, J. Opt. Soc. Am. B 18, 348 (2001).

[31] D. Modotto, Private communication

6. SECOND HARMONIC GENERATION IN GaAs/AlAs WAVEGUIDES USING MODAL-PHASE-MATCHING

6.1 Introduction

In previous chapters, a number of methods were presented aiming at overcoming the phase-matching complications in GaAs structures, thus allowing exploitation of the large nonlinear susceptibilities present in this material for second-order frequency conversion processes. These methods included SHG in GaAs/AlAs waveguides by use of birefringence enhancement through selective oxidation, as well as SHG in quasi-phase-matched GaAs waveguide structures with periodic modulation of the nonlinear susceptibility via quantum well intermixing.

Modal-phase-matching (MPM) is a simple alternative solution to the problem of phase velocity synchronism in nonlinear conversion processes and has been studied in polymer waveguides [1-5]. However, it has been of limited interest in inorganic semiconductors because of the poor spatial overlap between the interacting modes. Only recently proper waveguide (M-type) designs have been proposed [6-8] to permit sufficient increase of mode overlap and result in appreciable effective nonlinearities. Since there is no need for oxidation, as is the case with form birefringent waveguides, the modal-phase-matched structures can be combined with a laser diode on the same chip to provide a wholly integrated semiconductor light source based on nonlinear frequency conversion. Such a device could be of interest for a range of applications, for example as a source of entangled photons in quantum optics and quantum cryptography [9, 10].

In this chapter, a short introduction of modal-phase matching schemes is presented, followed by experimental results of femtosecond SHG in an $Al_xGa_{1-x}As$ structure optimised for modal-phase-matching. To our knowledge, this is the first demonstration of nonlinear conversion in GaAs-based waveguides using enhanced mode overlap based on M-type waveguides.

6.2 Modal-phase-matching schemes in semiconductor waveguides

6.2.1 Modal-phase-matching principles: The case study of the slab waveguide

Modal-phase-matching makes use of modal dispersion, which is a unique characteristic of waveguides, to compensate for normal (chromatic) material dispersion and hence phase-match nonlinear interactions [11]. This can be demonstrated through the simple case of the symmetric slab waveguide depicted in Fig. 6.1, consisting of a core of width *w* and index n_g and cladding layers of index n_s. Although a detailed study of the slab waveguide is in fact more complicated, a trivial geometrical optics model is sufficient to yield the dispersion relationships for the various possible modes of propagation. Confinement of light in this kind of waveguides is due to total internal reflection (TIR) in the interfaces between the higher index core and the lower index cladding layers. This is shown in a ray picture in Fig. 6.1, where $\vec{k}_g$ is the "actual" wavevector along the ray path and $\vec{k}$ is the "effective" wavevector along the waveguide propagaton axis *Z*., such that:

$$k = \frac{2\pi n}{\lambda_0} = k_g \sin\theta_i \tag{6-1}$$

where *n* is the effective waveguide refractive index, λ_0 is the free space wavelength and θ_i the angle of ray incidence. The dotted line normal to the ray represents the plane wavefront.

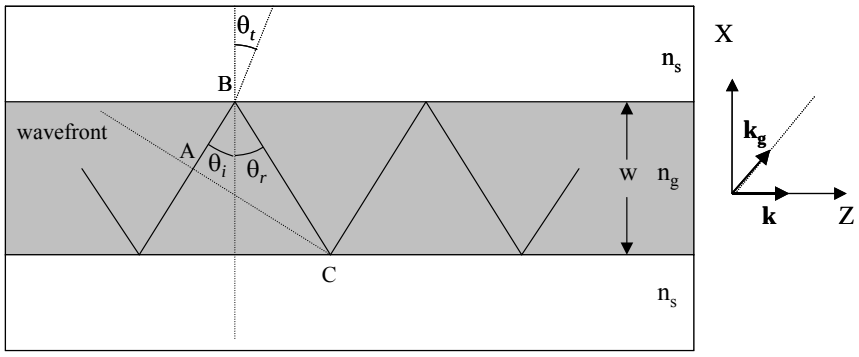

Fig. 6.1 Ray picture shown in a vertical cross-section of a symmetric slab waveguide.

The angles of incidence, reflection and transmission (θ_i, θ_r, and θ_t, respectively) are trivially related by Snell's law:

$$\theta_i = \theta_r \qquad \text{and} \qquad n_g \sin\theta_i = n_s \sin\theta_t$$

Therefore, total internal reflection ($\theta_t > 90^0$) occurs for angles of incidence exceeding a critical value θ^c, such that:

$$\sin\theta_i > \sin\theta^c = \frac{n_s}{n_g} \tag{6-2}$$

In order for the multiple reflected wave depicted in Fig. 6.1 to be coherent, it is evident that the phase difference at points *A* and *C* must be zero or equal to an integer multiple of 2π, which in turn implies that the following phase relation must hold:

$$\Delta\Phi^1 + \Delta\Phi^2 + 2k_g w\cos\theta_i = 2m\pi; \quad m=0,1,2,\ldots \tag{6-3}$$

where $\Delta\Phi^1$ and $\Delta\Phi^2$ are the phase shifts upon reflection at the two interfaces and $2k_g w\cos\theta_i$ is the phase shift contribution due to the extra path length $\overline{ABC}$[1]. The phase shift at the boundaries depends on the input polarisation and is given by the well-known Goos-Hänchen relations, the proof of which can be found elsewhere [12]:

$$\Delta\Phi_{TE} = 2\tan^{-1}\left[\frac{\sqrt{\sin^2\theta_i - (n_s/n_g)^2}}{\cos\theta_i}\right] = 2\tan^{-1}\left[\frac{n^2 - n_s^2}{n_g^2 - n^2}\right]^{1/2}$$

$$\Delta\Phi_{TM} = 2\tan^{-1}\left[\frac{\sqrt{\sin^2\theta_i - (n_s/n_g)^2}}{(n_s/n_g)^2\cos\theta_i}\right] = 2\tan^{-1}\left[\frac{1}{(n_s/n_g)^2}\left(\frac{n^2 - n_s^2}{n_g^2 - n^2}\right)\right]$$

Substituting the above relations into Eq. (6-3), after some rearrangement one can obtain the modal dispersion expression for the symmetric slab waveguide:

$$wk_0 = \left\{2\tan^{-1}\left[\gamma\left(\frac{n^2 - n_s^2}{n_g^2 - n^2}\right)^{1/2}\right] + m\pi\right\}\cdot\left[n_g^2 - n^2\right]^{-1/2} \tag{6-4}$$

where k_0 is the free space wavelength, γ=1 for TE and $(n_g/n_s)^2$ for TM, and *m* is the mode order.

Equation (6-4) suggests that the effective refractive index for the different modes depends on the dimensions of the high index region and takes values between n_g and n_s. A quantitative representation of the modal dispersion profile for the slab waveguide is illustrated in Fig. 6.2 a, where the effective index is shown against the normalised film thickness wk_0 for the first- and second-order TE and TM modes. Note that there is a maximum core width for which the waveguide remains single mode. It

[1] It is easy to see that $\overline{ABC} = 2w\cos\theta_i$

is evident that in the absence of birefringence and assuming normal material dispersion ($n_{TE,TM}(2\omega)>n_{TE,TM}(\omega)$), phase-matching SHG is not possible with use of same order modes. However, the existence of multiple allowed modes with different effective indices permits the realisation of suitably designed structures; where phase-matching of nonlinear processes is possible by use of different order modes. This is illustrated in the indicative Fig. 6.2 b, where a hypothetical phase-matching possibility exists, corresponding to the interception point of the TE_0 curve for the fundamental frequency and the TE_1 curve for the second harmonic.

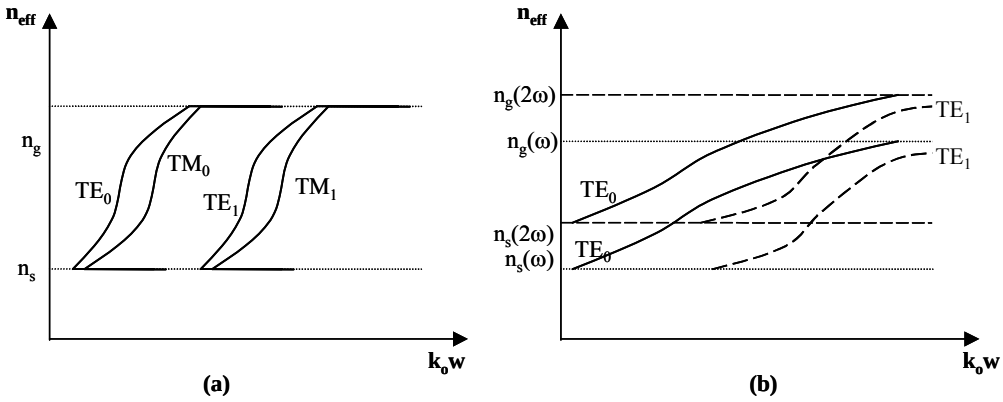

Fig. 5.2 Characteristic modal dispersion curves [11] in slab waveguides: (a) Effective index as a function of the normalised core thickness k_0w and (b) Typical guided-mode dispersion curves indicating phase-matching capability for $TE_0(\omega)\rightarrow TE_1(2\omega)$ process.

Based on the preceding principles of MPM, at least two early reports can be found on SHG in GaAs-based waveguides. In 1971, Anderson and Boyd [13] reported weak phase-matched SHG in a GaAs rectangular waveguide using a CO_2 laser fundamental near ~10 μm. Shortly after, in 1974, van der Ziel *et al* [14] demonstrated SHG in a slab AlGaAs waveguide with a fundamental at 2 μm. A third report by Wagner *et al* [15] involved SHG in ZnTe waveguides. Since then, MPM in semiconductor waveguides has been of limited interest, due to inherent disadvantages associated with this technique resulting from difficulties in combining modes that simultaneously offer phase-matching capability and sufficient overlap. In the next paragraph, issues related to conversion efficiency enhancement by means of overlap increase through design of proper structures are addressed.

6.2.2 M-type waveguides for efficient nonlinear frequency conversion

It has been outlined that it is possible to phase-match a lower-order fundamental mode with a higher-order second harmonic mode, exploiting modal dispersion to offset the natural material dispersion. It was also pointed out that, contrary to birefrigently and quasi-phase-matched guided wave interactions (where modes of the same order are used and the overlap integral can be taken equal to one), MPM in conventional waveguides results in weak mode overlap and thus limited conversion efficiencies. Considerable effort has been devoted to developing waveguide geometries that allow optimisation of the mode overlap. This includes the four-layer structure depicted in Fig. 6.3 a, in which only one of the two core layers is nonlinear. This design, proposed in 1978 by Ito and Inaba [16], avoids negative contribution to the overlap integral from regions where the two fields interact destructively. Although this design clearly exploits only a fraction of the available input power, the increase in mode overlap was such that the authors reported an overall efficiency improvement by a factor of 40.

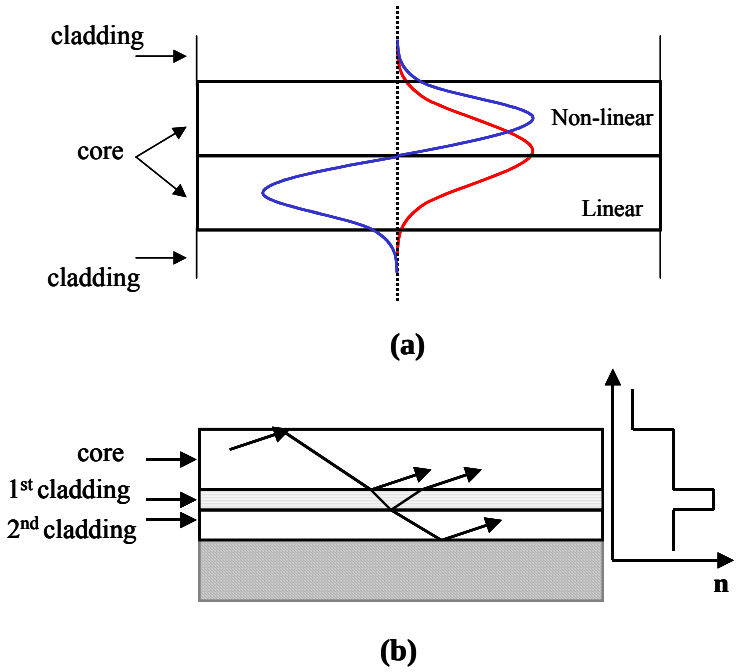

Fig 6.3 Proposed geometries for enhancement of mode overlap in directly phase-matched waveguides. (a) A two-layered core structure consisting of a linear and a nonlinear section, in which the area of destructive interference between the fundamental (red line) and second harmonic (blue line) is not active. (b) ARROW–type waveguide structure, offering novel phase-matching possibilities due to the design-dependent modal dispersion and field intensity distribution. These figures are based on ref. [11] and [17].

A second approach to increasing mode overlap relies on the employment of anti-resonant reflecting optical waveguides (ARROW) [17-20]. While conventional waveguides depend on total internal reflection (TIR) to confine the wave in a high index core layer, ARROWs generally consist of a system of cladding layers designed to form Fabry-Perot cavities which, operating at anti-resonance (minimum transmission), confine the wave in a low index core. The ARROW operational characteristics are illustrated in the typical structure of Fig. 6.3 b. This geometry comprises a low index core surrounded by air on one side, and an interference cladding on the other. In turn, the interference cladding consists of a thin high index film (first cladding) and a second cladding layer, which is usually made of the same material as the core. In this specific design, light experiences standard TIR in the upper core-air boundary. On the other side, the thin high index film acquires the transmission characteristics of a Fabry-Perot resonator, so that high reflection is attainable at the anti-resonant wavelengths of this Fabry-Perot interferometer. Similarly, the lower cladding forms a second cavity in series, which (with proper design) may also operate in anti-resonance to enhance the overall transmission. Note that, in accordance with the Fabry-Perot transmission characteristics, the critical parameter for achieving low-loss guiding at a given wavelength is the thickness of the first cladding layer and the refractive indices[1] of the different layers. Since the same parameters also determine the waveguide dispersion as well as the field profile, ARROW-type waveguides offer unique flexibility in designing directly phase-matched structures with optimised mode overlap.

A modified version of an ARROW waveguide, of special relevance to this work, is the M-type structure shown in Fig. 6.4, acquiring its name from the characteristic M-shaped refractive index profile. The core index is now slightly higher than that of the outer claddings, while the thickness of the inner claddings (often referred to as reflectors) is not necessarily anti-resonant. In other words, depending on the wavelength and the reflector thickness, M-type waveguides can operate either as: (a) an ARROW type waveguides, with the reflector layers used as the interference claddings, or (b) a TIR coupler, formed by a higher index “super-core” (consisting of the inner core and the reflectors) and two lower index claddings.

[1] Recall that transmission as a function of wavelength in a Fabry-Perot interferometer has peaks that are separated by $\Delta\lambda=\lambda^2/2nd$, where d is the mirror separation. Moreover, the width of the peaks becomes narrower as the reflectivity increases.

M-type waveguides have attracted attention for phase-matching purposes, because it is accepted that proper "super-core" design can provide high confinement of the wave, while the symmetry of the structure yields a good overlap between the interacting mode fields. From an alternative perspective, the coexistence of TIR and ARROW modes for a specific design and for different wavelengths yields a modulation in the dispersion profile for a set propagation mode in which both steep parts (TIR) and flat areas (ARROW) are present, resulting in the appearance of a greater number of phase-matching possibilities compared to the case of slab structures (*see* Fig. 6.2).

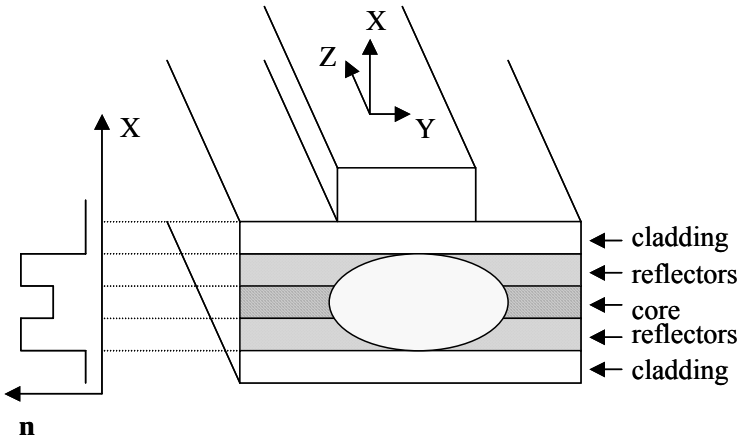

Fig. 6.4 Schematic of an M-type waveguide.

The first theoretical study on the use of M-type waveguides for optimised MPM was carried out by Chowdhury and McCaughan [6] and considered $LiNbO_3$ waveguides. The authors predicted conversion efficiency for the proposed structure exceeding 2.5 % of the efficiency corresponding to QPM waveguides in the same material. Their design was based on TIR guiding. Following this initial study, Oster and Fouckhardt extended the idea to AlGaAs waveguides [7,8]. They showed that several directly phase-matchable geometries exist, including interactions that exploit TIR, ARROW, as well as mixed TIR (for ω) and ARROW (for 2ω) guiding. Their numerical results indicated that in fact optimised mode overlap is attainable when the structure is operated in a TIR fashion. Although these theoretical studies revealed the potential of M-type waveguides for nonlinear frequency conversion, such structures have only been previously used for demonstration of third-order-mode optically pumped semiconductor lasers [9, 10]. In the remainder of this chapter, results are presented from what it is to our knowledge the first experimental demonstration of SHG in optimised M-type modal-phase-matched GaAs/AlGaAs waveguides.

6.3 Optical experiment

6.3.1 Sample details

The sample was designed and fabricated by collaborators[1] at Thomson CSF. It was grown on a semi-insulating GaAs substrate by a MBE machine. The epitaxial structure used was 1000 nm $Al_{0.98}Ga_{0.02}As$ / 130 nm $Al_{0.25}Ga_{0.75}As$ / 260 nm $Al_{0.5}Ga_{0.5}As$ / 130 nm $Al_{0.25}Ga_{0.75}As$ / 1000 nm $Al_{0.98}Ga_{0.02}As$ / 30 nm GaAs. Optical ridges were etched chemically in order to provide two-dimensional confinement. Ridge width varied from 3 to 5 μm and the waveguide was initially 3 mm in length.

This geometry is an M-type waveguide, the refractive index profile of which is shown in Fig. 6.5 (recall that the refractive index of $Al_xGa_{1-x}As$, as well as the nonlinearity, decreases with increasing Al concentration). Following simulation results that indicated stronger mode overlap for TIR modes, waveguiding in the structure was based on standard TIR rather than ARROW modes; that is, light is confined in the central, high-index super-core ($Al_{0.25}Ga_{0.75}As$ - $Al_{0.5}Ga_{0.5}As$ - $Al_{0.25}Ga_{0.75}As$), and bounded by the low-index $Al_{0.98}Ga_{0.02}As$ claddings. The structure is expected to provide maximum overlap between the TE_2 (third-order) mode at the second harmonic frequency and mixed TE_O / TM_0 modes at the fundamental frequency (type II interaction). The simulation results with respect to the intensity distribution for these propagation modes are also depicted in Fig. 6.5. In fact, the anticipated overlap integral in this optimised structure is expected to be lower, by a factor of >5, than in birefringent waveguides [21]. Type I phase-matching ($TE_0(\omega) \rightarrow TM_2(2\omega)$) is also allowed by the selection rules of GaAs second-order susceptibility tensor in the case of a <1,0,0> growth and a waveguide orientated along the <0,1,1> axis, but lower mode overlap and hence efficiencies are expected.

The phase-matching capabilities in this waveguide are illustrated in Fig. 6.6, where the effective refractive index of the structure is plotted as a function of wavelength for the first three order modes. These calculations, carried out by collaborators using suitable transfer matrix algorithms [22], predict type II phase-matching for a fundamental wavelength near 1.5 μm, as well as type I phase-matching at slightly shorter wavelengths.

[1] A. De Rossi, M. Calligaro, V. Ortiz and V. Berger

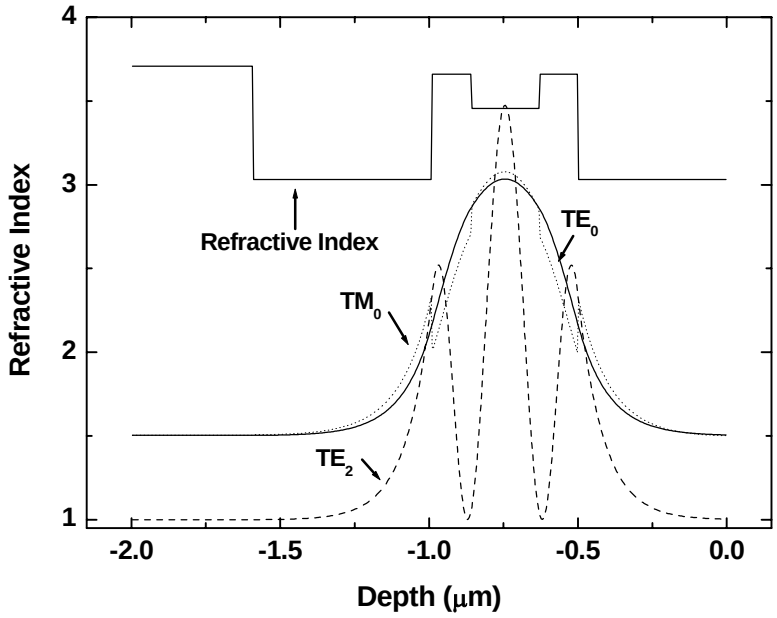

Fig. 6.5 Waveguide refractive index (upper solid) and intensity distribution $|\mathbf{E}^2|$ for: (a) the TE_0 (solid) and TM_0 (dotted) mode at the fundamental wavelength (1550 nm) and (b) the TE_2 (dashed) mode at the SHG wavelength (775 nm).

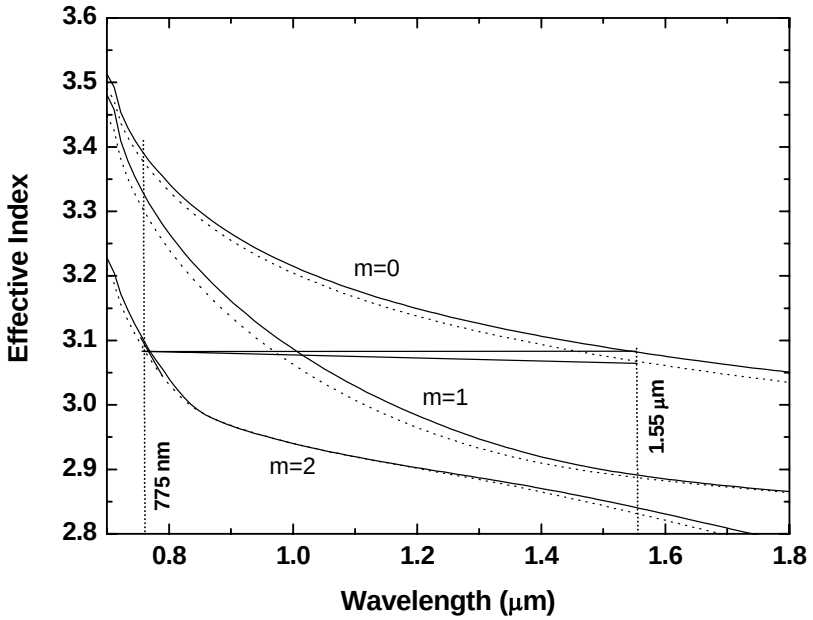

Fig. 6.6 Dispersion of the effective indices of the first three modes illustrating the principle of phase-matching in this structure: chromatic dispersion is compensated by the waveguide dispersion. Solid lines indicate TE polarisation and dotted lines TM polarisation. The waveguide geometry is such that phase-matching is possible near 1.55 μm. Both Figs. 6.5 and 6.6 were provided by A. De Rossi of Thomson CSF (THALES).

6.3.2 Experimental set-up

The experimental apparatus is illustrated in Fig. 6.7. The OPO pump source had the same operational characteristics as described in section 5.4.1: the system delivered near-transform-limited signal pulses of ~250 fs pulse duration and ~10 nm spectral FWHM, tuneable from ~1.35 to ~1.57 μm, with average power levels of more than 50 mW attainable throughout this band. A set of optics and filters were used to allow control over the input polarisation and power. The fundamental wavelength being near 1.5 μm allowed the use of a thermal power meter and a spectrometer for input beam measurements. The standard end-fire coupling was used comprising a x40 (input) and a x20 (output) microscope objective. A peltier cooler was added below the sample holder to vary the temperature, while a thermocouple was used to monitor the relative temperature of the sample. The waveguide output was then passed through a cubic polarising beam splitter centred at 750 nm to separate the TE and TM components. A semiconductor head power meter with a sensitivity band from 400 nm to 1000 nm was used to measure the SHG power. Finally, the output light was coupled into an IR spectrum analyser by use of a 1-meter long optical fibre, allowing for the resolution of the SHG and transmitted fundamental spectra.

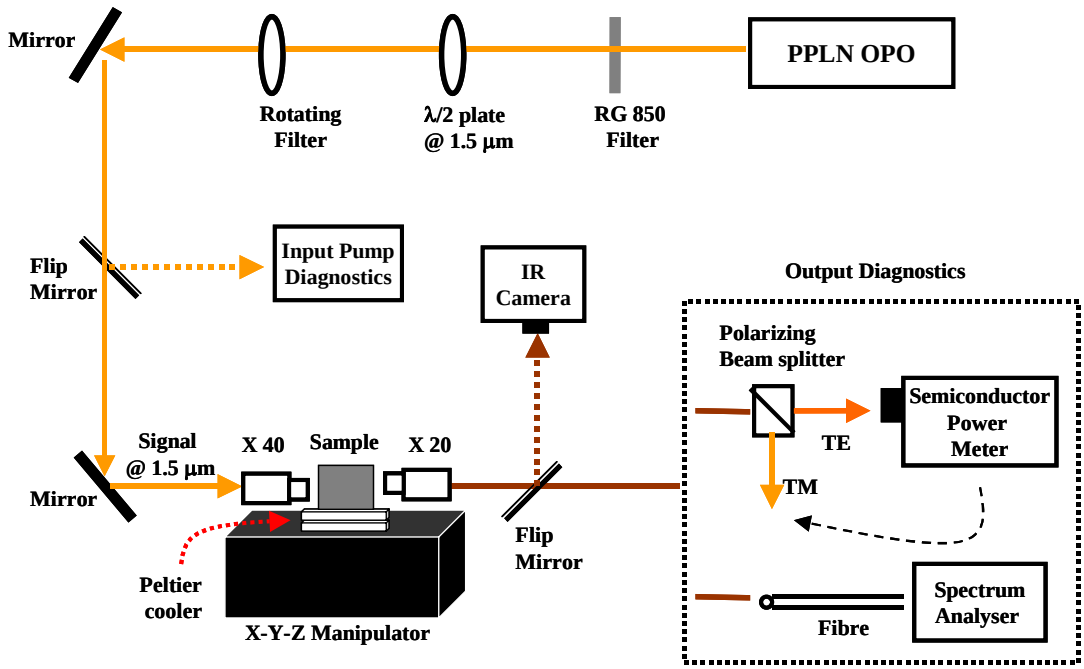

Fig. 6.7 Experimental apparatus.

6.3.3 Results and discussion

A number of samples of same design were tested and here results are only presented for the best waveguides. A clear growth of second harmonic signal was observed for appropriate tuning of the fundamental wavelength for both TE and mixed TE/TM input polarisations. For purely TM input the output power reduced to noise levels. At first, the selection rules were investigated and it was established that the input-output signal polarisations satisfied the type I and II phase-matching conditions: TE(ω)→TM(2ω) and TE(ω)+TM(ω)→TE(2ω).

With the aid of the IR spectrum analyser, the generated second harmonic as well as transmitted fundamental spectra were recorded. A selection of such spectra is shown in Fig. 6.8 for both types of interaction. It is evident that type I process takes place at ~ 1505 nm and type II at ~1540 nm. Note that as the input is tuned within the acceptance bandwidth, the second harmonic signal remains spectrally locked (only the strength of the nonlinear process changes), indicating that the interaction is indeed phase-matched. The SHG spectra present a FWHM spectral width of ~0.5 nm and ~1 nm for type I and type II geometries, respectively. As has been discussed previously, the pump acceptance bandwidth for SHG is twice the second harmonic linewidth. Combined with a fundamental spectral FWHM of ~10 nm, this shows that only a fraction of the input bandwidth is utilised in the conversion process. This effect can be viewed in the temporal domain as only one part of the pump wave packet having phase velocity that can be phase-matched at the second harmonic. When the conversion efficiency is high enough, the pump experiences a partial depletion reminiscent of spectral hole burning. This has indeed been observed in birefringent waveguides (see chapter 4). Under the same experimental conditions and with use of modal-phase-matched samples, only some incomplete depletion of the fundamental for type II process was observed, thus indicating lower conversion efficiency. At lower power levels (~200 nW) and for detuned pump wavelength, a non-phase-matched signal was detected. Spectra taken for this non-phase-matched signal are illustrated in Fig. 6.9. Note that for this non-phase-matched SHG the spectral width of the generated signal is ~5 nm (that is, half that of the pump spectral width), while a shift in the input wavelength results in a proportional shift in SH wavelength. The contrast in behaviour between the generated signals shown in figures 6.8 and 6.9 provides strong evidence that phase-matched SHG was indeed achieved.

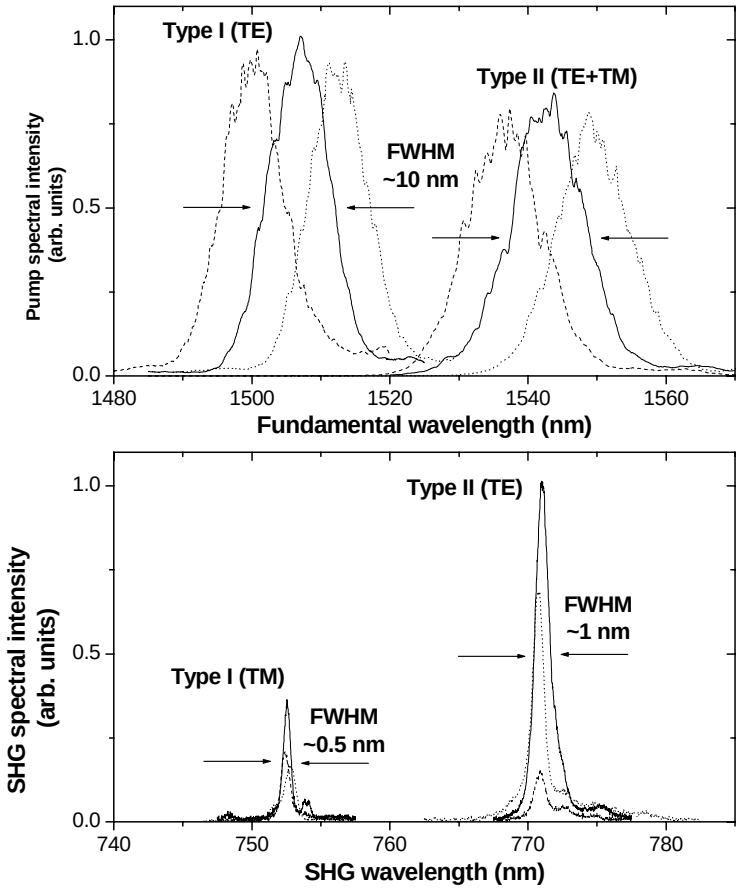

Fig. 6.8 Typical transmitted fundamental (top) for type I and II interactions, and the corresponding SHG spectra (bottom). The vertical axis indicates the relative strength of each process.

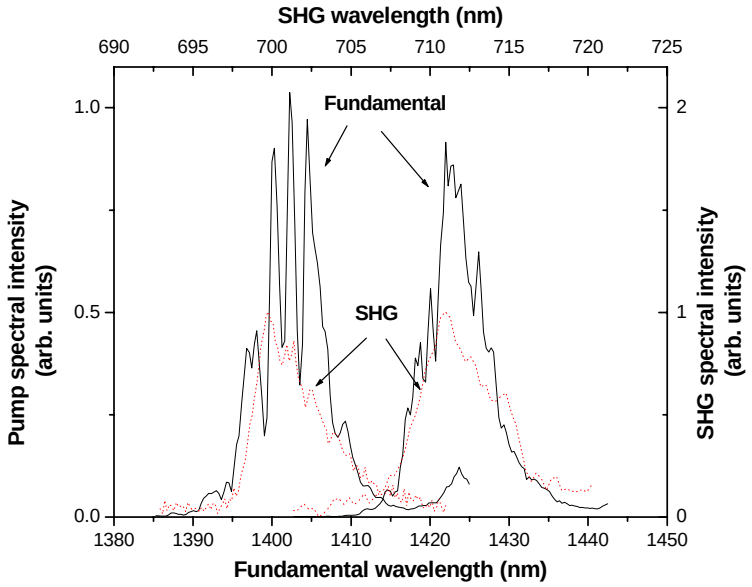

Fig. 6.9 Transmitted fundamental (in black) and SHG (in red) spectra for non-phase matched process. The strong modulation in these spectra originates from water vapour absorption lines.

Further evidence of phase-matching was obtained by measuring the generated SHG power as a function of the input power. The expected quadratic dependence was confirmed, with typical values of best fit to the slope on a log-log plot ranging from 1.9 to 2.1. A representative set of such measurements, for the same waveguide and for both type I and II interactions, is shown in Fig. 6.10. Strong saturation of gain was not observed, in agreement with the observed weak depletion of the pump, although a small reduction in the slope could be observed for a number of waveguides and average input power levels exceeding ~30 mW. The generated SH power was also measured against the central wavelength of the fundamental spectrum for fixed input power, as shown in Fig. 6.11. A clear peak was observed at ~1.505 μm (~1.540 μm) for type I (II) interaction, while the FWHM of these wavelength tuning curves is ~11 nm, that is comparable to the input spectral bandwidth.

Second harmonic spectra were also obtained after intentionally translating the waveguide in the direction normal to the input beam. Typical results are presented in Fig. 6.12, where the SHG spectrum corresponding to optimal alignment (curve a) is compared to spectra collected for ~ 1 mm of horizontal misalignment to either side (curves b and c). It can be seen that independent of the direction of translation, a second peak appears at longer wavelengths. This complementary peak is comparable in strength to the main SHG peak, and therefore should be attributed to phase-matched SHG process involving higher-order modes. It has not yet been possible to identify the exact interaction that yields this signal. Interestingly, a weak secondary peak to the longer wavelength side also seems to appear in the wavelength tuning curve shown in Fig. 6.11. The two observations are believed to be related. This has to be viewed in combination with the fact that tuning the OPO wavelength to obtain the data of Fig. 6.11 is indeed expected to result in a slight change in the angle of the signal beam and hence an effective displacement of the waveguide with respect to the pump beam. In fact, accounting for a ~1 m distance between the pump source and the coupling rig, a change in the angle of the OPO output as small as $\sim 10^{-2}$ degrees is enough to shift the pump beam by ~1 mm when it reaches the waveguide.

Since the refractive index of GaAs is temperature dependent [23], it is anticipated that the phase-matching wavelength varies with varying temperature. Relative studies were carried out and results are presented in Figs. 6.13 and 6.14. Here the sample

temperature was varied from ~ 10 to ~ 150^0 C and SHG spectra were collected for both types of interaction in steps of ~5 degrees. Fig. 6.13 shows a selection of recorded spectra, while Fig. 6.14 depicts the overall tuning of SHG wavelength in this temperature range. It can be seen that a nearly-linear fine tuning of >10 nm is attainable with ~ 140^0 C increase in temperature, resulting in a temperature tuning rate of $d\lambda/dT$ ~0.079 nm / ^{0} C. In fact, this value is in agreement with theoretical predictions carried out by collaborators at Thomson CSF [21] with an accuracy to the third decimal.

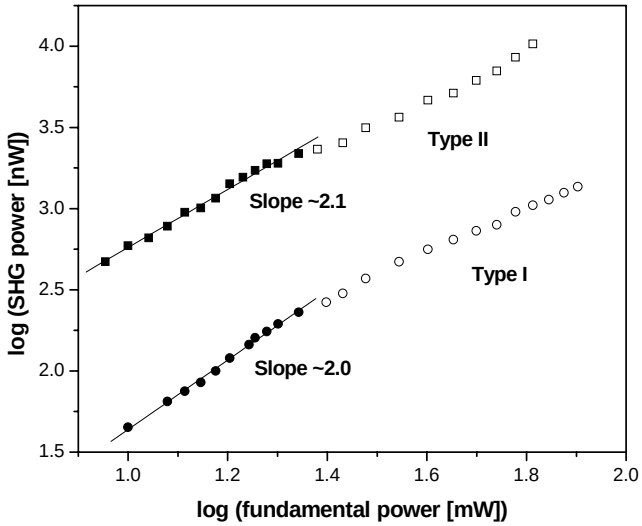

Fig. 6.10 Second harmonic output average power as a function of the fundamental input average power on a log-log scale.

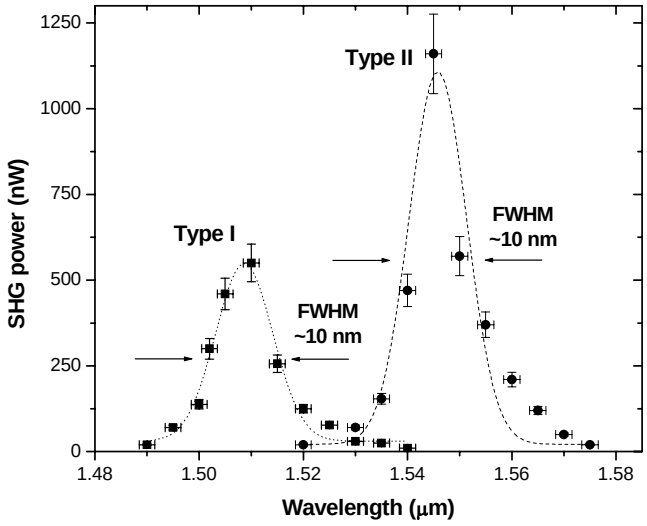

Fig. 6.11 Second harmonic average power as a function of the fundamental centre wavelength, for a constant input power (~20 mW).

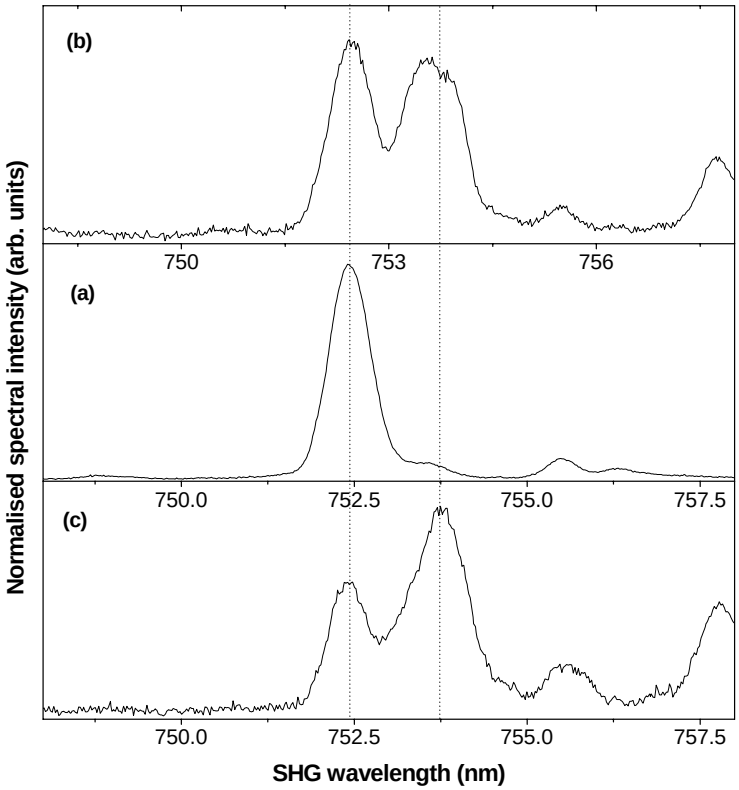

Fig. 6.12 SHG spectra for (a) optimised alignment, and (b), (c) a ~1 mm lateral displacement of the waveguide with respect to the input beam axis for a type I process.

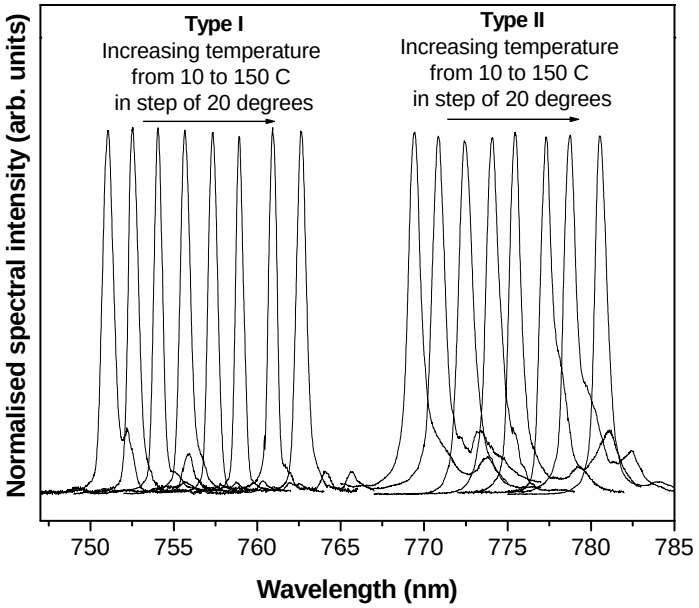

Fig. 6.13 Selected SHG spectra as a function of the temperature.

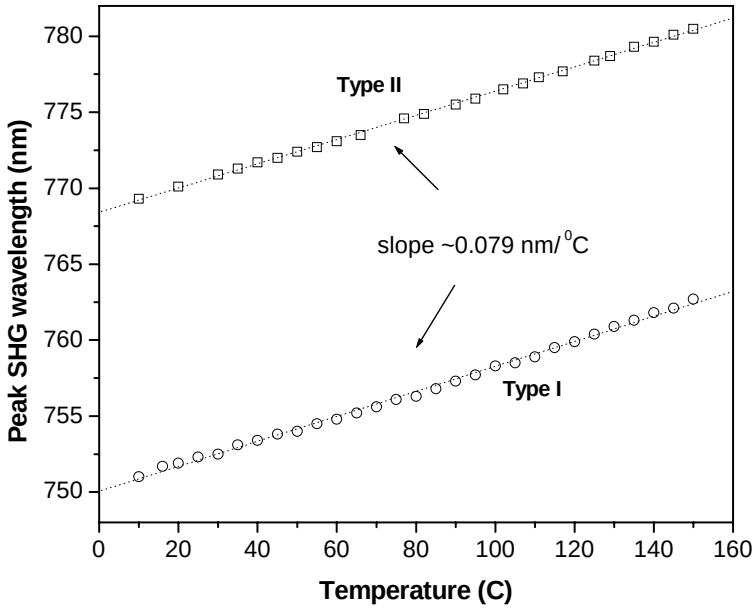

Fig. 6.14 Temperature tuning for type I and II interactions, in the range ~10 to ~150^0 C.

Maximum SHG power was measured after cleaving the sample to 1.5 mm, that is half its initial length. For type I interaction, up to ~ 2.6 μW of SHG power were obtained after the output objective for ~ 80 mW of fundamental power before the input microscope objective. For the more efficient (in accordance with the waveguide design) type II interaction, the maximum detectable SHG power was ~ 10.3 μW for ~65 mW of input. That only SHG power was measured in the output was ensured by use of appropriate wavelength filters. These values represent an increase of more than ~ 60 % compared to the available power for the initial 3 mm long waveguides. This effect, also observed with birefringent waveguides, is due to the fact that with femtosecond pulses the interaction length is limited by group velocity mismatch (GVD) to values much shorter than the physical length of the sample. Therefore, a longer device tends to have a lower yield because of propagation loss at the second harmonic. As discussed in chapter 4, this provides an indirect means of estimating the SHG propagation loss, which resembles the cut-back method. Calculating the GVD in the M-type waveguides is in fact not trivial, since the model used to obtain dispersion curves provides only numerical results. Adopting the calculations for bulk GaAs, however, an actual interaction length of ~ 100 μm should be expected. With use of the quoted values, an SHG propagation loss greater that ~15 dB/cm can be estimated.

Note that loss measurements using the scattering method, and presented in the following chapter, indicated a loss of ~ 10 dB/cm for the fundamental wavelength.

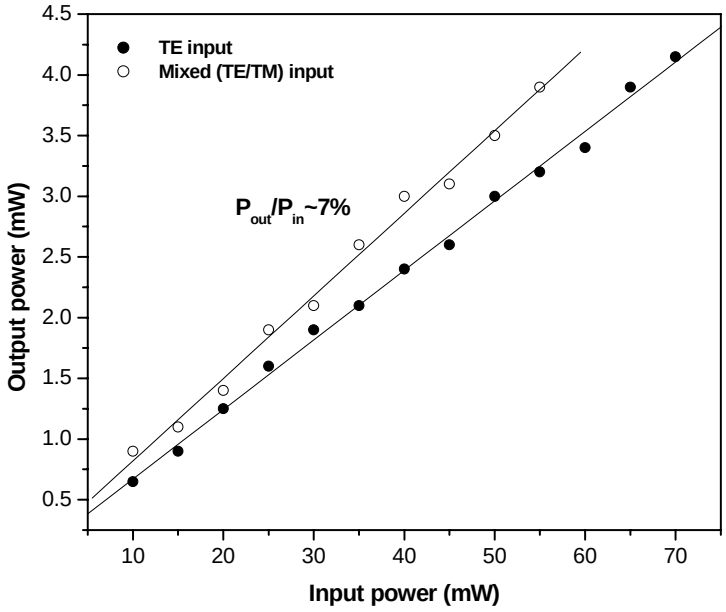

Fig. 6.15 Output power versus input power measurements at the fundamental wavelength, indicating a ~7 % overall transmission.

The maximum external efficiency of the present device, defined as the SHG power collected after the output objective divided by the launched power before the input objective, is ~0.015% for type II geometry. To estimate the internal efficiency (trivially defined as the coupled fundamental power divided by the generated SHG power in the waveguide), one has to account for the input objective loss, the input facet reflectivity, and the mode-matching factor. Experimental measurements presented in Fig. 6. 15 indicated an overall transmission for the pump beam of ~ 7%. Combined with an estimated 50% collection efficiency for the zero-order mode and a measured transmission of ~70% through 1.5 mm of the waveguide (i.e., 10 dB/cm loss), this suggests that the input coupling efficiency was smaller that 30%. It is worth pointing that this input coupling efficiency is significantly higher than in birefringent waveguides. Furthermore, the collection efficiency for the SHG is estimated to be of the order of 30%, that is slightly lower than in birefringent waveguides. Differences between modal and birefringent waveguides in fundamental input coupling and SHG output collection efficiencies arise from a) the higher numerical aperture of the modal waveguides, and b) the use of third-order modes with modal waveguides, resulting in an increased modal reflectivity of ~50% (compared to 30% reflectivity for zero-order modes) according to the model of reference [24].

Therefore, it is estimated that out of the ~65 mW of available input power only less than ~20 mW is actually coupled into the waveguide, while ~31 μW of SHG power is generated inside the waveguide under type II process. This implies that the internal efficiency was in fact greater than 0.15%. That the quoted efficiencies are not over-estimated is ensured, since the high SHG transmission losses have not been accounted for, along with the fact that only a part of the input spectrum contributes to the process.

Evaluation of the normalised internal efficiency, as defined in chapter 4, can be carried out by assuming an interaction length of ~ 100 μm, following the standard GVD calculations for bulk GaAs. Accounting for the duty cycle of the pump source, this results in a normalised internal efficiency for type II process of ~2 $\%W^{-1}cm^{-2}$. A direct comparison with the efficiency of the first-order QPM waveguides shows that the efficiency of the present scheme is about two times higher. However, it is approximately two orders of magnitude lower than the efficiency of the birefringent waveguides. The main difference between birefringent waveguides operating on fundamental modes and modal waveguides is the overlap integral, which yields a difference in efficiency by a factor of ~20. The additional factor of 5 could be explained by the poor confinement of the SH wave. Therefore, it is believed that further improvement of modal waveguides is possible. A more comprehensive discussion on the relative efficiencies achieved with birefringent, first/third-order QPM and modal-phase-matching is attempted in chapter 8.

6.4 Conclusions

It has been explained that the modal dispersion, which is a unique feature of waveguides, can be used to phase-match nonlinear processes. It was also discussed that in the case of modal phase-matching, where generally the interacting fields propagate in different-order modes, overlap becomes a critical and (in the case of conventional waveguides) limiting parameter. Following recent theoretical research that revealed the potential of M-type waveguides for achieving optimised modal phase-matching, a properly designed M-type structure was fabricated and tested.

Second-harmonic-generation in AlGaAs waveguides using modal phase-matching was demonstrated. Both type-I and II SHG were observed for fundamental wavelengths near 1.55 μm, using femtosecond pulses. Fine SHG tuning was available through temperature control, with a corresponding tuning rate of ~ 0.08 nm/^{0}C. Practical SHG powers up to 10 μW were obtained with an input power of ~65 mW for the most efficient type II interaction. For the present device, this translates into a maximum overall device efficiency of ~0.015 %, corresponding to an internal efficiency greater that 0.15 %. Furthermore, accounting for a GVD-limited interaction length of ~100 μm, an internal normalised efficiency of ~2 %W^{-1}cm^{-2} was calculated.

References

[1] K. Clays, J.S. Schildkraut, and D. Williams, *Phase-mathced second harmonic generation in a four-layered polymeric waveguide*, J. Opt. Soc. Am. B 11, 655, (1994)

[2] T.C Kowalczyk, K.D. Singer, and P.A. Cahill, *Anomalous dispersion phase-matched second harmonic generation in a polymer waveguide*, Opt. Lett. 20, 2273, (1995)

[3] M. Jäger, G.I. Stegeman, G.R. Mohlmann, M.C. Flipse, and M.B.J. Diemer, *Second harmonic generation in polymeric channel waveguides using modal dispersion*, Electron. Lett. 32, 2009, (1996)

[4] M. Jäger, G.I. Stegeman, M.C. Flipse, and M.B.J. Diemer and G. Mohlmann, *Modal dispersion phase matching over 7 mm length in overdamped polymeric channel waveguides*, Appl. Phys. Lett. 69, 4139, (1996)

[5] W. Wirges, S. Yilmaz, W. Brinker, S. Bauer-Gogonea, S. Bauer,] M. Jäger, G.I. Stegeman, M. Ahlheim, M. Stähelin, B. Zysset, F. Lehr, M. Diemeer, and M.C. Flipse, *Polymer waveguides with optimised overlap integral for modal dispersion phase matching*, Appl. Phys. Lett. 70, 3347, (1997)

[6] A. Chowdhury, and L. McCaughan, *Continuously phase-matched M-waveguides for second order nonlinear upconversion*, IEEE Photon. Tech. Lett. 12, 486, (2000)

[7] B. Oster, and H. Fouckhardt, *Variations of optical M-waveguides for direct phase matching in AlGaAs*, IEEE Photon. Tech. Lett. 13, 672, (2001)

[8] B. Oster, and H. Fouckhardt, *M-waveguide structures for direct phase matching in AlGaAs*, Appl. Phys. Lett. 73, 535, (2001)

[9] A. De Rossi, N. Semaltianos, E. Chiralis, B. Vinter, V. Ortiz, and V. Berger, *Third order mode optically pumped semiconductor laser*, Appl. Phys. Lett. 80, 4690, (2002)

[10] N. Semaltianos, *Power threshold and optical gain of a third order mode optically pumped AlGaAs laser*, J. Appl. Phys. 91, 949, (2002)

[11] G. Stegeman, and R.H. Stolen, *Waveguides and fibers for nonlinear optics*, J. Opt. Soc. Am. B 6, 652, (1989)

[12] M. Born, and E. Wolf, *Principles of optics*, Cambridge University Press (7^{th} Ed.), (1999)

[13] D. B. Anderson, and J. T. Boyd, *Wideband CO_2 laser second harmonic generation phase matched in GaAs thin film waveguides*, Appl. Phys. Lett. 19, 266, (1971)

[14] J. P. van der Ziel, R.C. Miller, R.A. Logan, W.A. Nordland, and R.M. Mikilyak, *Phase matched second harmonic generation in GaAs optical waveguides by focused laser beams*, Appl. Phys. Lett. 25, 238, (1974)

[15] H.P. Wagner, S. Wittmann, H. Schmitzer, and H. Stanzl, *Phase matched second harmonic generation using thin film ZnTe optical waveguides*, Appl. Phys. Lett. 77, 3637, (1995)

[16] H. Ito, and H. Inaba, *Efficient phase matched second harmonic generation method in four layered optical waveguide structure*, Opt. Lett. 2, 139, (1978)

[17] M. A. Duguay, Y. Kohubun, T. L. Koch, and L. Pfeiffer, *Antiresonant reflecting optical waveguides in SiO_2 – Si multiplayer structures*, Appl. Phys. Lett. 49, 13, (1986)

[18] L. J. Mawst, D. Botez, C. Zmudzinski, and C. Tu, *Design optimization of ARROW-type diode laser*, IEEE Photon. Tech. Lett. 4, 1204, (1992)

[19] Y. Kokubun, T, Baba, T. Sasaki, and K. Iga, *Low-loss antiresonant reflecting optical waveguide on Si substrate in visible wavelength region*, Electron. Lett. 22, 892, (1986)

[20] M. Mann, U. Trutschel, C. Wachter, L. Leine, and F. Lederer, *Directional coupler based on an antiresonant reflecting optical waveguide*, Opt. Lett. 16, 805, (1991)

[21] A. DeRossi, private communication

[22] P. Yeh, *Optical waves in layered media*, Wiley Publications, New York, (1988)

[23] A. McCaulley, V. M. Donnelly, M. Vernon, and I. Taha, *Temperature dependence of the near-infrared refractive index of Silicon, Gallium Arsenide and Indium Phosphide*, Phys. Rev. Lett. B 49, 7408, (1994)

[24] C. M. Herzinger, C.C. Lu, A. De Temple, *The semiconductor facet reflectivity problem*, IEEE J. Quant. Electron. 29, 2273, (1993)

7. OPTICAL LOSS ANALYSIS IN SEMICONDUCTOR WAVEGUIDES

7.1 Introduction

Measurement of optical loss represents a vital component in the assessment of nonlinear waveguides. Accurate knowledge of this parameter is particularly important in the performance evaluation and implementation of resonant devices, most notably integrated optical parametric oscillators, where the magnitude of loss can have a dramatic impact on the oscillation threshold. In single-pass devices, such as nonlinear frequency shifters, wavelength mixers, and harmonic generators, optical loss is also vitally important since it sets an upper limit to the maximum attainable conversion efficiency.

Unlike in their organic and inorganic counterparts, losses in semiconductor nonlinear waveguides are more difficult to characterize due to the inaccurate knowledge of effective refractive indices and facet reflectivities. Over the past few years several techniques including the cutback method [1], prism coupling [2,3], photo-thermal deflection [4], Fabry-Perot (FP) interference method [5-8], and scattering technique [9], [10-14] have been employed for the evaluation of loss. Many of these techniques are not universally appealing due either to their complexity or destructive nature. The FP interference technique has proved to be the most favourable and successful approach for evaluation of losses below 1 dB/cm. However, even though the technique is simple, robust, and non-destructive, it has a number of drawbacks including stringent requirements for frequency stability of the optical source, accurate knowledge of facet reflectivities and precision in the waveguide facet parallelism. On the other hand, scattering technique is uncomplicated and does not suffer from restrictions with regard to the optical source. This makes the femtosecond scattering technique a unique tool of loss analysis for nonlinear frequency conversion as well as a variety of other applications for which ultrashort pulses are commonly used.

In this chapter, the scattering technique is demonstrated for the first time using a femtosecond tunable OPO.

7.2 Development of a femtosecond scattering technique for transmission loss measurements

7.2.1 Operating principles and experimental set-up

Three mechanisms are primarily responsible for waveguide attenuation, namely linear absorption, Rayleigh scattering and nonlinear (multi-photon) absorption. The former, related to inter- and intra-band transitions, is relatively small within the transparency range of the structure. Rayleigh scattering at interfaces and waveguide imperfections is the dominant loss factor and scales with the inverse of the fourth power of wavelength [15-18]. Finally, due to large peak powers of the femtosecond pulses, the presence of nonlinear two-photon absorption (TPA), in particular at wavelengths close to half-band-gap (below 1.7 μm), should be addressed.

The basic principle behind the scattering method for measuring optical transmission loss in waveguides is based on the fact that the intensity of the light scattered normal to the waveguide at a given point is proportional to the intensity of the light inside the waveguide at that point. The overall loss coefficient (accounting for all loss processes) can then be determined by mapping the decay of scattered light intensity along the propagation length of the guide. This decay follows an exponential form according to:

$$I_L = I_0 e^{-\alpha L} \tag{7-1}$$

where I_L is the scattered intensity after a propagation length L through the waveguide, I_0 is the initial intensity at the start of the path, and α (in cm^{-1}) is the overall loss coefficient to be determined. The presence of any defects and inhomogeneities in the propagation path would only affect the uniformity of the exponential decay. The above equation can be re-written in the form:

$$\ln(I_L) = \ln(I_0) - \alpha L$$

The loss coefficient, α, can therefore be readily calculated as the linear slope of the naperian logarithm of the scattered intensity plotted against the propagation length. Evidently, the loss coefficient translates into a loss per unit length given by:

$$\frac{I_L}{I_0 \cdot L} = \frac{e^{-\alpha L}}{L} (\%cm^{-1})$$

$$\frac{10}{L} \cdot \log[-\frac{I_L}{I_0}] = \alpha \cdot \log(e)(dBcm^{-1})$$

The schematic of experimental set up is shown in figure 7.1. The optical source was the OPO described in detail in Chap. 3. The OPO provided more than 50 mW of signal and idler pulses with duration of ~250 and ~200 fs, respectively, at ~90 MHz repetition rate, tunable over an aggregate range of ~1.30-1.58 μm (signal) and ~1.8-2.1 μm (idler). A half-wave-plate was used to control input polarisation and a flipper mirror to direct the input beam into power and spectral diagnostics. An end-fire coupling rig was used for mounting the semiconductor waveguide samples. The input pulses from the OPO were focused into the waveguide using a 40X microscope objective and the transmitted pulses were collected using a second 20X microscope objective. An infrared camera was used for optimizing the coupled light into the waveguide. The scattered light intensity out of the plane of the guide was monitored using an imaging system comprising a microscope, an IR camera, a frame grabber card and a computer to analyze the data. To increase the resolution, a mask was inserted above the sample to block the strong scattering at the input and output facets, as well as any residual reflected light from the top surface of the sample in the lateral directions.

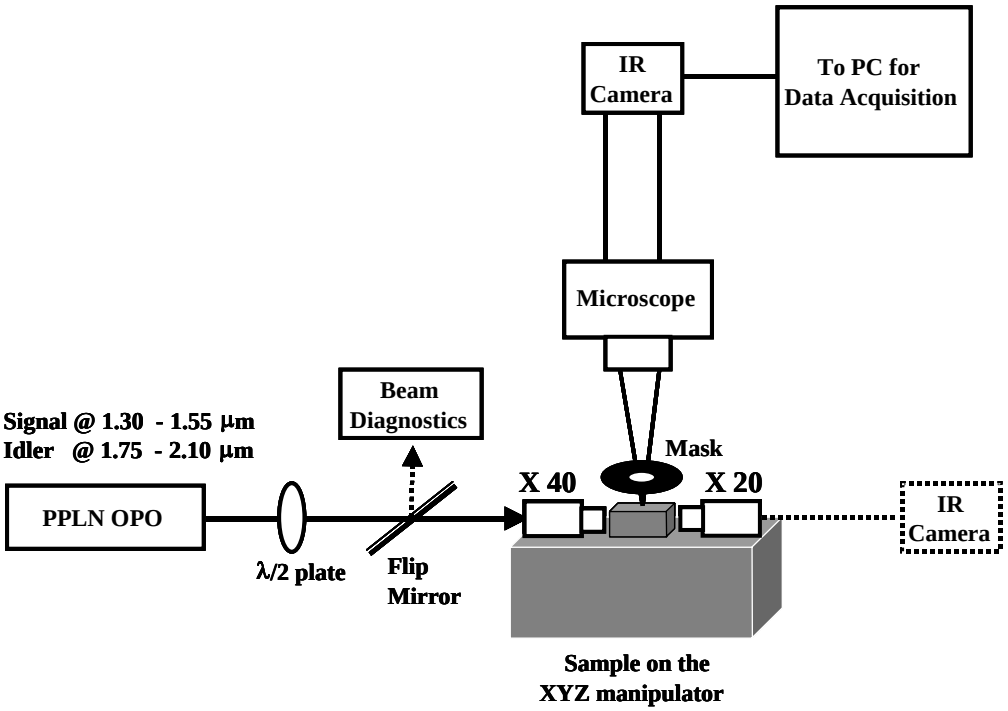

Fig. 7.1 Experimental set-up.

7.2.2 Results and discussion

The set-up was routinely used for loss measurements in a variety of samples. Here, a selection of results is presented mainly for 3.5-mm-long oxidised waveguides identical to those used for the SHG experiment discussed in Chapter 4. Unless otherwise specified, measurements were carried out for TE input polarisation.

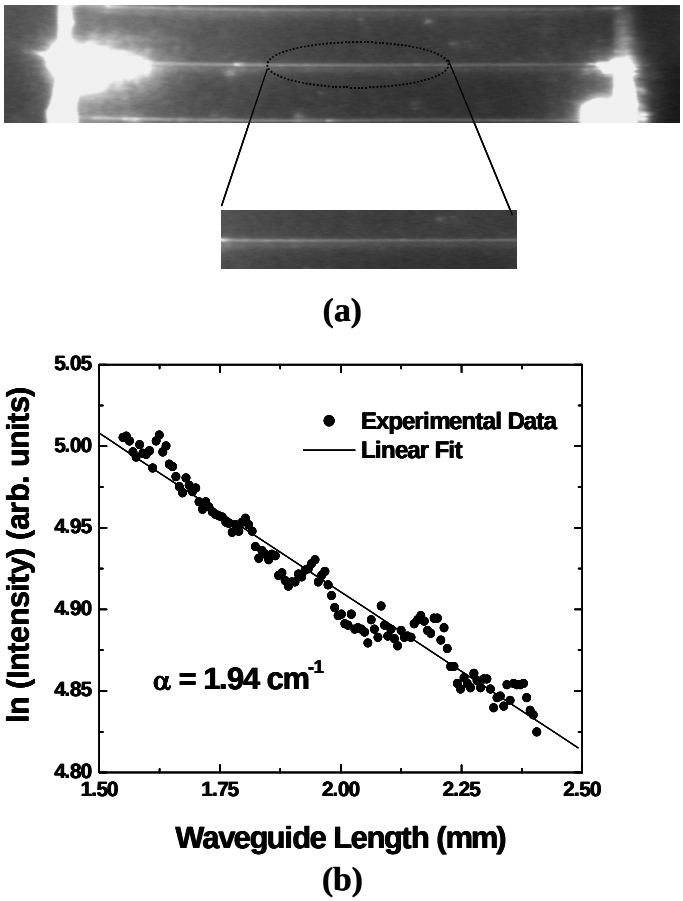

Fig 7.2 (a) Photograph of a typical image of scattered light in the waveguide at 1.5 μm. Light is coupled into the waveguide from the left-hand side. Magnified image of the area is selected for loss evaluation. (b) Intensity profile of the scattered light inside the waveguide at 1.5 μm with a loss of 1.94 cm^{-1}.

Figure 7.2(a) shows a representative scattering profile for a typical waveguide at 1.5 μm and ~15 mW of input power. The intense profiles observed at the input and output extremes correspond to the coupling losses at facets of the waveguide. Other isolated areas of non-continuous intensity are due to the scattering from either dust particles or defects. The clear streak is the scattered light while propagating through the waveguide. A small change in the waveguide position or misalignment of the input

beam resulted in the disappearance of the streak, confirming that it corresponded to the guided propagation mode only. Measurements of loss were, therefore, conducted over this path. As shown in the magnified part of figure 7.2(a), the section of the path comprising only the scattered light from the waveguide and devoid of any other spurious light is selected for further analysis[1]. Figure 7.2(b) shows the data for such selected portions of the scattered light. The main source of error in the calculation arises from the selection of proper region of scattered light and the fitting procedures. Numerous waveguides were tested and typical losses of 5-10 dB/cm were measured for the best of them at this wavelength as well as at ~ 2 μm, while losses as high as ~25 dB/cm were obtained for others. Similar tests with non-oxidised samples showed reduced loss (as low as ~3.5 dB/cm), indicating that oxidisation adds to the waveguide attenuation. Repetition of the measurements several times revealed reproducibility to a satisfactory level. The validity of the quoted values is also supported by Fabry-Perot measurements carried out independently by collaborators.

The wavelength versatility of the femtosecond OPO enabled the measurements over a wide wavelength range from 1.3 to 2.1 μm. A typical set of such measurements is presented in Fig. 7.3. The streak was found to be stronger at shorter wavelengths, which could be due to higher losses of the optics and lower sensitivity of the IR camera at longer wavelengths. The loss coefficients extracted from the linear fit to the data for a typical high quality waveguide were ~1.15-2.55 cm^{-1}, corresponding to propagation losses of 5-11 dB/cm, with higher loss observed at shorter wavelengths. This is in agreement with the wavelength dependence of all loss mechanisms.

The variation of loss with power was examined. As the intensity increased, the scattering at the input facet also increased, thereby reducing the selected portion of waveguide for further analysis. For input power levels exceeding 50 mW, it was almost impossible to obtain a clear image. With increasing input power the slope of the fit and thereby the overall loss increased systematically. Figure 7.4 depicts the variation in loss as a function of input power for specific wavelengths for a high quality waveguide. The loss increased from ~1 cm^{-1} to ~2.5 cm^{-1} with an increase in input power from ~5 mW to ~35 mW. This behaviour, typical for many waveguides

[1] Evidently, availability of an efficient section for analysis limits the minimum waveguide length that can be resolved using the scattering method. In fact, this is the first time loss was measured via monitoring the scattering light in sub-cm waveguides.

that were tested, indicates that intensity-dependent nonlinear loss mechanisms add more than 1 dB/cm at high power levels. The cumulative effect of loss dependence on wavelength and power is shown in Fig. 7.5, where separate measurements of loss against wavelength are presented for three different input powers.

Measurements of loss were performed for different waveguide modes (TE_{00} and other higher-order modes) and typical results as shown in Fig. 7.6 did not reveal any drastic variation in the loss coefficients, confirming good confinement within the waveguide. Loss measurements were also carried out in a good quality waveguide for different polarization configurations of the input beam and it was found that attenuation increased with increasing TM polarisation component. Figure 7.7 presents typical data for TE, diagonal and TM geometries. A study of the loss dependence on the waveguide width was attempted but later abandoned, since no systematic results could be obtained. In fact, a clear dependence of loss on the width could have only be resolved if waveguides of different width but identical in all other aspects were available. This was not possible due to random parameters influencing attenuation, such as dust particles, imperfections and so on.

Finally, a collection of results obtained for three M-type waveguides that were modally-phase-matched (Chapter 6) is presented in Fig. 7.8. Here, measurements were taken for TE and diagonal polarisation at 1.5 μm and for TE and TM polarisation at 800 nm. The input power levels were such that the coupled light intensities corresponded to the guided intensities during the SHG experiment (~4 mW of fundamental and ~ 10 μW of second harmonic). The Ti:Sapphire laser was used as the 800 nm source. Calculations resulted in ~10 dB/cm (15 dB/cm) loss for TE (TE/TM) geometry at 1.5 μm and ~5 dB/cm (~4 dB/cm) for TE (TM) configuration at 800 nm. The lower attenuation at the shorter wavelength in this case is due to better confinement in the waveguide and lower power levels, which resulted in negligible nonlinear loss. It should be noted that only fundamental modes were accessible in this waveguides and therefore the actual loss experienced by the second harmonic wavelength in the SHG experiment is expected to be much larger than ~5 dB/cm.

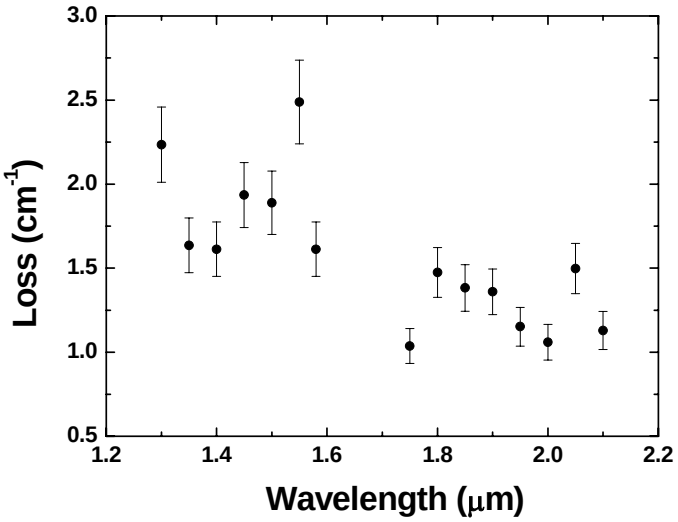

Fig 7.3 Loss coefficient for a high-quality waveguide plotted as a function of wavelength.

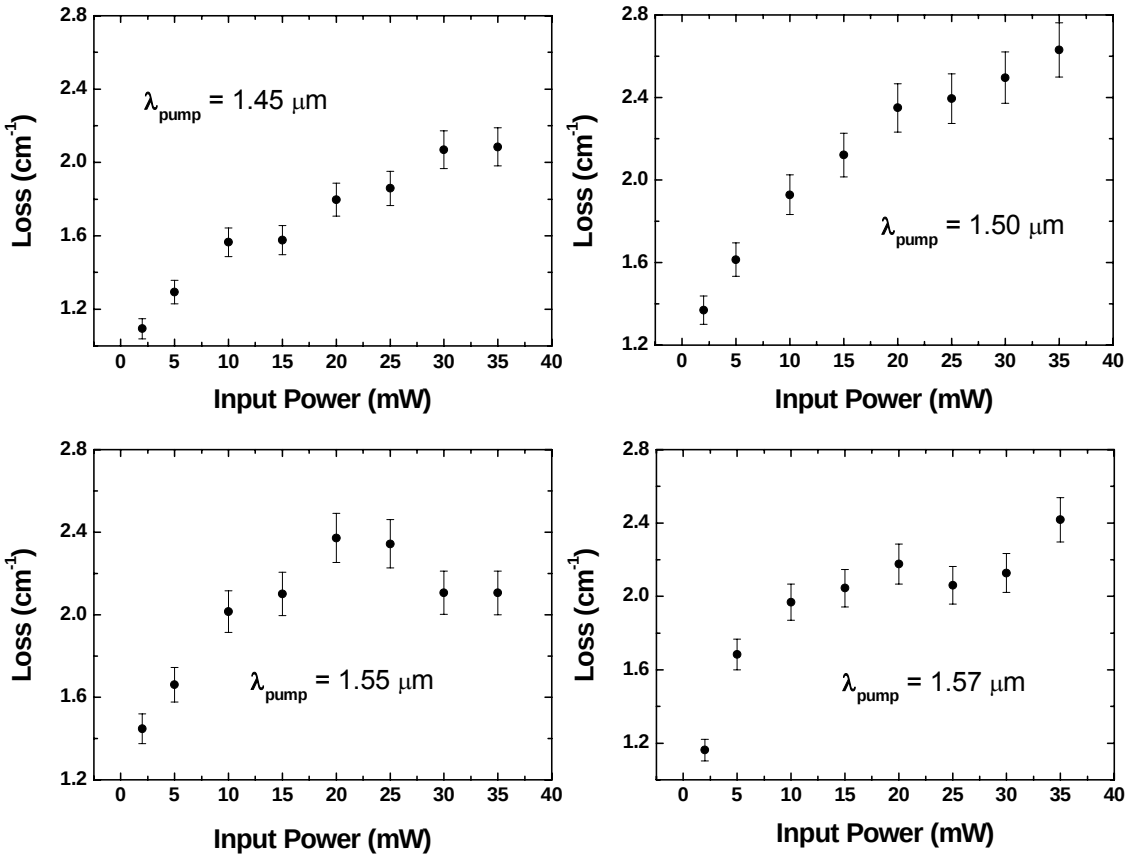

Fig 7.4 Loss coefficient for a high-quality waveguide as a function of input power (measured before the input objective) at different wavelengths: a) 1.45 μm, b) 1.50 μm, c) 1.55 μm, and d) 1.57 μm.

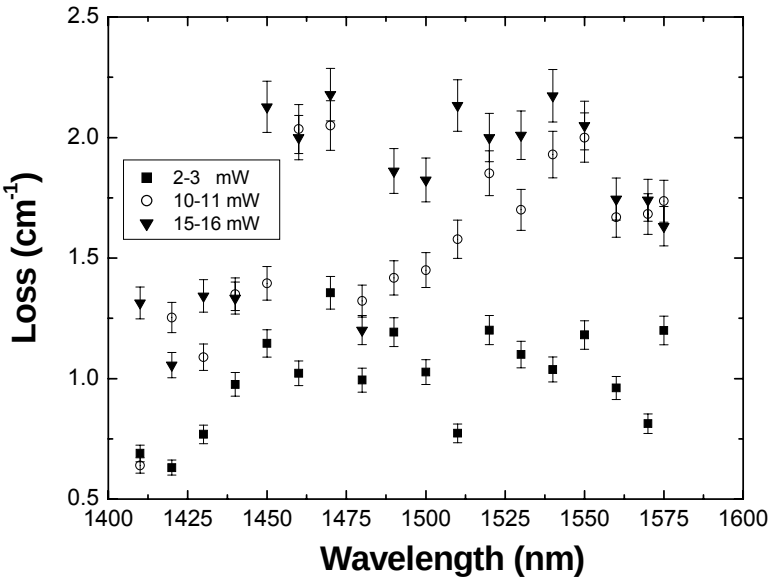

Fig 7.5 Loss coefficients plotted as a function of wavelength for different input intensities. Squares (■) are for ~2 mW, open circles (O) are for ~ 5 mW, and inverted triangles (▼) are for ~15 mW.

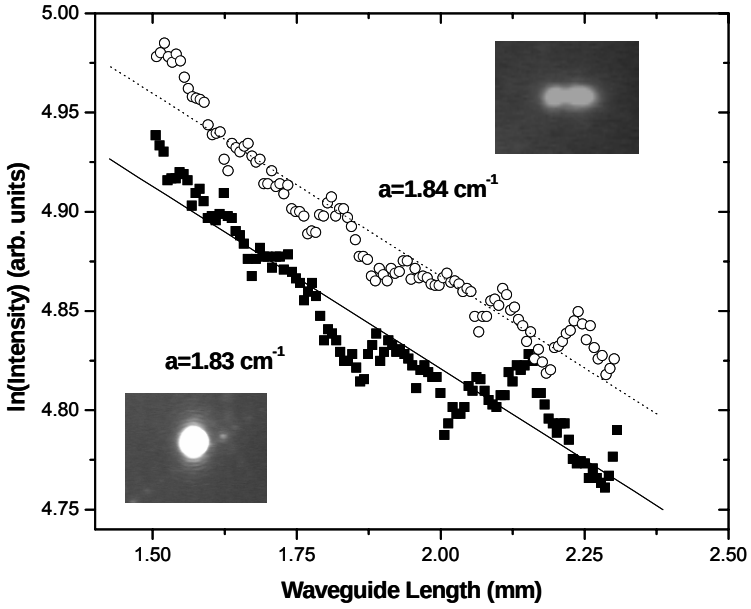

Fig 7.6 Intensity profile along propagation length, for the fundamental mode (TE_{00}), as well as for a higher-order mode. Inset photos depict the spatial profile as sheen in the output. Measurements were made at 1.5 μm for a high-quality waveguide.

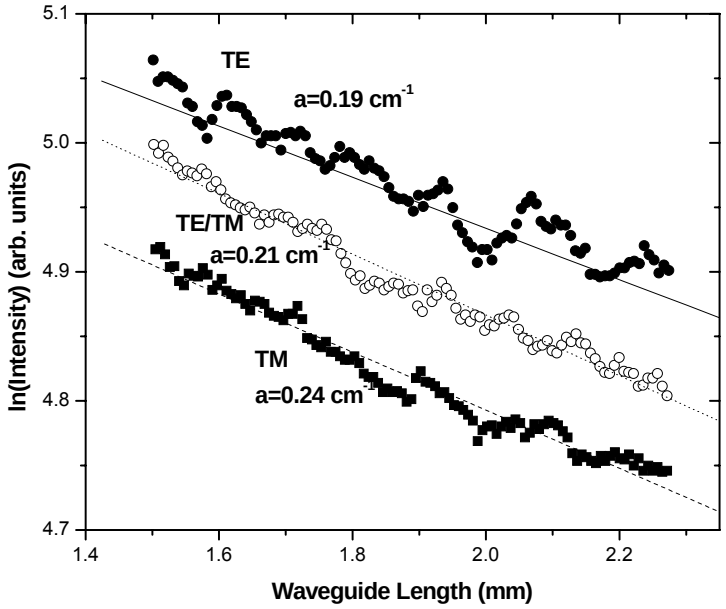

Fig 7.7 Intensity profile along propagation length for a high-quality waveguide at 1.5 μm and for TE, TE/TM and TM polarisation.

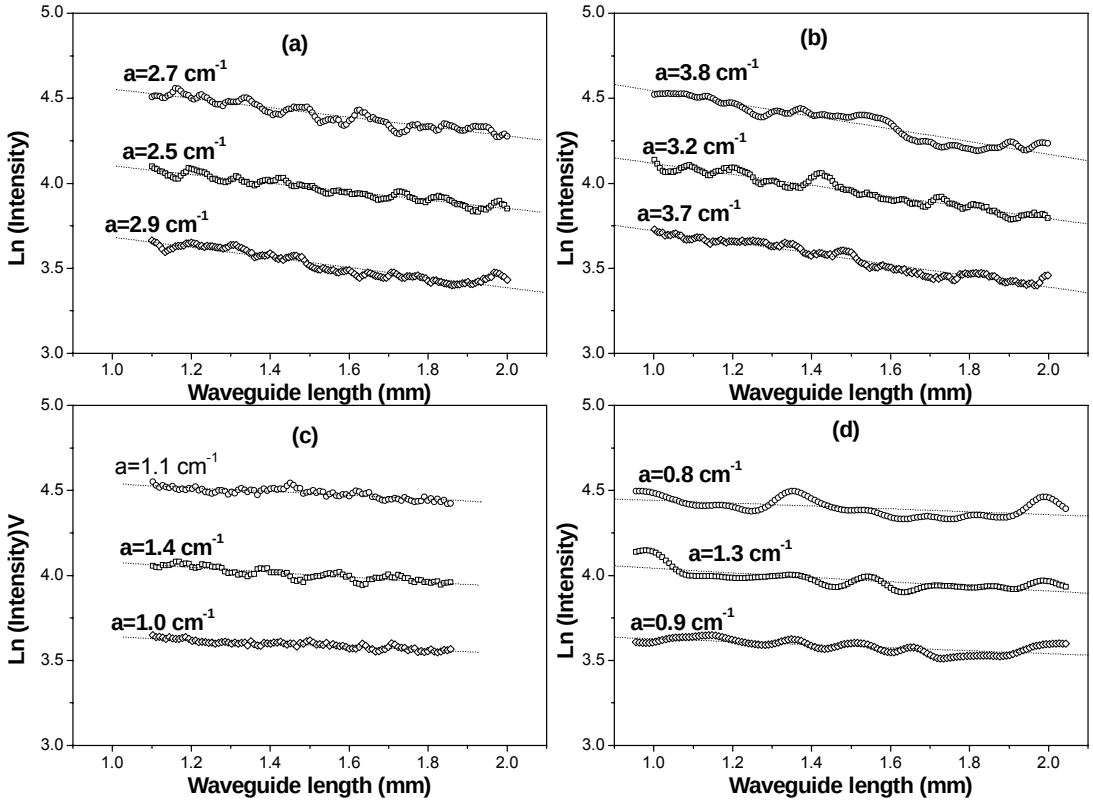

Fig 7.8 Intensity profile for three M-type waveguides at 1.5 μm (a and b) and at 0.8 μm (c and d). Input polarisation and power was chosen so that measurements correspond to the SHG experiment: Transmitted power: 3 mW for (a),(b) and 10 μW for (c), (d). Input polarisation: TE (a), TE/TM (b), TE (c), and TM (d).

7.2.3 Nonlinear loss studies

In the previous section the overall loss coefficient, α, was evaluated based on Eq. (7-1). However, in presence of nonlinear attenuation the transmission of optical intensity is best described by:

$$\frac{dI(r,z,t)}{dz} = -\alpha_0 I(r,z,t) - \beta I^2(z,r,t)$$

The solution of the above equation is conventionally given in bibliography [19-20] by:

$$I(r,z,t) = \frac{(1-R)\cdot I(r,0,t)\cdot e^{-\alpha_0 l}}{1+\alpha\beta(1-R)\cdot I(r,0,t)\cdot \dfrac{(1-e^{-\alpha_0 l})}{\alpha_0}} \qquad (7\text{-}2)$$

where α_0 is the linear absorption coefficient, β is the two-photon absorption coefficient, l is the length of the nonlinear medium, R is the reflectivity of the medium, $I(r,z,t)$ is the transmitted irradiance after a path length, z, and a is the modal structure factor.

The coefficient β can, therefore, be extrapolated through data of transmitted irradiance as a function of the coupled irradiance. Such measurements were collected and are presented[2] in Fig. 7.9 for the oxidised sample, TE input polarisation and two representative wavelengths. The peak input and output irradiance were calculated from the measured average power taking into account the duty cycle of the source, an estimated ~10% coupling efficiency and ~50% detection efficiency. The spot area was assumed ~20 μm^2. Large uncertainties in the estimate of the spot size and coupling/detection efficiencies were the main source of error in the calculations, which can only provide indicative values. The solid lines in Fig. 7.9 represent a fit according to Eq. (7-2), using values of a ~0.5, R ~0.3 and l=0.35. Furthermore, α_0 was fixed at ~0.8-1.2 cm^{-1}, corresponding to measurements at low input powers (~2 mW), assuming that at such low power levels only linear loss is present. Typical

[2] It can be seen from Fig. 7.9 that transmission is of the order of ~10%. In the SHG experiment, a transmission of ~80% was estimated. This should not be a source of confusion, since in the present studies a) the input wavelength was ~1.5 μm and therefore according to Fig. 7.5 loss is more than twice as high as for the fundamental phase-matched wavelength (2 μm) and b) the waveguides used here were 3.5 times longer than the ones used for the SHG experiment.

values of β ranging from ~10 to ~18 cm/GW were calculated for wavelengths between 1.43 and 1.70 μm. In the above calculations, temporal broadening of the pulse due to GVD and self-phase-modulation effects have been neglected. The magnitude of TPA coefficients obtained in this study matches very well with the theoretical values (1-15 cm/GW) of bulk GaAs reported in [21] and those obtained experimentally (5-33 cm/GW) for GaAs waveguides in [22].

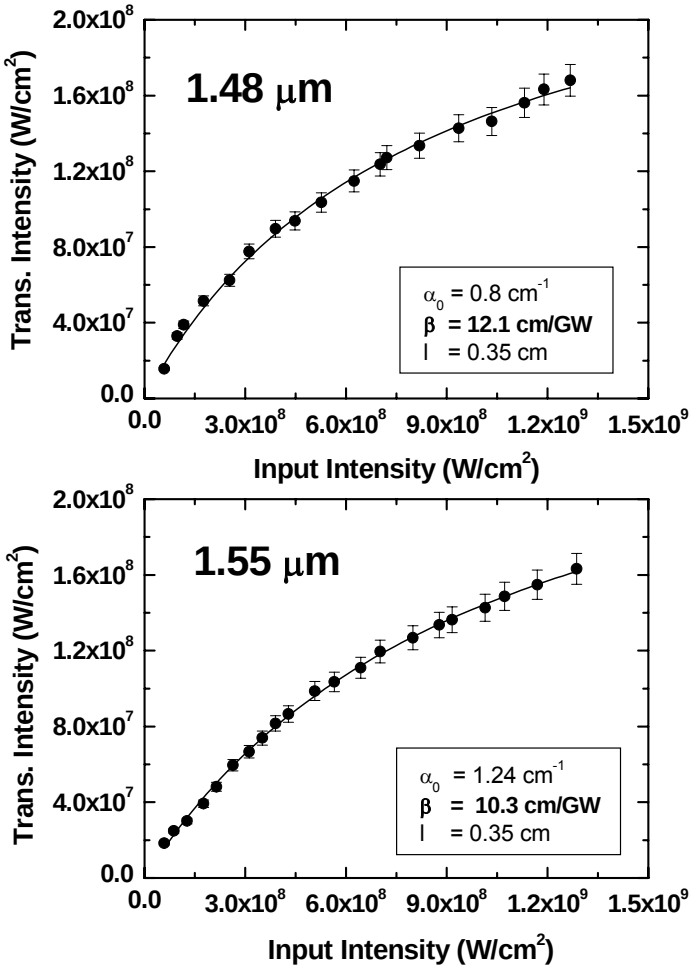

Fig. 7.9 Nonlinear transmission data for a good-quality waveguide plotted as a function of input intensity within the waveguide. The scattered points are the experimental data and the solid line is the fit given by Eq. (7-2) at (a) 1.48 μm and (b) 1.55 μm.

7.3 Conclusions

Using the scattering technique and femtosecond pulses from the OPO, optical loss was evaluated over an extended wavelength range from 1.3 to 2.1 μm. It was established that this technique combined with the wavelength versatility of the femtosecond OPO represents a general and simple method for accurate determination of waveguide losses across the near- and mid-IR, where few other practical optical sources are available. The desirability of this spectral range is evident since it includes the telecommunication window (near 1.55 μm), as well as the wavelength regime in which these waveguides are proven to be strong candidates for nonlinear frequency conversion applications.

Measurements in oxidised waveguides revealed that typical loss is expected to be ~1 cm^{-1} near 2 μm and ~2-2.5 cm^{-1} near 1.5 μm. Approximately one half of the loss is due to nonlinear two-photon absorption, the contribution of which vanishes for input power levels of a few mW. Nonlinear transmission measurements allowed an estimate of the β-coefficient, which was fount to be ~10-18 cm/GW in the 1.45-1.55 μm range. The dependence of loss on input polarisation and waveguide mode was also studied. Finally, loss measurements for the M-type waveguides showed that attenuation is significantly higher in these structures.

Compared to previous reports, this chapter has presented advances of the scattering technique arising from: a) use of femtosecond pulses, allowing nonlinear loss contribution to be resolved, b) exploitation of OPO tunability, allowing for wavelength dependence loss measurements, and c) appropriate instrumentation for loss measurements in samples shorter than 0.5 cm.

References

[1] R.G. Hunsperger, in *Integrated Optics: Theory and Technology*, Springer Verlag, New York, 3rd ed., 1991

[2] H.P. Weber, F.A. Dunn, and W.N. Leibolt, *Loss measurements in thin-film optical waveguides*, Appl. Opt. 12, 755, (1973)

[3] A. Boudrioua and J.C. Loulergue, *New approach for loss measurements in optical planar waveguides*, Opt. Commun. 137, 37, (1997)

[4] R.K. Hickernell, D.R. Larson, R.J. Phelan, Jr., and L.E. Larson, *Waveguide loss measurement using photothermal deflection*, Appl. Opt. 27, 2636, (1988)

[5] R.G. Walker, *Simple and accurate loss measurement technique for semiconductor optical waveguides*, Electron. Lett. 21, 581, (1985)

[6] R. Regener and W. Sohler, *Loss in low-Finesse Ti:$LiNbO_3$ optical wave resonators*, Appl. Phys. B 36, 143, (1985)

[7] T. Feuchter and C. Thirstrup, *High precision planar waveguide propagation loss measurement technique using a Fabry-Perot Cavity*, IEEE Phot. Tech. Lett. 6, 1244, (1994)

[8] K.H. Park, M.W. Kim, Y.T. Byun, D.Woo, S.H. Kim, S.S. Choi, Y. Chung, W.R. Cho, S.H. Park, and U. Kim, *Nondestructive propagation loss and facet reflectance measurements of GaAs/AlGaAs strip-loaded waveguides*, J. Appl. Phys. 78, 6318, (1995)

[9] Y. Okamura, S. Yoshinaka, and S. Yamamoto, *Measuring mode propagation losses of integrated optical waveguides: a simple method*, Appl. Opt. 22, 3892-3894, (1983)

[10] M. Kumar, V. Gupta, G.N. DeBrabander, P. Chen, J.T. Boyd, A.J. Steckl, A.G. Choo, H.E. Jackson, R.D. Burnham, and S.C. Smith, *Optical channel waveguides in AlGaAs multiple quantum-well structures formed by focused ion-beam-induced compositional mixing*, IEEE Phot. Tech. Lett. 4, 435, (1993)

[11] A.F. Evans, D.G. Hall, and W.P. Maszara, *Propagation loss measurements in silicon-on-insulator optical waveguides formed by the bond-and-etchback process*, Appl. Phys. Lett. 59, 1667, (1991)

[12] M. Kumar, J.T. Boyd, H.E. Jackson, J.M. Zavada, H.A. Jenkinson, R.G. Wilson, B. Theys, and J. Chevallier, *Channel optical waveguides formed by deuterium passivation in GaAs and InP*, J. Appl. Phys. 82, 3205, (1997)

[13] L. Beckers, J. Schubert, W. Zander, J. Ziesmann, A. Eckau, and P. Leinenbach, and Ch. Buchal, *Structural and optical characterization of epitaxial waveguiding $BaTiO_3$ thin films on MgO*, J. Appl. Phys. 83, 3305, (1998)

[14] H. Hu, F. Lu, F. Chen, F.-X Wang, J.-H. Zhang, X.-D, Liu, K.-M. Wang, and B.-R Shi, *Optical waveguide formation by MeV H^+ implanted into $LiNbO_3$ crystal*, Opt. Commun. 177, 189, (2000)

[15] M.S. Stern, P.C. Kendall, R.C. Hewson-Browne, P.N. Robson, and D.A. Quinney, *Scattering loss from rough sidewalls in semiconductor rib waveguides*, Electron. Lett. 25, 1231, (1989)

[16] R.C. Hewson-Browne, P.C. Kendall, and D.A. Quinney, *Roughness scattering into substrate radiation modes of rib waveguides*, IEE Proc. 136, 281, (1989)

[17] J.P.R. Lacey and F.P. Payne, *Radiation loss from planar waveguides with random wall imperfections*, IEE Proc. 137, 282, (1990)

[18] M.S. Stern, P.C. Kendall, and P.N. Robson, *Estimation of rib waveguide radiation losses*, Electron. Lett. 24, 17, (1988)

[19] J.H. Bechtel and W.L. Smith, *Two-photon absorption in semiconductors with picosecond laser pulses*, Phys. Rev. B 13, 3515, (1976)

[20] C.C. Yang, A. Villeneuve, G.I. Stegeman, C.-H. Lin, and H.-H. Lin, *Anisotropic two-photon transitions in GaAs/AlGaAs multiple quantum well waveguides*, IEEE J. Quant. Electron. 29**,** 2934, (1993)

[21] J.B. Khurgin, *Nonlinear response of the semiconductor quantum-confined structures near and below the middle of the band gap*, J. Opt. Soc. Am. B 11, 624, (1994)

[22] A. Villeneuve, C.C. Yang, G.I. Stegeman, C.N. Ironside, G. Scelsi, and R.M. Osgood, Nonlinear absorption in a GaAs waveguide just above the half the bang gap, IEEE J. Quant. Electron. 30**,** 1172, (1994)

8. GENERAL CONCLUSION

8.1 Summary of results

This thesis has presented details of experimental work aimed at the demonstration of efficient nonlinear frequency conversion in GaAs-based waveguides. The motivation for such a study was outlined in the opening chapter: GaAs offers the opportunity for the construction of numerous nonlinear optical devices operating in the near- and mid-IR, providing that the fundamental problem of phase-matching nonlinear interactions in this isotropic medium can be overcome.

In Chapter 2, a brief introduction to the basic concepts of nonlinear optics was attempted. The breaking in the harmonicity of the atomic dipole oscillators was shown to give rise to nonlinearities in light-matter interactions and the second-order polarisation and susceptibility of matter were introduced. Substitution of these quantities into Maxwell equations yielded a wave-motion equation which, in turn, was solved to produce the coupled-wave equations that describe the nonlinear interaction of three waves in a medium exhibiting second-order response. The coupled wave equations also revealed that the strength of a nonlinear process is maximised when the phase velocities of the interacting waves are matched (phase-matching). The complications in achieving phase-matching in disperssive media were discussed and the two established phase-matching methods presented. The first approach to phase-matching nonlinear interactions was shown to depend on the natural optical anisotropy of a suitable medium (birefringent-phase-matching). It was also shown that phase-matching can be engineered through a spatial modulation of the nonlinear coefficients (quasi-phase-matching). Finally, a short discussion was permitted to expose the effects of the use of beams with Gaussian profiles (at is most commonly the case) in a nonlinear interaction.

Chapter 3 provided details regarding the design, construction and performance of the femtosecond optical parametric oscillator (OPO) that was built and served as the main experimental tool for the material characterisation. The OPO was based on a periodically poled lithium niobate (PPLN) crystal. Following phase-matching and group velocity mismatch calculations, the chosen PPLN crystal comprised eight evenly spaced grating periods ranging from Λ=20.6 μm to Λ=22 μm and was 1-mm-

long. The OPO was configured in a semimonolithic, singly resonant (at the signal) cavity design. It was synchronously pumped by a self-mode-locked Ti:Sapphire laser at a ~90 MHz repetition rate. The device offered continuous coverage over the ~1.28-1.58 μm and ~1.71-2.28 μm spectral range for the signal and idler, respectively, with corresponding average powers exceeding 100 mW (signal) and 50 mW (idler). Output signal pulses of ~250 fs and idler pulses of ~ 185 fs duration were obtained, with a corresponding spectral FWHM bandwidth of ~10 nm (signal) and ~ 26 nm (idler), resulting in a duration-bandwidth product of ~0.33 (signal) and 0.36 (idler), indicating near-transform limited pulses. The pump power threshold was ~200 mW with an 87 % output coupler and typical operation was approximately four times above threshold. The device operated in a stable fashion for many hours and major maintenance work was not required for periods of many months.

Chapter 4 discussed the first approach to solve the phase-matching problem in GaAs, that is, by using form birefringence. Results were also presented from what we believe is yet the most efficient experimental demonstration of frequency conversion in this material. Artificial birefringence was induced by means of embedding native oxide layers (Alox) in a GaAs-based waveguide structure. Using femtosecond pump pulses at 2.01 μm, efficient type I second harmonic generation was observed in these GaAs/Alox waveguides, which had typical measured transmission loss of ~5 to 10 dB/cm. Useful average SHG powers of ~650 μW were collected, for an available average pump power of ~50 mW, resulting in an overall external efficiency of ~1.3%. This hybrid set-up had a coupling efficiency of ~10% and a collection efficiency of ~50%, hence the internal waveguide conversion efficiency was greater than 20%. Group velocity mismatch calculations indicated that the interaction length was shorter than ~200 μm, allowing for the extrapolation of the normalised conversion efficiency which was found to be greater than 1000 $\%W^{-1}cm^{-2}$. This large efficiency value was supported by depletion measurements that revealed a pump power depletion of ~40% and a spectral depletion greater than 80% within the conversion bandwidth.

Chapter 5 outlined the principles of quasi-phase-matching in semiconductor quantum well waveguides via quantum well intermixing technologies. It also detailed results from two experiments that resulted in demonstration of second harmonic generation in such waveguides. To our knowledge, these were the first reports of nonlinear

frequency conversion in GaAs-based structures using quantum well intermixing methods to modulate the large bulk-like nonlinear coefficients. The first of the two experiments utilised sputtered silica defect-induced intermixing to produce third-order gratings in a GaAs/AlGaAs superlattice structure. Type I SHG was demonstrated for fundamental wavelengths from 1480 nm to 1520 nm, using third-order gratings with periods varying from 10.5 μm to 12.4 μm. The SHG spectra exhibited spectral narrowing due to the finite acceptance bandwidth of the QPM gratings. An average SHG power of ~25 nW was collected for an available input pump power of ~80 mW, indicating an overall conversion efficiency as low as ~$3x10^{-5}$ %. Accounting for the coupling and collection efficiencies of the set-up, the internal waveguide efficiency was estimated to be ~0.005%, while considering a calculated interaction length of ~100 μm the normalised conversion efficiency was found to be on the order of ~0.15 $\%W^{-1}cm^{-2}$. Subsequent efforts to achieve first-order gratings and higher efficiencies using this intermixing technique were not successful. Better quality, first-order QPM samples were fabricated by means of ion implantation induced intermixing. The second experiment presented inhere was based on such an improved sample. In this case, useful average SHG power levels up to 1.5 μW were obtained corresponding to an overall device efficiency of ~0.002%. Again, taking into account the coupling and collection efficiencies of the set up, as well as the calculated interaction length, it was shown that the internal efficiency of the process was ~ 0.06%, while the normalised conversion efficiency reached the level of ~1.2 $\%W^{-1}cm^{-2}$.

Chapter 6 was dedicated to presenting details of the last phase-matching approach, which employs modal dispersion to compensate for the material dispersion, along with results from the corresponding experiment that demonstrated second harmonic generation in an M-type GaAs/AlAs waveguide designed for optimised mode-overlap. To our knowledge, this was the first report of frequency conversion in inorganic semiconductors by use of modal phase-matching in an optimised M-type structure. Type I and II SHG were observed for fundamental wavelengths near 1.55 μm using femtosecond pulses. Fine temperature tuning of the output wavelength was demonstrated at a rate of ~0.08 $nm/^0C$. Practical SHG powers up to ~10 μW were obtained for an available input power of ~65 mW and for the most efficient type-II process. This indicated a maximum overall efficiency of ~ 0.015%, corresponding to an internal waveguide efficiency greater than 0.15%. Finally, accounting for a group

velocity mismatch-limited interaction length of ~100 μm, the normalised efficiency of the process was found to be ~ 2 $\%W^{-1}cm^{-2}$.

Chapter 7 presented the operating principles of, and results from, the femtosecond scattering technique used to measure the transmission loss of the waveguides. The flexible nature of this method, combined with the wavelength versatility of the OPO source, allowed the determination of optical loss over an extended spectral range in the infrared, from ~1.3 μm to 2.1 μm. Additionally, this method allowed loss measurements under the same experimental conditions as those during the material characterisation (e.g. loss measurements using femtosecond pulses), something which would have not been possible with alternative loss measurement techniques (e.g. Fabry-Perot method). Typical losses of ~5-10 dB/cm were measured in the oxidised waveguides, while quasi and modally phase-matched waveguides presented higher losses (~20 dB/cm and >10 dB/cm, respectively) in the infrared. Compared to previous reports on loss measurements using the same technique, the results presented inhere are the first to our knowledge that were carried out using ultrashort pulses, at such a broad spectral range and on sub-cm length waveguides. Power-dependent loss measurements were carried out and it was established that at the maximum available input power levels approximately one half of the loss was due to nonlinear mechanisms (two-photon absorption). Loss measurements were also carried out as a function of the input polarisation, waveguide mode and width. Nonlinear transmission measurements permitted an evaluation of the β-coefficient, which was found to be ~10-18 cm/GW in the 1.45 to 1.55 μm wavelength range.

In the following section a comparative discussion of the different phase-matching techniques presented in this thesis is attempted, along with a short review of related work carried out in this field by a number of different groups.

8.2 BPM, QPM, MPM: A comparative discussion

To allow for a comparative discussion between the different phase-matching approaches investigated in this work, the (device, internal and normalised) efficiencies obtained in each case are summarised in Table 8.1. In addition, Table 8.2 outlines the corresponding measured losses together with the estimated coupling and collection efficiencies, as well as the practical SHG powers that were collected at the output of the different waveguides.

	Device efficiency	**Internal efficiency**	**Normalised efficiency**
BPM	1.3 %	~20 %	~1000 % $W^{-1}cm^{-2}$
QPM (1st order)	0.002 %	~0.06 %	~1.2 % $W^{-1}cm^{-2}$
QPM (3rd order)	0.00003 %	~0.005 %	~0.15 % $W^{-1}cm^{-2}$
MPM	0.015 %	~0.15 %	~2 % $W^{-1}cm^{-2}$

Table 8.1 Device, internal and normalised efficiencies obtained by the different waveguides.

	Loss (dB/cm)	**Coupling efficiency**	**Collection efficiency**	**Collected SHG power**
BPM	~5-10	~10 %	<50 %	~650 μW
QPM (1st order)	~20	~ 18 %	~20 %	1.5 μW
QPM (3rd order)	~20	~3 %	~20 %	0.025 μW
MPM	~10-15	< 30 %	~30 %	~10 μW

Table 8.2 Transmission losses, coupling anc collection efficiencies and collected SHG output powers obtained by the different waveguides.

Evidently, birefringently-phase-matched (BPM) waveguides resulted in significantly higher generated power levels and conversion efficiencies, with estimated SHG powers inside the waveguide in the mW-regime. On the other hand, the 3rd order quasi-phase-matched (QPM) waveguides resulted in almost negligible efficiencies. These waveguides, however, maintain their "historical" value as the first demonstrators of quasi-phase-matching in quantum well structures by means of quantum well intermixing. The 1st order QPM as well as the modally-phase-matched (MPM) waveguides resulted in similar SHG powers (μW power levels) and conversion efficiencies, but compare relatively poorly with the oxidised BPM samples.

It is interesting to attempt a qualitative discussion on the factors responsible for the differences between the obtained efficiencies. In this context, the measured losses should be taken into account as a first priority. As can be seen in Table 8.2, BPM samples presented significantly lower transmission losses, while the QPM samples exhibited the higher loss amongst all the available waveguides. This difference in propagation loss (which should be attributed to process-related factors) is also reflected on the resulting efficiencies. When comparing the generated power levels as well as the overall device efficiencies[1], one should also take into account the estimated coupling and collection efficiencies, which varied significantly due to differences in the waveguide design (e.g. core size, cladding thickness and refractive index, etc).

A more thorough efficiency comparison can only be carried out in terms of the normalised conversion efficiencies, which for the case of guided wave second harmonic generation can be expressed as [1-5]:

$$n = \frac{P_{2\omega}}{P_{\omega}^2 \cdot L^2} = \frac{8\pi^2}{\lambda^2} \frac{1}{c\varepsilon_0} \frac{d_{eff}^2}{n_{\omega}^2 n_{2\omega}} |K|^2 \tag{8-1}$$

Note that the above definition is identical to the plane wave result that was deduced in Chapter 2, with the addition of the mode-overlap integral factor ***K*** which accounts for the mode profiles of the interacting waves and reads as [1-5]:

[1] Evidently, the coupling and collection efficiencies are included as inherent parameters in the internal and normalised efficiencies.

$$K = \left| \int_{-\infty}^{\infty} \int_{-\infty}^{\infty} E_{\omega}^{2}(x,y) E_{2\omega}(x,y) dxdy \right| \tag{8-2}$$

where propagation is taken along *z*-axis and E_{ω}, $E_{2\omega}$ are the field profiles normalised in the following way:

$$\int_{-\infty}^{\infty} \int_{-\infty}^{\infty} E_{i}^{2}(x,y)(x,y) dxdy = 1 \qquad i = \omega, 2\omega \tag{8-3}$$

It is evident from Eq. 8.1 that in carrying out a theoretical prediction of the expected normalised conversion efficiencies for the present samples three factors should be accounted for[1]:

1. The fundamental wavelength
2. The effective nonlinearity of the specific heterostructure
3. The mode overlap integral

For the effective nonlinear coefficient an averaged value over all layers that constitute the waveguide core area should be used. In fact, for a N-layer stack with layer thicknesses $h_1 \ldots h_N$ and bulk-nonlinear coefficients $d_1 \ldots d_N$, the average nonlinear coefficient is commonly expressed as [5]:

$$d_{eff}^{2} = \frac{d_1^2 h_1 + d_2^2 h_2 + \ldots + d_N^2 h_N}{h_1 + h_2 + \ldots + h_N} \tag{8-4}$$

By using the above formula, the average nonlinearity of the waveguides under investigation was calculated. Values for the bulk AlGaAs coefficients as a function of the Al concentration were obtained from ref. [6], while for the oxidised waveguides the nonlinearity of the Alox layers was taken as zero. Note that in the case of the QPM waveguides, the spatial Fourier component is also taken into account for the calculation of the effective nonlinearity, assuming a 50% duty cycle and the ideal case of domain disordering (i.e, γ=0). Table 8.3 presents values for the three factors on which the normalised efficiency depends (that is, wavelength of interaction, effective nonlinearity and mode overlap integral). It also shows the calculated theoretical limit in normalised efficiency that can be achieved with the present samples. In doing that, the normalised efficiency of the BPM samples is taken as unity, since these waveguides appear to have reached the maximum attainable conversion efficiency (in

[1] It has been assumed that the effective refractive indices of all waveguides in the infrared do not vary significantly.

the femtosecond regime), with nearly full spectral depletion in the acceptance bandwidth.

	λ (μm)	d_{eff}/d_{GaAs}	K/K_0	n/n_{BPM}
BPM	2	~ 0.93	1	~ 1
QPM (1st order)	1.5	~ (0.74/π) = 0.24	1	~ 0.12
QPM (3rd order)	1.5	~ (0.74/3π) = 0.08	1	~ 0.01
MPM	1.5	~ 0.85	~0.2	~ 0.06

Table 8.3 Parameters used to calculate the theoretical limit of the normalised efficiency for the different waveguides with respect to the efficiency attainable by means of birefringent-phase-matching: (a) Wavelength of interaction, (b) averaged nonlinear coefficient (normalised to the coefficient of bulk GaAs) and (c) Mode overlap integral (normalised to the value $\mathbf{K_0}$ for a type I process with fundamental guided modes). The last column presents the predicted conversion efficiency limit.

According to the theoretical predictions shown in Table 8.3, one may conclude that:

1. The 1st (3rd) order QPM waveguides are inherently limited to approximately one (two) orders of magnitude lower conversion efficiency than the BPM waveguides. However, the experimental results indicated a reduction in efficiency of three and four orders of magnitude, respectively, compared to the efficiency of the BPM waveguides (see Table 8.1). The modest performance of the present QPM samples should be primarily attributed to restrictions in current fabrication technology that prohibit large depths of modulation and accurate definition of a 50:50 grating period. Therefore, it is estimated that improvement in QPM technology could lead to an increase in the observed conversion efficiencies by a factor of up to ~100.

2. The MPM waveguides are by first principles limited to approximately fifteen times lower efficiency than the BPM waveguides. Again, the experimentally obtained efficiencies (Table 8.1) indicate a reduction by a factor of ~500. This additional reduction should be attributed to the poor confinement of the waves

inside the waveguide core, which was approximately twice as small compared to the BPM waveguides. Hence, significant improvement is believed to be possible using modal-phase-matching by further optimising the waveguide design.

To place the results presented in this thesis into a broader perspective, a selection of results on frequency conversion experiments, performed by various groups over the last decade, in semiconductor, PPLN, and polymer waveguides are summarised in Table 8.4. Rafailov *et al*. [7,8] demonstrated SHG from a first-order QPM GaAs/AlGaAs waveguide crystal using periodic modulation of nonlinear coefficient and predicted a conversion efficiency of 0.1% near 2.0 μm. Koh *et al*. [9] devised sublattice reverse epitaxy of GaAs/Ge/GaAs and achieved a normalized internal conversion efficiency of 2.0 x 10^{-3} $\%W^{-1}$ near 1.575 μm, which was three orders of magnitude lower than the predicted theoretical efficiency of $1.5\%W^{-1}$. The low efficiency was attributed to high waveguide losses that were induced by the corrugation of the guide layer. Using all-epitaxially fabricated thick, orientation-patterned GaAs films, Eyres *et al*. [10] demonstrated SHG with fundamental near 10.0 μm and obtained efficiencies close to 4 x 10^{-3} $\%W^{-1}$. Skauli *et al*. [11] designed quasi-phase-matched orientation-patterned GaAs structures by a combination of molecular-beam epitaxy and hydride vapour phase epitaxy and obtained an internal conversion efficiency of 33% in their SHG experiment using an uncoated sample with nanosecond pulses near 4.0 μm. Yu *et al*. [12] fabricated low-loss orientation-patterned AlGaAs waveguides and obtained 2 nW of SHG power, for an input power of 10 mW at 1.56 μm, comparable to an estimated output power of 20 nW. The transfer of corrugation of the template to the waveguide core resulted in high transmission losses for both fundamental and second harmonic. Lallier *et al*. [13] achieved efficient SHG (~24%) of a 10.6-μm, 60-ns CO_2 laser pulses with a quasi-phase-matched diffusion bonded GaAs crystals. Lallier *et al*. [14] also reported an infrared DFG conversion efficiency of 3.4 x 10^{-4} with diffusion-bonded QPM GaAs at 11.35 μm using a $LiNbO_3$ OPO. For an input energy of 17 mJ they detected 2 μJ of DFG energy (~180 W of peak power).

Among the various reports of frequency conversion in other waveguides [15-22], only $LiNbO_3$ and doped $LiNbO_3$ waveguides have proved marginally more efficient (in

terms of recorded output power and internal efficiency) than the reported structures in the present study, with a few of the $LiNbO_3$ experiments in the visible range. One of the first reports of mid-infrared generation in PPLN waveguides was by Lim *et al*. [23], who reported 1.8 μW of 2.1 μm radiation for 160 mW of 0.81 μm and 1 mW of 1.32 μm radiation coupled into the waveguide, corresponding to a normalized efficiency of ~ $4\%W^{-1}cm^{-2}$. Very recently, Parameswaran *et al*. [24] achieved the highest normalized SHG conversion efficiency of $150\%W^{-1}cm^{-2}$ in the 1.5-μm communication band in buried waveguides formed by annealed and reverse proton exchange in PPLN. Hofmann *et al*. [15] produced mid-infrared radiation near 2.8 μm though QPM DFG in periodically poled $Ti:LiNbO_3$ channel waveguides by mixing 1.55 μm radiation from a diode laser and 3.391 μm radiation from a He-Ne laser. They obtained a conversion efficiency of $105\%W^{-1}$, corresponding to a normalized value of 1.6 $\%W^{-1}cm^{-2}$. Mizuuchi *et al* [16] achieved a normalized SHG conversion efficiency of 1200 $\%W^{-1}cm^{-2}$ in *x*-cut $MgO:LiNbO_3$ waveguides using QPM and Nb_2O_5 as a cladding layer. They observed 5.5 mW of SHG power for a pump power of 42 mW at fundamental wavelength of 0.867 μm. Sugita *et al*. [19] successfully generated highly efficient ($1000\%W^{-1}$) ultraviolet light at 0.386 μm in periodically-poled $MgO:LiNbO_3$ waveguides. Sato *et al*. [20] demonstrated a QPM-DFG device for the 1.5-μm band using annealed-proton-exchanged PPLN waveguides with a high-index cladding layer of As_2S_3, which enhanced the mode overlap thereby improving the efficiency. They observed a normalized SHG conversion efficiency of $790\%W^{-1}$ for a fundamental wavelength of 1.533 μm. They also estimated a DFG conversion efficiency of –6 dB at 1.528 μm for 30-mW of pump power (1.534 μm + 0.765 μm).

Amongst an array of polymer waveguides investigated for frequency conversion using QPM and MPM techniques, Jäger *et al*. [25] demonstrated efficient SHG of 14 $\%W^{-1}cm^{-2}$ in over-damped polymeric channel waveguides using modal dispersion phase-matching near 1.55 μm, using of 6-8 ps pulses from a color center laser. Wigres *et al*. [26] obtained efficiencies up to $7\%W^{-1}cm^{-2}$ with optimized overlap integral for modal dispersion phase-matched SHG in new class of polymer waveguides. Jäger *et al*. [27] also reported SHG in poled polymer channel waveguides at 1.5 μm utilizing the QPM technique. Using 6-9 ps pulses, they achieved an efficiency of $0.05\%W^{-1}cm^{-2}$. They suggest that in order to utilize the high nonlinearity of polymers, better geometry,

poling procedure and materials are critical to realize complete modulation of the nonlinearity. The highest efficiency (up to 245%$W^{-1}cm^{-2}$) in a polymer waveguide was achieved by Dai *et al*. [28] for an interaction length of 36.7 μm, using high-repetition-rate 100-femtosecond pulses from a Ti:sapphire laser.

It is clearly evident from the above discussion, and the values presented in Table 8.4, that semiconductor waveguides have excellent performance compared to PPLN and polymer waveguides. The present results confirm that these waveguides are highly promising for ultra short pulse applications, including telecommunication. It should also be noted that the above experiments were all performed at room temperature and we could easily couple ~100 mW of 200 fs pulses without any sign of optical damage. The waveguides also remained chemically stable over a period of time of typically a few months with reproducible results.

In conclusion, using birefringent, quasi- and modal-phase-matching in GaAs-based waveguides, efficient second harmonic generation has been demonstrated and practical output powers obtained. Birefringent samples were found to be the most efficient among the samples investigated, followed by MPM and QPM samples. By employing even better waveguide design, improved coupling efficiency, lower fundamental and nonlinear wavelength losses, these waveguides could be pushed further into the mW-output power regime. The rapid progress from pW and nW output powers, in the initial stages of development of these techniques, to the μW and mW range at the present time is highly encouraging for this field, which is still in its infancy.

Sample	**Techniq.**	**Input Power/ Energy**	**Output Power**	**Effici-ency**	**Norm. Efficiency ($\%W^{-1}cm^{-2}$)**	**Source(s)**	**Ref**
AlGaAs/ AlAs	BPM/ DFG	0.44 mW^2	90 pW	-	3.0	cw, 1.32 μm +1.0 μm	**29**
GaAs/ Alox (I)	BPM/ SHG	1.1 mW	2.3 μW	0.21 %	4.5	8 ps, 1.605 μm	**30**
GaAs/ AlAs	BPM/ DFG	7 mW^2	0.12 μW	-	500	cw, 1.32 μm+1.0 μm	**31**
GaAs/ Alox (II)	**BPM/ SHG**	**5 mW[a]**	**650 μW**	**1.3 %**	**>1000**	**200 fs, 2.01 μm**	**32**
AlGaAs	BPM/ P.F.	-	4 nW	-	1000	cw, 0.95-1.064 μm	**33**
GaAs/ AlAs (I)	**QPM/ SHG**	**2.3 mW[a]**	**25 nW**	**3×10^{-5} %**	**0.15**	**250 fs, 1.48-1.52 μm**	**34**
GaAs/ AlAs (II)	**QPM/ SHG**	**11 mW[a]**	**1.5 μW**	**0.002 %**	**1.2**	**250 fs, 1.534 μm**	**35**
AlGaAs	QPM/ SFG	0.0165 mW^2	0.4 nW	-	810	cw, 1.54 + 1.575 μm	**36**
AlGaAs	QPM/ SHG	-	-	4.9 $\%W^{-1}$	-	cw, 1.466 μm	**37**
AlGaAs	QPM/ SHG	-	-	15 $\%W^{-1}$	-	cw, 1.542 μm	**38**
$Al_xGa_{1-x}As$	QPM/ SHG	-	-	-	0.02 pm/V[b]	cw, 1.48-1.62 μm	**39**
MgO: $LiNbO_3$	QPM/ SHG	12.3 mW	1.2 mW	-	1000	cw, 0.75-0.84 μm,	**19**
PPLN	QPM/ SHG	-	-	-	150	cw, 1.5365 μm	**24**
Ti: $LiNbO_3$	QPM/ DFG	2 +110 μW	-	105 $\%W^{-1}$	1.6	cw, 1.56 μm+3.39 μm	**15**
MgO: $LiNbO_3$	QPM/ SHG	42 mW	5.5 mW	-	1200	cw, 0.867 μm	**16**
$LiTaO_3$	QPM/ SHG	34 mW	4.5 mW	13 %	-	Quasi cw, 0.856 μm	**18**
Polymer	QPM/ SHG	-	-	-	0.05	6 ps, 1.62 μm	**27**

GaAs/ AlAs	**MPM/ SHG**	**20 mW[a]**	**10.3 μW**	**0.015 %**	**2**	**250 fs, 1.505/1.54 μm**	**40**
Polymer	MPM/ SHG	133 mW	1.2 μW	-	39	cw, 0.815 μm	**41**
Polymer	MPM/ SHG	-	-	-	14	6-8 ps, 1.55 μm	**25**
Polymer	MPM/ SHG	4.5 mW	38 μW	-	245	95 fs, ~0.8 μm	**28**
GaAs/Ge /GaAs	OPQPM/ SHG	-	-	0.002 $\%W^{-1}$	-	cw, 1.5761 μm	**9**
GaAs/ AlGaAs	PSNQPM/ SHG	1 mW	1 μW	0.1 %	-	250 fs, 2.0 μm	**8**
AlGaAs	CDI[c]/ SHG	475 μW	0.2 nW	1.4 % W^{-1}	-	cw, 1.5118 μm	**42**
GaAs	OPQPM/ SHG	100 μJ	-	33 %	-	65 ns, 4.135 μm	**11**
AlGaAs	OPQPM/ SHG	2 nW	10 mW	-	-	1.564 μm	**12**
GaAs	Diffusion Bonding/ SHG	-	-	24 %	-	60 ns, 10.59 μm	**13**
GaAs	Diffusion Bonding/ DFG	17 mJ	2 μJ	0.034 %	-	60 ns, 1.95μm+2.34 μm	**14**

a Estimated coupled power ***b*** Effective nonlinear susceptibility modulation **c** Crystal domain inversion.

Table 8.4 Review of experiments that demonstrated nonlinear frequency conversion in different waveguides using various techniques.

8.3 Future work

The promising results obtained in the present work leave open scope for further research and development in the area of nonlinear frequency conversion in GaAs-based waveguides. In close relation to the experiments presented in this thesis, a subsequent step forward would involve demonstration of second harmonic generation in the same waveguides using picosecond and continuous-wave pump sources. Such an effort would result in a better understanding of the dynamics of the process (since group velocity related effects would vanish) and thus allow a more accurate calculation of the efficiencies. It is also possible that in the picosecond regime larger efficiencies are available (despite the lower peak powers), due to the fact that in this time scale longer interaction length and complete exploitation of the pump bandwidth is expected. Additionally, pulse duration measurements for the generated second harmonic signal would be interesting for a deeper insight into the process, although such a measurement is non-trivial due to the low power levels available.

Accessing longer wavelengths in the mid-IR is also possible in these waveguides, through difference frequency generation. For example, a tunable mid-IR source around ~6 μm could be obtained by means of difference frequency mixing of the signal and idler beams from the OPO. However, the ultimate infrared source based on GaAs-waveguides is unquestionably an integrated optical parametric oscillator. Two main intermediate steps are necessary towards the realisation of such a device: a) parametric fluorescence measurements, which are vital for the improvement of the available technology by providing information on parametric gain, potential conversion efficiency and tuning range, and b) Bragg-mirror deposition on GaAs facets. With regard to the latter, the technology developed by collaborators at Thomson CSF and Glasgow is achieving improved results and high reflecting Si/SiO_2 mirrors have been demonstrated by use of chemical assisted ion-beam deposition.

A final task of great interest for the realisation of a truly monolithic device is the integration of the nonlinear waveguide with the pump laser source. This is indeed a realistic target that would offer a compact, tunable source, which would suffer to a lesser extend from the coupling complications and losses that dominate the hybrid schemes investigated in the present work.

References

[1] R. Regener, and W. Sohler, *Efficient second harmonic generation in Ti:LiNbO$_3$ channel waveguide resonators*, J. Opt. Soc. Am. B 5, 267, (1988)

[2] G.I. Stegeman, and R.H. Stolen, *Waveguides and fibers for nonlinear optics*, J. Opt. Soc. Am. B 6, 652, (1988)

[3] D. Modotto, *private communication*

[4] A. De Rossi, *private communication*

[5] B. Oster, and H. Fouckhardt, *M-waveguide structures for direct phase matching in AlGaAs*, Appl. Phys. B 73, 535, (2001)

[6] M. Ohashi, T. Kondo, R. Ito, S. Fukatsu, Y. Shiraki, K. Kumata, and S.S. Kano, *Determination of quadratic nonlinear optical coefficient of $Al_xGa_{1-x}As$ system by the method of reflected second harmonics*, J. Appl. Phys. 74, 596, (1993)

[7]] E.U. Rafailov, P.L. Alvarez, C.T.A. Brown, W. Sibbett, R.M. De La Rue, P. Millar, D.A. Yanson, J.S. Roberts, P.A. Houston, *Second-harmonic generation from a first-order quasi-phase-matched GaAs/AlGaAs waveguide crystal*, Opt. Lett. 26, 1984, (2001)

[8] E.U. Rafailov, P. Loza-Alvarez, D. Artigas, M.B. Flynn, W. Sibbett, *Novel type semiconductor waveguide crystal for efficient frequency up/down conversion*, NLMD5-1, OSA Digest, Nonlinear guided waves and their applications, Italy, September 1-4, (2002)

[9] S. Koh, T. Kondo, Y. Shiraka, R. Ito, *GaAs/Ge/GaAs sublattice reversal expitaxy and its application to nonlinear optical devices*, J. Cryst. Growth 227-228, 183, (2001)

[10] L.A. Eyres, P.J. Tourreau, T.J. Pinguet, C.B. Ebert, J.S. Harris, M.M. Fejer, L. Becouarn, B. Gerard, E. lallier, *All-epitaxial fabrication of thick, orientation-patterned GaAs films for nonlinear optical frequency conversion*, Appl. Phys. Lett. 79, 904, (2001)

[11] T. Skauli, K.L. Vodopyanov, T.J. Pinguet, A. Schober, O. Levi, L.A. Eyres, M.M. Fejer, J.S. Harris, B. Gerard, L. Becouarn, E. Lallier, G. Arisholm, *Measurement of the nonlinear coefficient of orientation-patterned GaAs and demonstration of highly efficient second-harmonic generation*, Opt. Lett. 27, 628, (2002)

[12] X. Yu, L. Scaccabarozzi, O. Levi, T.J. Pinguet, M.M. Fejer, J.S. Harris Jr., *Template design and fabrication for low-loss orientation-patterned nonlinear AlGaAs waveguides pumped at 1.55 μm*, J. Cryst. Growth. 251, 794, (2003)

[13] E. Lallier, M. Brévignon, J. Lehoux, *Efficient second-harmonic generation of a CO_2 laser with a quasi-phase-matched GaAs crystal*, Opt. Lett. 23, 1511, (1998)

[14] E. Lallier, L. Becouarn, M. Brévignon, J. Lehoux, *Infrared difference frequency generation with quasi-phase-matched GaAs*, Electron. Lett. 34, 1609, (1998)

[15] D. Hofmann, G. Schreiber, C. Haase, H. Hermann, W. Grundkötter, R. Ricken, W. Sohler, *Quasi-phase-matched difference-frequency generation in periodically poled Ti: LiNbO$_3$ channel waveguides*, Opt. Lett. 24, 896, (1999)

[16] K. Mizuuchi, H. Ohta, K. Yamamoto, M. Kato, *Second-harmonic generation with a high-index-clad waveguide*, Opt. Lett. 22, 1217, (1997)

[17] K. Mizuuchi, K. Yamamoto, *Waveguide second-harmonic generation device with broadened flat quasi-phase-matching response by use of a grating structure with located phase shifts*, Opt. Lett. 23, 1880, (1998)

[18] K. Yamamoto, K. Mizuuchi, Y. Kitoaka, M. Kato, *Highly efficient quasi-phase-matched second-harmonic generation by frequency doubling of a high-frequency superimposed diode laser*, Opt. Lett. 20, 273, (1995)

[19] T. Sugita, K. Mizuuchi, Y. Kitaoka, K. Yamamoto, *Ultraviolet light generation in a periodically poled MgO: LiNbO3 waveguide*, Jap. J. Appl. Phys. 40, 1751, (2001)

[20] D. Sato, T. Morita, T. Suhara, M. Fujimara, *Efficiency improvement by high-index cladding in $LiNbO_3$ waveguide quasi-phase-matched wavelength converter for optical communication*, IEEE Phot. Tech. Lett. 15, 569, (2003)

[21] B. Zhou, C.-Q. Xu, B. Chen, *Comparison of difference frequency generation and cascaded $\chi^{(2)}$ based wavelength conversions in $LiNbO_3$ quasi-phase-matched waveguides*, J. Opt. Soc. Am. B 20, 846, (2003)

[22] J. Webjörn, S. Siala, D.W. Nam, R.G. Waarts, R.J. Lang, *Visible laser sources based on frequency doubling in nonlinear waveguide*, IEEE J. Quant. Electron. 33, 1673, (1997)

[23] E.J. Lim, H.M. Hertz, M.L. Bortz, M.M. Fejer, *Infrared radiation generated by quasi-phase-matched difference-frewuency mixing in a periodically poled lithium niobate waveguide*, Appl. Phys. Lett. 59, 2207, (1991)

[24] K.R. Parameswaran, R.K. Route, J.R. Kurz, R.V. Roussev, M.M. Fejer, M. Fujimara, *Highly efficient second-harmonic generation in buried waveguides formed by annealed and reverse proton exchange in periodically poled lithium niobate*, Opt. Lett. 27,179, (2002)

[25] M. Jäger, G.I. Stegeman, M.C. Flipse, M. Diemeer, G. Möhlmann, *Modal dispersion phase matching over 7 mm length in over damped polymeric channel waveguides*, Appl. Phys. Lett. 69, 4139, (1996)

[26] W. Wirges, S. Yilmaz, W. Brinker, S. Bauer-Gogonea, S. Bauer, M. Jäger, G.I. Stegeman, M. Ahlheim, M. Stähelin, B. Zysset, F. Lehr, M. Diemeer, M.C. Flipse, *Polymer waveguides with optimized overlap integral for modal dispersion phase-matching*, Appl. Phys. Lett. 70, 3347, (1997)

[27] M. Jäger, G.I. Stegeman, W. Brinker, S. Yilmaz, S. Bauer, W.H.G. Horsthuis, G.R. Mohlmann, *Comparison of quasi-phase-matching geometries for second-harmonic generation in poled polymer channel waveguides at 1.5 μm*, Appl. Phys. Lett. 68, 1183, (1996)

[28] T. Dai, K.D. Singer, R.J. Twieg, T.C. Kowalczyk, *Anomalous-dispersion phase-matched second-harmonic generation in polymer waveguides: chromophores for increased efficiency and ultraviolet stability*, J. Opt. Soc. Am. B 17, 412, (2000)

[29] A. Fiore, V. Berger, E. Rosencher, P. Bravetti, N. Laurent, J. Nagle, *Phase-matched mid-infrared difference frequency generation in GaAs-based waveguides*, Appl. Phys. Lett. 71, 3622, (1997)

[30] A. Fiore, S. Janz, L. Delobel, P. van der Meer, P. Bravetti, V. Berger, E. Rosencher, J. Nagle, *Second-harmonic generation at λ = 1.6 μm in AlGaAs/Al_2O_3 waveguides using birefringence phase matching*, Appl. Phys. Lett. 72, 2942, (1998)

[31] P. Bravetti, A. Fiore, V. Berger, E. Rosencher, J. Nagle, O. Gauthier-Lafaye, *5.2–5.6 μm source tunable by frequency conversion in a GaAs-based waveguide*, Opt. Lett. 23, 331, (1998)

[32] K. Moutzouris, *PhD Thesis, also:* K. Moutzouris, S. Venugopal Rao, M. Ebrahimzadeh, A. De Rossi, V. Berger, M. Calligaro, V. Ortiz, *Efficient second-harmonic generation in GaAs/AlGaAs waveguides using birefringent phase matching*, Opt. Lett. 26, 1785, (2001)

[33] A. De Rossi, V. Berger, M. Calligaro, G. leo, V. Ortiz, X. Marcadet, *Parametric fluorescence in oxidized aluminum gallium arsenide waveguides*, Appl. Phys. Lett. 79, 3758, (2001)

[34] K. Moutzouris, *PhD Thesis, also:* A.S. Helmy, D.C. Hutchings, T.C. Kleckner, J.H. Marsh, A.C. Bryce, J.M. Arnold, C.R. Stanley, J.S. Aitchison, C.T.A. Brown, K. Moutzouris, M. Ebrahimzadeh, *Quasi-phase matching in GaAs–AlAs superlattice waveguides through bandgap tuning by use of quantum-well intermixing*, Opt. Lett. 25, 1370, (2000)

[35] K. Moutzouris, *PhD Thesis, also:* K. Zeaiter, D. C. Hutchings, R. M. Gwilliam, K. Moutzouris, S. Venugopal Rao, M. Ebrahimzadeh, Quasi-phase matched second-harmonic generation in GaAs/AlAs superlattice waveguide using ion-implantation induced intermixing, Opt. Lett.28, 911, (2003)

[36] C.Q. Xu, K. Takemasa, K. Nakamura, H. Okayama, T. Kamihoh, *AlGaAs semiconductor quasi-phase-matched wavelength converters*, Jap. J. Appl. Phys. 37, 823, (1998)

[37] S.J.B. Yoo, R. Bhat, C. Caneau, M.A. Koza, *Quasi-phase-matched second-harmonic generation in AlGaAs waveguides with periodic domain inversion achieved by wafer bonding*, Appl. Phys. Lett. 66, 3410, (1995)

[38] S. Janz, C. Fernando, H. Dai, F. Chatenoud, R. Normandin, *Quasi-phase-matched second-harmonic generation in reflection from $Al_xGa_{1-x}As$ heterostructures*, Opt. Lett 18, 589, (1993)

[39] J.-P. Bouchard, M. Tetu, S. Janz, D.-X. Xu, Z. R. Wasilewski, P. Piva, U. G. Akano, I. V. Mitchell, *Quasi-phase matched second-harmonic generation in an $Al_xGa_{1-x}As$ asymmetric quantum-well waveguide using ion-implantation-enhanced intermixing*, Appl. Phys. Lett. 77, 4247, (2000)

[40] K. Moutzouris, *PhD Thesis, also:* K. Moutzouris, S. Venugopal Rao, M. Ebrahimzadeh, A. De Rossi, M.Calligaro, V. Ortiz, and V. Berger, *Femtosecond second-harmonic generation through optimised modal phase matching in semiconductor waveguides*, Appl. Phys. Lett. In Press

[41] T.C. Kowalczyk, K.D. Singer, P.A. Cahill, *Anomalous-dispersion phase-matched second-harmonic generation in a polymer waveguide*, Opt. Lett. 15, 2273, (1995)

[42] C.-Q. Xu, K. Takemasa, K. Nakamura, H. Wada, T. Takamori, H. Okayama, T. Kamijoh, *Confirmation of AlGaAs crystal domain inversion using asymmetric wet etching and optical second-harmonic generation methods*, Jap. J. Appl. Phys. 35, 1419, (1996)

APPENDIX A. ULTRASHORT PULSE CONSIDERATIONS

A.1 Pulse propagation

Ultrashort (femtosecond) and short (pico- and nano-second) pulses are of great interest for a number of applications including the purposes of this thesis. In this section, only a brief account of basic concepts related to pulse propagation is given. Analytical discussion on the formulation that follows can be found in a number of sources [1-3]. We start by considering an optical signal at a central frequency ω_0 enclosed in a pulse envelope, which assumes a Gaussian shape. The signal amplitude can then be written as:

$$E(t,z) \propto \exp(-iat^2)\exp(i\phi) \tag{A-1}$$

In the simplest case, the total phase is $\phi = \omega_o t - kz$ (where k is the propagation constant) and relates to the instantaneous frequency ω_i of the sinusoidal signal within the envelope by $\omega_i = d\phi/dt = \omega_0$. This behaviour indicates that no sub-structure appears within the envelope and such a pulse is often referred to as unchirped. However, it is possible that the total phase has a quadratic (or even more complicated) dependence on time given by an equation of the form:

$$\phi = \omega_0 t + bt^2 - kz \tag{A-2}$$

Thus, the instantaneous frequency acquires a linearly varying time dependence:

$$\omega_i = d\phi/dt = \omega_0 + 2bt \tag{A-3}$$

Such a signal is usually called chirped and b is the chirp parameter. Positive chirp (b>0) suggests that the instantaneous frequency increases in time, implying that the leading edge of the pulse is red-shifted in relation to the central wavelength and the trailing edge is blue-shifted. Negative chirp (b<0) is the opposite situation.

It has been discussed in Chapter 2 that time-harmonic fields can be represented in the frequency domain through a Fourier transform integral. Following a Fourier analysis, it can be shown [2] that a pulsed signal with a temporal duration $\Delta\tau$ has a frequency content defined by the spectral FWHM bandwidth $\Delta\nu$, which is given by:

$$\Delta\nu\Delta\tau = X\sqrt{1+(b/a)^2} \tag{A-4}$$

The coefficients a and b have been defined before and X has a value that depends on the exact envelope profile. For example, a Gaussian envelope results in X~0.44, while

a sech^2 pulse profile gives X~0.31. Clearly, Eq. (A-4) indicates that a specific frequency bandwidth supports a minimum pulse duration for b=0. Such a pulse is termed transform limited. In presence of pulse chirping (b≠0), a temporally broader pulse corresponds to the same frequency bandwidth.

Due to the large frequency bands that accompany short pulses, a number of effects have to be considered to describe the propagation of a pulse in a dispersive medium. Dispersion is usually introduced through the definition of the propagation constant:

$$k(\omega) = \frac{\omega}{c} n(\omega) \tag{A-5}$$

The physical interpretation of the dispersion-related effects is greatly assisted by expanding k in a Taylor series around the central carrier frequency ω_0 as:

$$k(\omega) = k(\omega_0) + \frac{dk(\omega)}{d\omega}\Big|_{\omega_0}(\omega-\omega_0) + \frac{1}{2!}\frac{d^2k(\omega)}{d\omega^2}\Big|_{\omega_0}(\omega-\omega_0)^2 + \\ + \frac{1}{3!}\frac{d^3k(\omega)}{d\omega^3}\Big|_{\omega_0}(\omega-\omega_0)^3 + \ldots \tag{A-6}$$

Clearly, for a pulse with "infinitely" small frequency bandwidth –and hence infinitely large pulse duration- (monochromatic, continuous wave operation) all terms of the expansion but the first can be neglected. This first term is related to the phase velocity v_ϕ, which measures the propagation velocity of the central frequency line ω_0. The exact behaviour of the phase velocity in a specific medium depends on the dispersion relation, as this is semi-empirically determined by the Sellmeier equations of the medium. Conventionally, when the refractive index $n(\omega)$ and its derivative $dn(\omega)/d\omega$ increase with frequency dispersion is said to be positive or normal. In the opposite situation the system possesses negative or abnormal dispersion. Since different frequency lines travel with different phase velocities, for short pulses with large frequency bandwidths the group velocity is introduced to measure the propagation velocity of the pulse envelope. The group velocity v_g appears in the second term of the above equation. In presence of positive dispersion both the phase and group velocity decrease with frequency[1].

Higher order terms in Eq. (A-6) are connected to higher order dispersion effects. In particular, the third term represents group velocity dispersion (GVD), which is

[1] This is clear considering the expressions presented in Table 1.

responsible for changes in the shape of the temporal pulse envelope. The following term represents third order dispersion (TOD) and so forth higher order terms. It should be noted that for higher order terms in Eq (A-6) to be significant, larger bandwidths are required. In fact, to a first approximation, third and higher order dispersion can be neglected for pulses exceeding ~50 fs in duration. Table A1 depicts the exact expressions for these quantities.

v_ϕ	$\left[\frac{m}{s}\right]$	$\left[\frac{k(\omega_0)}{\omega_0}\right]^{-1} = \frac{c}{n(\omega_0)}$
v_g	$\left[\frac{m}{s}\right]$	$\left[\frac{dk(\omega)}{d\omega}\Big\|_{\omega_0}\right]^{-1} = \left[\frac{1}{c}\left(n(\omega_0) + \omega_0 \frac{dn(\omega)}{d\omega}\Big\|_{\omega_0}\right)\right]^{-1} = \left[\frac{1}{c}\left(n(\lambda_0 - \lambda_0 \frac{dn(\lambda)}{d\lambda}\Big\|_{\lambda_0}\right)\right]^{-1}$
GVD	$\left[\frac{s^2}{m}\right]$	$\frac{d^2k(\omega)}{d\omega^2}\Big\|_{\omega_0} = \frac{1}{c}\left(2\frac{dn(\omega)}{d\omega}\Big\|_{\omega_0} + \omega_0 \frac{d^2n(\omega)}{d\omega^2}\Big\|_{\omega_0}\right) = \frac{\lambda_0^3}{2\pi c^2}\frac{d^2n(\lambda)}{d\lambda^2}\Big\|_{\lambda_0}$
TOD	$\left[\frac{s^3}{m}\right]$	$\frac{d^3k(\omega)}{d\omega^3}\Big\|_{\omega_0} = \frac{1}{c}\left(3\frac{d^2n(\omega)}{d\omega^2}\Big\|_{\omega_0} + \omega_0 \frac{d^3n(\omega)}{d\omega^3}\Big\|_{\omega_0}\right) = \frac{-\lambda_0^4}{2\pi^2c^4}\left(3\frac{d^2n(\lambda)}{d\lambda^2}\Big\|_{\lambda_0} + \lambda_0 \frac{d^3\lambda(\omega)}{d\lambda^3}\Big\|_{\lambda_0}\right)$

Table A.1 Units and expressions for the phase velocity v_ϕ, group velocity v_g, group velocity dispersion (GVD) and third order dispersion (TOD).

In the context of nonlinear frequency conversion with use of ultrashort pulses, a number of issues related to the above quantities have to be addressed. First of all, matching the phase velocities of the interacting waves is required for the process to build up in useful material lengths. This problem (phase matching) has been discussed extensively in Chapter 2. However, even under perfect phase matching conditions the interaction length is limited by mismatch of the group velocities of the interacting pulses. Evidently, the group velocity mismatch (GVM) between two pulses with central frequencies ω_1 and ω_2 is given by:

$$GVM[s/m] = \frac{1}{v_g(\omega_1)} - \frac{1}{v_g(\omega_1)} \tag{A-7}$$

The group velocity mismatch (or temporal walk-off) as defined above measures the time separation of the two pulses after a unit length of propagation in the dispersive medium. This can be used to define the actual interaction length, as the length L over which the two pulses of duration $\Delta\tau$ do not overlap any more:

$$L = \frac{\Delta\tau}{GVM} \tag{A-8}$$

In turn, group velocity dispersion is responsible for temporal broadening of the pulse by introducing a linear phase chirp across the pulse. This can be understood as follows: Form table A.1 it is clear that GVD can be written as:

$$GVD = \frac{d}{d\omega}\left(\frac{1}{v_g}\right) = -\frac{1}{v_g^2}\frac{dv_g}{d\omega} \tag{A-9}$$

Eq. (A-9) suggests that the value of GVD is positive when the group velocity decreases as frequency increases. In this case, blue components travel slower and therefore can be found in the trailing edge of the pulse (normal dispersion). Thus, the instantaneous frequency increases in time, suggesting that the pulse is positively chirped (b>0). Applying similar argumentation, one can easily conclude that in presence of negative GVD (abnormal dispersion) the pulse is negatively chirped (b<0). The pulse broadening of an initially transform limited, unchirped pulse with duration $\Delta\tau$, after propagation of length z in a dispersive medium, can be quantified as [1]:

$$\Delta\tau_z = \Delta\tau \cdot \sqrt{1 + \frac{z^2}{z_D^2}} \tag{A-10}$$

where $\Delta\tau_z$ is the pulse duration at z and z_D is referred to as the dispersion length[2] given by:

$$z_D = \frac{\Delta\tau^2}{4\ln(2)}(GVD)^{-1} \tag{A-11}$$

It should be noted that in Eqs. (A-4) and (A-10) the second power of GVD and the chirp parameter b are involved. Therefore, a pulse travelling in a dispersive medium (irrespectively of the sign of GVD) faces a two-fold effect: a) it experiences temporal broadening and b) it departs from the transform limit value of the bandwidth-duration product. The effects of third and higher order dispersion will not be further discussed, since they are not of special interest for the purposes of this work.

[2] Clearly from Eq. (A-9) the dispersion length indicates the length of propagation during which the pulse is broadened by a factor of $\sqrt{2}$.

The preceding discussion described phenomena related to the linear refractive index profile of materials. Nonlinear polarisation components can also give rise to pulse shaping effects, mainly via the $\chi^{(3)}$ process known as the optical Kerr effect [4]. In particular, the Kerr effect describes the instantaneous change of the refractive index in presence of intense fields described by:

$$n = n_0 + n_2 I \tag{A-12}$$

The nonlinear refractive index n_2 is responsible for the modulation of optical signals both spatially (self-focusing) and in the time domain (self-phase modulation). Self-phase modulation (SPM) denotes the change in the instantaneous frequency across the pulse envelope due to the Kerr effect, which according to Eq.(A-12) after propagation in a Kerr-type material of length L is given by:

$$\phi = \omega_0 t - kz = \omega_0 t - \frac{2\pi}{\lambda}(n_0 - n_2 I)L \Rightarrow$$

$$\omega_i = \omega_0 - \frac{2\pi}{\lambda} n_2 L \frac{dI}{dt} \tag{A-13}$$

Thus, the carrier frequency is linearly dependent on the negative time derivative of the corresponding light intensity. Interestingly, around the peak of the pulse (that is, in the area where the pulse's time profile is nearly parabolic) the intensity derivative can be taken as a linear function of time with negative values. In combination with the fact that n_2 is positive for most materials, this suggests that SPM gives rise to an approximately linear positive chirp, equivalent to the chirp produced by propagation through material exhibiting positive GVD. Clearly, the linear chirp due to GVD and the nearly linear positive chirp due to SPM add up (cancel out) in a positively (negatively) dispersive medium.

It has been shown that group velocity dispersion, third and higher order dispersion as well as self-phase modulation set the temporal limit in pulse generation. Of all these effect GVD is the dominating obstacle for pulse durations of the order of ~100 fs. In the following section available mechanisms for compensating for GVD are presented.

A.2 Group velocity dispersion compensation

A number of designs using pairs of prisms [5], pairs of diffraction gratings [6] and chirped mirrors [7] have been proposed to compensate for GVD. The first scheme is of special interest for this work and its working principle will be outlined. The prism pair set-up is shown in Fig. A.1. The prism apex angle is cut such that at minimum deviation of the centre wavelength (i.e., with incidence angle equal to exiting angle), the angle of incidence is the Brewster angle. Thus, the Fresnel reflection losses for the correct linear polarization are minimized. In essence, this arrangement creates a longer path through the prism material for the red wavelengths compared to the blue, introducing a negative dispersion (even though the dispersion of the glass material itself is positive). Provided the prism separation, *l* (defined tip to tip) is sufficiently large, the positive dispersion of the prism material can be balanced.

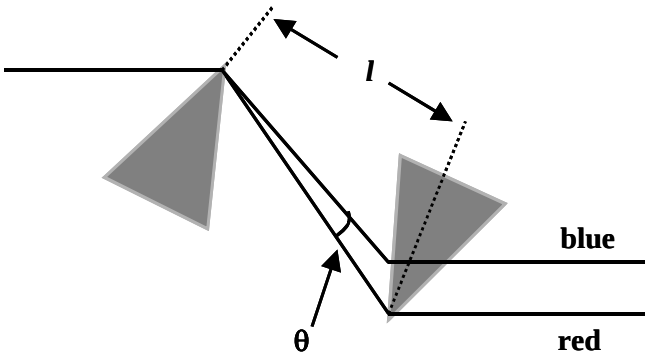

Fig. A.1 Pair of prism scheme exhibiting negative and controllable GVD.

It can be shown that the double pass total dispersion of the prism pair is given by:

$$GVD = \frac{\lambda}{cL}\frac{d^2P}{d\lambda^2} \tag{A-14}$$

In the above, P is the optical path length, L the physical length of the light path and the derivative $d^2P/d\lambda^2$ is the following function of angular divergence θ, the refractive index of the prism glass n and the apex separation *l*:

$$\frac{d^2P}{d\lambda^2} = 4l\left\{\left[\frac{d^2n}{d\lambda^2} + \left(2n - \frac{1}{n^3}\right)\left(\frac{dn}{d\lambda}\right)^2\right]\sin(\theta) - 2\left(\frac{dn}{d\lambda}\right)^2\cos(\theta)\right\} \tag{A-15}$$

Eqs. (A-14), (A-15) suggest that continuous adjustment of dispersion from negative to positive values through zero can be achieved by translating individual prisms to vary the amount of glass as well as by changing the prism separation.

A.3 Pulse duration measurements

Measuring the exact duration of light pulses is necessary for most of the applications they are used for. For instance, knowledge of the pulse duration of the OPO source used in the SHG experiments presented earlier is vital, since it is needed to calculate the interaction length and the conversion efficiency of the process. It is self-evident that to resolve temporally an event, a second event of the same or shorter time duration is required. Fast photo-detectors and electron-optical streak cameras can provide information for pulses in the picosecond regime. Events with time durations of tens or a few hundreds of femtoseconds, however, are “instantaneous” for all instruments engineered to this day. Therefore, the only direct way to measure a femtosecond pulse is by use of the pulse itself. On this direction, the simplest and most widely used pulse measurement is achieved through autocorrelation [8]. More recently, less direct time-frequency domain methods have been developed, namely the frequency-resolved optical grating technique [9] and sonogram tracing [10].

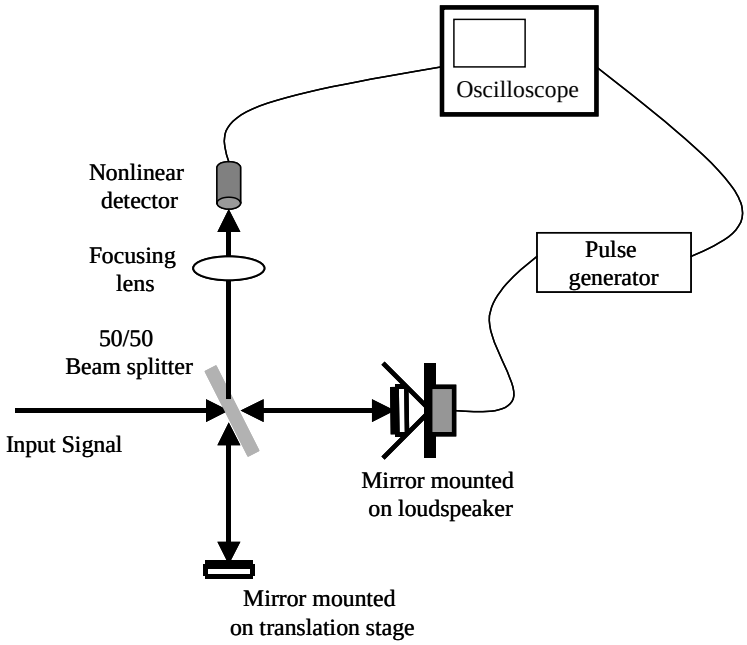

Fig. A.2 Standard autocorrelator arrangement

The typical autocorrelation arrangement is depicted in Fig. A.2. The incoming train of pulses is split into two trains of identical intensity by a symmetric beam splitter. The pulses are passed through a Michelson-type interferometer, which delivers spatially collinear and temporally overlapped beams on a second-order nonlinear detection scheme. One of the two arms of the interferometer is terminated by a mirror that is mounted on a translation stage and allows manual control of the optical delay. The

other arm uses a mirror mounted on an audio loudspeaker that introduces the necessary variable delay τ for autocorrelation tracing. The nonlinear response of the detection scheme ensures that the signal observed in an oscilloscope is proportional to the degree of overlap of the pulses: when the path lengths for the two replica beams are equal, the pulses exactly coincide at the detector and the amount of generated signal is maximised. As the speaker changes the delay, the temporal overlap of the pulses reduces and the signal drops. Standard detection methods involve second harmonic generation (SHG) in nonlinear crystals [8]. Alternatively, the quadratic response of a semiconductor device to light wavelengths below the bandgap via two-photon absorption (TPA) has been demonstrated [11]. TPA autocorrelation has a number of advantages over SHG autocorrelation, including low cost, accessibility of the mid-IR wavelengths, lack of phase matching complications and was exclusively used for the OPO characterisation.

It can be shown that the second order autocorrelation signal oscillate according to:

$$g_2(\tau) = 1 + \frac{2\int_{-\infty}^{\infty} E^3(t)E(t+\tau)dt + 2\int_{-\infty}^{\infty} E(t)E^3(t+\tau)dt + 3\int_{-\infty}^{\infty} E^2(t)E^2(t+\tau)dt}{\int_{-\infty}^{\infty} E^4(t)dt} \quad \text{(A-16)}$$

where the time-dependent electric field E(t) assumes a form similar to Eq. (A-1). At zero time delay (τ=0) the signal is maximum and obtains a normalised value of $g_2(0)=8$, as Eq. (A-16) indicates. For a delay increment of one-half light period, the two fields add with opposite phase resulting in a near-zero signal. Hence, the fringe separation in the signal corresponds to one optical period at the centre wavelength, providing a direct self-calibration of the measurement. For large delay times ($\tau\rightarrow\infty$) the two pulses are no longer overlapping and the intensity of the signal reduces to a background level, which according to Eq. (A-16) is equal to $g_2(\infty)=1$. Therefore, the fringes are expected to have a peak-to-background ratio of $g_2(0)/ g_2(\infty)=8:1$. This ratio may not be satisfied in the case a frequency chirp is present in the pulse. In fact, a variation of the instantaneous frequency across the pulse results in a reduced interference between the delayed pulses and thus, compromises the fringe visibility.

It should be noted that autocorrelation as described above presupposes that the detection response time is fast enough to resolve individual fringes[3]. In turn, this requires that the frequency of the loudspeaker is relatively low, so that the mirror scans through one fringe within the response time of the detector. This type of autocorrelation is referred to as fast or interferometric. With increasing scanning frequency, the time average of $g_2(\tau)$ can be obtained, which can be shown as:

$$G_2(\tau) = < g_2(\tau) > = 1 + \frac{2\int_{-\infty}^{\infty} E^2(t)E^2(t+\tau)dt}{\int_{-\infty}^{\infty} E^4(t)dt} \qquad \text{(A-17)}$$

This output is known as the slow or intensity autocorrelation. Applying similar arguments as before, it is clear that the intensity autocorrelation trace exhibits a contrast ration between the signal peak and the background of $G_2(0)/ G_2(\infty)=3:1$. Translating the stationary mirror by a set length, results in a shift of the trace across the horizontal axis of the oscilloscope. This shift corresponds to the time needed for the light to double-pass the length of translation, providing a means of time-calibration of the measurement. It should be mentioned that, unlike the interferometric, no phase information is contained within intensity autocorrelations.

It is practically impossible to retrieve the exact pulse profile from an autocorrelation trace. This induces an ambiguity to the measurement, since the actual FWHM pulse duration $\Delta\tau$ is related to the FWHM of the autocorrelation Δt width via:

$$\Delta\tau = \frac{\Delta t}{k}$$

where k is a constant that depends on the pulse shape. Values of k for different pulse profiles are given in table A.2

Intensity Profile	Interferometric autocorrelation	Intensity autocorrelation
Gaussian	k=1.697	k=1.414
$Sech^2$	k=1.897	k=1.543

Table A.2 Theoretical conversion factors for interferometric and intensity autocorerlation

[3] It is common practise to improve the time response of the detector by impedance matching the oscilloscope to the detector with a suitable termination resistor.

References

[1] G.P. Agrawal, *Nonlinear fibre optics*, Academic Press, London, (1989)

[2] A.E. Siegman, *Lasers*, University Science Books, Mill Valley, (1986)

[3] O. Svelto, *Principles of lasers*, 4th edition, Plenum Press, (1998)

[4] R.W. Boyd, *Nonlinear optics*, Academic Press, California, (1992)

[5] R.L. Fork, O.E Martinez, and J.P. Gordon, *Negative dispersion using a pair of prisms*, Opt. Lett. 9, 150, (1984)

[6] E.B. Treacy, *Optical pulse compression with diffraction gratings*, IEEE J. Quantum Elctron. 5, 454, (1969)

[7] R. Szipocs, K. Ferencz, C. Spielmann, and F. Krauz, *Chirped multiplayer coatings for broadband dispersion control in femtosecond lasers*, Opt. Lett. 19, 204, (1994)

[8] H.P. Weber, *Method for pulsewidth measurement of ultrashort light pulses generated by phase-locked lasers using nonlinear optics*, J. Appl. Phys. 38, 2231, (1967)

[9] D.J. Kane, G. Rodriguez, A.J. Taylor, and T.S. Clement, *Simultaneous measurement of two ultrashort laser pulses from a single spectrogram in a single shot*, J. Opt. Soc. Am. B 14, 935, (1997)

[10] D.T. Reid, *Algorithm for complete and rapid retrievel of ultrashort pulse amplitude and phase from a sonogram*, IEEE J. Quantum Electron. 35, 1584, (1999)

[11] D.T. Reid, M. Padgett, C. McGowan, W. Sleat, and W. Sibbett, *Light-emitting diodes as measurement devices for femtosecond laser pulses*, Opt. Lett. 22, 233, (1997)

APPENDIX B. PUBLICATIONS ARISING FROM THIS WORK

(a) Publications in refereed journals

1. S. Venugopal Rao, K. Moutzouris, and M. Ebrahimzadeh, "*Nonlinear frequency conversion in semiconductor optical waveguides using birefringent, modal, and quasi-phase-matching techniques*"
   Journal of Optics A: Pure and Applied Optics 6, 569, (2004)
2. K. Moutzouris, S. Venugopal Rao, M. Ebrahimzadeh, A. De Rossi, M.Calligaro, V. Ortiz, and V. Berger, "*Second harmonic generation through optimized modal phase matching in semiconductor waveguides*",
   Applied Physics Letters 83, 620, (2003)
3. K. Zeaiter, D.C. Hutchings, R.M. Gwilliam, K. Moutzouris, S. Venugopal Rao and M. Ebrahimzadeh, "*Quasi-phase matched second harmonic generation in GaAs/AlAs superlattice waveguide using ion-implantation induced intermixing*",
   Optics Letters 28, 911, (2003)
4. V. Loyo-Maldonado, H.K. Lee, C.R. Stanley, S. Venugopal Rao, K. Moutzouris, M. Ebrahimzadeh, and J.S. Aitchison, "*Generation of ultra short electrical pulses in semiconductor waveguides*",
   IEEE Photonics Technology Letters 15, 428, (2003)
5. S. Venugopal Rao, K. Moutzouris, M. Ebrahimzadeh, A. De Rossi, M.Calligaro, V. Ortiz, G. Ginitz, and V. Berger, "*Influence of scattering and two-photon absorption on the optical loss in GaAs/Al_2O_3 nonlinear waveguides measured using femtosecond pulses*",
   IEEE Journal of Quantum Electronics 39, 478, (2003)
6. S. Venugopal Rao, K. Moutzouris, M. Ebrahimzadeh, A. De Rossi, M.Calligaro, V. Ortiz, G. Ginitz, and V. Berger, "*Measurements of optical loss in GaAs/Al_2O_3 nonlinear waveguides in the infrared using femtosecond scattering technique*",
   Optics Communications 213, 223, (2002)
7. K. Moutzouris, S. Venugopal Rao, M. Ebrahimzadeh, A. De Rossi, V. Berger, M. Calligaro and V. Ortiz, "*Efficient second harmonic generation in GaAs/Al_2O_3 waveguides using birefringent phase matching*",
   Optics Letters 26, 1785, (2001)
8. A.S. Helmy, D.C. Hutchings, T.C. Kleckner, J.H. Marsh, A.C. Bryce, J.M. Arnold, C.R. Stanley, J.S. Aitchison, C.T.A. Brown, K. Moutzouris and M Ebrahimzadeh, "*Quasi phase matching in GaAs-AlAs superlattice waveguides through bandgap tuning by use of quantum-well intermixing*",
   Optics Letters 25, 1370, (2000)

(b) Publications in international conference proceedings

9. K. Moutzouris, S. Venugopal Rao, M. Ebrahimzadeh, R.M. Gwilliam, K. Zeaiter, and D. Hutchings, "*Second harmonic generation in first-order quasi-phase-matched GaAs/AlAs superlattice waveguides by use of ion implantation induced intermixing*"
   Conference on Lasers and Electro Optics, Baltimore, USA, June 2003
   CLEO-USA Conference Proceedings, paper CThU4, (2003)
10. K. Moutzouris, S. Venugopal Rao, M. Ebrahimzadeh, A. De Rossi, M.Calligaro, V. Ortiz, and V. Berger, "*Modal phase matching in GaAs/AlGaAs waveguides: second harmonic generation with femtosecond pulses near 1.5 μm*"
    Conference on Lasers and Electro Optics, Baltimore, USA, June 2003
    CLEO-USA Conference Proceedings, paper CtuG1, (2003)

11. K. Moutzouris, S. Venugopal Rao, M. Ebrahimzadeh, A. De Rossi, M.Calligaro, V. Ortiz, and V. Berger, "*Second harmonic generation in GaAs/AlGaAs waveguides with femtosecond pulses near 1.55 mm using modal phase matching technique*"
Conference on Lasers and Electro Optics, Munich, Germany, June 2003
CLEO-EUROPE Conference Digest, paper CE1-3, (2003)

12. K. Zeaiter, D. Hutchings, R.M. Gwilliam, K. Moutzouris, S. Venugopal Rao, and M. Ebrahimzadeh, "*First-order quasi-phase-matched second harmonic generation in GaAs/AlAs superlattice waveguides by use of ion-Implantation induced intermixing*"
Conference on Lasers and Electro Optics, Munich, Germany, June 2003
CLEO-EUROPE Conference Digest, paper CE5-5, (2003)

13. K. Zeaiter, D. Hutchings, K. Moutzouris, S. Venugopal Rao, and M. Ebrahimzadeh, "*Quasi-phase-matched second harmonic generation in an GaAs/AlAs superlattice waveguide using ion-implantation induced intermixing*"
15th Annual Meeting-IEEE Lasers and Electro-Optics Society, Glasgow, Nov 2002
IEEE Annual Meeting Conference Proceedings 1, 81, (2002)

14. K. Moutzouris, S. Venugopal Rao, M. Ebrahimzadeh, A. De Rossi, M. Calligaro, V. Ortiz, G. Ginitz, and V. Berger "*Measurements of optical loss in GaAs/Al_2O_3 nonlinear waveguides in the infrared using femtosecond scattering technique*"
Conference on Lasers and Electro Optics, Long Beach, California May 2002
In Conference Digest and reprinted in: **Trends in Optics and Photonics 73**, **317, (2002)**

15. S. Venugopal Rao, K. Moutzouris, M. Ebrahimzadeh, A. De Rossi, V. Berger, M, Calligaro and V. Ortiz, "*Efficient second harmonic generation in birefringently phase-matched GaAs/Al_2O_3 waveguides using femtosecond pulses at 2.01 mm*"
Conference on Lasers and Electro Optics, Long Beach, California May 2002
In Conference Digest and reprinted in: **Trends in Optics and Photonics 73**, **255, (2002)**

16. V. Loyo-Maldonado, J.S. Aitchison, E. S. Rogers, S. Venugopal Rao, K. Moutzouris, and M. Ebrahimzadeh, "*Generation of ultra short electrical pulses in semiconductor waveguides*"
Conference on Lasers and Electro Optics, Long Beach, California May 2002
In Conference Digest and reprinted in: **Trends in Optics and Photonics 73**, **256, (2002)**

17. A.S. Helmy, D.C. Hutchings, T.C. Kleckner, J.H. Marsh, A.C. Bryce, J.M. Arnold, C.R. Stanley, J.S. Aitchison, C.T.A. Brown, K. Moutzouris, and M. Ebrahimzadeh, "*Quasi-phase-matching in GaAs-AlAs superlattice waveguides via bandgap tuning using quantum well intermixing*"
Conference on Nonlinear Optics: Materials, Fundamentals and Applications, Hawaii, Aug 2000
In Conference Digest and reprinted in: **Trends in Optics and Photonics 46**, **159, (2000)**

18. A.S. Helmy, D.C. Hutchings, T.C. Kleckner, J.H. Marsh, A.C. Bryce, J.M. Arnold, C.R. Stanley, J.S. Aitchison, C.T.A. Brown, K. Moutzouris, M. Ebrahimzadeh, "*Quasi phase matched second harmonic generation by modulating bulk-like $\chi^{(2)}$ coefficients in GaAs-AlAs superlattices superlattices by quantum-well intermixing*"
Conference on Lasers and Electro Optics, San Francisco, May 2000, Post-deadline
In Conference Digest and reprinted in: **Trends in Optics and Photonics 39, 707, (2000)**

19. A.S. Helmy, D.C. Hutchings, T.C. Kleckner, J.S. Aitchison, A.C. Bryce, J.H. Marsh, P. Martin, J.P. Landesman, C.T.A. Brown, K. Moutzouris, M. Ebrahimzadeh, and S.G. Ayling, "*Quantum well intermixing technologies for quasi-phase-matching gratings in GaAs/AlAs superlattice waveguides*"
13th Ann. Meeting-IEEE Lasers and Electro-Optics Society, Puerto Rico, Nov 2000, Invited
IEEE Annual Meeting Conference Proceedings, (2), 712, (2000)

(c) Presentations in meetings

20. K. Moutzouris, S. Venugopal Rao, M. Ebrahimzadeh, A. De Rossi, M.Calligaro, V. Ortiz, G. Ginitz, and V. Berger, "*Measurements of optical loss in GaAs/Al_2O_3 nonlinear waveguides in the infrared using femtosecond scattering technique*"
IEEE Laser and Electro-Optics Society - Scottish Chapter meeting
Edinburgh, Scotland, May 2002

21. S. Venugopal Rao, K. Moutzouris, C.T.A. Brown, M. Ebrahimzadeh, A. De Rossi, V. Berger, M. Calligaro and V. Ortiz, "*Efficient second harmonic generation in GaAs/AlGaAs waveguides using birefringent phase- matching*"
15th biennial meeting of the Institute of Physics
Glasgow, Scotland, September 2001

22. D.C. Hutchings, A.S. Helmy, T.C. Kleckner, K. Zeaiter, J.H .Marsh, J.M Arnold, J.S. Aitchison, C.T.A Brown, K. Moutzouris and M. Ebrahimzadeh, "*Quasi-phase-matching of optical parametric processes in semiconductor waveguides*"
IEEE Laser and Electro-Optics Society - Scottish Chapter meeting
Edinburgh, Scotland, October 2000.

23. S. Venugopal Rao, K. Moutzouris, **M. Ebrahimzadeh,** A. De Rossi, M.Calligaro, V. Ortiz, G. Ginitz, and V. Berger, "Measurements of optical loss in GaAs/Al2O3 nonlinear waveguides in the infrared using femtosecond scattering technique: The role of two-photon absorption"
Scottish Summer School in Physics on Ultrafast Photonics
St Andrews, Scotland, September 2002

The end